**JULIANE RESGES ORIVES**

# SÍNTESE E CARACTERIZAÇÃO DE DIFERENTES FAMÍLIAS DE VIDROS E VITRO-CERÂMICAS (ÓXIDOS, FOSFATOS E FLUORETOS) COM PROPRIEDADES MAGNÉTICAS

Relatório de Pós-doutorado realizado na Universidade Estadual Paulista (UNESP), Instituto de Química, Câmpus Araraquara.

Supervisor: Prof. Dr. Marcelo Nalin

FAPESP- 2019/19609-1

Araraquara

2024

**Instituto de Química – UNESP - Araraquara**

**Departamento de Química Geral e Inorgânica**

## RELATÓRIO FINAL DE ATIVIDADES

# Título: Síntese e caracterização de diferentes famílias de vidros e vitro-cerâmicas (óxidos, fosfatos e fluoretos) com propriedades magnéticas.

Bolsa de pós Doutorado – FAPESP processo 2019/19609-1

Período de vigência do projeto: 01-11-2019 a 31/07/2024

/Período coberto pelo relatório cientifico: 01/11/2021 a 30/07/2024 (sendo que de 01/05/22 a 30/04/22 corresponde ao período do BEPE)

Bolsista: Dra. Juliane Resges Orives

Supervisor: Prof. Dr. Marcelo Nalin

Araraquara – Julho 2024

## 1- Visão geral do projeto

Os vidros têm uma história única e um papel importante no desenvolvimento de novos materiais que mudaram e continuam mudando a sociedade e estão amplamente presentes em aplicações de alta tecnologia.[1-3] O desenvolvimento de novas composições de vidro com propriedades especiais é essencial para enfrentar os principais desafios atuais em aplicações como armazenamento de energia, sistemas de comunicação avançados e dispositivos magneto-ópticos, sensores operando no infravermelho.[3]

Uma classe interessante de vidros que vem se destacando nos últimos anos são os chamados vidros magnéticos e magneto-ópticos, esses materiais possuem propriedades que podem ser moduladas pela aplicação de um campo magnético, como por exemplo o efeito Faraday no qual a luz transmitida é elipticamente polarizada com seu longo eixo girando em relação à direção do plano de polarização da onda incidente.[4-7] Esses vidros têm despertado o interesse de pesquisadores ao redor do mundo, e muitos trabalhos, tanto do ponto de vista fundamental como de aplicações estão se tornando comuns na literatura.[6,7]

Os efeitos magneto-ópticos são mais pronunciados nos cristais, mas a grande dificuldade em preparar monocristais com dimensões práticas limita seu uso em dispositivos fotônicos. Uma maneira interessante de contornar este problema é a simbiose entre vidro e cristais magnéticos em um único material.

A síntese de novas composições de vidro, bem como a compreensão sobre a química de sua formação, nos permite a obtenção de composições onde a formação de cristais na fase vítrea pode ser controlada. Os cristais do tipo granada com fórmula geral $TR_3Ga_5O_{12}$ (TRGG onde TR = terras raras) têm importantes propriedades fundamentais e tecnológicas, dentre eles o composto mais conhecido é a granada de térbio e gálio (TGG), usado como cristal magneto-óptico em dispositivos para a detecção de campos eletromagnéticos, dispositivos de rotação de Faraday, etc.[7-9] Além do Tb, os ions Gd, Ho e Dy também apresentam propriedades magnéticas. O crescimento da fase cristalina de TRGG dentro de uma matriz vítrea, sem comprometer as propriedades ópticas, é uma tarefa complicada. O principal desafio é obter um vidro homogêneo e transparente com íons ativos dentro da fase cristalina.

Além das propriedades magnéticas os vidros à base de óxidos de metais pesados, dependendo da composição química, podem apresentar uma janela de transmissão que pode se estender até 6-7 μm e possui altos valores de índice de refração. Além disso, a possibilidade de dopagem dos vidros com íons terras raras ativos nesta região espectral, como por exemplo o Dy, Ho, Gd, Tb promove o casamento ideal para a obtenção de dispositivos com potencial para uso em detectores na região do infravermelho médio para detecção de gases de efeito estufa,[10] uma vez que suas identidades vibracionais, ou seja, suas absorções de energia estão localizadas na região de 2 a 8 μm (Figura 1).

Devido a imensa possibilidade de aplicações dos vidros de metais pesados contendo cristais de $TR_3Ga_5O_{12}$, a importância da obtenção de vitrocerâmicas contendo terras raras fica evidente, além disso é importante ter controle sobre o tamanho dos cristais formados e sobre a reprodutibilidade dos materiais obtidos. Além de podermos explorar as propriedades das vitrocerâmicas existe também a possibilidade da retirada dos cristais da matriz vítrea o que gera uma nova gama de aplicações.

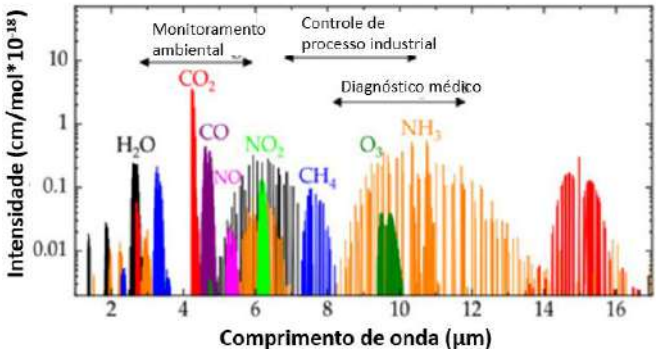


**Figura 1** - Diferentes moléculas e suas respectivas absorções na região do infravermelho médio. (adaptado de 11)

O presente relatório refere às atividades desenvolvidas durante 01/11/2021 a 30/07/2024. Nele estão descritos os resultados mais expressivos obtidos até o momento, bem como as dificuldades encontradas. Durante o período foram preparadas vitrocerâmicas contendo cristais de TRGG (TR = Tb, Dy, Ho, Gd), o crescimento dos cristais em diferentes condições foi explorado e suas propriedades foram investigadas.

## 2- Realizações no período

**2.a)** Durante o período de 01/11/2021 a 30/07/2024 o projeto no Brasil foi desenvolvido em duas frentes:

1 – Obtenção e caracterização de vitrocerâmicas contendo Tb (TGG), Dy (DyGG), Ho (HoGG) e Gd (GdGG).

3- Controle do tamanho dos cristais de Tb (TGG), Dy (DyGG), Ho (HoGG) e sua extração da matriz vítrea.

Os resultados obtidos mostraram grande reprodutibilidade na obtenção e extração desses cristais. Os cristais foram caracterizados por EDX, Micro-Raman, Micro Luminescência, DRX e UV-vis.

**2.b)** Durante o período contemplado por este relatório, um BEPE (processo 2020/15395-4) foi realizado por um ano (01/05/2022-30/04/2023) na *Université de Bordeaux* na França sob supervisão do Prof. Dr. Thierry Cardinal.

Durante o BEPE a polarização térmica foi utilizada para polarizar vidros borogermanatos contendo íons térbio, a técnica empreendida consiste em posicionar dois eletrodos, um de cada lado da amostra vítrea, e então aplicar uma diferença de potencial em função da temperatura. Em altas temperaturas, os íons têm sua mobilidade aumentada, proporcionando a migração dos cátions em direção ao cátodo. Com a migração, uma camada de alguns mícrons de espessura muda a composição vítrea próximo à superfície, resultando em um forte campo elétrico estático próximo ao ânodo. Nesse período de estágio no exterior foi realizado um trabalho muito acurado sobre os mecanismos de microimpressão termoelétrica da composição $96(46GeO_2\text{-}29B_2O_3\text{-}16Na_2O\text{-}5BaO\text{-}4Al_2O_3)\text{-}4Tb_4O_7$. O interesse em estudar essa composição contendo esses íons paramagnéticos foi verificar como o tratamento de polarização pode modificar as propriedades ópticas, estruturais e magnéticas desse vidro. Os resultados obtidos demostraram um controle espacial micrométrico de uma mudança de estado de oxidação de íons $Tb^{3+}$ para $Tb^{4+}$. Observou-se uma grande mudança nas propriedades ópticas de absorção e luminescência, decorrente das propriedades distintas

dos íons térbio trivalentes e tetravalentes. Medidas correlativas de Micro-Luminescência, Micro-Raman e Geração de Segundo Harmônico foram realizadas na superfície de vidro que sofreu tratamento de polarização. Demonstrou-se uma modificação concomitante precisa da estrutura do vidro acompanhando grandes mudanças na intensidade da luminescência e o aparecimento de uma resposta óptica de segunda ordem que pode ser atribuída a uma implantação de carga espacial localizada. Esses resultados originais demonstram como um processo elétrico simples permite o gerenciamento de múltiplas propriedades ópticas em escala micrométrica, mas também abre caminho para induzir funcionalidades elétricas estáticas em um sistema vítreo opto-magnético.

Como mostrado no Relatório Científico do BEPE (Anexo A), diversas caracterizações foram realizadas resultando em um artigo publicado na revista Journal Of Physics - Materials e outro que está sendo redigido para *Journal of Materials Chemistry C*.

## 2.c) Publicações, artigos submetidos e manuscritos em fase de finalização

### Publicações

**2.c.1- Juliane Resges Orives,** Lia Mara Marcondes, Lara karam, Frédéric Adamietz, Thierry Cardinal, Marc Dussauze, Marcelo Nalin. Micrometric patterning of a borogermanate glass containing terbium by thermal poling to manage luminescence and second order optical properties**.** *Journal Of Physics - Materials*, 7 (2024) 03LT01. ***Ver anexo B.***

**2.c.2- Juliane Resges Orives,** Wesley Renato Viali, Fabrício Benedito Destro, **Sebastiao W. da Silva,** Sidney J. L. Ribeiro, Marcelo Nalin**,** Embedding CoPt magnetic nanoparticles within a phosphate glass matrix. *Journal of Alloys and Compounds*, 848 (2020) 156576. ***Ver anexo C.***

**2.c.3- Juliane Resges Orives,** Benoit P. Pichon, Damien Mertz, Kevin Sartori, Sylvie Begin-Colin, Wesley Renato Viali, Sidney J. Lima Ribeiro, Marcelo Nalin, Phosphate glasses containing monodisperse $Fe_{3-\delta}O4@SiO_2$ stellate nanoparticles obtained by melt-quenching process. *Ceramics International*, 46 (2020) 12120. ***Ver anexo D.***

**2.c.4-** Lia Mara Marcondes**, Juliane Resges Orives**, Frédéric Adamietz, Gael Y. Porier, Thierry Cardinal, Marc Dussauze, Marcelo Nalin. Nonlinear properties and structural rearrangements in thermally poled niobium germanate glasses. *Journal of non-crystalline solids*, 627, (2024) 122809. ***Ver anexo E.***

**2.c.5-** Sara Novac, **Juliane Resges Orives** Marcelo Nalin, Irem Unalan, Aldo R. Boccaccini, Emerson R. de Camargo. Quaternary bioactive glass-derived powders presenting submicrometric particles and antimicrobial activity. ***Ceramics International***, *48* (20), (2022) 29982-29990. **Anexo F.**

### Manuscritos em fase de finalização

**2.c.6- Juliane Resges Orives**, Thiago A. Lodi, Lia Mara Silva Marcondes, Camila Batista Pinto, Victória Mamelli, Antonio Eduardo Souza, Fabricio B. Destro, Juliani Caland, Javier Alcides Ellena**,** Thierry Cardinal, Marc Dussauze, Jorlandio Felix, Marcelo Nalin, Managing the growth

of micrometer-sized TGG single crystals from heavy metal oxide glass melts -The supersaturated solution methodology.
Revista pretendida: *Journal of alloys and compounds.* ***Anexo G.***

**2.c.7-** **Juliane Resges Orives**, Lia Mara Marcondes**,** Lara Karam, Frédéric Adamietz, Thierry Cardinal, Marc Dussauze, Marcelo Nalin**.** Non-classical effects obtained by thermal poling in borogermanate glass containing terbium.
Revista pretendida: *Journal of Materials Chemistry C*

**2.c.8-** Lia Mara Marcondes**, Juliane Resges Orives**, Frédéric Adamietz, Gael Y. Porier, Thierry Cardinal, Marc Dussauze, Marcelo Nalin. Imprinting microstructure in niobium germanate glasses by thermal poling: structural and nonlinear properties.
Revista pretendida: *Journal of Materials Chemistry C*

**3 - Participação em evento científico.**

**3.1**- Juliane R. Orives, Wesley R. Viali, Sidney J. L. Ribeiro, Marcelo Nalin, **Phosphate glasses containing cobalt platinum magnetic nanoparticles**, apresentado na forma de eposter em II WORKSHOP INFO Araraquara, 12 – 15 de fevereiro 2020.

**3.2-** Avaliadora dos trabalhos apresentados no XXXII Congresso de Iniciação Científica da Unesp, realizado nos dias 20, 21 e 22 de outubro e 24 e 25 de novembro de 2020. Universidade Estadual paulista Júlio de Mesquita Filho, Araraquara- Sp.

**3.3**- Curso **Unesp química - formação inovagrad Google for Education,** com carga de 8 horas em 206/10/2020. 4- Curso de Extensão de Curta duração: **Como transformar seus dados brutos em Figuras de alto impacto**, realizado entre os dias 01 de março a 04 de março de 2021. Universidade Federal de São Carlos, São Carlos-Sp.

**3.4** - Webinar **Fotônica: a ciência e tecnologia da luz**, ministrado pelo Dr. Cid B. Araújo em 14/05/2021, na plataforma Zoom realizado pelos OSA & SPIE Student Chapters Recife.

**3.5-** 26th International Congress on Glass (ICG2022), 03 Jul 2022 - 08 Jul 2022, Berlin, One-step obtention of TGG single crystals embedding in heavy metal oxide glasses, Orives, J. (Speaker); Albino, L.; Destro, F.; Mameli, V.; Marcondes, L.; Souza, A.E.; Cardinal, T.; Nalin, M.

**3.6-** Juliane Resges Orives, Lia Mara Silva Marcondes, Thierry Cardinal, Marc Dussauze e Marcelo Nalin. **Controlling the oxidation state of terbium ions of a borogermanate Tb glass by thermo-electrical imprinting treatment.** *XXI Brazilian Materials Research Society (B-MRS) Meeting* em Maceio-Alagos entre os dias 01 e 05 de outubro de 2023.

**3.7-** Participação no evento 12th NanoAndes Workshop occurred between 9 - 17 October at Chemistry Institute - UNESP Araraquara and LNLS - CNPEM – Campinas

**3.8- Juliane Resges Orives participou como organizadora** do 1º Workshop de Materiais Fotônicos do IQAr, realizado no período de 31 de Julho a 02 de Agosto de 2023, no Instituto de Química da UNESP em Araraquara – SP. **(Anexo H)**

## 3. Resultados e discussão das realizações no período

### 3.a) Obtenção e caracterização de vitrocerâmicas contendo Tb (TGG), Dy (DyGG), Ho (HoGG) e Gd (GdGG).

Os cristais de TRGG podem ser obtidos em diferentes formatos, como fibras, nanopartículas, cerâmicas policristalinas e bulk.[12-16]. Mas apesar dos diversos métodos de síntese, a produção em larga escala enfrenta algumas dificuldades como baixa qualidade do cristal, tempo significativo para o seu crescimento e alto custo de fabricação.[12-16]

Desta forma, novos métodos de obtenção de monocristais de TRGG permanecem em foco. Os materiais de vidro têm uma estrutura semelhante ao seu líquido super-resfriado original, e a partir deles é possível crescer nanocristais e cristais na matriz vitrea.[8,17]

Vidros de óxidos de metais pesados podem ser uma boa alternativa para a obtenção de monocristais de TRGG, por este motivo a composição molar (100-x)(40PbO-25$Bi_2O_3$-20$GeO_2$-15$Ga_2O_3$)-x TRGG, onde os terras raras usados foram: Tb, Dy, Ho, Gd, foi escolhida com base em um estudo anterior de Nalin, M et al, em que a possibilidade de obtenção de cristais únicos $Yb_3Ga_5O_{12}$ dopados com $Er^{3+}$/$Tm^{3+}$ em um vidro germano-galato sistema contendo 3 mol% de óxido de terras raras foi demonstrado.[8]

A técnica de fusão seguida de choque térmico foi combinada com a química de soluções supersaturadas para obter vidros contendo cristais de TRGG, nomeadas de PGBG-TB, PGBG-Dy, PGBG-Ho e PGBG-Gd. Os precursores vítreos foram fundidos a 1250 °C por 2 h para homogeneização completa e em seguida as composições foram vertidas em um molde de aço pré-aquecido a 350 ºC, e levadas para tratamento térmico nesta temperatura por 5 h para eliminação de tensões internas devido ao choque térmico.

Os difratogramas de Raios X das amostras na Figura 2 a-d) mostraram um halo difuso de difração em 28°, característico dos vidros amorfos, o que indicou que o estado amorfo permanece nas amostras apesar da grande quantidade de cristais observada microscopicamente.

O difratograma da amostra PGBG-Tb mostraram picos de difração em 28,9°, 32,3°, 35,5°, 53,3° e 59,7° que foram indexados à fase cristalina $Tb_3Ga_5O_{12}$ pertencente ao grupo espacial cúbico Ia-3d (ICSD-20831), os picos foram atribuídos aos planos 004, 420, 422, 046 e 080, respectivamente, confirmando a formação dos cristais TGG, assim como os difratogramas das amostras PGBG-Ho, PGBG-Dy e PGBG-GD apresentaram os picos de difração das fases cristalinas $Ho_3Ga_5O_{12}$, $Dy_3Ga_5O_{12}$ e $Gd_3Ga_5O_{12}$, respectivamente.

Os espectros de absorção óptica das amostras na faixa de comprimento de onda UV-Vis-NIR entre 300 e 2500 nm são mostrados na Figura 3. Para o vidro contendo Tb as bandas ao redor de 488, 1780, 1890, 1950 e 2215 nm aparecem devido a transições entre o nível de energia fundamental $^7F_6$ dos íons $Tb^{3+}$ para os níveis excitados $^5D_4$, $^7F_0$, $^7F_1$, $^7F_2$ e $^7F_3$, respectivamente.[18] Para o vidro contendo Ho, as bandas de absorção centradas em 484, 536, 642, 900, 1152 e 1950 nm, correspondem às transições a partir do estado fundamental $^5I_8$ para os níveis excitados $^5F_3$, ($^5F_4$ + $^5S_2$), $^5F_5$, $^5I_5$, $^5I_6$, $^5I_7$, respectivamente.[19]

Para o vidro contendo Dy as bandas são originadas devido às transições f-f do seu estado fundamental $^6H_{15/2}$ para vários níveis de energia excitados, como $^4I_{15/2}$, $^6F_{3/2}$, $^6F_{5/2}$, $^6F_{7/2}$,

$^6F_{9/2}$, $^6F_{11/2}$ e $^6H_{11/2}$, centralizados em 473, 754, 804, 905, 1098, 1280 e 1689 nm respectivamente.[20] Já para os vidros contendo os íons Gd nenhuma absorção é esperada já que a absorção deste íon se encontra nos comprimentos de onda de 276 e 315 nm e a borda de absorção do vidro é em torno de 500 nm.

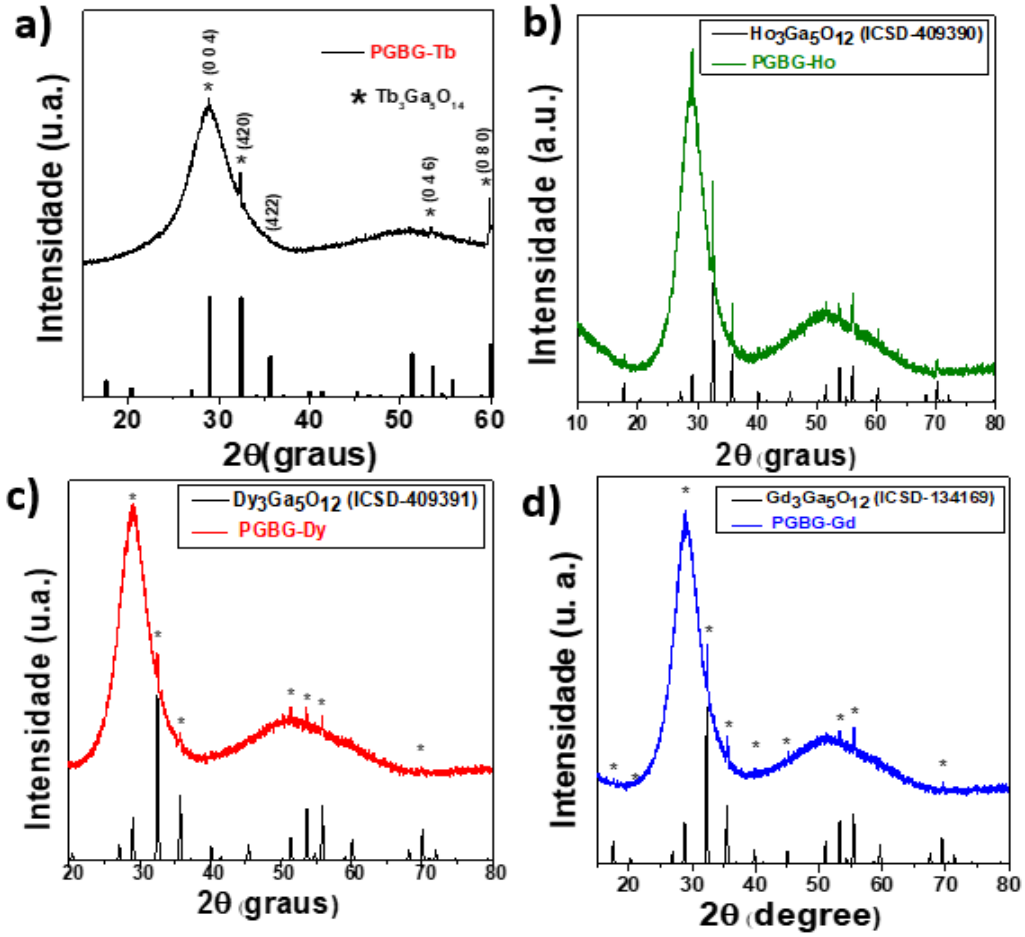


**Figura 2-** a) Difratograma de Raios X amostra PGBG-Tb comparada ao padrão $Tb_3Ga_5O_{12}$ (ICSD- 20831). b) Difratograma de Raios X amostra PGBG- Ho comparada ao padrão $Ho_3Ga_5O_{12}$ (ICSD- 409390), c) Difratograma de Raios X amostra PGBG-Dy comparada ao padrão $Dy_3Ga_5O_{12}$ (ICSD- 409391) e d) Difratograma de Raios X amostra PGBG-Gd comparada ao padrão $Gd_3Ga_5O_{12}$ (ICSD- 134169).

Os espectros de absorção na região de UV-Vis-Nir obtidos foram importantes na escolha dos comprimentos de onda utilizados para as medidas de espectroscopia Raman, já que é importante escolher um comprimento de onda fora da região de absorção do íon terra rara, para que os espectros obtidos não tenham influência da luminescência. Os comprimentos de onda escolhidos foram 532 nm para os vidros contendo cristais TGG e DyGG, e 785 para os vidros contendo cristais de HoGG e GdGG.

Na Figura 4 a) estão dispostas as imagens de microscopia óptica obtidas para os cristais, pode-se observar a semelhança entre os cristais obtidos com diferentes íons terras raras, todos apresentaram um formato quase estrelado, e tamanhos entre 15 e 40 µm, sendo os cristais de TGG e HoGG mais próximos de 20 µm e os cristais de DyGG e GdGG mais próximos de 30 µm. Em todas as amostras ocorreu cristalização em todo o volume do vidro e não em um ponto preferencial, os cristais se espalham no volume em diferentes profundidades.

É importante ressaltar os cristais foram formados com estreita faixa de tamanho e boa homogeneidade no bulk, em uma única etapa durante o vertimento, sem a necessidade de qualquer tratamento térmico adicional para sua obtenção.

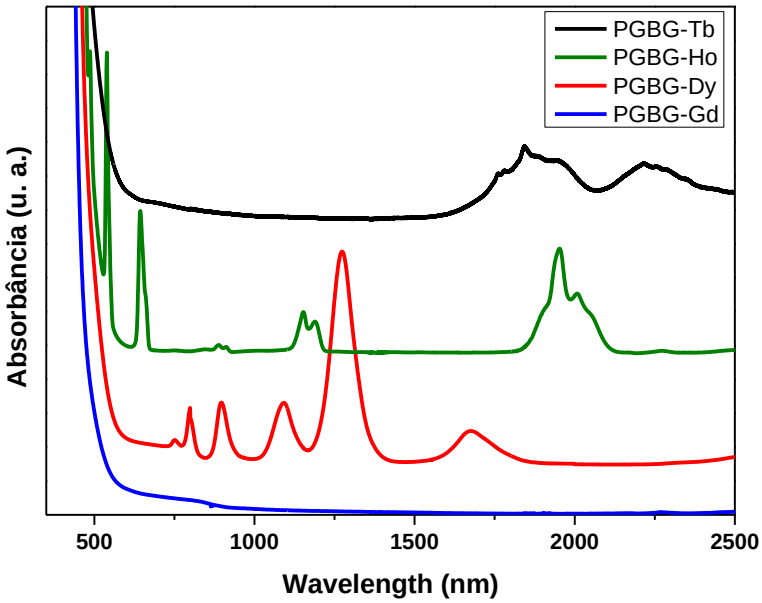


**Figura 3 –** Espectros de absorção na região de UV-Vis-Nir obtidos para amostras PGBG-Tb, PGBG-Ho, PGBG-Dy e PGBG-Gd.

O mapeamento Raman, Figura 4 a) foi utilizado para criar uma imagem coletando-se um espectro a cada 1 µm em uma área contendo um cristal TRGG e uma parte vítrea, como o objetivo de mapear a estrutura do cristal, podemos verificar nos mapas a homogeneidade de cristalização. O perfil dos espectros Raman obtidos para as amostras a partir do mapeamento Raman pode ser visto na Figura 4 b) e c). Os espectros foram coletados na fase vítrea e na superfície do cristal de cada amostra. O espectro para o cristal TGG padrão comercial também foi obtido.

Para as medidas realizadas na região vítrea (Figura 4b)) os espectros obtidos apresentaram bandas largas características de um material vítreo correspondendo à faixa de 300~800 $cm^{-1}$.[8] Na região de 380 $cm^{-1}$ se encontram as vibrações Ga-O-Bi/Ge-O-Bi (ou Ga-O-Pb/ Ge-O-Bi), devido às semelhanças entre poliedros $GaO_4$ e $GeO_4$, é difícil separar essas vibrações. A banda Raman em 525 $cm^{-1}$ é atribuída às vibrações de $GaO_4$ e $GeO_4$. A banda em 770 $cm^{-1}$ é atribuída às ligações $Ga\text{-}O^-$ e $Ge\text{-}O^-$ envolvendo os oxigênios não ligados.[8]

As granadas de gálio $RE_3Ga_5O_{12}$ são isoestruturais e normalmente tem um espectro Raman semelhante.[21-23] O espectro Raman do $Tb_3Ga_5O_{12}$ não foi encontrado na literatura, mas foi realizada uma medida para o padrão comercial TGG que confirmou a similaridade dos espectros obtidos com os relatados para as estruturas $RE_3Ga_5O_{12}$. As bandas obtidas para os cristais TGG dentro do vidro mostraram o mesmo perfil do cristal comercial e podem ser encontradas em 237, 258, 270, 356, 526, 587, 602 e 745 $cm^{-1}$ (Figura 4c)). Como observado os cristais TGG, HoGG, DyGG e GdGG apresentam assinaturas espectrais muito semelhantes, sendo mais um indício de que as fases desejadas foram obtidas.

As vibrações dos diferentes poliedros na estrutura estão fortemente acopladas entre si e, portanto, é difícil atribuir cada banda Raman a um único poliedro. Nas regiões de baixa frequência, as vibrações entre 200-300 $cm^{-1}$ são atribuídas aos modos de translação dos poliedros de $TRO_8$ e $GaO_4$. Enquanto os modos rotacionais do $GaO_4$ e $GaO_6$ estão presentes

na faixa de 300-450 $cm^{-1}$. Nas regiões de alta frequência, são encontrados os modos de flexão simétricos (450−650 $cm^{-1}$) e os modos de alongamento (acima de 650 $cm^{-1}$) dos poliedros de $GaO_6$ e $GaO_4$.[23]

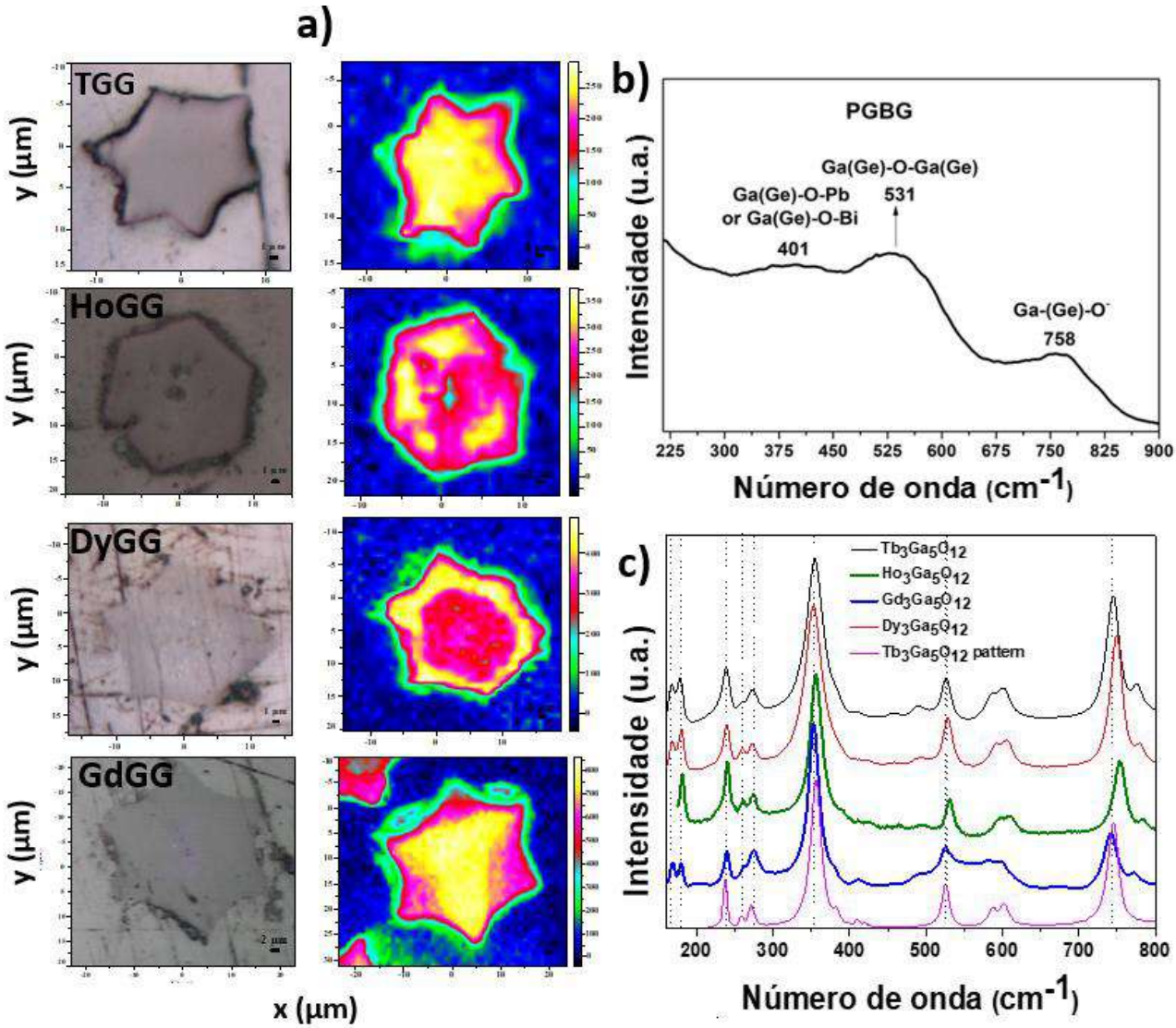


**Figura 4-** a) Espectro Raman normalizado obtidos na superfície dos cristais de TGG e) Raman normalizado obtidos na região vítrea.

Afim de investigar as propriedades luminescentes dos cristais obtidos medidas de micro-luminescência foram coletadas utilizando-se o espectrômetro Raman com um comprimento de onda de 488 nm para excitação dos íons terras raras. Podemos observar que para os cristais TGG, HoGG, e GdGG os mapas mostraram uma intensidade de luminescência maior dentro dos cristais, e uma menor intensidade na região vítrea devido à parte dos íons permanecerem nesta fase, enquanto que para o cristal DyGG observamos o oposto (Figura 5 a).

Os espectros de emissão do vidro contendo íons $Tb^{3+}$ apresentaram tanto no vidro quanto no cristal TGG uma banda de emissão em 547 nm, que é originada da transição $^5D_4 \rightarrow {}^7F_5$. Além dessa emissão verde, bandas de emissão amarela e vermelha foram observadas em 587 e 624 nm atribuídas as transições $^5D_4 \rightarrow {}^7F_j$ (J= 4 e 3) dos íons $Tb^{3+}$.[24]

Nos cristais observa-se uma definição dos níveis de energia dos íons $Tb^{3+}$, tal comportamento pode ser atribuído à formação de níveis de Stark onde os íons $Tb^{3+}$ estão em ambientes cristalinos com menor número de sítios de simetria e, consequentemente, menor degenerescência dos níveis de energia de $Tb^{3+}$.

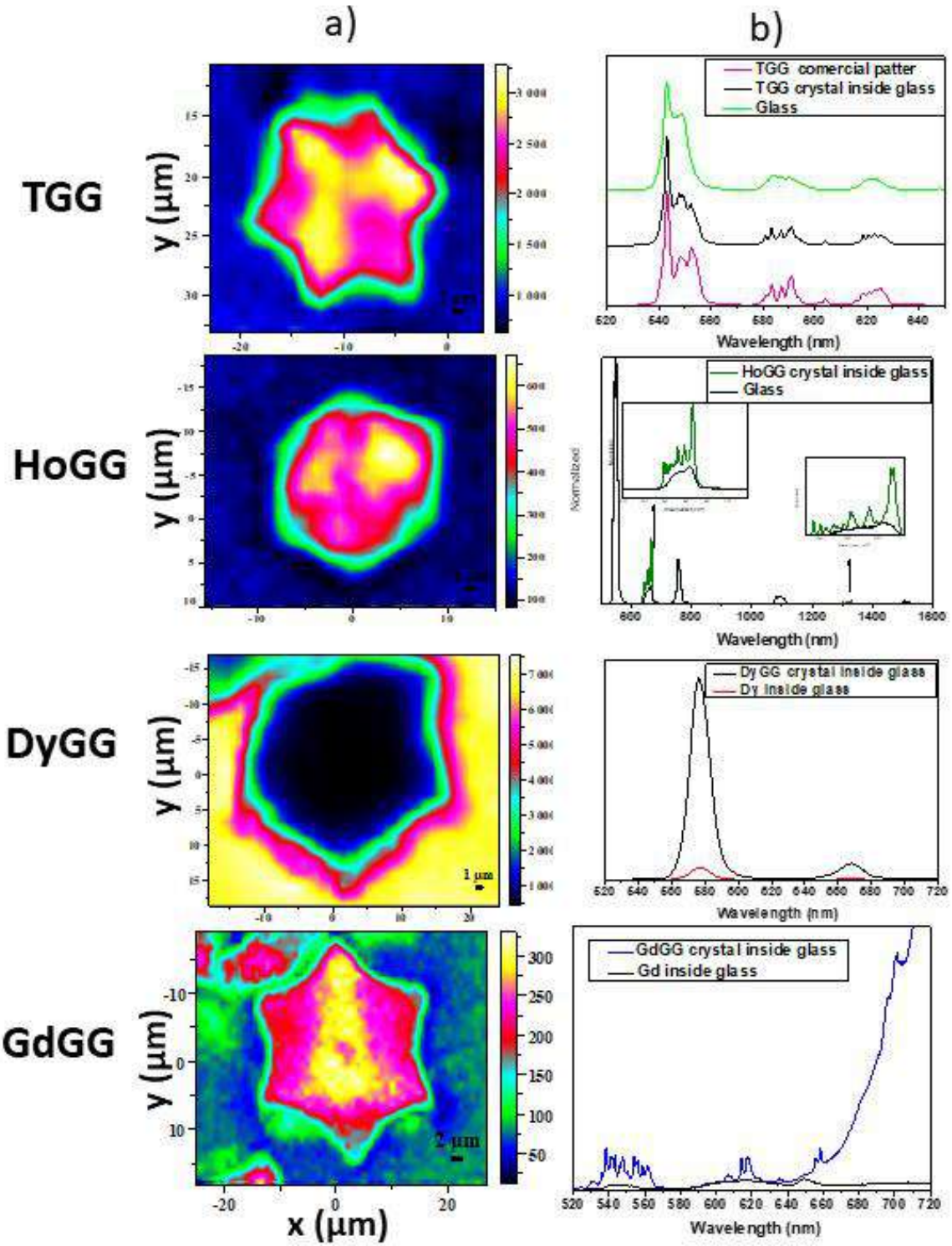


**Figura 5-** a) Mapeamento da luminescência dos cristais TGG, HoGG, DyGG e GdGG, b) espectros de emissão dos íons Tb, Ho, Dy e Gd na matriz vítrea e na fase cristalina

Os espectros do cristal de TGG comercial foram obtidos para comparação e corroboração da presença de íons térbio em cristais de TGG precipitados na matriz vítrea, conforme ilustrado na Figura 5 b). Além disso, também foi observada a presença de íons $Tb^{3+}$ na matriz de vidro remanescente, uma vez que ainda é observada uma emissão de alargamento não homogêneo, a qual ocorre devido ao grande número de diferentes sítios de simetria, característicos da emissão de terras raras em vidros.

Para o vidro contendo íons $Ho^{3+}$, foi observado o mesmo comportamento, uma definição dos níveis de energia dos íons $Ho^{3+}$ bem como uma emissão de alargamento não homogêneo na região vítrea. Enquanto que para o vidro contendo íons $Dy^{3+}$, observou-se um quenching na luminescência devido a quantidade de íons Dy próximos dentro da estrutura cristalina. Uma maneira de resolver esse problema é fazendo um cristal contendo ítrio e disprósio aumentando a distância entre os íons disprósio. O mapeamento Raman da amostra contendo a composição molar (100-3)(40PbO-25$Bi_2O_3$-20$GeO_2$-15$Ga_2O_3$)-2,25$Y_2O_3$+0,75$Dy_2O_3$ ($Y_{2,25}DY_{0,75}GG$) apresenta o mapa oposto do apresentado para a amostra DyGG, com maior luminescência dentro do cristal e um espectro apresentando uma definição dos níveis de energia dos íons $Dy^{3+}$, mostrando que essa metodologia é eficaz para evitar o quenching de luminescência (Figura 6).

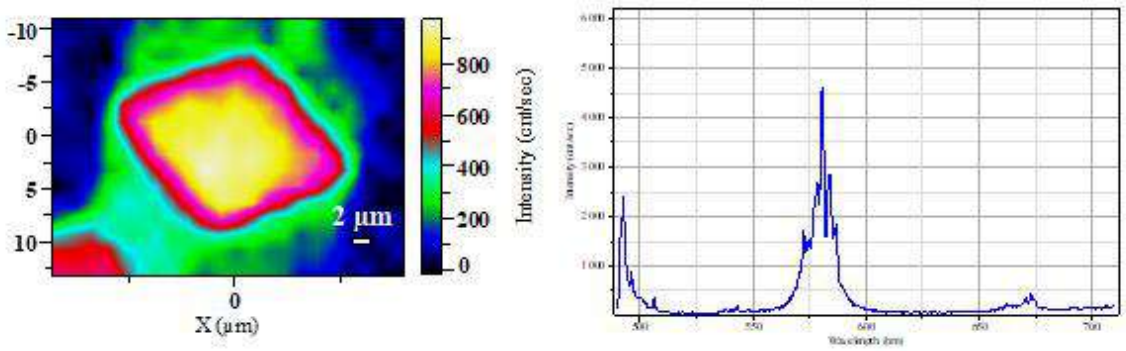


**Figura 6-** a) Mapeamento da luminescência do cristal $Y_{2,25}DY_{0,75}GG$.

Já para o vidro contendo íons $Gd^{3+}$ não se esperava luminescência já que o íon não apresenta banda de absorção próximo de 488 nm, portanto uma investigação está sendo conduzida para verificar a presença de impurezas que possam estar contribuindo para a luminescência observada.

A distribuição dos elementos químicos nas regiões vítrea e cristalina das amostras PGBG-Tb, PGBG-Dy, PGBG-Ho e PGBG-Gd e na área do cristal de TGG foi estudada por EDS e mapeamento elementar utilizando-se microscopia eletrônica de varredura (MEV) em uma amostra polida com um cristal exposto na superfície (Figura 7).

Para a amostra PGBG-Tb na região vítrea foram obtidos sinais de todos os elementos da composição como esperado, enquanto que na região do cristal observa-se que a composição química na superfície do cristal contém o térbio com sinais em 1,24 (Ec(M5)), 6,27 (La1), 6,97 (Lβ1) e 7,36 (Lβ2), o Ga com energias atribuídas em 0,95 (L1) e 1,098 keV (La1) e O em 0.5 (Ka1). Esses resultados confirmam que o cristal observado por microscopia óptica é um cristal de TGG.

O mapeamento elementar mostra a distribuição dos elementos químicos nas fases do cristal e do vidro. O mapeamento da região cristalina é predominantemente composto por Ga e Ge, esse fato ocorre porque esses elementos possuem números atômicos próximos, exibindo transições semelhantes, dificultando a separação dos dois sinais, mas os dados de

EDS deixam claro que o cristal é composto por Ga ao invés de Ge. O mapeamento elementar exclui a presença de íons Bi e Pb no cristal. As mesmas conclusões foram obtidas para os demais cristais. Além disso em todos os casos observa-se uma maior concentração dos íons terras raras dentro do cristal.

Como discutido acima, os dados de Raios X, micro- Raman, micro-luminescência e EDS indicam que as fases cristalinas TGG, HoGG, DyGG e GdGG foram obtidas com sucesso a partir de um vidro contendo os íons terras raras precursores por uma metodologia simples, sem a necessidade de tratamento térmico posterior e reprodutível.

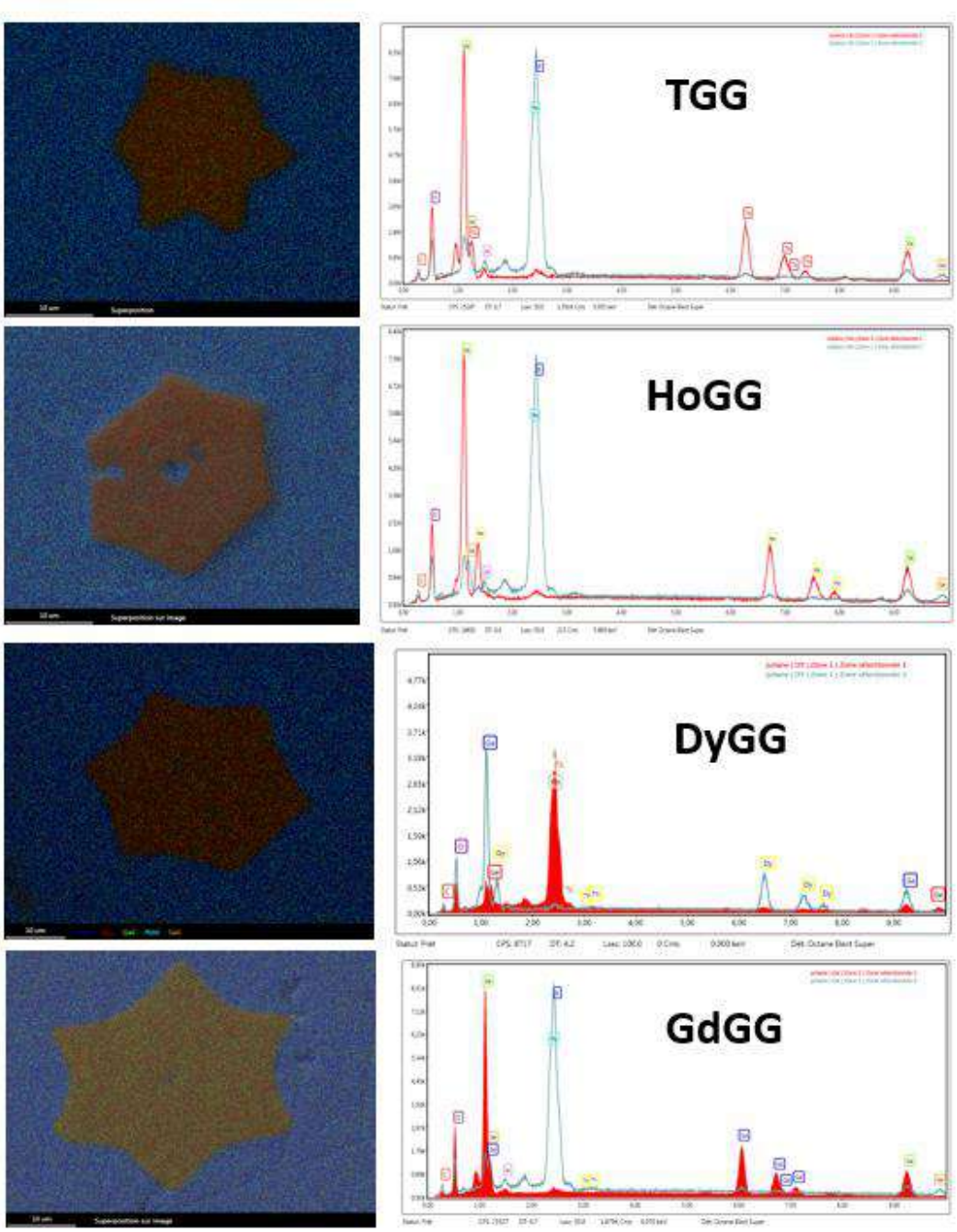


**Figura 7-** Mapa elementar de cada elemento que compõe as amostras PGBG-Tb, PGBG-Dy, PGBG-Ho e PGBG-Gd e Espectro de EDS da região vítrea e da superfície do cristal.

**3.b) Controle do tamanho dos cristais de Tb (TGG), Dy (DyGG), Ho (HoGG) e Gd (GdGG) e sua extração da matriz vítrea.**

Afim de verificar-se a possibilidade de aumentar o tamanho dos cristais de TGG, HoGG e DyGG os precursores vítreos foram fundidos a 1250 °C por 2 h para homogeneização completa e em seguida as composições foram resfriadas dentro do forno a 10 ° C/ min até atingirem 900 ° C e retiradas do forno nesta temperatura. Utilizando-se esta metodologia foi possível obter cristais acima de 50 µm em todos os casos como observado na Figura 8a).

Além disso foi observado que os cristais obtidos dessa forma possuem formato cúbico, este tamanho e formado podem ter sido obtidos devido ao maior tempo que a estrutura teve para se organizar durante o resfriamento lento, diferentemente do ocorrido para as amostras apresentadas na seção 2.

Após a obtenção dos vidros foi adicionado aos mesmos ácido concentrado por um período de 10 a 24 h e desta forma a parte vítrea foi dissolvida e os cristais puderam ser recuperados como observado na figura 8 b), de maneira intacta. Isso é muito interessante e abre uma gama de novas aplicações magnéticas e em sensores na região do infravermelho que serão ainda exploradas.

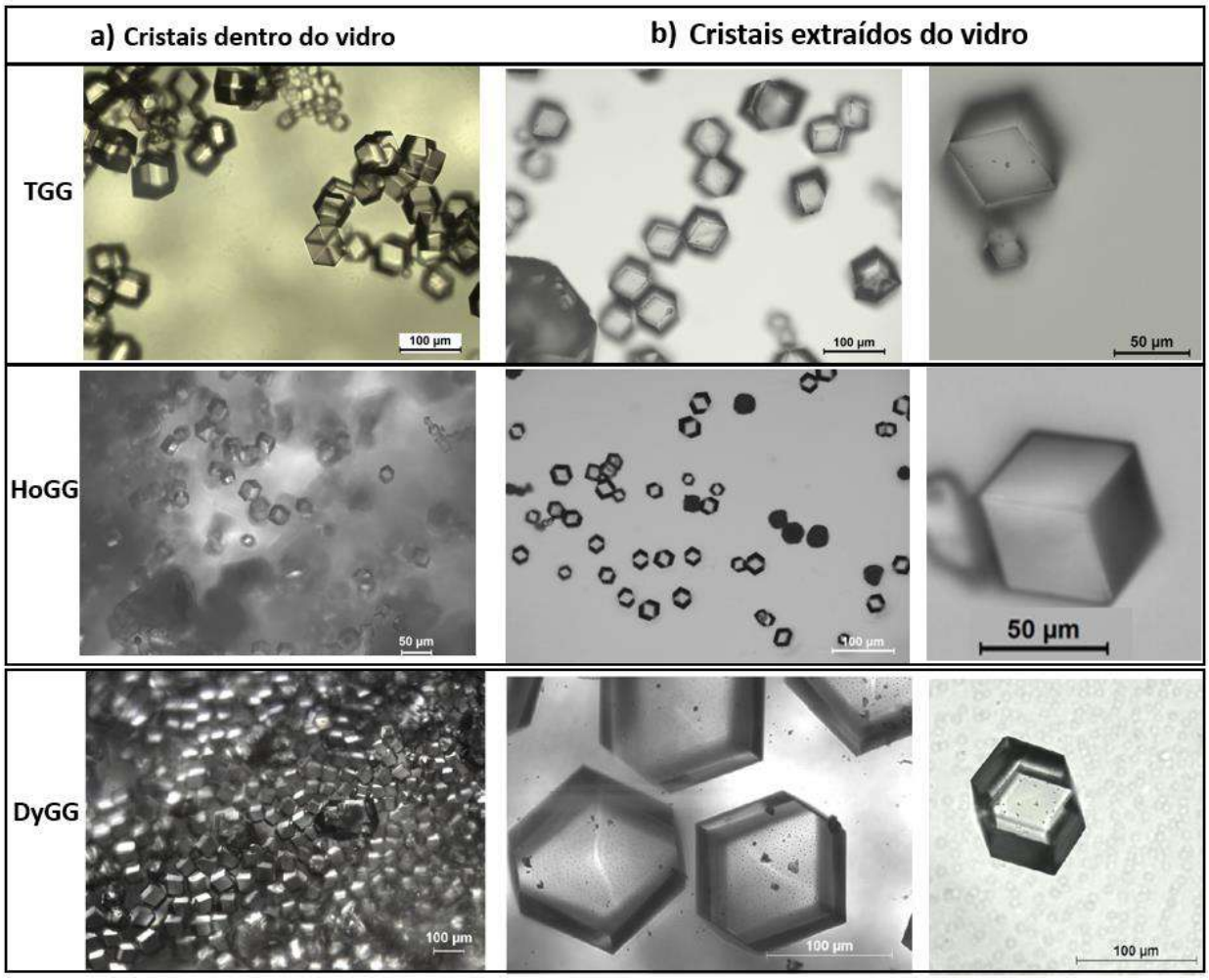


**Figura 8**- Imagens de microscopia óptica dos cristais de TGG, HoGG e DYGG a) dentro e b) fora do vidro PGBG.

A Figura 9a) mostra uma imagem de microscopia optica de um cristal TGG dentro do vidro enquanto a Figura 9b) apresenta uma imagem eletrônica de varredura de um dos cristais de TGG obtidos e extraídos do vidro mostrando em detalhes a topografia do TGG monocristalino (TGG-SC), é possível observar que o ácido não ataca a superfície da estrutura cristalina. Esta nova metodologia para obtenção do TGG-SC abre uma gama de novas aplicações nas quais estes microcristais únicos podem ser explorados, como os microleds.

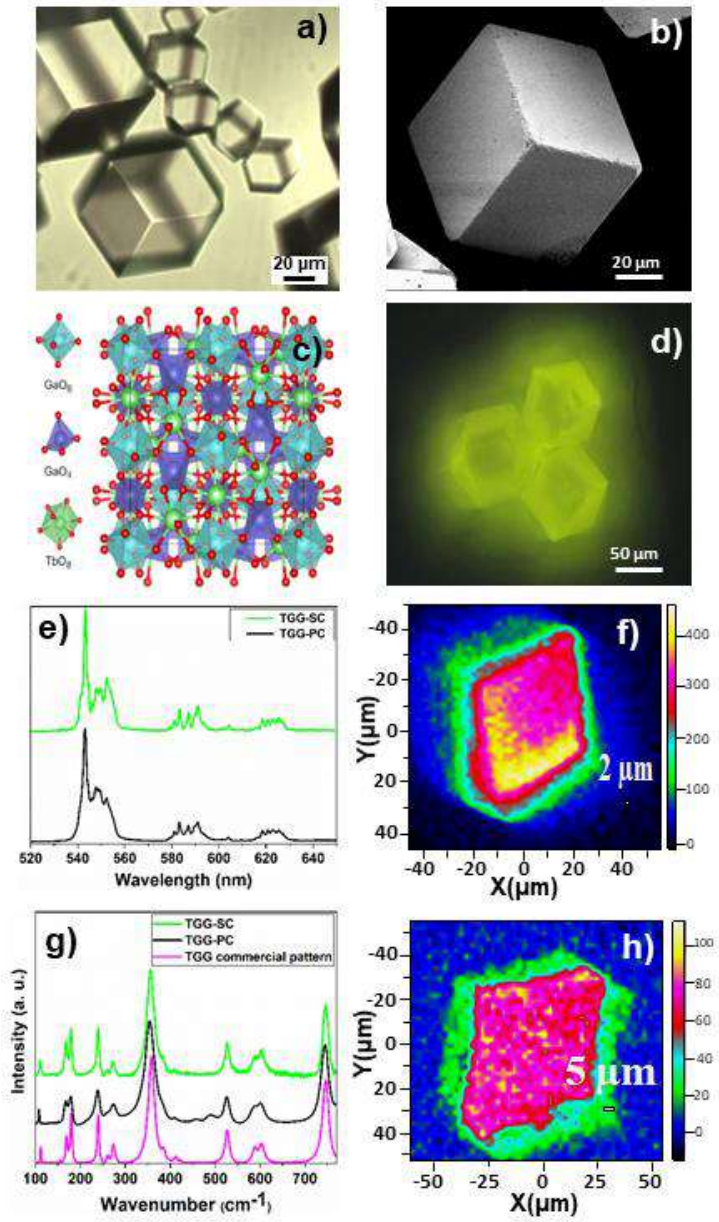


**Figura 9- a)** Imagem de microscopia óptica de cristais individuais de TGG dentro do vidro. b) Imagem de microscopia eletrônica de varredura de TGG-SC. c) Embalagem de cristal para TGG-SC obtida usando o software Vesta, destacando as unidades $TbO_8$, $GaO_6$ e $GaO_4$. d) Fotografia dos cristais sob lâmpada ultravioleta. e) espectros de emissão adquiridos para o padrão comercial TGG-SC, TGG-PC e TGG. f) Mapa de luminescência

para bandas de emissão entre 530 e 560 nm. g) Espectros Raman normalizados adquiridos para o padrão comercial TGG-SC, TGG-PC e TGG. h) Mapa micro-Raman TGG-SC para banda em 356 $cm^{-1}$.

A determinação estrutural do cristal foi realizada usando difração de raios X de monocristal que confirma que os minerais sintetizados são compostos de monocristais de granadas de térbio e gálio (TGG-SC). O mineral cristaliza no sistema cúbico, com a = 12,3539 Å e grupo espacial $Ia\bar{3}d$, como esperado para o TGG.

A estrutura cristalina obtida é representada na Figura 9c), na qual é possível ver os cátions $Tb^{3+}$ coordenados a oito átomos de oxigênio, e duas unidades independentes de cátions $Ga^{3+}$, uma das quais é hexacoordenada em uma geometria octaédrica, enquanto a outra é tetracoordenada, em uma geometria tetraédrica, com τ'4 = 0,98. O índice de distorção calculado (D) para Tb é 0,02017, enquanto é zero para os átomos de Ga, destacando a regularidade da esfera de coordenação. O alongamento quadrático (<λ>) para os átomos de Ga é de 1,0077 para o Ga hexacoordenado (Ga1) e 1,0148 para o tetracoordenado (Ga2).

Os cátions $Tb^{3+}$ estão a 3,783 Å um do outro, enquanto a separação entre diferentes átomos $Ga^{3+}$ (Ga1–Ga2) é de 3,453 Å e entre dois átomos Ga tetracoordenados (Ga2–Ga2) é de 3,783 Å. Enquanto isso, as distâncias Tb1–Ga1 e Tb1–Ga2 são 3,453 Å e 3,088 Å, respectivamente, e Ga1–Ga1 é 5,349 Å.

Na Figura 9d) é possível observer a emissão verde decorrente dos cristais cúbicos TGG após excitação com uma luz LED azul (488 nm). Como já explicado, tal emissão vem da transição $^5D_4 \leftarrow {}^7F_6$ de $Tb^{3+}$ presente em sítios cristalinos da estrutura, como confirmado pelo aparecimento das emissões de Starks observadas na Figura 9e. Mesmo que o conteúdo molar de $Tb^{3+}$ nos cristais levasse à extinção da emissão, a luminescência dos cristais é intensa o suficiente sob iluminação de um LED fraco de fonte de 488 nm. Assim, o uso de tais cristais como micro-LEDs verdes também é promissor.

Os mapeamentos de microluminescência e microRaman foram obtidos da superfície da face de um cristal e é possível observar a homogeneidade dos espectros de luminescência e Raman em toda a superfície (Figura 9 f-g)).

Além disso, o espectro de luminescência do cristal único, Figura 9f), exibe uma definição mais alta dos níveis de energia do íon $Tb^{3+}$ em comparação ao policristal. O espectro TGG-SC é muito semelhante ao do TGG comercial obtido por Czochralski.

Este conjunto de dados apresentado na Figura 9 mostra a precisão da metodologia de solução supersaturada para obter monocristais de TGG a partir do vidro fundido.

## Referências

1- Mauro, J. C.; Zanotto, E. D. International Journal of Applied Glass Science, 5 (2014) 313–327.
2- Zanotto, E. D.; Mauro, J. C. Journal of Non-Crystalline Solids, 471 (2017) 490–495.
3- Morse, D. L.; EVenson, J. W. International Journal of Applied Glass Science, 4 (2016) 409.
4- Mo, X. Z. et al. Journal of Alloys and Compounds, 658 (2016) 967-972.
5- Shen, Y. et al. Optik, 127 (2016) 2069-2073.
6- Faraday, M. Transactions of the Royal Society of London, 5 (1846) 592.
7- Munin, E.; Roversi, J. A.; Villaverde, B. Journal of Physics D: Applied Physics, 25 (1992) 1635-1639.
8- Souza, A. E. et al. Journal of Alloys and Compounds, 864 (2021) 158804.
9-Franco, F. D. et al. Journal of Materials Research and Technology, 11 (2021) 312-327.
10-F, Starecki. et al. Sensors and Actuators A: Physical, 2015, 207 (2015) 518-525.
11-Su, X et al. Photonics, 9 (2022) 372.
12- Chani, V. I. et al. Journal of Crystal Growth, 210 (2000) 663.
13- Feng Y. et al. Optics Letters, 13 (2015) 031602.
14- Sawada, K.; Adachi, S Journal of Luminescence,16 (2015)138.
15- Chen, Z. et al. Optical Materials, 46, 12 (2015).
16- Tsidaeva, N. I. et al. IEEE Transactions on Magnetics, 50 (2014) 1001704.
17-Varshineya, A. K.; Fundamental of Inorganic Glasses, Academic Press Inc.: San Diego, 1994.
18- Sontakke, A. D.; Biswas, K.; Annapurna, K. Journal of Luminescence, 129, (2009) 1347-1355.
19- Cai, M. et al. Optical Materials Express, 5, (2015) 1431-1439.
20- Rao, H. V., et al. Spectrochimica Acta Part A: Molecular and Biomolecular Spectroscopy, Volume 188, 2018, Pages 516-524,
21- Sawada, K.; Nakamura, T.; Adachi,S. Journal of Applied Physics, 120 (2016)143102.
22- Middletona, R. C.; Muthua, D.V.S.; Kruger, M. B. Solid State Communications, 148 (2008) 310–313.
23- Monteseguro, V. et al. The Journal of Physical Chemistry C, 118 (2014) 13177-13185.
24- Sales, T.O. et al. Journal of Luminescence, 205 (2019) 282-286.

**Instituto de Química – UNESP - Araraquara**

**Departamento de Química Geral e Inorgânica**

# BEPE TITLE

# Development of glass materials containing magnetic nanoparticles and rare earth ions for magneto-optical applications

post doctorate grant – FAPESP -2020/15395-4

BEPE period: 01-05-2022 a 30/04/2023

Bolsista: Dra. Juliane Resges Orives

Supervisor: Prof. Dr. Marcelo Nalin

Araraquara – may, 2023

## Abstract

This report refers to the activities performed during the postdoctoral BEPE at the Université de Bordeaux. It describes the most expressive results obtained. The thermal poling, technique present at the ISM and ICMCB, consists of placing two electrodes, one on each side of a glass slide and, subsequently applying a potential difference as a function of temperature. At high temperatures, the ions have their mobility increased, providing the migration of cations in the direction of the cathode. With migration, a layer, a few microns thick, changes its composition close to the surface resulting in a strong static electric field near the anode. A very interesting work regarding the thermo-electrical micro-imprinting processes of a Borogermanate composition containing $Tb^{3+}$ ions was carried out. The interest in studying this composition containing these paramagnetic ions was to verify how the poling treatment can modify the optical, structural and magnetic properties of this glass. The results in this report results shows that the treatment was efficient in modifying the glass surface. The absorption measurements presented a large change in the absorption coefficient, indicating that oxidation of $Tb^{3+}$ ions to $Tb^{4+}$ had occurred. The Luminescence measurements showed that in the poled zones the luminescence decreases around 10x, while in the unpoled zones the luminescence was not modified, confirming the oxidation of $Tb^{3+}$ ions in the contact zone. For the first time, the oxidation of rare earth ions was demonstrated by means of thermal polling and, consequently, the control of luminescence on a microscale.

## 1- Introduction

Borogermanate glasses containing $Tb^{3+}$ ions are interesting materials due to their luminescent and magnetic properties emerging from the partially filled 4f electronic configurations of terbium[1-3]. In recent years, these glasses have been investigated and their potential for photonics and magneto-optical devices has been highlighted[1-6].

The most stable oxidation state of terbium ions is trivalent, but terbium also can present the tetravalent state, having a standard $Tb^{4+}/Tb^{3+}$ reduction potential of +3.1V.[7-8] Regarding the particularities of these two oxidation states $Tb^{3+}$ has a $4f^8$ electronic configuration, while $Tb^{4+}$ is $4f^7$ and the effective magnetic moment for $Tb^{3+}$ and $Tb^{4+}$ ions are 9.72 µB and 7.94 µB, respectively.[1,9] In addition, $Tb^{3+}$ ion exhibits its green emission near 544

nm due to the $^5D_4 \rightarrow {}^7F_5$ transition, while the $Tb^{4+}$ ions do not exhibit emission and due to its absorption band in the visible region it acts as a quenching center.[8,10]

Some glasses may show coexistence between $Tb^{3+}/Tb^{4+}$ and the existence of this ratio may depend on the oxidation-reduction conditions of the melt or on the oxide concentrations of the matrix.[5,11-13] When same composition and melting conditions are used, the increase in terbium oxide concentration induces an increase in optical basicity creating favorable conditions for the oxidation process to occur, as reported by Nalin et al.[3]

Having in view that glasses containing $Tb^{3+}$ and/or $Tb^{4+}$ can present differences in their structural, luminescent, optical, and magnetic properties, this opens up important opportunities in finding a way to control and/or modulate the oxidation state of terbium at the microscale. Which can lead to new applications in the field of integrated photonic devices that constantly needs the merging of multiple functionalities.[14-18]

A technique that has been effectively used for surface modification is the thermal polling, from which it is possible to implement and modulate different properties in various types of glasses such as chalcogenides, silicates, phosphates, fluorides, heavy oxide metal glasses, among others.[18-28] This glass surface polarization process consists of heating a glass matrix positioned between the anode and cathode, followed by the application of high DC voltage for a certain time, during which there is an increase in the mobility of ionic charge carriers, commonly alkaline and alkaline earth cations, towards the cathode.[19,29-31]

Over the years this technique has been improved to modify the surface in a patterned way, with spatial resolution on the micrometric scale, employing a structured anodic electrode that acts as a stamp during an imprinting process.[32-34] This transfer of periodical micro-structured motifs to the treated glass makes it possible to control several properties, such as chemical reactivity[35], surface durability[36], surface topology[20], surface electrical potential[37]. With regard to optical properties, it is possible to induce second-order nonlinear response[18, 38], to prepare waveguides[39], micro-lenses with gradient of refractive index[17] and linear[40] and nonlinear diffraction gratings[33].

In addition, Lipoviski's group showed the possibility of using poling to oxidize Ag and Cu nanoparticles in the contact zones with the electrode, creating optical structures with transparent and colored zones with different absorptions.[32,41]

Although poling has already been used for several purposes, it has not- yet been explored to modulate properties of rare earth ions. In this context, we focus our attention on

demonstrating the control of the oxidation state of terbium ions induced by the polarization treatment. Raman and Luminescence mappings are used to show, respectively, the structural modifications and spatial micrometric control of luminescence in the poled layer.

## 2- Experimental details

Borogermanate-$Tb^{3+}$ glasses with molar composition of 96(46$GeO_2$-29$B_2O_3$-16$Na_2O$-5BaO-4$Al_2O_3$)-4$Tb_4O_7$, were prepared by the melt-quenching method from chemical-grade germanium oxide $GeO_2$ (Sigma-Aldrich), boric acid ($H_3BO_3$, Sigma-Aldrich), aluminum oxide ($Al_2O_3$, Sigma-Aldrich), sodium carbonate ($Na_2CO_3$, Sigma-Aldrich), barium carbonate (BaCO3, Sigma-Aldrich), and terbium oxide ($Tb_4O_7$, Sigma-Aldrich), this pristine glass was labeled as BGTb. In the first step, the thermal decomposition of $H_3BO_3$ was performed at 500 °C for 30 min in a resistive furnace.

The vitreous boron oxide glass was ground to fine powder and homogenized with the other components in an agate mortar and then placed in a platinum crucible for sintering treatment at 1450 °C for 2 h under ambient atmosphere. The melt was cooled in a preheated stainless steel mold at 500°C and then annealed at the same temperature for 5 h, to minimize its mechanical stress, followed by slowly cooling to room temperature during 12 h. Then glasses were optically polished on both sides to obtain 0.6 mm thick samples to undergo the poling treatment.

Figure 1 illustrates the Thermo-electrical imprinting process that was performed in a sealed enclosure under a $N_2$ flow of 6 L/min. A piece of silicon wafer was used as cathode and a borosilicate slide was placed between the silicon and the sample as a sacrificial layer in order to preserve the optical quality of the sample.

Different platinum electrodes configurations were used as anode to pattern the surface: first homogeneous platinum film everywhere conductive electrode and the second was a structured electrode of a 100 nm thick platinum film deposited on a silicate glass slide of 5 × 5 × 1 $mm^3$, prepared by a classical lithography process resulting in non-conductive squared motifs of 40 x 40 $\mu m^2$ delimited by 10 µm width electrically conductive Pt grid in a side and covered with 100 nm gold film in the other side.

Glass samples were heated up to 300 °C and a DC voltage of 1 kV was applied (at a 300 V/min rate) and left at these conditions for 30 min. Then the system temperature was

cooled to room temperature and finally the electric field was removed. The poled samples using the structured and homogeneous electrode were labeled as BGTb-H and BGTb-S, respectively.

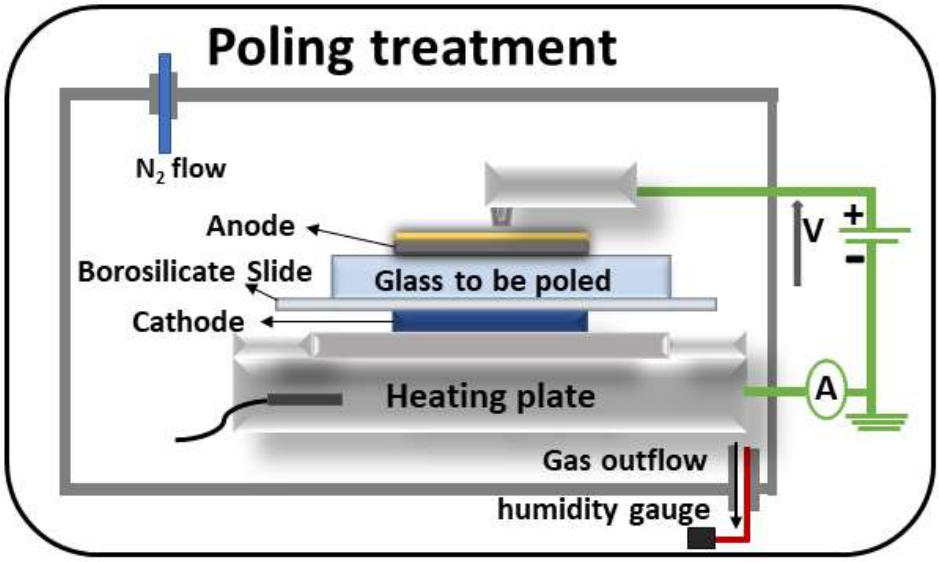


**Figure 1**- Schematic representation of system used to carry out the thermo-electrical micro-imprinting process.

For the pristine glass the Differential scanning calorimetry (DSC) measurements of the were performed using a Netzsch DSC Pegasus 404F3 apparatus. The BGTb sample was placed in a platinum crucible and heated from 25 to 1000 °C, at a rate of 10 °C $min^{-1}$, under an atmosphere of nitrogen (20 mL $min^{-1}$). The maximum errors were ± 2 °C for Tg and Tx, and ± 4 °C for ΔT. The linear refractive indices (RI) were measured on the bulk samples using the Brewster's angle method at different wavelengths (532, 639, 785 and 935 nm). The dispersion curves were obtained by fitting the experimental data with a Cauchy fit. TThe optical window has been reconstructed from transmittance spectra obtained in the UV−Vis−NIR between 200 nm and 2 μm using a double-beam Agilent Cary 5000 spectrophotometer and transmittance spectra in the infrared between 2 and 10 μm using a FTIR Bruker Equinox 55 spectrophotometer.

After thermal poling treatment samples poled with homogeneous electrode were characterized by secondary ion mass-spectrometry (SIMS) on a PHI Adept 1010 dynamic SIMS system. Excitation of secondary ion emission was made by a focused primary ion beam of $Cs^+$ at 2 KeV. For the negative secondary ions, sample was biased to - 30 keV and for positive ions

+ 30 kV. A qualitative distribution of elements in poled sample was examined by etching of the surface with ion beam. An area of 300 × 300 $\mu m^2$ was scanned. Etching rate was obtained from the depth of the crater measured by optical profilometry. The absorption spectra for BGTb and BGTb-H were obtained in the UV-Vis-NIR between 200nm and 800 nm using a double beam Agilent Cary 5000 spectrophotometer.

Micro-Raman measurements and two-dimensional spatial Raman intensity maps were recorded with laser sources at 532 and 785 nm using the confocal spectrometers HR800 (Horiba/Jobin Yvon) and Xplora (Horiba), respectively, using in both cases a 100× (N.A.= 0.9) objective. Micro-luminescence data were acquired using a Labram (Horiba) spectrometer with laser source at 488 $cm^{-1}$, a 150 grooves·$cm^{-1}$ grating and 50× (N.A.= 0.75) objective.

The second order optical susceptibility [$\chi^{(2)}$] was quantified by the Maker Fringe technique using a 1550 nm intracavity optical parametric oscillator nanosecond laser operating at 30 Hz with a maximum impulsion of 100 μJ during a 20 ns pulse and with a spot size of 100 μm. Two sets of experiments were performed: θ-scan (changing the incident angle with incident light polarized p or s and collecting p polarized light) and ψ-scans (at a fixed incidence angle, changing the incident polarization and collecting p or s polarized light. The SHG response depends on the incident intensity, the indices at ω and 2ω of both the bulk and the poled layer, the thickness of the poled layer, and the induced $\chi^{(2)}$.

Atomic Force Microscopy (AFM) measurements were performed at the samples by an AFM Dimensions Icon (Bruker) using a PFQNE-AL cantilever. The refractive index change Δn was evaluated using a commercial quantitative phase imaging QWLSI sensor, SID4Bio by PHASICS in transmission mode placed on a microscope. An intensity image and a phase image showing the optical path difference (OPD) produced by the transmitted light is the final output of the wave front sensor.

## 3- Results and discussion

The initially proposed composition was the one already well studied by our group with 8% of $Tb_4O_7$, 37.7$GeO_2$-23$B_2O_3$-3.7$Al_2O_3$-9.2$Na_2O$-18.4BaO-8$Tb_4O_7$.[3] However, poling was not possible in this sample. Afterwards, the sample was modified for a higher % of sodium and lower % of barium and terbium, both bulky ions that could interfere with the process of migration

of sodium ions. After some modifications we arrived at this new composition (96(46$GeO_2$-29$B_2O_3$-16$Na_2O$-5BaO-4$Al_2O_3$)-4$Tb_4O_7$) with 4% of 8$Tb_4O_7$.

The DSC curve in Figure 2a) shows for this pristine sample a glass transition temperature (Tg) of 554 °C and a thermal stability of 131° C. The refractive index (RI), Figure 2b), obtained for the wavelengths of 775 and 1550 nm were 1.646 and 1.642, respectively. Figure 2c) shows the transmittance spectra of BGTb recorded from UV to NIR, in which the absorption bands are assigned to the 4f-4f electronic transitions of $Tb^{3+}$ ions. This glass presents an optical window from 0.5 µm up to 1.60 µm.

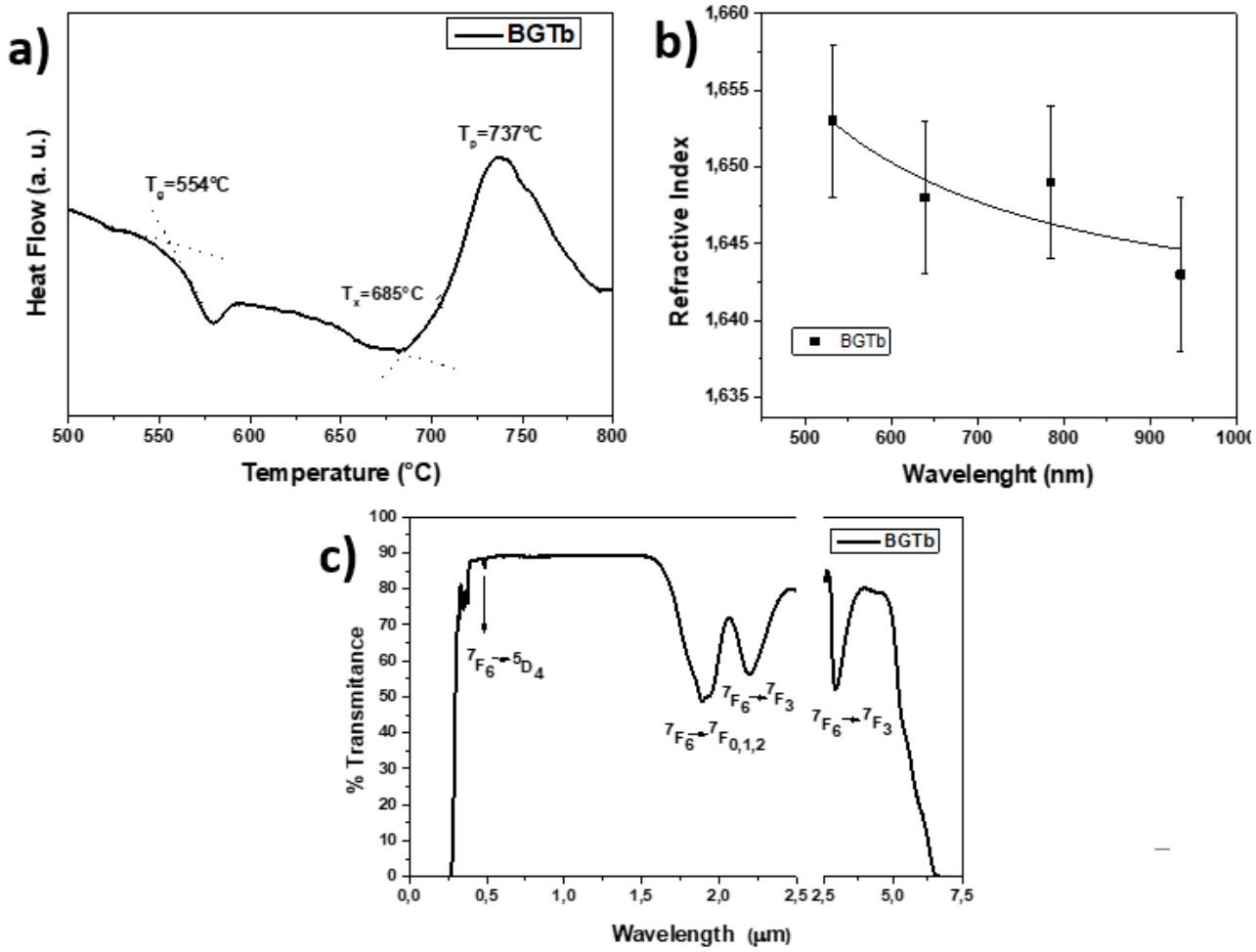


**Figure 2-** a) DSC curve, b) Refractive index dispersion prior to poling measured between 532 and 1550 nm and c) transmission spectra.

Poling using a homogeneous electrode was carried out at 3 different voltages 800, 1000 and 1200 volts (BGTb-H0.8kV, BGTb-H1kV and BGTb-H1.2kV). After the poling

treatment it is expected to see a series of changes in this pristine material, and to follow each one of them a different technique is used.

To verify the thickness of the sodium depleted layer, time-of-flight secondary ion mass spectrometry (TOF-SIMs) measurements were performed, this technique allows verifying the composition of a multilayer surface and thus quantifying the displacement of sodium in the polarized glass and allows to obtain the concentration of the elements in the glass. And then by optical profilometry the depth of the hole created is measured and corresponds to the thickness of the poled zone.

The Figure 3a) illustrates the profiles obtained for the different components of the glass matrix and a sodium depleted zone of approximately 0.7 µm is observed for the glass treated at 800 V, 0.92 µm for 1000V and 1.52 µm for sample poled at 1200V (Figure 3b).

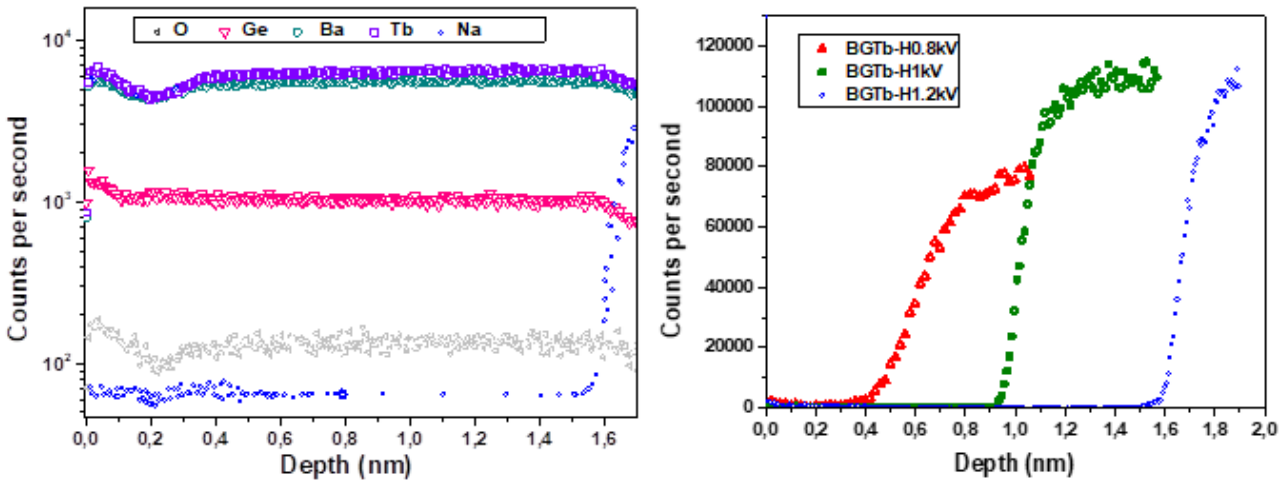


**Figure 3-** a) SIMS depth profile of various glass constituents of BGTb glass after poling. The 0 nm mark corresponds to the glass surface at the anode side and b) SIMS measured post-poled Na-depleted layer thickness at different voltages.

With the absence of sodium in the poled layer a structural change in the glass network is expected, and this structural change is evaluated by Raman spectroscopy (Figure 4). The bands at 500 $cm^{-1}$ it's assigned to antisymmetric stretching due to the Ge-O-Ge bond connecting rings with less than six members, while the band at 770 $cm^{-1}$ it's assigned to the asymmetric stretching in Ge-O-B bridges. It's possible to verify that the changes in the Ge network are not very large, a small decrease is observed in the non-bridging oxygen $(Ge_{ø3}O)^-$

band at 830 $cm^{-1}$ indicating that they are connecting with other units in the glass after de structural rearrangement.

Structural changes seem to be more pronounced in the bands between 1200 and 1500 and are related to borates units. There is an increase in the band at 1365 $cm^{-1}$ which is assigned to the vibrations of borate triangles. So, the initial interpretation is that due to the migration of $Na^{+}$ ions, the poled region becomes richer in negative charges leading to restructuring of borate units to achieve charge compensation, and in this way the change from $BO_4^{-}$ negatively charged to $BO_3$ occurs with release of molecular oxygen that presents a band at 1551 $cm^{-1}$.

This release of $O_2$ it's observed in several ionic glasses poled in blocked electrodes and it's evidence of this compensation mechanism in action. Infrared studies are in progress to complement these initial observations.

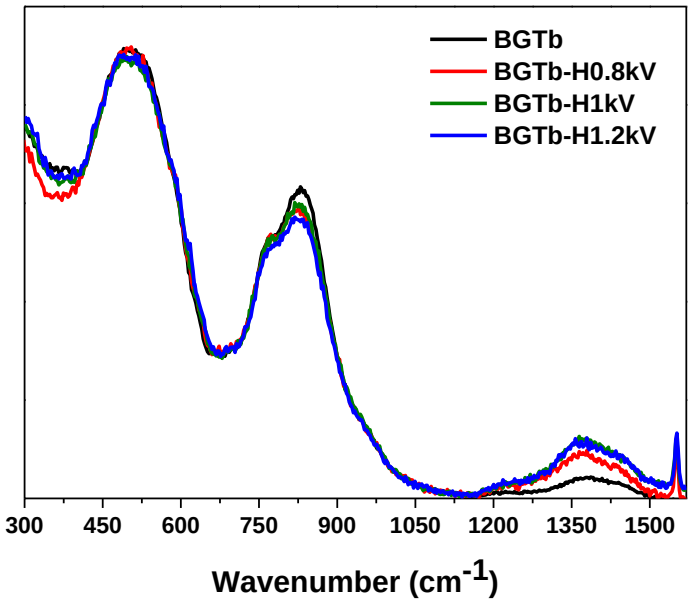


**Figure 4-** Raman response as a function of voltage. (Raman spectra of the different samples collected with the same objective and the same laser intensity and normalized at 500 $cm^{-1}$)

One of the observations that most called our attention was the fact that the BGTb glass obtained by melting quenching was colorless, while the BGTb-H samples showed a change in color to yellow only in the poled area located under the structured electrode as seen in the Figure 5a). No bleaching occurred after the poling experiments. This color change may indicate that an oxidation process from $Tb^{3+}$ to $Tb^{4+}$ occurred as reported for calcium

aluminosilicate and borogermanate glasses containing $Tb^{3+}$ homogeneously in the entire bulk volume.[5,12]

The optical absorption spectra of samples in UV-Vis from 250 to 800 nm range are shown in Figure 5b). The band located at 299 nm is related to the spin allowed transition from $4f^8 \rightarrow 4f^7\ 5d^1$ do $Tb^{3+}$ which occurs between 220 and 300 nm, while the recorded absorption bands centered at 318, 340, 350, 358, 370, 378, and 488 nm at were assigned to 4f–4f transitions from the $^7F_6$ ground state of $Tb^{3+}$ to the excited levels of ($^5D_{0,1}$, $^5H_7$), ($^5G_2$, $^5L_6$), ($^5L_9$, $^5G^4$), $^5L_{10}$, ($^5D_3$, $^5G_6$), and $^5D_4$, respectively.[42]

Looking at the absorption of the poled region in the BGTb-H, there is a large absorption in the visible region between 300 and 650 nm which is assigned to the $Tb^{4+}$ ions due to several electronic transitions from ligand-to-metal charge transfer states.[43-44] Its presence explains the yellow coloration of the sample and confirms the oxidation of ions $Tb^{3+}$ during the polling process.

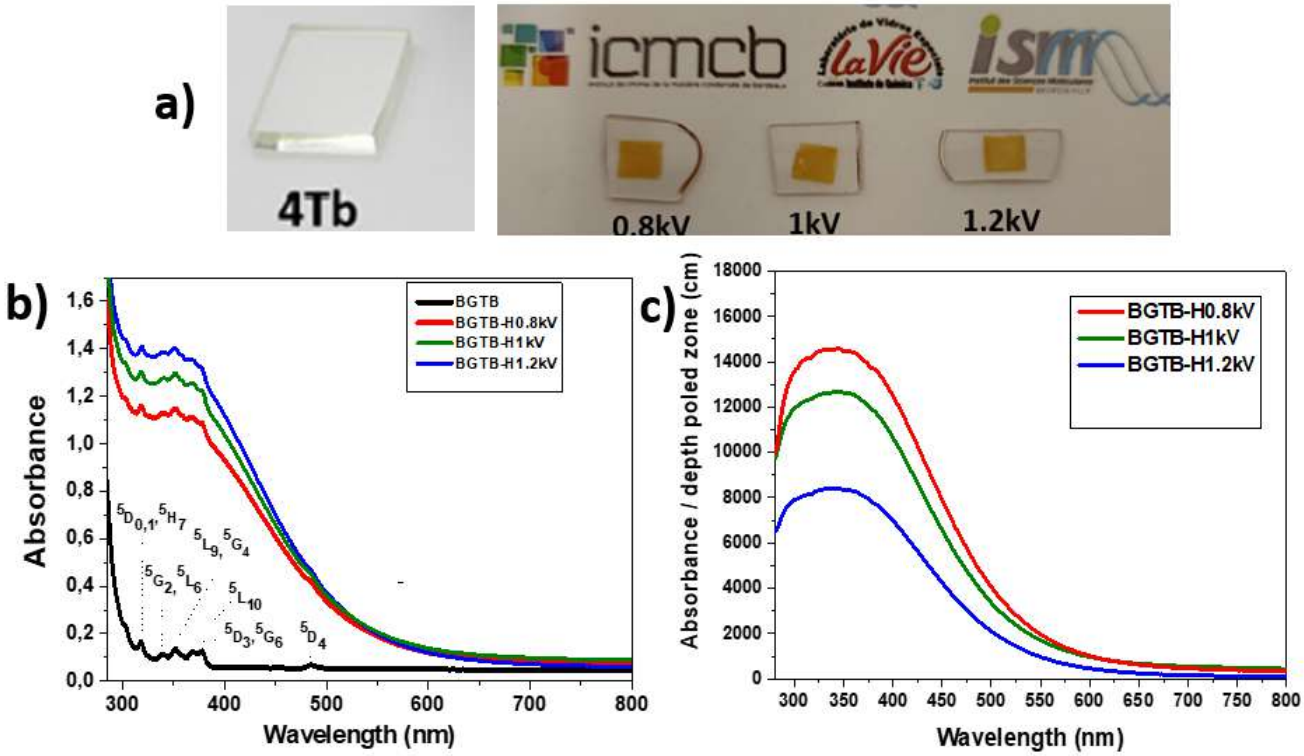


**Figure 5**- a) photograph of BGTb and poled glasses at different voltages, b) Absorbance spectra in the UV-Vis region obtained for BGTb before poling and BGTb-H homogeneously poled and c) absorbance divided by the depth of poled zone.

In addition to this broad band, it's possible to observe that this spectrum is a mix between the components of the $Tb^{3+}$ and $Tb^{4+}$ spectra, this occurs because the absorption spectrum is collected for the entire thickness of the sample (0.6 mm) while the area containing $Tb^{4+}$ is limited to the thin layer created through the process of thermal polarization on the order of a few micrometers.

Because of this the spectrum of pristine glass was subtracted from the poled zone spectra in order to obtain only the $Tb^{4+}$ spectrum. And since the absorption of $Tb^{4+}$ is a function of the poled layer it's possible to have an idea of the $Tb^{4+}$ concentration in the poled layer, dividing the absorption spectra by the size of the layer. In this way a normalized spectrum as a function of $Tb^{4+}$ concentration in the poled zone its obtained and presented in Figure 5 c). It is possible to observe that there is more $Tb^{4+}$ in the poled sample at a lower voltage, and what was expected was an increase in $Tb^{4+}$ with increasing thickness of the poled zone. For this reason, more experiments were done to try to understand this effect.

Glasses are isotropic systems and have third-order nonlinear properties. Second-order nonlinear properties, linked to the $\chi^{(2)}$ tensor, only exist in materials with asymmetric macroscopic centers. Thus, in centrosymmetric materials, such as glasses, no second-order nonlinear phenomenon occurs. On the other hand, is it's possible to "break" the isotropy of the glass using the thermal poling treatment, which generates a permanent polarization in the material and second harmonic generation signal (SHG).

To verify if the glass presents SHG response after poling treatment, Maker Franges measurements were performed. This experiment consists in measure the SHG intensity as a function of the incident angle using a p-polarization for both the incident beam and detected SHG (θ−pp scan). And the first observation was that the BGTB-0.8kV did not present a second harmonic generation signal, while BGTb-H1kV and BGTb-H1.2kV showed a non-linear response (Figure 6a) and b)).

A model described in Ref. 45. was used to understand the origin of this SHG signal in these two samples, and the fitting obtained by the model showed that the origin is an EFISH (electric-field-induced second harmonic), an electrooptic effect resulting from the implementation of space charge close to the surface triggered by sodium depletion, and this static electric field interacts with the third order susceptibility of the glass $\chi^{(2)} = 3\chi^{(3)} E_{stat}$.

To go into more detail in the poling induced-$\chi^{(2)}$ tensor characterization, SHG-polarization scans (called Ψ-scans) were processed. Figure c) and d) d presents the SHG

intensity versus the incident polarization state, Ψ, for a p- and s polarized SHG measured intensity (respectively called Ψ−p and Ψ−s scans). These SHG polarization scans were simulated considering the EFISH mechanism and the $\chi^{(2)}$ values obtained for BGTb-H1kV and BGTb-H1.2kV were 0.24 and 0.3 pm/V, respectively.

The SHG sign is linked with the I implementation of a space charge at the end of the treatment, it is necessary to have a charge density per volume of trapped charges in this layer in the order of $10^3$–$10^4$ C/m$^3$ to reach an internal field in the range of $10^8$ V/m$^3$ to present SHG signal, so the sample polled at 0.8 kV did not reach this internal field and showed no signal.

There are many things happening in the BGTb glass after poling: sodium migration, structural change, oxidation of terbium, implementation of SHG signal, how to understand the mechanisms that lead to these responses?

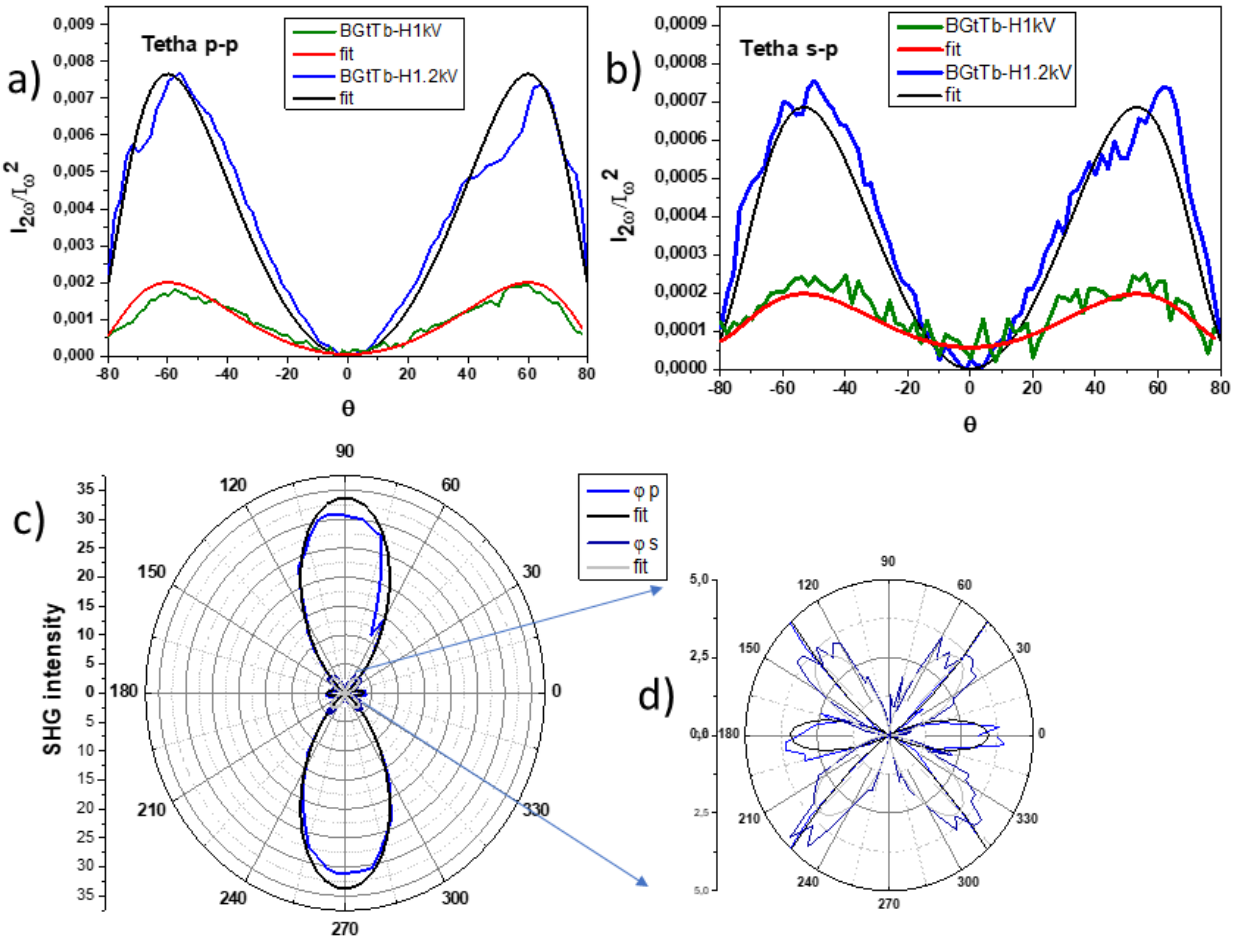


**Figure 6-** Macro-SHG measurements on BGTb-1kV and BGTb-1.2kV a) SHG measurements as a function of the incident angle with a fixed p-polarization state for both incident beam and detected SHG, and b) SHG measurements as a function of the incident angle with a fixed p-polarization state and s-polarization detected SHG, c) as a function of the incident polarization state with a fixed incident angle

of 30° and either a p- or s-polarization detection (respectively Ψ−p and Ψ−s). d) shows a zoom of the central part of figure c).

Looking to the Figure 7, interestingly we see that in this case two compensation mechanisms for sodium migration are taking place but they don't appear simultaneously in the same way as a function of voltage.

First at 0.8 kV it's possible to see a rapid increase in the concentration of $Tb^{4+}$ and no charge implementation is observed in the poled zone, then for high voltages (1 and 1.2 kV) the concentration of $Tb^{4+}$ starts to decrease and the field starts to be implemented, this this unexpected behavior is happening due to the increase of negative charges coming from the structural rearrangement at these voltages. As the glass begins to release more molecular oxygen, more electrons are released and terbium starts to trap these electrons and returning to $Tb^{3+}$ and now we have a second order non-linear response.

These observations about this unique system have led to the question: Is it possible to control this effect locally by thermoelectric imprinting?

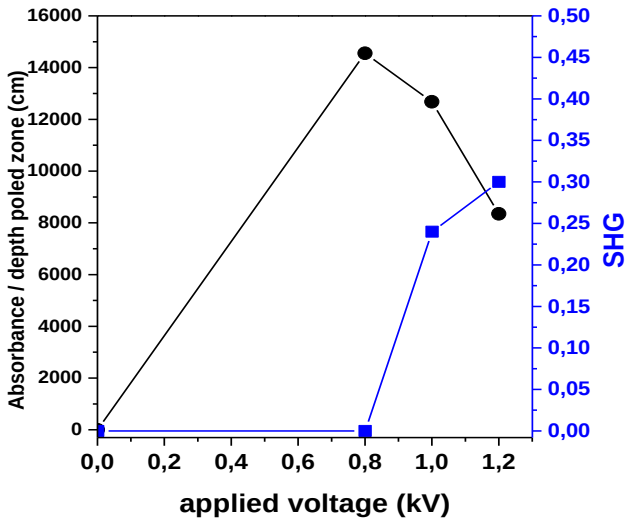


**Figure 7-** Absorbance divided by the depth of poled zone and SHG response as function of applied voltage (kV).

A 40 by 40 µm structured electrode separated by a 10 µm of Pt conductive zone was used for the micro-imprinting process. In Figure 8 a) and b) we it's possible to observe that the micro-imprinting resulted in a very nice patter perfectly reproduced at a microscale on the glass surface.

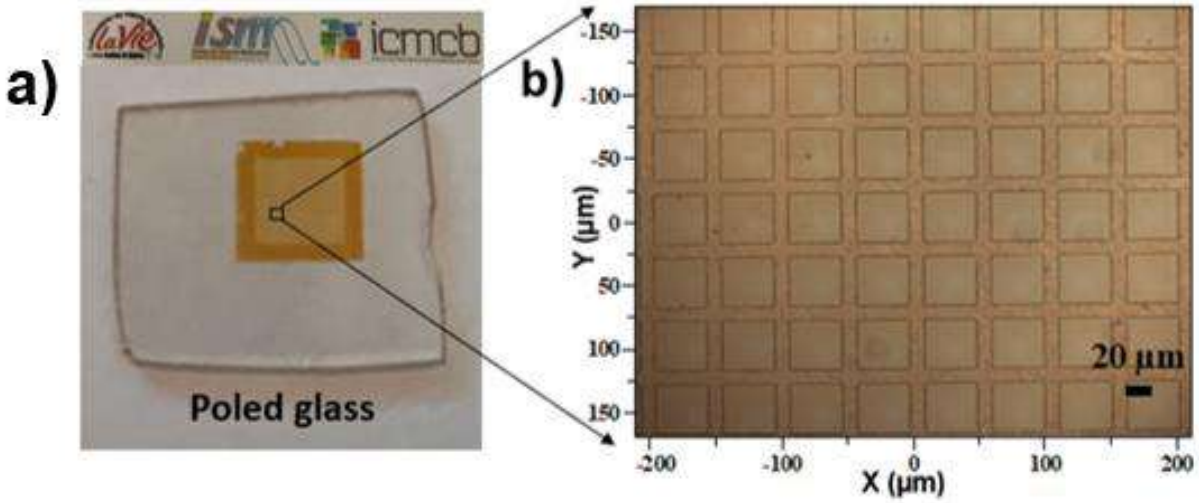


**Figure 8-** a) photograph of BGTb-S1kV poled glass and b) Microscope image of the structured micro-imprinting surface after poling (20x lens).

The µ-luminescent measurements, Figure 9a), were carried out for the poled zone, border and center of the square using for excitation the wavelength of 488 nm, the bands at 541, 582, and 620 nm were assigned to the transitions from $^5D_4$ to $^7F_j$ (j = 5,4,3) multiplet.[3]

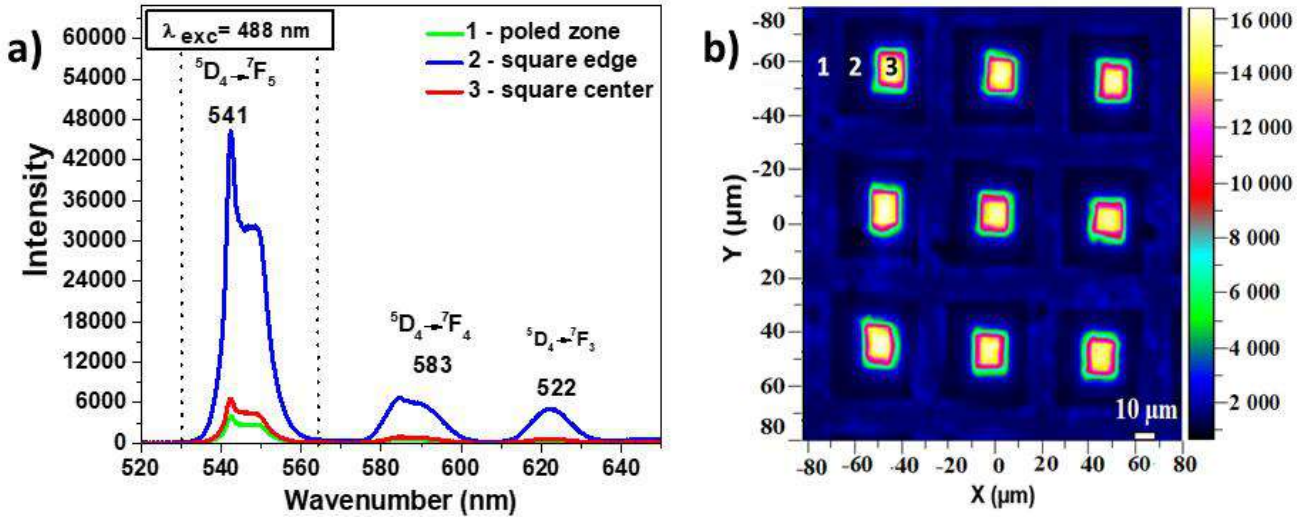


**Figure 9-** a) emission spectra for BGTb-S poled using structured electrode. b) µm-Luminescence map for emission bands between 530 and 560 nm.

Having in view that $Tb^{3+}$ ion present green emission at 541 nm, while the $Tb^{4+}$ ions have no emission a very interesting luminescence pattern was obtained after poling

treatment, in which in the center of the square the luminescence was not affected by the poling treatment, but for the poled zone and the borders of the square a decrease in luminescence around 10x occurred. This result shows for the first time the control of terbium oxidation from $Tb^{3+}$ to $Tb^{4+}$ in a patterned way using the poling thermic.

The Raman measurements were made with a wavelength of 532 nm and presents the same profile that for the samples poled with homogeneous electrode. Besides that it's also possible to observe in these spectra a contribution from luminescence, because the band at 355 $cm^{-1}$ corresponds to emission at 541 nm, and both Raman and Luminescence effects can be obtained with one spectrum.

The mapping for the band at 355 $cm^{-1}$ shows exactly the same profile that Figure 9 b). It is also observed that the spectrum for pure glass and the center of the square is the same, indicating that the center was not affected by poling and because of that there is a high luminescence in this region.

The Mapping for the band at 1551 $cm^{-1}$ shows the formation of molecular oxygen in the contact zone, confirming the migration of sodium with release of $O_2$ and electrons towards the anode. Another important observation is that for the Raman mapping in the contact zone there is a high concentration of molecular oxygen and a gradient towards the center where we do not have the formation of molecular oxygen, in other words the poling was not effective in the center.

But looking at the luminescence map there isn't a gradient, there is a high luminescence in the center, almost no luminescence at the edges and in the contact zone the luminescence increases again a little. This can be seen in the profile of the mapping for the band at 355 $cm^{-1}$ is shown in the Figure 11a).

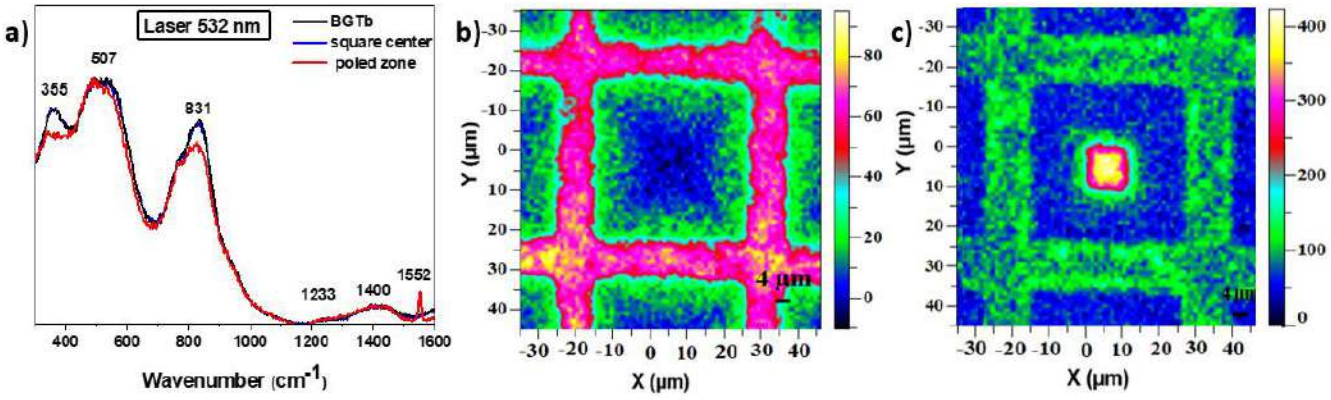

**Figure 10-** a) Raman spectra in the poled zone and square center surfaces at 532 nm. μm-Raman maps for: b) the band located at 1552cm$^{-1}$ and c) for the band at 355 cm$^{-1}$.

For patterned samples, we can think about the effective voltage decreasing as a function of distance, when 1 kV it's applied, there is a maximum efficiency of effective voltage in the contact zone, and the effective voltage decreases at the borders until it reaches zero, this effect it's exemplified by the scheme in Figure 11b).

In this poled zone, first all the terbium is oxidized and, in the sequence, the $Tb^{4+}$ starts to trap negative charges coming from the restructuring of network and then it's reconverted to $Tb^{3+}$ which results in a higher luminescence in the poled zone now, as shown for the homogeneous sample poled at 1 kV. In the borders of the square there is a lower effective voltage around 0.8 kV and we see that in this region of the curve the concentration of $Tb^{4+}$ is higher and consequently the luminescence is lower. Going to the center that was not affected by the poling the concentration of $Tb^{3+}$ is the same as that of pure glass and we have a high luminescence.

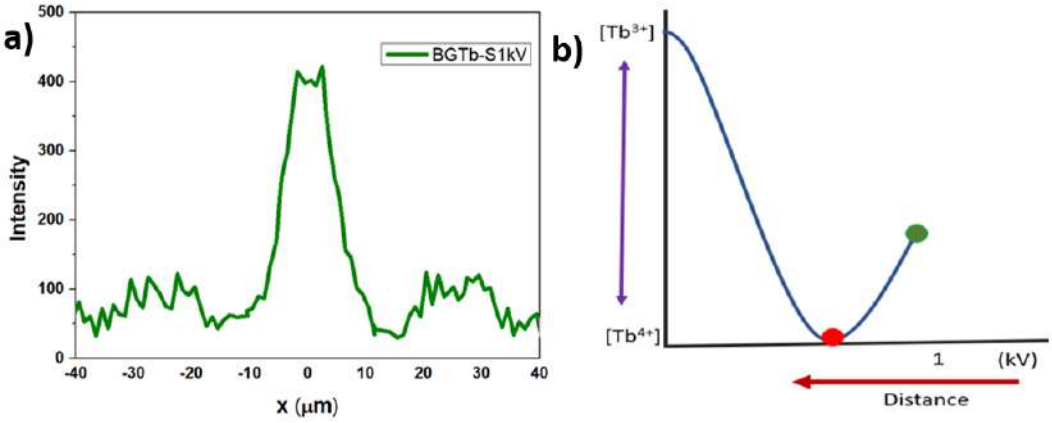


**Figure 11-** a) Profile of Raman mapping at 355 cm$^{-1}$ and b) Scheme of variation of $Tb^{3+}$/$Tb^{4+}$ concentration as function of effective voltage.

The variation in composition between the poled and unpoled zone affects the optical properties, resulting in a change in the RI. From the topological profile obtained by AFM it's obtained that in the poled zone there was a contraction of 12 nm due to the migration of sodium (Figure 12 a) and b)).

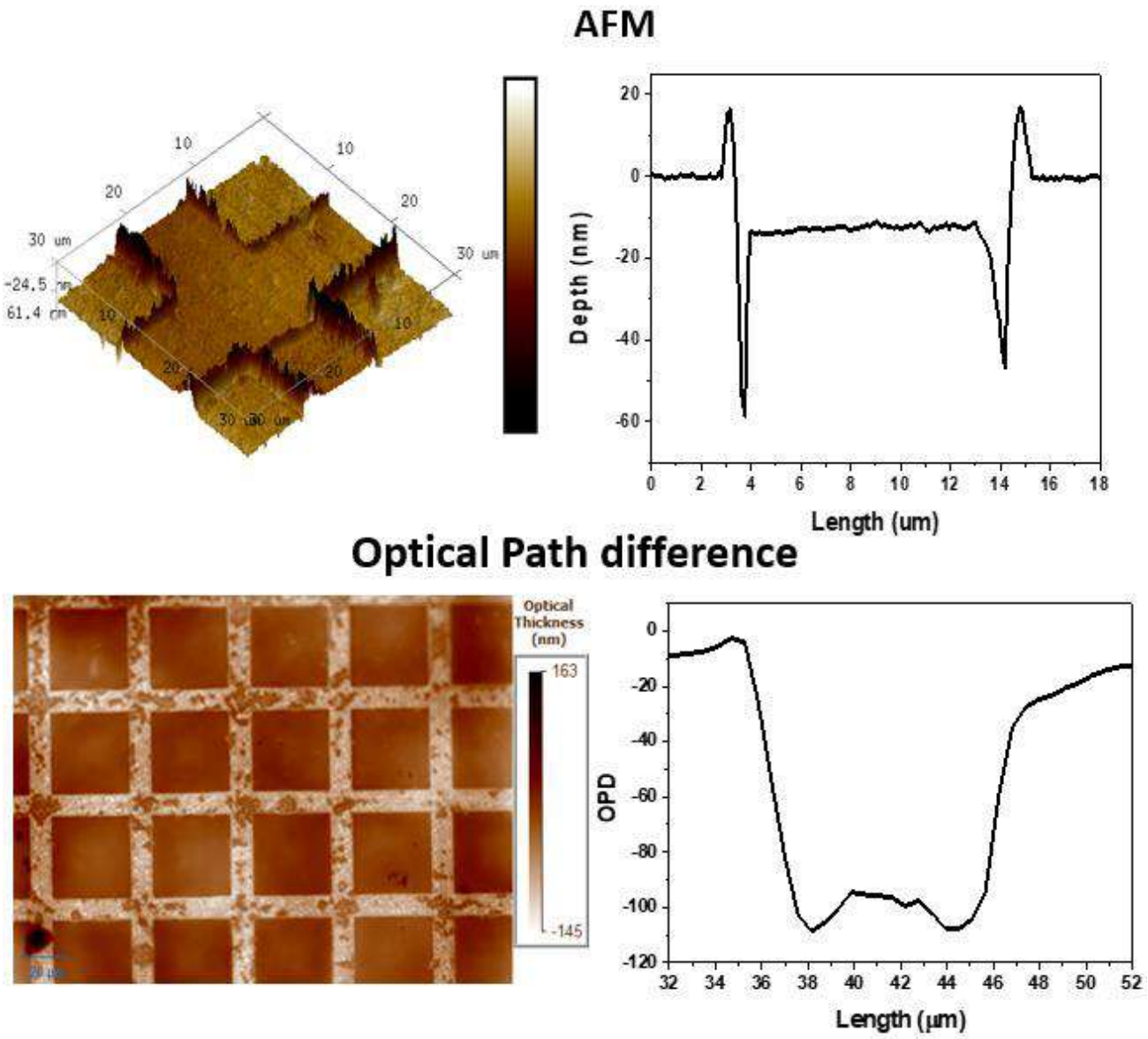


**Figure 12**- a) 3D AFM image of BGTb-S1kV, b) AFM profile, c) Phase contrast images in the sample and d) the Respective optical thickness profile.

A white light is sent into the sample, and the optical path variation is recorded and depends on the product of the index variation and the thickness, when the two are changing the topological variation needs to be taken into account. The OPD difference found was 93. The new RI of the poled zone is obtained by the following expression:

$$n_x = (n*d - d_x - OPD)/d_p - d_x$$

were $d_x$ it's the topological depth (measured by AFM), $d_p$ it's the depth of poled layer, n it's the RI of pristine glass and $n_x$ it's the RI of poled zone. The necessary data for the calculation it's shown in Table 1.

**Table 1-** Data used to calculate the new Ri in the poled zone.

| **λ (nm)** | **n** | **$d_p$** | **$d_x$** | **OPD** | **Δn** | **$n_x$** |
|---|---|---|---|---|---|---|
| 550 nm | 1.653 | 920 | 12 | 93 | -0,1110 | 1.559 |

The negative value of delta n (Δn=-0,1110) obtained indicates a lower IR in the poled zone and is attributed to a decrease in local density due to a decrease in sodium concentration after poling treatment.

## 4- Conclusion

The poling thermic was effective for modifying the surface and controlling the oxidation state of the ions. $Tb^{3+}$ to $Tb^{4+}$. Different electrodes were used to demonstrate that for glasses containing terbium two charge compensation mechanisms are happening according to the voltage used for the poling treatment. In this work, for the first time was demonstrate the control the terbium oxidation on a microscale and consequently the luminescence in a pattered way. It was also possible to modify the index of refraction of the poled zone with a Δn=-0.1110. These results are very promising in the in the field of integrated photonic devices that constantly needs the merging of multiple functionalities and also can lead to obtaining of magneto-optical diffraction gratings.

## 5 – Acknowledgments

To FAPESP for the BEPE grant, to Professor Marcelo Nalin for the support and encouragement for the completion of higher education. To Dr. Thierry Cardinal (ICMCB) and Dr. Marc Dussauze (ISM), for receive-me at their laboratories, for all the shared knowledge, and for providing all the necessary resources for the execution of the project at the University of Bordeaux.

## 5- Congress presentation

26th International Congress on Glass (ICG2022), 03 Jul 2022 - 08 Jul 2022, Berlin, One-step obtention of TGG single crystals embedding in heavy metal oxide glasses, Orives, J. (Speaker); Albino, L.; Destro, F.; Mameli, V.; Marcondes, L.; Souza, A.E.; Cardinal, T.; Nalin, M.

## 6- Articles in the writing phase

Two articles are being written from the data obtained, the first concerns to report the control of luminescence in microscale and is in the final writing phase and it will be sent to Applied physics letters (IF 3,97).

“Juliane Resges Orives, Lia Mara Marcondes, Lara Karam, Thierry Cardinal, Marc Dussauze, Marcelo Nalin, **Micrometric spatial control of the luminescence of a borogermanate glass containing terbium by thermo-electrical imprinting treatment**. Applied physics letters.

A second paper, regarding the compensation mechanism and space charge implementation in the poled zone is also being written.

## 7- Dissemination of results

The results will be presented at international congresses and two articles will be submitted. A seminar will be presented for the Brazilian research group to disseminate the techniques used at the University of Bordeaux.
The advanced training in the technique of cartography using Micro Raman will be widely used in our laboratory that has this equipment, and will be shared with the students of the group. In addition, the Group of Prof. Gael Poirier from UNIFAL in Poços de Caldas, with whom our group maintains cooperation, has just set up a system similar to the one used in France and will allow other studies are carried out in Brazil.

# References


1- GAO, Guojun et al. Faraday rotation and photoluminescence in heavily $Tb^{3+}$-doped $GeO_2$-$B_2O_3$-$Al_2O_3$-$Ga_2O_3$ glasses for fiber-integrated magneto-optics. **Scientific reports**, v. 5, n. 1, p. 1-6, 2015.

2- FRANCO, Douglas F. et al. Fundamental studies of magneto-optical borogermanate glasses and derived optical fibers containing $Tb^{3+}$. **journal of materials research and technology**, v. 11, p. 312-327, 2021.

3- FRANCO, Douglas F. et al. Magneto-optical borogermanate glasses and fibers containing $Tb^{3+}$. **Scientific Reports**, v. 11, n. 1, p. 9906, 2021.

4- GUO, Hongwei et al. Optical band gap and photoluminescence in heavily $Tb^{3+}$ doped $GeO_2$-$B_2O_3$-$SiO_2$-$Ga_2O_3$ magneto-optical glasses. **Journal of Alloys and Compounds**, v. 686, p. 635-640, 2016.

5- SAVINKOV, V. I. et al. Borogermanate glasses with a high terbium oxide content. **Journal of non-crystalline solids**, v. 356, n. 33-34, p. 1655-1659, 2010.

6- YIN, Hairong et al. Effect of $B_2O_3$ content and microstructure on Verdet constant of $Tb_2O_3$-doped GBSG magneto-optical glass. **The Journal of Physical Chemistry C**, v. 122, n. 29, p. 16894-16900, 2018.

7- AKAHOSHI, Daisuke et al. Magnetic properties of $Tb^{4+}/Tb^{3+}$ mixed valence oxide $Ba1-xLa_xTbO_3$ (x= 0–0.2). **Journal of Solid State Chemistry**, v. 303, p. 122452, 2021.

8- KASZEWSKI, Jarosław et al. Reduction of $Tb^{4+}$ ions in luminescent $Y_2O_3$:Tb nanorods prepared by microwave hydrothermal method. **Journal of rare earths**, v. 34, n. 8, p. 774-781, 2016.

9- HINATSU, Yukio. Magnetic susceptibility and electron paramagnetic resonance studies of tetravalent terbium ions in BaTbO3 and SrTbO3. **Journal of Solid State Chemistry**, v. 100, n. 1, p. 136-140, 1992.

10- VERMA, R. K.; KUMAR, K.; RAI, S. B. Inter-conversion of $Tb^{3+}$ and $Tb^{4+}$ states and its fluorescence properties in MO–$Al_2O_3$: Tb (M= Mg, Ca, Sr, Ba) phosphor materials. **Solid state sciences**, v. 12, n. 7, p. 1146-1151, 2010.

11- CHEN, Qiuling et al. Magneto optical properties of rare earth $Tb_2O_3$ doped PbO-$Bi_2O_3$-$B_2O_3$ glass. **Journal of Non-Crystalline Solids**, v. 470, p. 99-107, 2017.

12- SONTAKKE, Atul D.; ANNAPURNA, K. Study on $Tb^{3+}$ containing high silica and low silica calcium aluminate glasses: Impact of optical basicity. **Spectrochimica Acta Part A: Molecular and Biomolecular Spectroscopy**, v. 94, p. 180-185, 2012.

13- CULEA, Eugen. Structural and magnetic behaviour of lead–bismuthate glasses containing rare earth ions. **Journal of non-crystalline solids**, v. 357, n. 1, p. 50-54, 2011.

14- QIN, Jun et al. Nanophotonic devices based on magneto-optical materials: recent developments and applications. **Nanophotonics**, 2022.

15- SYOUJI, Atsushi; TOMINAGA, Hiroki. Magneto-optical effects of transparent magnetic diffraction gratings. **Journal of magnetism and magnetic materials**, v. 347, p. 47-50, 2013.

16- LIU, Bin et al. Effects of alkali metal ion on imprinting GRIN microstructure in $GeS_2$-$Ga_2S_3$-MCl (M= Na, K, Cs) glasses for visible to mid-infrared microgratings. **Ceramics International**, v. 48, n. 22, p. 33122-33134, 2022.

17- LEPICARD, Antoine et al. Long-lived monolithic micro-optics for multispectral GRIN applications. **Scientific reports**, v. 8, n. 1, p. 7388, 2018.

18- KARAM, Lara et al. Second-Order Optical Response in Electrically Polarized Sodo-Niobate Amorphous Thin Films: Particularity of Multilayer Systems. **Advanced Photonics Research**, v. 2, n. 6, p. 2000171, 2021.

19- DUSSAUZE, Marc et al. Thermal poling of optical glasses: mechanisms and second-order optical properties. **International Journal of Applied Glass Science**, v. 3, n. 4, p. 309-320, 2012.

20- KARAM, Lara et al. Spatially microstructured topology of chalcogenide glasses by a combination of the electrothermal process and selective etching for functional infrared media. **Optical Materials Express**, v. 12, n. 5, p. 1920-1931, 2022.

21- LEPICARD, A. et al. Demonstration of dimensional control and stabilization of second harmonic electro-optical response in chalcogenide glasses. **Optical Materials Express**, v. 8, n. 6, p. 1613-1624, 2018.

22- RASKHODCHIKOV, D. et al. Mechanism of thermal charge relaxation in poled silicate glasses in a wide temperature range (From liquid nitrogen to glass melting temperature). **The Journal of Physical Chemistry B**, v. 124, n. 36, p. 7948-7956, 2020.

23- REDKOV, Alexey V.; MELEHIN, Vladimir G.; LIPOVSKII, Andrey A. How does thermal poling produce interstitial molecular oxygen in silicate glasses?. **The Journal of Physical Chemistry C**, v. 119, n. 30, p. 17298-17307, 2015.

24- DUSSAUZE, Marc et al. Structural rearrangements and second-order optical response in the space charge layer of thermally poled sodium− niobium borophosphate glasses. **The Journal of Physical Chemistry C**, v. 111, n. 39, p. 14560-14566, 2007.

25- GALLEANI, Gustavo et al. Fluorine and sodium depletion followed by refractive index modification imprinted on fluorophosphate glass surface by thermal poling. **Journal of Non-Crystalline Solids**, v. 601, p. 122054, 2023.

26- POIRIER, Gael et al. Second harmonic generation in sodium tantalum germanate glasses by thermal poling. **The Journal of Physical Chemistry C**, v. 123, n. 43, p. 26528-26535, 2019.

27- GUIMBRETIERE, G. et al. Correlation between second-order optical response and structure in thermally poled sodium niobium-germanate glass. **Applied Physics Letters**, v. 97, n. 17, p. 171103, 2010.

28- NASU, Hiroyuki et al. Second-harmonic generation from thermally poled PbO-$GeO_2$ glasses. **Journal of the Ceramic Society of Japan**, v. 109, n. 1268, p. 366-368, 2001.

29- FLEMING, Lauren AH; GOLDIE, David M.; ABDOLVAND, Amin. Imprinting of glass. **Optical Materials Express**, v. 5, n. 8, p. 1674-1681, 2015.

30- QUIQUEMPOIS, Yves; GODBOUT, Nicolas; LACROIX, Suzanne. Model of charge migration during thermal poling in silica glasses: Evidence of a voltage threshold for the onset of a second-order nonlinearity. **Physical Review A**, v. 65, n. 4, p. 043816, 2002.

31- LIU, Xue-Ming; ZHANG, Ming-De. Theoretical study for thermal/electric field poling of fused silica. **Japanese Journal of Applied Physics**, v. 40, n. 6R, p. 4069, 2001.

32- LIPOVSKII, A. A.; MELEHIN, V. G.; PETRIKOV, V. D. Electric-field-induced bleaching of ion-exchanged glasses containing copper nanoparticles. **Technical physics letters**, v. 32, n. 3, 2006.

33- DUSSAUZE, Marc et al. Accurate second harmonic generation microimprinting in glassy oxide materials. **Advanced Optical Materials**, v. 4, n. 6, p. 929-935, 2016.

34- REDUTO, Igor et al. Relief micro-and nanostructures by the reactive ion and chemical etching of poled glasses. **Optical Materials Express**, v. 9, n. 7, p. 3059-3068, 2019.

35- LEPICARD, Antoine et al. Surface reactivity control of a borosilicate glass using thermal poling. **The Journal of Physical Chemistry C**, v. 119, n. 40, p. 22999-23007, 2015.

36- CHAZOT, Matthieu et al. Enhancement of mechanical properties and chemical durability of Soda-lime silicate glasses treated by DC gas discharges. **Journal of the American Ceramic Society**, v. 104, n. 1, p. 157-166, 2021.

37- ALVARADO, Ricardo et al. Patterning of the surface electrical potential on chalcogenide glasses by a thermoelectrical imprinting process. **The Journal of Physical Chemistry C**, v. 124, n. 42, p. 23150-23157, 2020.

38- KARAM, Lara et al. Electrically Micro-Polarized Amorphous Sodo-Niobate Film Competing with Crystalline Lithium Niobate Second-Order Optical Response. **Advanced optical materials**, v. 8, n. 13, p. 2000202, 2020.

39- MARGULIS, W.; LAURELL, F. Fabrication of waveguides in glasses by a poling procedure. **Applied physics letters**, v. 71, n. 17, p. 2418-2420, 1997.

40- KAMENSKII, A. N. et al. Effective diffraction gratings via acidic etching of thermally poled glass. **Optical Materials**, v. 62, p. 250-254, 2016.

41- LIPOVSKII, A. A. et al. Electric field imprinting of sub-micron patterns in glass–metal nanocomposites. **Nanotechnology**, v. 19, n. 41, p. 415304, 2008.

42- SONTAKKE, Atul D.; BISWAS, Kaushik; ANNAPURNA, K. Concentration-dependent luminescence of $Tb^{3+}$ ions in high calcium aluminosilicate glasses. **Journal of Luminescence**, v. 129, n. 11, p. 1347-1355, 2009.

43- LÓPEZ-PACHECO, Germán et al. Revisiting the Charge Transfer State in Tetravalent Lanthanide Doped Oxides: Up to Date Phenomenological Description. **ECS Journal of Solid State Science and Technology**, v. 10, n. 11, p. 116007, 2021.

44- HOEFDRAAD, H. E. Charge-transfer spectra of tetravalent lanthanide ions in oxides. **Journal of Inorganic and Nuclear Chemistry**, v. 37, n. 9, p. 1917-1921, 1975.

45- RODRIGUEZ, Vincent; SOURISSEAU, Claude. General Maker-fringe ellipsometric analyses in multilayer nonlinear and linear anisotropic optical media. **JOSA B**, v. 19, n. 11, p. 2650-2664, 2002.

JPhys Materials

LETTER • OPEN ACCESS

# Micrometric patterning of a borogermanate glass containing terbium by thermal poling to manage luminescence and second order optical properties

To cite this article: Juliane Resges Orives *et al* 2024 *J. Phys. Mater.* **7** 03LT01

View the article online for updates and enhancements.

You may also like

- Promoting future sustainable utilization of rare earth elements for efficient lighting technologies
Chen Zhong, Yong Geng, Zewen Ge et al.
- Optical properties of ZnO:$SiO_2$:$Tb^{3+}$ films: the effect of DNA
E A Boruleva, G K Chudinova, I A Hayrullina et al.
- Enhancement of Green Terbium-Related Photoluminescence from Highly Doped Microporous Alumina Xerogels in Mesoporous Anodic Alumina
N. V. Gaponenko, I. S. Molchan, O. V. Sergeev et al.

This content was downloaded from IP address 177.141.247.143 on 28/07/2024 at 13:48

IOP Publishing J. Phys. Mater. 7 (2024) 03LT01 https://doi.org/10.1088/2515-7639/ad4ba0

Journal of Physics: Materials

CrossMark

OPEN ACCESS

RECEIVED
26 October 2023

REVISED
11 April 2024

ACCEPTED FOR PUBLICATION
14 May 2024

PUBLISHED
31 May 2024

Original content from this work may be used under the terms of the Creative Commons Attribution 4.0 licence.

Any further distribution of this work must maintain attribution to the author(s) and the title of the work, journal citation and DOI.

LETTER

# Micrometric patterning of a borogermanate glass containing terbium by thermal poling to manage luminescence and second order optical properties

**Juliane Resges Orives[1,*], Lia Mara Marcondes[3], Lara Karam[2], Frédéric Adamietz[2], Thierry Cardinal[3], Marc Dussauze[2,*] and Marcelo Nalin[1]**

[1] Institute of Chemistry, São Paulo State University (UNESP) —, Araraquara, SP, Brazil
[2] Institut des Sciences Moléculaires, UMR 5255, Université de Bordeaux, 351 cours de la Liberation, 33405 Talence Cedex, France
[3] Institut de Chimie de la Matière Condensée de Bordeaux, Université de Bordeaux, 87 Avenue du Dr Schweitzer, F-33608 Pessac, France
[*] Authors to whom any correspondence should be addressed.

**E-mail:** juliane_resges@hotmail.com and marc.dussauze@u-bordeaux.fr

**Keywords:** thermo-electrical imprinting, control of oxidation, multifunctional glassy material

## Abstract

Borogermanate glasses containing terbium ions are interesting materials due to their luminescent and magnetic properties. Terbium can present two different oxidation states and the thermal poling technique can be a pertinent way to modulate spatially the oxidation state of these ions. In this work, we demonstrate using a thermo-electrical imprinting process the transfer of micro scaled motifs on the surface of a borogermanate glass containing $Tb^{3+}$ resulting in a micrometric structuring of the oxidation state of $Tb^{3+}/Tb^{4+}$ ions. A large change in absorption and luminescence optical properties is observed, arising from the distinct properties of trivalent and tetravalent terbium ions. Correlative micro luminescence, Raman and second harmonic generation measurements were carried out on the patterned poled glass surface. This has demonstrated an accurate concomitant modification of the glass structure accompanying large luminescence changes and the appearance of a second order optical response which could be attributed to a localized space charge implantation. These original results demonstrate how a simple electrical process allows managing multi optical properties but also paves the way to induce static electrical functionalities in a magnetic optical glassy system.

## 1. Introduction

Designing new materials for which various optical properties are manageable at micrometric scales can lead to new applications in various fields of photonics. As an example, for integrated photonic circuits (PICS) the large variety of devices being developed constantly requires the merging of multiple optical functionalities, including diffractive elements, non-linear responses, and efficient light emission management, among others [1–6].

Among the wide range of materials available for the manufacture of PICS, glasses stand out due to the versatility of their compositions, as well as their simple and low-cost preparation. In addition, glasses are great hosts for rare-earth (RE) ions, which favors the search for luminescent materials with improved optical properties [5–7]. Borogermanate glasses containing $Tb^{3+}$ ions have been investigated in recent years and their potential for photonics and magneto-optical devices have been highlighted [8–13]. Indeed, they are interesting materials due to their luminescent and magnetic properties emerging from the partially filled 4f electronic configurations of terbium [8–10].

The most stable oxidation state of terbium ions is trivalent, but terbium can also present the tetravalent state, having a standard $Tb^{4+}/Tb^{3+}$ reduction potential of +3.1 V [14, 15]. Regarding the particularities of these two oxidation states, $Tb^{3+}$ has a $4f^8$ electronic configuration, while $Tb^{4+}$ is $4f^7$ and the effective magnetic moment for $Tb^{3+}$ and $Tb^{4+}$ ions are 9.72 $\mu$B and 7.94 $\mu$B, respectively [1, 16]. In addition, $Tb^{3+}$

© 2024 The Author(s). Published by IOP Publishing Ltd

ion exhibits its green emission near 544 nm due to the $^5D_4 \rightarrow {}^7F_5$ transition, while the $Tb^{4+}$ ions do not exhibit emission and due to its absorption band in the visible region it acts as a quenching center [15, 17].

Some glasses may show coexistence between $Tb^{3+}/Tb^{4+}$ and the existence of this ratio may depend on the oxidation-reduction conditions of the melt or on the oxide concentrations of the matrix [12, 18–20]. Knowing that in glasses, terbium can present two different oxidation states influencing structural, luminescent, optical, and magnetic properties, this opens up opportunities for finding a way to control and/or modulate spatially the oxidation state of terbium.

A technique that has been effectively used for surface modification is thermal poling, which allows modulating different properties in various types of glasses [5, 21–30]. The glass surface modification of the surface consists of heating a glass matrix followed by the application of a high DC voltage for a certain time, during which dissociation processes of ionic charge carriers, commonly alkaline and alkaline earth cations, occurs at the anodic interface [21, 31–33]. It induces both (i) a cationic depletion layer forming a new glassy composition at the anodic surface and (ii) the implantation of a strong static electric field linked to a space charge formed within a layer ranging from a few nanometers to a few micrometers in thickness depending on the parameters used [5, 34–36]. Once this process is carried out, the temperature is decreased to ambient, thus freezing the polarized state on the poled surface.

Over the years, this technique has been improved employing a structured anodic electrode to modify the surface in a patterned way with spatial resolutions on the micrometric scale. This transfer of micro-structured motifs allows controlling several properties, such as chemical reactivity [37], surface durability [38], surface topology [22], surface electrical potential [39]. With regard to optical properties, it is possible to induce a second-order response [5, 40], to prepare waveguides [41], micro-lenses with gradient of refractive index [4] and diffraction gratings [35, 42].

In addition, Lipovskii *et al* showed the possibility of using poling to oxidize Ag and Cu metallic nanoparticles to create optical structures with transparent and colored zones with different absorptions [34, 43]. Recently, thermal poling has been used for the electric field manipulation of magnetic and Faraday rotation performances of a diamagnetic glass, which is of great interest for spintronics devices [44].

Although poling has already been used for several purposes, it has not yet been explored to modulate the properties of rare earth ions. In this context, we focus our attention on demonstrating the control of the oxidation state of terbium ions induced by the thermo-electrical imprinting treatment. Raman, luminescence and second harmonic generation (SHG) correlative imaging are used to show, respectively, the structural modifications, spatial micrometric control of luminescence and second order optical properties on the patterned glass surface.

## 2. Methods

Borogermanate-$Tb^{3+}$ glasses with a molar composition of $96(46GeO_2\text{-}29B_2O_3\text{-}16Na_2O\text{-}5BaO\text{-}4Al_2O_3)\text{-}4Tb_4O_7$ was prepared by the melt-quenching method, which consists of melting of precursor components at 1400 °C for 2 h in a platinum crucible followed by quenching into a stainless-steel mold preheated at 450 °C and annealed for 2 h [9]. This composition was chosen due to its high sodium concentration, which is important for the poling process, and because it contains terbium ions, making it possible to study the oxidation of rare earth ions during this process. This pristine glass was labeled as BGTb.

Figure 1(a) illustrates the thermo-electrical imprinting process that was performed in a sealed enclosure under an $N_2$ flow of 6 l $min^{-1}$. A piece of silicon wafer was used as cathode and a borosilicate slide was placed between the silicon and the sample as a sacrificial layer in order to preserve the optical quality of the sample at the cathode.

The anode configuration used to pattern the surface was a 100 nm thick platinum film deposited on a silicate glass slide of 25 $mm^2$, prepared by a classical lithography process resulting in non-conductive squared motifs of 40 × 40 $\mu m^2$ delimited by 10 $\mu$m width electrically conductive Pt grid (figure 1(b)). A second electrode of the same size with a homogeneous platinum film was also used. Glass samples were heated up to 300 °C and a DC voltage of 1 kV was applied (at a 300 V $min^{-1}$ rate) and left at these conditions for 30 min. Then, the system was decreased to room temperature and finally the external voltage was removed. The poled samples using the structured and the homogeneous electrode were labeled BGTb-S and BGTb-H, respectively.

After thermal poling treatment, the absorption spectra for BGTb and BGTb-H were obtained between 200 and 800 nm using a double beam Agilent Cary 5000 spectrophotometer. Micro-luminescence data was acquired for BGTb-S using a Labram (Horiba) spectrometer with a laser source at 488 $cm^{-1}$, a 150 grooves $cm^{-1}$ grating and 50× (N.A. = 0.54) objective. In this configuration, the efficient signal of luminescence allows mapping for large areas (above 0.1 $mm^2$) to determine the spatial reproducibility of the imprinting process. Then, correlative Raman, luminescence and SHG maps were acquired for the same

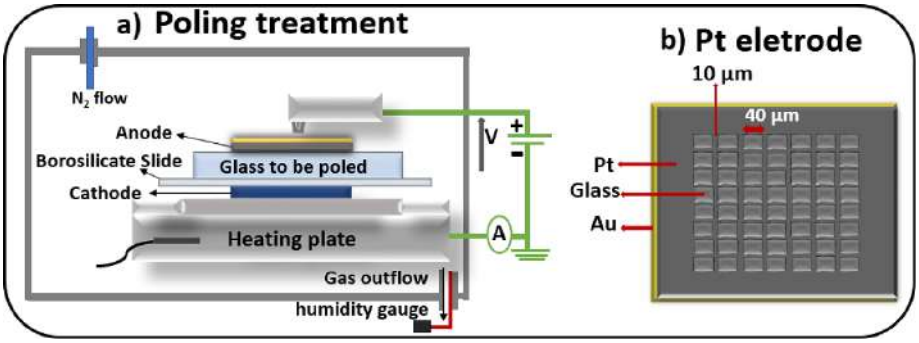


**Figure 1.** Schematic representation of: (a) the system used to carry out the thermo-electrical micro-imprinting process and (b) the platinum patterned electrode used.

imprinted motif. It consists of a modified confocal micro-Raman spectrometer HR800 (Horiba/Jobin Yvon) with a 100× (N.A. = 0.9) objective. A CW laser operating at 532 nm was used for Raman and luminescence and a picosecond pulsed laser at 1064 nm was used for SHG. All measurements were done in backscattering mode. For the SHG measurements, the incident laser polarization and the analyzed SHG signal polarization states can be linearly polarized either vertically or horizontally.

## 3. Results and discussion

The BGTb glass obtained by melting quenching is colorless, while the BGTb-S sample after poling treatment showed a change in color to yellow only in the area located under the structured electrode as seen in figure 2(a).

This color change may indicate that an oxidation process from $Tb^{3+}$ to $Tb^{4+}$ occurred as reported for calcium aluminosilicate and borogermanate glasses containing $Tb^{3+}$ [12, 19]. In figure 2(b) we can see by optical microscopy that the imprinting process resulted in a very precise pattern, reproducing the electrode geometry on the glass surface.

The optical absorption spectra of samples BGTb and BGTb-H are shown in figure 2(c). The recorded absorption bands centered at 302 (1), 318 (2), 340 (3), 350 (4), 358 (5), 370 (6), 378 (7), and 488 (8) nm were assigned to 4f–4f transitions from the $^7F_6$ ground state of $Tb^{3+}$ to the excited levels of $^5H_6$, ($^5D_{0,1}$, $^5H_7$), ($^5G_2$, $^5L_6$), ($^5L_9$, $^5G_4$), $^5G_5$, $^5L_{10}$, ($^5D_3$, $^5G_6$), and $^5D_4$, respectively [9, 10, 45]. Looking at the absorption of the poled region in the BGTb-H, there is a large absorption between 300 and 500 nm which is assigned to the $Tb^{4+}$ ions electronic transitions from ligand-to-metal charge transfer states coming from one molecular orbital of the oxygen to one f-state of terbium [46, 47]. This broadband covers the blue visible region and gives the sample a yellow color exactly in the poled area and confirms the oxidation of $Tb^{3+}$ ions during the poling process.

In addition to this broad band, it is also possible to notice the absorption band $Tb^{3+}$ as observed for the pristine glass, this occurs because the absorption spectrum is collected for the entire thickness of the sample (0.6 mm) while the glass matrix containing $Tb^{4+}$ is supposed to correspond to the sodium depletion layer which have been measured around 1 $\mu$m by time-of-flight secondary ion mass spectrometry (ToF-SIMS) as depicted in figure 2(d). Within this polarized layer, the oxidation of terbium ions is supposed to contribute to the compensation of the positive charge ($Na^+$) displacement.

For the BGTb-S sample, a micro-luminescence mapping was performed in a 160 × 160 $\mu m^2$ area using for excitation a 488 nm wavelength. The map was generated for emission bands between 530 and 560 nm (figure 3(a)). Due to the fact that $Tb^{3+}$ ions present green emission at 541 nm, while the $Tb^{4+}$ ions have no emission [15, 17], a very contrasted luminescence pattern with a reproducible spatial distribution was created after poling treatment.

Three luminescence spectra (figure 3(b)) were extracted from the map (region 1–3) and shows the bands at 541, 582, and 620 nm assigned to the characteristic transitions of $Tb^{3+}$ ions from $^5D_4$ to $^7F_j$ ($j = 5, 4, 3$) [9]. In the poled zone (region 1) and the borders of the square (region 2) we observe a decrease in the luminescence intensity of 86% and 92% as compared to the center of the square (region 3), where the luminescence was not affected by the poling treatment.

Indeed, the thermal poling allows forming a controlled oxidation layer in a patterned way under the glass surface in contact with the anode and around the square motifs. We have calculated the emission decrease expected if a complete oxidation of $Tb^{3+}$ is induced within a one micron thick polarized layer by taking in to

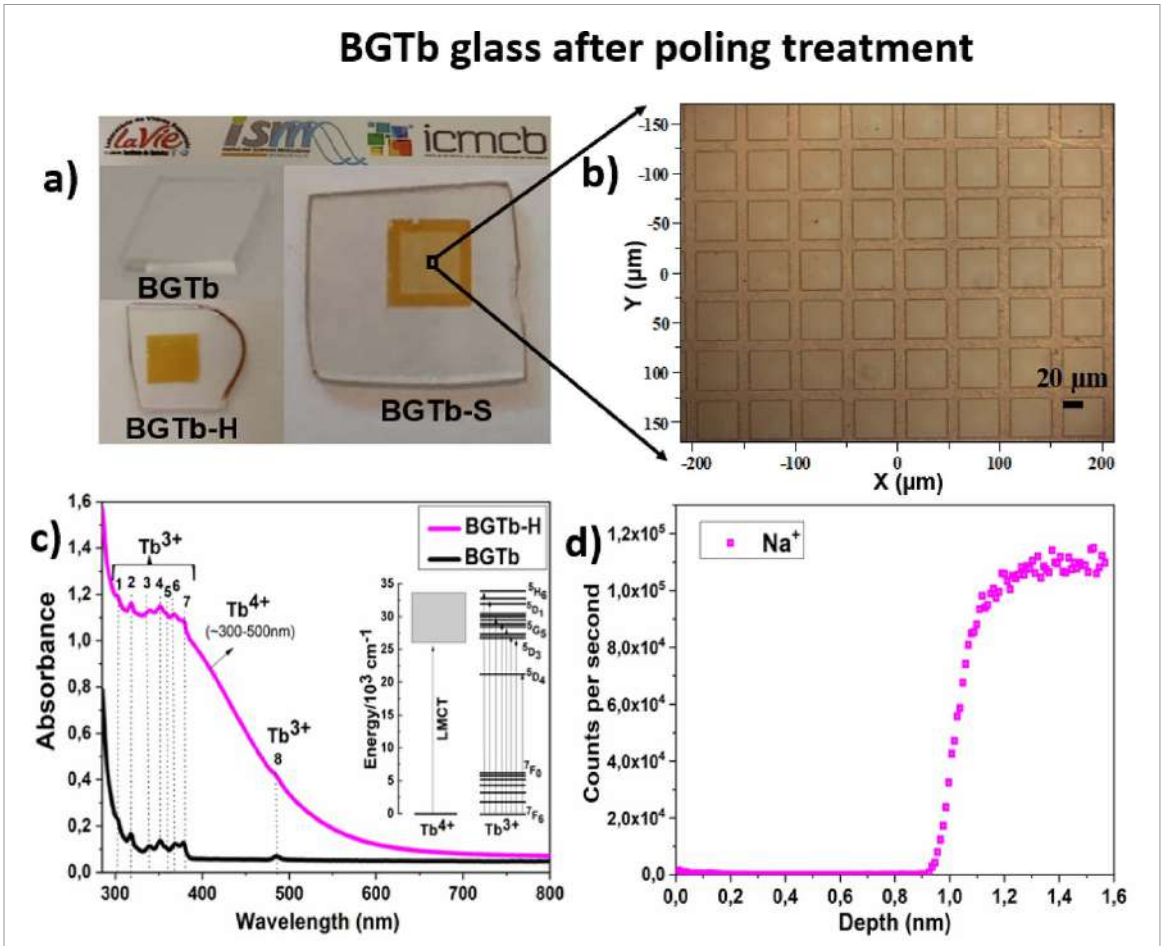


**Figure 2.** (a) Photograph of BGTb, BGTb-H and BGTb-S samples and (b) microscope image of the structured micro-imprinting surface after poling. (c) Absorbance spectra in the UV-Vis region obtained for BGTb before poling and BGTb-H homogeneously poled. (Insert shows the partial energy diagram of $Tb^{3+}$ and $Tb^{4+}$) (d) TOF-SIMS depth profile of sodium content of BGTb-H.

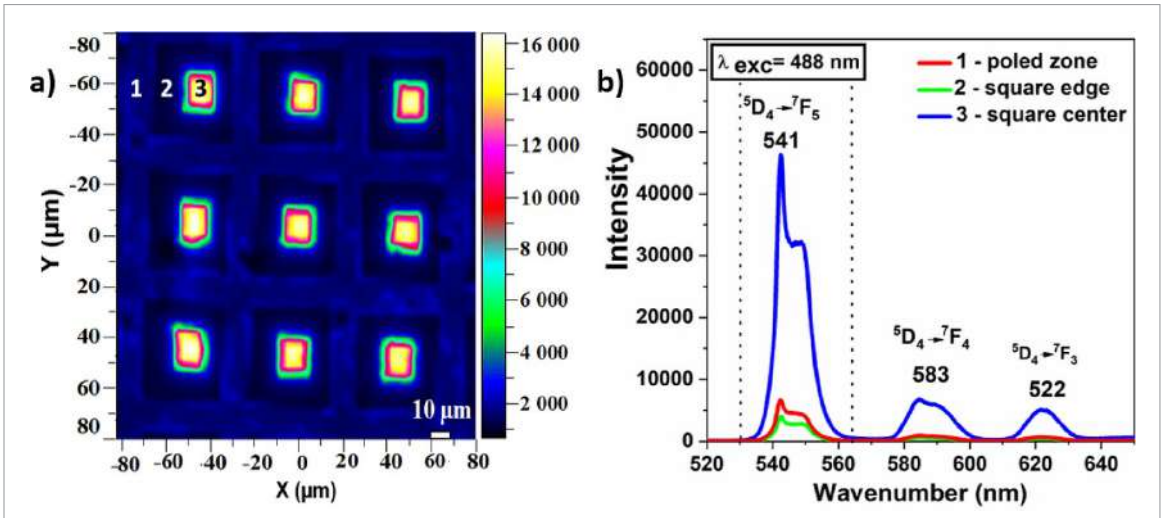


**Figure 3.** (a) Luminescence map for emission bands between 530 and 560 nm. (b) Emission spectra for BGTb-S poled using structured electrode.

account the focal volume and the induced absorption for both the excitation and the back scattered emission. To this aim, if we assume (i) the same laser intensity for all measurements, (ii) no refractive index change between the pristine glass and the poled sample and (iii) a complete oxidation of $Tb^{3+}$ within a layer of thickness $L = 1$ $\mu$m at the anode surface inducing within this layer a complete loss of emission and additional

absorptions at both excitation (488 nm) and emission wavelengths (521 nm), we can estimate the ratio of emission intensities between the pristine glass and the poled glass (BGTb-H) using this equation:

$$\frac{Iemission\,(pristine\ glass)}{Iemission\,(poled\ glass)} = \frac{Dof}{Dof - L} \times 10^{Abs(488\,\mathrm{nm})} \times 10^{Abs(521\,\mathrm{nm})} \quad (1)$$

where $Dof$ is the depth of focus calculated for a numerical aperture of 0.54, $L$ the thickness of the sodium depletion layer (1 $\mu$m as shown in figure 2(d)) and Abs (521 nm) and Abs (488 nm) are obtained from the absorbance curve of BGTb-H depicted from figure 1(c).

An emission decrease of 85% has been estimated corresponding well with the luminescence variations reported in figure 3. It denotes that this poling process could induce locally up to a complete oxidation of Tb ions and this first estimation will be subjected to XPS analysis in a future set of experiments.

The structural changes were evaluated using Raman spectroscopy. Figure 4(a) shows spectra acquired for the poled zone, square center and pristine glass surfaces. The spectra were normalized in intensity at 515 $cm^{-1}$, corresponding to the $Ge^{[4]}$–O–$Ge^{[4]}$ vibrational modes of a fully interconnected germanate network [48, 49].

The stretching modes at high frequency are almost inactive for a $GeO_2$ glass, but they can be observed due to the presence of non-bridging oxygen attributed to the band at 838 $cm^{-1}$ for $(Ge\emptyset_3O)^-$ structural units stabilized by $Na^+$ (where $\emptyset$ and O represent bridging and non-bridging oxygen respectively) [49, 50]. This is also due to the presence of a mixture of glass formers for the shoulder at 780 $cm^{-1}$ linked to asymmetric stretching of Ge–O–B bridges [49, 51]. The intensity of the Raman band at 838 $cm^{-1}$ is sensitive to the thermal poling and a decrease is observed indicating a polymerization of the germanate network in the poled layer compensating the excess of negative charge after sodium departure.

The restructuring of Ge–$O^-$ terminal bonds into Ge–O–Ge results in the formation of trapped molecular oxygen in the polarized glassy matrix that presents a stretching mode at 1551 $cm^{-1}$ [52]. The presence of $O_2$ trapped in the poled glass was observed in several poled ionic glasses and is a result of charge compensation mechanisms linked to the structural rearrangement of the glassy matrix [25, 35, 53]. The bands between 1200 and 1500 $cm^{-1}$ are related to borate triangular units vibrations [54–56]. It is also possible to observe a shoulder around 930 $cm^{-1}$ due to vibrational modes of borate tetrahedral units [56]. Structural rearrangements of $[B\emptyset_4]^-$ units due to the cation migration are not ruled out, but they were not detected by Raman.

Micro-Raman mapping experiments were carried out in order to follow the spatial locations of structural changes, and an area of 80 × 80 $\mu m^2$ was mapped. The mapping for the band at 1551 $cm^{-1}$ in figure 4(b) shows the formation of molecular oxygen under the contact zone with the conductive parts of the electrode. As the formation of $O_2$ is directly related to the restructuring of the network, the mapping of this band tracks the region where the sodium departure occurred, and shows the imprinting accuracy related to compositional and structural glass variations.

For an excitation at 532 nm, in addition to the Raman response of the glass network, a contribution from the luminescence emission of $Tb^{3+}$ ions can be measured. This contribution corresponds to the $^5D_4$ to $^7F_5$ transition and is observed at 541 nm or 355 $cm^{-1}$ in Raman shift. Taking advantage of this, we used the same set of data to correlate the Raman and the luminescence signals and thus to spatially correlate structural rearrangements with the oxidation of $Tb^{3+}$ within the same imprinted pattern. In figure 4(c), the image corresponding to the integration of the band at 355 $cm^{-1}$ in Raman shift depicts exactly the same spatial information as that for a luminescence excited at 488 nm as reported in figure 3(a), confirming that our correlative Raman/Luminescence approach is suitable.

Such accurate spatial correlation allows us to observe that for Raman mapping, in the contact zone with the electrode there is the highest concentration of molecular oxygen. This is followed by a gradient at the square edges until it reaches the center where no $O_2$ can be detected (profile depicted in figure 4(d)).

To explain such spatial gradient, one should consider that the amount of $O_2$ trapped in the poled glass matrix probed by Raman gives an indication on the oxidation mechanism of the glass matrix occurring during the sodium layer depletion. This signal varies mainly as a function of the polarized layer thickness, which is supposed to be maximum within the zone in direct contact with the electrode (highest local applied voltage) and decreases gradually from the edges of the electrode toward the center of the square motif.

Differently, looking at the luminescence map we do not observe a simple gradient, there is a high luminescence in the center, almost no luminescence at the edges and a slight increase in the zone which was in direct contact with the electrode (luminescence profile provided in figure 4(d)). Finally, one cannot explain the luminescence spatial distribution with a simple variation of local potential linked to the electrode geometry as observed for the $O_2$ distribution, i.e. for the oxidation of the glass matrix upon the sodium dissociation/depletion process.

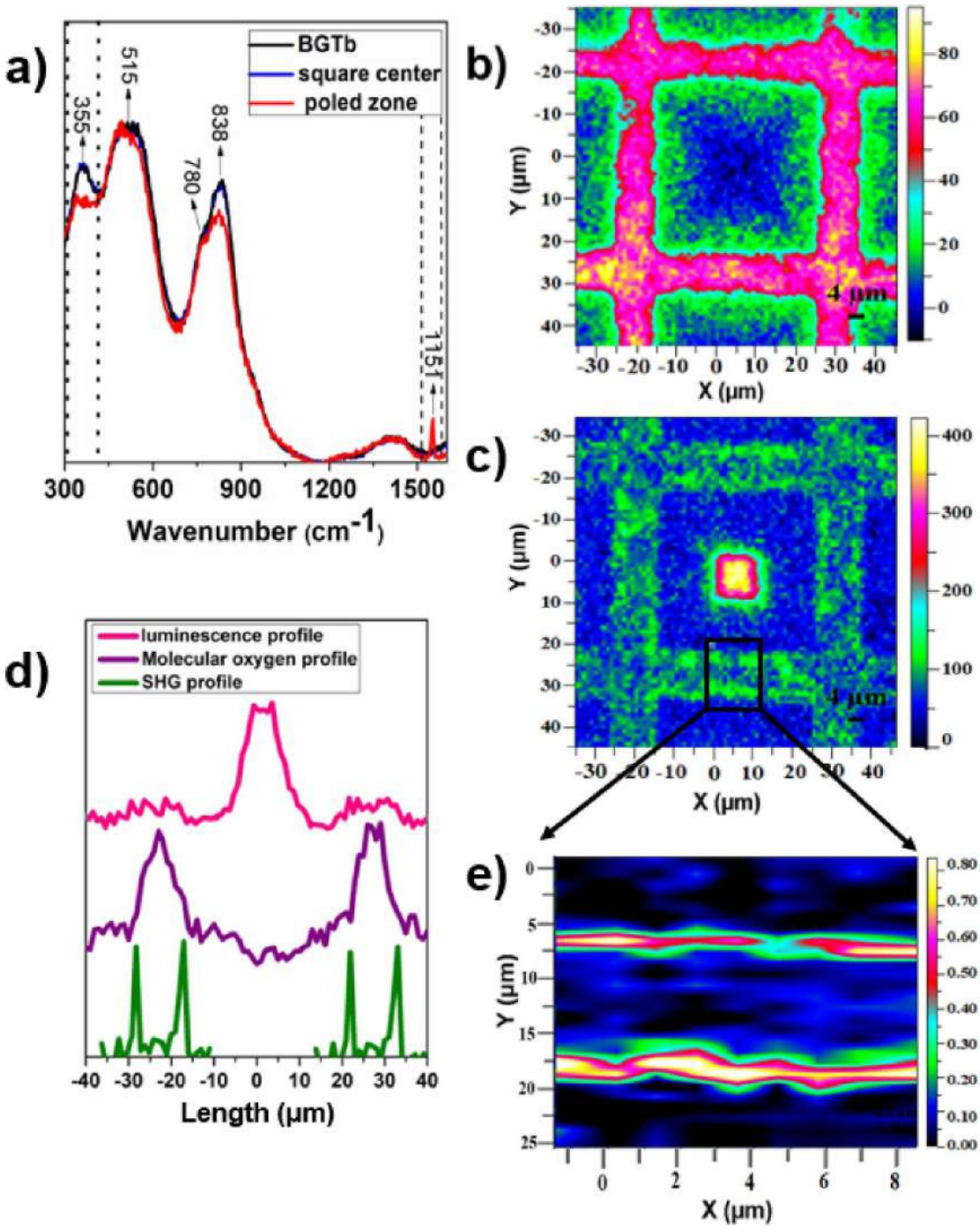


**Figure 4.** (a) Raman spectra in the poled zone, square center and pristine glass surfaces at 532 nm. $\mu$-Raman maps for: (b) the band of molecular oxygen at 1551 $cm^{-1}$, (c) for the $Tb^{3+}$ luminescence band at 355 $cm^{-1}$. (d) Profile of molecular oxygen, Luminescence and SHG plotted along a vertical line centered in the middle of the correlative maps. (e) SHG intensity map realized within the rectangular area depicted in part (C). The SHG mapping was not done for the whole area due to measurement duration consideration.

The reason why the $Tb^{3+}$ oxidation spatial distribution does not follow simply the local applied voltage during this imprinting process is under investigation and will be reported in a following study including a systematic variation of the poling voltage to determine how both oxidation mechanisms ($Tb^{3+}$ and glass matrix) can be described within a global polarization mechanism adapted for such Terbium rich ionic glassy system.

The effects of the imprinting process on the second order optical response have been mapped by SHG confocal microscopy in reflection mode with steps of 1 $\mu$m along *X* and *Y* axes (figure 4(e)). The correlative microscopies setup allows probing for the same area structural changes, luminescence and nonlinear optical properties. In the present case, the in-plane SHG components were probed, using the incident beam and the harmonic signal linear and parallel light polarization states.

In figure 4(e), it is possible to observe accurate spatial location of the SHG signal confined at the borders of each imprinted line only if the SHG configuration of polarization is perpendicular to the axis defined by the square pattern. Such an observation is typical for SHG poled patterns in glasses as already reported in the literature [35, 40, 52]. By analogy to these previous reports, one can make the assumption that our observation is linked to an in-plane static field located preferentially at the edges of the electrode breaking the centro symmetry of the glass, inducing a localized second order optical response.

The precise location of the polarization effect on the glass nonlinear optical properties is attributed to an in-plane charge concentration gradient promoted by local field enhancements on the edges of the structured electrode. Such an assumption can also be correlated with the location of the SHG signal within the concentration gradient of trapped $O_2$ measured by Raman (see SHG and Raman profiles in figure 4(d)).

To sum up the signal intensities coming from $\mu$-luminescence, $\mu$-Raman and $\mu$-SHG measurements are spatially correlated with the electrode's square patterns, showing the accuracy of the thermal poling treatment to modify the surface structurally, to control luminescence at the microscale and to implement localized space charge resulting in second order optical responses.

## 4. Conclusion

In this work, the control of the oxidation state of terbium ions induced by thermo-electrical imprinting treatment control has been demonstrated. Our present results show that not only has the sodium migration been obtained for classical thermally poled ionic glass, resulting in a sodium-free layer around 1 $\mu$m and molecular oxygen formation at 1551 $cm^{-1}$, but we also demonstrate the possibility to manage the degree of oxidation of terbium ions upon poling treatment as a charge compensation mechanism for sodium departure.

The oxidation of $Tb^{3+}$ ions to $Tb^{4+}$ created a pattern of luminescence signal from high in the region not affected by the polling to low in the region in contact with the electrode due to the $Tb^{4+}$ ions not showing luminescence. Furthermore, the sample showed an SHG signal on the edges of the squares patterned on the glass surface. Besides structuring the luminescence properties on a micrometric scale, one should keep in mind that the glass used has magnetic properties, and therefore, the structuring of the magnetic properties is also expected since the magnetic response changes with the oxidation of the $Tb^{3+}$ paramagnetic ions.

Finally, this study opens new perspectives for managing optical functionalities but also strong static electric fields in Terbium rich magnetic glasses, which is a key milestone of progress towards very original multi-functional glassy systems.

## Data availability statement

The data cannot be made publicly available upon publication because they are not available in a format that is sufficiently accessible or reusable by other researchers. The data that support the findings of this study are available upon reasonable request from the authors.

## Acknowledgments

The authors acknowledge the financial supports from São Paulo Research Foundation Agency, FAPESP (Grant Nos. 2013/07793-6, 2019/19609-1, 2020/15395-4, 2020/01786-1 and 2021/11494-0) and Sistema Nacional de Laboratórios de Fotônica-Ministério da Ciência, Tecnologia e Inovações (SISFOTON-MCTI). The Raman experiments were conducted using the SIV platform at the University of Bordeaux founded by the FEDER and the Region Aquitaine. This project has also received funding from the European Union's Horizon 2020 research program under the Marie Skłodowska Curie Grant Agreement No. 823941 (FUNGLASS), New Aquitaine region (Grant 2016-1R10107) and Idex Bordeaux (Research Program GPR Light).

## Conflict of interest

The authors have no conflicts to disclose.

## ORCID iD

Juliane Resges Orives https://orcid.org/0000-0002-3950-0040

## References


[1] Qin J *et al* 2022 *Nanophotonics* **11** 2639
[2] Syouji A and Tominaga H 2013 *J. Magn. Magn. Mater.* **347** 47
[3] Liu B, Mo Y, Liu Y, Lu Y, He X, Xu Y, Lipovskii A and Yang G 2022 *Ceram. Int.* **48** 33122
[4] Lepicard A, Bondu F, Kang M, Sisken L, Yadav A, Adamietz F, Rodriguez V, Richardson K and Dussauze M 2018 *Sci. Rep.* **8** 7388
[5] Karam L, Adamietz F, Michau D, Murugan G, Cardinal T, Fargin E, Rodriguez V, Richardson K and Dussauze M 2021 *Adv. Photonics Res.* **2** 2000171
[6] Molina P, Ramírez M O, García-Santizo J V, Álvarez-García S, Pazik R, Strek W, Dereń P J and Bausá L E 2009 *Appl. Phys. Lett.* **95** 051103
[7] Wang W and Qi L 2019 *Adv. Funct. Mater.* **29** 1807275
[8] Gao G, Winterstein-Beckmann A, Surzhenko O, Dubs C, Dellith J, Schmidt M A and Wondraczek L 2015 *Sci. Rep.* **5** 8942
[9] Franco D F, Fernandes R G, Felix J F, Mastelaro V R, Eckert H, Afonso C R M, Messaddeq Y, Messaddeq S H, Morency S and Nalin M 2021 *J. Mater. Res. Technol.* **11** 312
[10] Franco D F, Ledemi Y, Correr W, Morency S, Afonso C R M, Messaddeq S H, Messaddeq Y and Nalin M 2021 *Sci. Rep.* **11** 9906
[11] Guo H, Wang Y, Gong Y, Yin H, Mo Z, Tang Y and Chi L 2016 *J. Alloys Compd.* **686** 635
[12] Savinkov V I, Sigaev V N, Golubev N V, Sarkisov P D, Masalov A V and Sergeev A P 2010 *J. Non-Cryst. Solids* **356** 1655
[13] Yin H, Gao Y, Guo H, Wang C and Yang C 2018 *J. Phys. Chem.* C **122** 16894
[14] Akahoshi D, Hosouchi Y, Inoue R, Kuwahara H and Saito T 2021 *J. Solid State Chem.* **303** 122452
[15] Kaszewski J, Witkowski B S, Wachnicki Ł, Przybylińska H, Kozankiewicz B, Mijowska E and Godlewski M 2016 *J. Rare Earth* **34** 774
[16] Hinatsu Y 1992 *J. Solid State Chem.* **100** 136
[17] Verma R K, Kumar K and Rai S B 2010 *Solid State Sci.* **12** 1146
[18] Chen Q, Chen Q, Wang H, Wang G and Yin S 2017 *J. Non-Cryst.* **470** 99
[19] Sontakke A D and Annapurn K 2012 *Spectrochim. Acta* A **94** 180
[20] Culea E 2011 *J. Non-Cryst. Solids* **357** 50
[21] Dussauze M, Cremoux T, Adamietz F, Rodriguez V, Fargin E, Yang G and Cardinal T 2012 *Int. J. Appl. Glass. Sci.* **3** 309
[22] Karam L, Alvarado R, Calzavara F, Dahmani R, Kang M, Blanco C, Adamietz F, Richardson K and Dussauze M 2022 *Opt. Mater. Express* **12** 1920
[23] Lepicard A, Adamietz F, Rodriguez V, Richardson K and Dussauze M 2018 *Opt. Mater. Express* **8** 1613
[24] Raskhodchikov D, Reshetov I, Brunkov P, Kaasik V, Lipovskii A and Tagantsev D 2020 *J. Phys. Chem.* B **124** 7948
[25] Redkov A V, Melehin V G and Lipovskii A 2015 *J. Phys. Chem.* C **119** 17298
[26] Dussauze M, Kamitsos E I, Fargin E and Rodriguez V 2007 *J. Phys. Chem.* C **111** 14560
[27] Galleani G, Abou Khalil A, Canioni L, Dussauze M, Fargin E, Cardinal T and de Camargo A S S 2023 *J. Non-Cryst. Solids* **601** 122054
[28] Poirier G, Dussauze M, Rodriguez V, Adamietz F, Karam L, Cardinal T and Fargin E 2019 *J. Phys. Chem.* C **123** 26528
[29] Guimbretiere G, Dussauze M, Rodriguez V and Kamitsos E I 2010 *Appl. Phys. Lett.* **97** 171103
[30] Nasu H, Ito Y, Yamamoto Y, Hashimoto T and Kamiya K 2001 *J. Ceram. Soc. Japan* **109** 366
[31] Fleming L A H, Goldie D M and Abdolvand A 2015 *Opt. Mater. Express* **5** 1674
[32] Quiquempois Y, Godbout N and Lacroix S 2002 *Phys. Rev.* A **65** 043816
[33] Liu X-M and Zhang M-D 2001 *Jpn. J. Appl. Phys.* **40** 4069
[34] Lipovskii A A, Melehin V G and Petrikov V D 2006 *Tech. Phys. Lett.* **32** 275
[35] Dussauze M, Rodriguez V, Adamietz F, Yang G, Bondu F, Lepicard A, Chafer M, Cardinal T and Fargin E 2016 *Adv. Opt. Mater.* **4** 929
[36] Reduto I, Kamenskii A, Brunkov P, Zhurikhina V, Svirko Y and Lipovskii A 2019 *Opt. Mater. Express* **9** 3059
[37] Lepicard A, Cardinal T, Fargin E, Adamietz F, Rodriguez V, Richardson K and Dussauze M 2015 *J. Phys. Chem.* C **119** 22999
[38] Chazot M *et al* 2021 *J. Am. Ceram. Soc.* **104** 157
[39] Alvarado R *et al* 2020 *J. Phys. Chem.* C **124** 23150
[40] Karam L *et al* 2020 *Adv. Opt. Mater.* **8** 2000202
[41] Margulis W and Laurell F 1997 *Appl. Phys. Lett.* **71** 2418
[42] Kamenskii A N, Reduto I V, Petrikov V D and Lipovskii A A 2016 *Opt. Mater.* **62** 250–4
[43] Lipovskii A, Kuittinen M, Karvinen P, Leinonen K, Melehin V G, Zhurikhina V V and Svirko Y P 2008 *Nanotechnology* **19** 415304
[44] Chen Q, Li Z and Chen W 2021 *J. Non-Cryst. Solids* **564** 120850
[45] Sontakke A D, Biswas K and Annapurna K 2009 *J. Lumin.* **129** 1347
[46] López-Pacheco G, Padilla-Rosales I, López-Juárez R and González F 2021 *ECS J. Solid State Sci. Technol.* **10** 116007
[47] Hoefdraad H E 1975 *J. Inorg. Nucl. Chem.* **37** 1917
[48] McKeown D M and Merzbacher C I 1995 *J. Non-Cryst. Solids* **183** 61
[49] Zaiter R, Dussauze M, Nalin M, Fargin E, Adamietz F, Danto S, Toulemonde O and Cardinal T 2022 *J. Alloys Compd.* **912** 165181
[50] Henderson G S, G.Soltay L and Wang H M 2010 *J. Non-Cryst. Solids* **356** 2480
[51] Skopak T, Kroeker S, Levin K, Dussauze M, Méreau R, Ledemi Y, Cardinal T, Fargin E and Messaddeq Y 2018 *J. Phys. Chem.* C **123** 1370
[52] Poirier G, Karam L, Rodriguez V, Adamietz F, Cardinal T, Evelyne F and Dussauze M 2022 *J. Mater. Chem.* C **10** 10310
[53] Cremoux T, Dussauze M, Fargin E, Cardinal T, Talaga D, Adamietz F and Rodriguez V 2014 *J. Phys. Chem.* C **118** 3716
[54] Sun X-Y, Jiang D-G, Chen S-W, Zheng G-T, Huang S-M, Gu M, Zhang Z-J, Zhao J-T and Ballato J 2013 *J. Am. Ceram. Soc.* **96** 1483
[55] Koroleva O N, Shtenberg M V, Zainullina R T, Lebedeva S M and Nevolina L A 2019 *Phys. Chem. Chem. Phys.* **21** 12676
[56] Möncke D, Dussauze M, Kamitsos E I, Varsamis C P E and Ehrt D 2009 *Phys. Chem. Glasses: Eur. J. Glass Sci. Technol.* B **50** 229 (available at: www.ingentaconnect.com/contentone/sgt/ejgst/2009/00000050/00000003/art00018)

Journal of Alloys and Compounds 848 (2020) 156576

Contents lists available at ScienceDirect

Journal of Alloys and Compounds

journal homepage: http://www.elsevier.com/locate/jalcom

# Embedding CoPt magnetic nanoparticles within a phosphate glass matrix

Juliane Resges Orives [a, *], Wesley Renato Viali [a, d], Fabrício Benedito Destro [b], Sebastião W. da Silva [c], Sidney J.L. Ribeiro [a], Marcelo Nalin [a]

[a] Institute of Chemistry - São Paulo State University - UNESP, P. O. Box 355, Araraquara, SP, 14800-060, Brazil
[b] Federal University of Sao Carlos (UFSCar), Graduate Program in Materials Science and Engineering, Department of Materials Engineering, São Carlos, SP, Brazil
[c] Instituto de Física, Núcleo de Física Aplicada, Universidade de Brasília, UNB, Brasília, DF, 70910-900, Brazil
[d] Instituto Federal Goiano, Rio Verde, GO, 75901-970, Brazil

ARTICLE INFO

*Article history:*
Received 22 April 2020
Received in revised form
22 July 2020
Accepted 28 July 2020
Available online 8 August 2020

*Keywords:*
Coacervate
Magnetic nanoparticles
Cobalt platinum alloy
Hybrid materials
Magnetic glass

ABSTRACT

Glasses are materials with highly flexible compositions and high chemical and physical durability. These characteristics make them suitable materials for hosting nanoparticles for different purposes. Hybrid glasses containing magnetic nanoparticles have been highlighted due to their potential for application as ultra-sensitive magnetic sensors and magnetic devices. In this work, phosphate bulk glasses containing 0.5%, 1.0%, and 2.0% in mass of metallic CoPt alloy nanoparticles were prepared by melt-quenching technique. The CoPt nanoparticles were synthesized by reducing metal precursors in a high temperature organic solvent and, in the second step, they were covered with a silica layer in order to protect the nanoparticles for the subsequent melting. The nanoparticles were treated at different temperatures. Heat treatment at 900 °C showed the highest values of saturation magnetization and coercivity, and for that reason these nanoparticles were chosen for incorporation into glass. In the transmission electron microscopy images of the glass containing 2.0% in mass of nanoparticles, the interplanar distance of 0.21 nm was identified and indexed to the 111 plane of CoPt, confirming that the nanoparticles were successfully embedded into the matrix. The UV–Vis spectra presented $Co^{2+}$ characteristic bands at 528, 578, and 626 nm, indicating that these ions are tetrahedrally coordinated in the matrix. Themagnetic measurements presented behavior close to ferromagnetic, showing that it is possible to prepare a magnetic glass containing bimetallic nanoparticles.

© 2020 Elsevier B.V. All rights reserved.

## 1. Introduction

Combining glasses and nanotechnology has paved the way for the development of new hybrid materials, contributing to technological advances and pushing the boundaries of material science in recent years [1–6].

The incorporation of nanoparticles in glass allows advanced devices such as biocompatible glasses to be idealized for use in hyperthermia, lighting devices, waveguides, ultra-sensitive magnetic sensors, data storage, magneto-optical fibers, among others [4–14].

These applications take advantage of the great flexibility of compositions, wide range of refractive índices, and high chemical durability of glassy materials [15–18]. In addition, glass immobilizes the nanoparticles, protecting them from factors that deteriorate its properties, such as corrosive environments, heat, and humidity [1].

Two approaches have been used to obtain glasses containing nanoparticles. In the first, known as the in situ method, nanoparticles are obtained by heat treatment or laser irradiation [19–22].

In the second, the ex situ method, nanoparticles are previously synthesized and incorporated into the precursors by one of the following methods: glass melt doping, glass powder doping, and sol–gel doping [1,4,12,23,24]. The great advantage of this approach is the possibility of a wide variety of nanoparticles synthesizing with different properties, which provides high size and shape

* Corresponding author.
*E-mail addresses:* juliane_resges@hotmail.com, juliane.resges@unesp.br (J.R. Orives).

https://doi.org/10.1016/j.jallcom.2020.156576
0925-8388/© 2020 Elsevier B.V. All rights reserved.

control [25–27].

The incorporation of magnetic nanoparticles in glass has drawn attention due to their potential for magneto-optical materials and also to a fundamental point of view for studies with femtosecond lasers [12,28–39]. However, the challenge remains obtaining magneto-optical glasses with ideal functionality parameters such as nanoparticles with a narrow size distribution, controlled shape, and dispersed homogeneously into the bulk remains a challenge [31].

In the ex situ method, an additional concern is preserving the as-synthetized nanoparticles during glass obtention due to their possible dissolution at elevated temperatures. Our group recently developed a method of covering the magnetic nanoparticles with a protective layer of silica to avoid these sensitive metallic nanoparticles dissolving during the melting and oxidizing. This technique has previously shown good results [12,34,35].

In recent literature, we find several studies on glasses containing magnetic nanoparticles as Co, NiO, $CdFe_2O_4$, $Fe_2O_3$, or $Fe_3O_4$ [10,12,30–35]. However, to the best of our knowledge, there is no research dedicated to embedding bimetallic magnetic nanoparticles.

The CoPt alloy nanoparticles are viable candidates because of their strong ferromagnetism, high anisotropy, chemical stability, resistance to corrosion, and excellent magneto-optical properties [39–45].

These nanoparticles have good chemical stability due to interactions between the atoms of cobalt and platinum, which emerge from the spin-orbit coupling and hybridization between the 3d states of cobalt and 5d of platinum [40]. Their magnetic properties are strongly correlated with the structure, which can be adjusted by controlling the atomic ratio between Co and Pt, by the size of the synthesized nanoparticles, and by heat treatment [46,47].

CoPt alloys can be obtained with compositions $Co_3Pt$, $CoPt_3$, and CoPt. The $Co_3Pt$ and $CoPt_3$ alloys have a face-centered cubic (fcc) structure, which is called $L1_2$, and the $Co_{50}Pt_{50}$ has a face-centered tetragonal structure (fct) known as $L1_0$ [48]. The CoPt $L1_0$ alloy has greater thermodynamic stability, coercivity, and anisotropy than the $L1_2$ structure [48,49].

General methods of preparing nanoparticles of CoPt $L1_0$ involve the initial formation of CoPt nanoparticles with fcc structure, and subsequent heat treatment, usually above 580 °C, to achieve atom ordering [40,49].

In this context, the objective of this work is to report on embedding CoPt nanoparticles covered by a layer of silica into a phosphate glass using the melt-quenching technique. Phosphate glass can be obtained with a low melting temperature (about 950°C–1150 °C) and this may be an advantage in avoiding nanoparticles dissolving into the glass material [12,50].

A systematic study was proposed of the structural, morphological, thermal, optical, and magnetic properties of the hybrid glasses by Raman spectroscopy, transmission electron microscopy (TEM), differential scanning calorimetry (DSC), UV–Vis spectroscopy, and superconducting quantum interference device (SQUID).

## 2. Experimental procedures

### 2.1. Synthesis of CoPt–$SiO_2$ nanoparticles (CoPtSiNPs)

CoPt–$SiO_2$ nanoparticles were synthesized by reducing metal precursors in a high temperature organic solvent [51]. Initially, 0.48 g of cobalt chloride (II) hexahydrated (Sigma–Aldrich 99%), 1.00 g of hexachloroplatinic (IV) acid hexahydrated (Cennabras), and 40 mL of triethylene glycol dimethyl ether (Sigma–Aldrich) were added to a three-neck round bottom flask. The system was kept under nitrogen atmosphere with a controlled heating rate of 5 °C per min up to 120 °C, under magnetic stirring. Sodium borohydride reducing agent (Sigma–Aldrich 98%) was then added, and the system heated to 216 °C. The total solution was kept at this temperature for 3 h to complete the formation of CoPt nanoparticles. The nanoparticles were washed four times with ethanol and then dispersed using ultrasound bath in ethanol 99%. An aliquot was dried at room temperature in $N_2$ atmosphere for further characterization.

Subsequently, 0.191 mL of (3-Aminopropyl) triethoxysilane (Sigma–Aldrich 98%) was added to the remaining dispersion of the nanoparticles and then remained under ultrasound agitation. After 30 min, 3.6 mL of tetraethylorthosilicate (Sigma–Aldrich) and 1.3 mL of 25% ammonium hydroxide solution (P.A Synth) were added. The system remained under mechanical stirring for 24 h at inert atmosphere.

After this step the solid formed was washed five times with ethanol and isolated by centrifugation. The material was dried and divided into five samples that were heat treated for 2 h in argon atmosphere at the following temperatures: 25 °C (CoPtSi25), 500 °C (CoPtSi500), 700 °C (CoPtSi700, 900 °C (CoPtSi900) and 1100 °C (CoPtSi1100).

### 2.2. Polyphosphate glasses (PG)

The coacervate glass precursor was prepared by slowly mixing an equal volume of 2.0 M of $CaCl_2 \cdot 2H_2O$ (P.A. Synth), and 4.0 M of $Na(PO_3)n$ (Sigma– Aldrich 99%) solutions under constant stirring [50]. Next, six samples using 5 g of coacervate for each one were prepared: one without nanoparticles, one containing 0.1% in mass of $Co^{2+}$, one containing 1.0% of CoPtSi25 and three containing 0.5, 1.0, and 2.0% in mass of CoPtSi900.

After samples were homogenized, the CoPtSiNPs + coacervate mixture was transferred to an alumina crucible and heat treated at 600 °C for 15 min, to remove residual water. Next, the samples were melted at 1000 °C for 15 min and cast into a preheated stainless-steel mold at 340 °C. An electric EDG furnace, model EDG F1800 Sinter 10P operating in the range of 25–1800 °C, was used to melt the compositions. The glasses were then annealed at 340 °C for 2 h. The samples were finished by polishing with SiC sandpaper and ethanol.

### 2.3. CoPtSiNPs and PG characterization

The X-ray powder diffraction of CoPtSiNPs was carried out with a Bruker D8 Advance diffractometer operating with a Ni filtered CuKα radiation source at 2θ angle ranging from 10° to 80° with a step pass of 0.02° and a step time of 2 s.

Transmission electron microscopy (TEM) of CoPtSiNPs was carried out using a Tecnai FEI $G^2$ TEM/STEM 200 kV and equipped with energy dispersive X-ray detector. Samples were prepared using 0.1 mg of nanoparticles, the powder was dispersed in 1 mL of isopropyl alcohol using ultrasound and some drops of this suspension were applied on a copper grid coated with carbon film. The HR-TEM of glasses used a JEOL 2100 LaB operating at 200 kV with a 0.2 nm point to point resolution. Glass samples were prepared by grinding a piece of glass and dispersing the powder in 1 mL of isopropyl alcohol, using ultrasound. The nanoparticle sizes were calculated from TEM images using Image J software.

Magnetization measurements were performed using a VSM-SQUID (Vibration Sample Magnetometer with superconducting quantum interference device –SQUID) MPMS3 by Quantum Design a 300 K.

DSC was measured using a DSC404 F3 Pegasus equipment from NETZSCH. Small pieces of glasses (typically 15 mg) were heated on

a platinum crucible from 25 to 750 °C at a heating rate of 10 °C.min$^{-1}$, in $N_2$ atmosphere (70 mL min$^{-1}$) and estimate errors are ± 2 °C for glass transition, Tg and onset of crystallization, Tx and ±1 °C for the maximum of the crystallization peak, Tp.

UV–Vis absorption spectra (in the spectral range from 200 to 800 nm) were recorded using a Varian Cary 5000 UV–Vis–Near infrared (NIR) spectrophotometer, on the polished samples of 1.5 mm thickness. Raman scattering spectra were recorded at room temperature in a HORIBA Jobin Yvon model LabRAM HR micro Raman apparatus equipped with a 632.8 nm laser, delivering 17 mW, in a frequency range from 200 to 1300 cm$^{-1}$.

## 3. Results and discussion

### 3.1. CoPtSiNPs characterization

Fig. 1a, shows the synthesis steps for obtaining CoPt nanoparticles coated with silica. First, the precursor metals were reduced at high temperature and functionalized with APTS, which acts as a silane coupling agent for further $SiO_2$ layer growth [52]. The silica coating aims to protect the CoPt magnetic core from dissolving during the glass melting process, which takes place at 1000 °C. In addition, the $SiO_2$ layer has good compatibility with the phosphate glass and decreases its hygroscopicity [12,34].

Fig. 2 shows the XRD patterns of CoPt and CoPtSiNPs heat treated at different temperatures. As already mentioned, heat treatment is necessary for ordering atoms and forming the $L1_0$ structure. In addition, heat treatment eliminates the organic compounds that remained after washing.

For CoPtSiNP25 sample, the 111, 200, and 220 planes are observed at 40.3°, 46.9°, and 68.8°, respectively, corresponding to the $L1_2$ $CoPt_3$ alloy structure type (JCPDS 29–499). For CoPtSi500 sample, the diffraction peaks slightly shifted to the right and show intermediate values to those of the cubic and tetragonal structures, suggesting the coexistence of both phases, as also reported by Zhang et al. [53].

For CoPtSiNP700 sample, the planes 110, 111, 200, and 220 are located at 33.1°, 40.8°, 47.5° 69.5°, respectively. These planes were indexed to the CoPt alloy with structure type $L1_0$ (JCPDS 43–1358). The planes 111, 200 and 220, corresponding to platinum excess, (JCPDS 87–0647) were also observed. In addition to these phases, CoO traces (JCPDS 1–1227) were identified due to nanoparticle oxidation. Wang et al. also observed the cobalt oxide in the CoPt@$SiO_2$ nanoparticles and they suggest that CoO may come from surface oxidation during the formation of the CoPt alloy and also by the oxygen ions released by the decomposition of TEOS during coating to form the silica layer [54].

The CoPtSi900 sample presented the same peaks as the CoPtSi700 sample, but with the most intense peaks from the tetragonal structure, and two new planes indexed as 201 and 202, at 54.1° and 70.8°, respectively, showing that the crystallization of this phase has been improved. Very slight traces of cristobalite (JCPDS 1–438) were also observed, showing that at 900 °C the silica shell begins to crystallize.

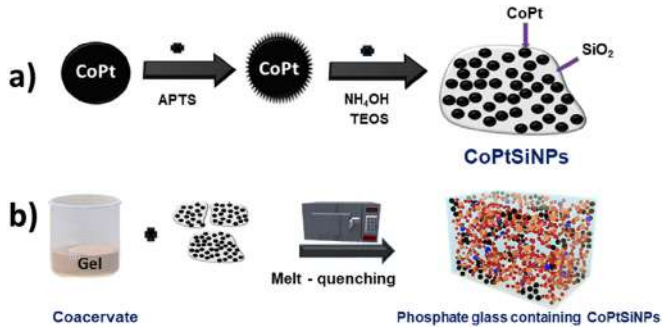


**Fig. 1.** Schematic illustration of **a)** obtaining the CoPt–$SiO_2$ nanoparticles, **b)** preparing glasses containing CoPtSiNPs.

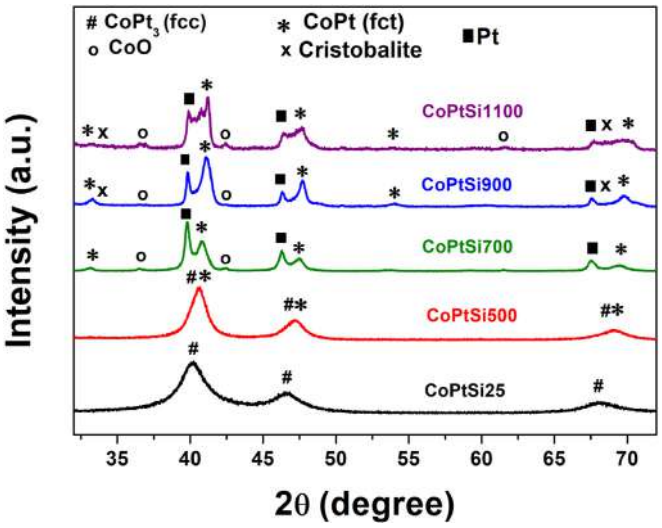


**Fig. 2.** XRD patterns off CoPtSiNPs heat treated at different temperatures for 2 h [the numbers in the label refer to the temperature of thermal treatment (CoPtSi1100–1100 °C)].

At 1100 °C it is possible to observe Pt, CoPt alloy, CoO traces, and cristobalite indexed peaks. In addition to these phases, (JCPDS 1–1227) were identified due to nanoparticle oxidation.

The CoPtSi25 sample was measured with X-ray fluorescence to find out the CoPt/$SiO_2$ ratio in order to adjust the magnetization curves. The percentages obtained were 12.40% Co, 41.65% Pt, 21.44% Si, and 24.49% O, resulting in a Pt/Co ratio of 3.4, with the alloy composition being $CoPt_{3.4}$, which agrees with the XRD and confirms an excess of platinum. The total proportion of $CoPt_{3.4}$ and $SiO_2$ is 54.04% and 45.93%, respectively.

Fig. 3 shows the magnetization curves as a function of the applied field. For CoPtSi25 sample, the saturation magnetization value ($M_s$) is 7.4 emu/g and is far from saturation in the investigated field. The value found agrees with that reported by Chinnasamy

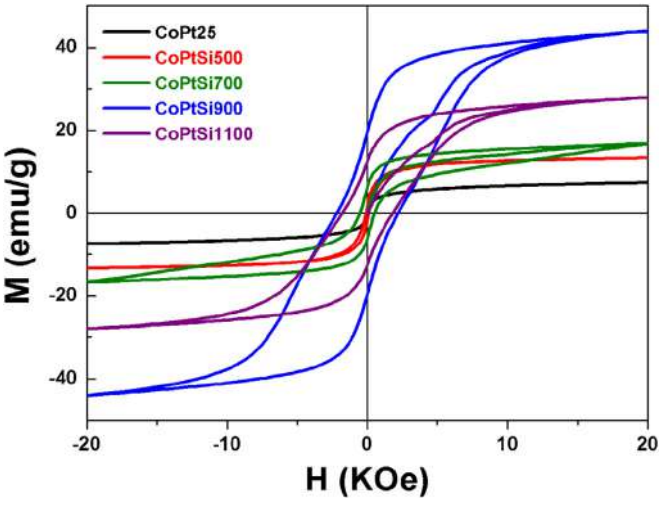


**Fig. 3.** Magnetization as a function of applied magnetic field for CoPtSiNPS samples heat treated at different temperatures for 2 h.

et al. [55] of 8 emu/g for 4 nm nanoparticles. The sample did not present coercive field (Hc), and the observed behavior for nanoparticles is superparamagnetic. The CoPtSi500 sample showed an increase in $M_s$ to 13.3 emu/g and a small Hc of 98 Oe, attributed to the presence of the $L1_0$ phase, while the CoPt700 sample showed $M_s$ of 16.8 emu/g and and $H_c$ of 512 Oe.

The highest values of Ms (44.0 emu/g) and Hc (2187 Oe) were obtained for CoPtS900 sample, with ferromagnetic behavior. These high values are due to nanoparticles forming with $L1_0$ structure as a result of the increased temperature with heat treatment. Structural changes that promote magnetocrystalline anisotropy induce strong ferromagnetic coupling; furthermore, the increase in coercivity is also related to the increase in size and in interparticle interaction that is controlled by the distance between nanoparticles.

Thus, CoPtSi900 nanoparticles, which showed better magnetic response, were chosen for incorporation into the phosphate matrix. Fig. 4 shows TEM images of the CoPtSi900 sample; it is possible to notice that the nanoparticles do not present a monodisperse coating, resulting in larger $SiO_2$ agglomerates. The nanoparticles size distribution ranged from 4.0 to 40 nm with an average diameter of 16.4 ± 2.06 nm.

The interplanar distances of 0.21 nm and 0.23 nm were identified and indexed to the 111 plane of CoPt and 111 plane of Pt, respectively. The presence of the Pt plane 111 is explained by the Pt layer that forms during the heat treatment of $Pt_3M$ alloys. Studies suggest that during heat treatment, these alloys form an outer layer of atomic monolayers rich in Pt [56,57]. The high crystallinity and the larger average diameter of the CoPtSi900 particles corroborate the magnetic results of higher $M_s$ and $H_c$ presented by this sample.

TEM images were also obtained for nanoparticles after heat treatments at different temperatures (Fig. S1 Support Information). The average size of CoPtSi25 sample was 3.3 ± 0.02 nm, while CoPtSi500 and CoPtSi700 samples had average diameters of 4.7 ± 0.04 nm and 6.1 ± 0.04 nm, respectively, showing that heat treatment promotes the approximation of nanoparticles because the pores of the silica matrix collapse, allowing nanoparticles to diffuse in the matrix, resulting in their growth by coalescence [58].

### 3.2. PG glasses containing CoPtSiNPs

In previous works, the polyphosphate glasses obtained using the coacervate glass precursor proved to be good hosts for magnetic nanoparticles coated with silica [12,34]. The phosphate glasses prepared by the coacervation technique, mainly those compositions containing $Ca^{2+}$ ions, are not hygroscopic as those glasses are prepared using high contents of $P_2O_5$ or $NaPO_3$ [12,51,59–61]. The main reason for the lower hygroscopicity comes from the structural backbone of the phosphate prepared by such methodology, which leads to lower quantity of P–O- terminal groups, with part of the remaining charges compensated by $Ca^{2+}$ ions [59–61].

Samples containing CoPtSi900 nanoparticles were prepared in three different mass percentages: 0.5% (PG-0.5CoPtSi900), 1.0% (PG-1CoPtSi900), and 2.0% (PG-2CoPtSi900).

A sample containing 0.1% in mass of $Co^{2+}$ ions (PG-0.1$Co^{2+}$) and another of 1% in mass of CoPtSi25 nanoparticles (PG-1CoPtSi25) were also prepared and studied for comparison. The samples were analyzed by XRD and present the halo characteristic for amorphous materials. The XRD curves are shown in the supplementary section as Fig. S2.

The HR-TEM images of the sample PG-2CoPtSi900, Fig. 5a–c, show that the nanoparticles were successfully incorporated into the vitreous matrix.

In Fig. 5a, we observe the presence of CoPt nanoparticles embedded into the silica shell while the phosphate glass can be seen in the border, as shown by the arrows. (The images were obtained from grounded glass dispersed in isopropyl alcohol and dripped on a copper grid).

In Fig. 5b–c, it is possible to observe the crystalline planes of the nanoparticles inside the glass, with interplanar distances of 0.21 and 0.27 nm, which are indexed to the 111 and 110 planes of the CoPt alloy, respectively. Also, the 0.23 nm interplanar distance corresponds to the plan 111 of the Pt. These results confirm the possibility bimetallic nanoparticles incorporating in phosphate glasses.

### 3.3. Thermal analysis of PGs

Fig. 6 presents the DSC curves and Table 1, the characteristic temperatures $T_g$, $T_x$ and $T_p$, as well as the stability parameter, $T_x$-$T_g$.

For PG-0.1$Co^{2+}$ glass, besides Tg increasing 4 °C, the stability parameter did not change, denoting that small contents do not promote significant changes in the structure of the glasses and that

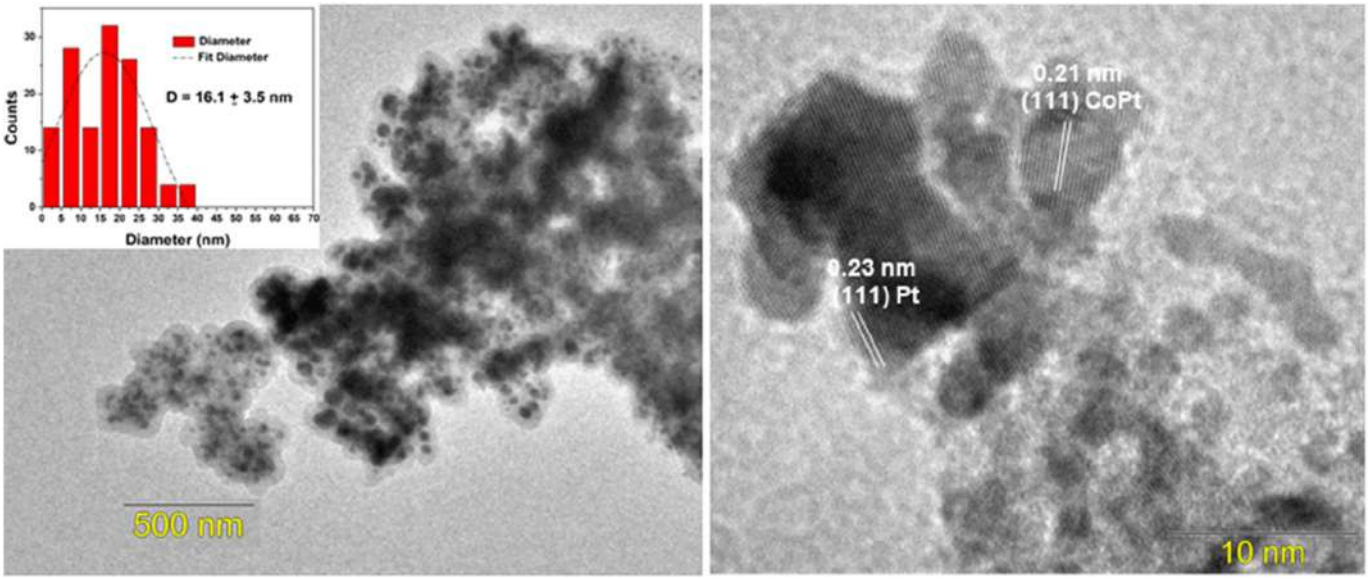


**Fig. 4.** a) TEM of CoPTSi900 nanoparticles with scale of 500 nm. Inset: size distribution of nanoparticles, and b) Magnification and identification of the crystalline plane of CoPt.

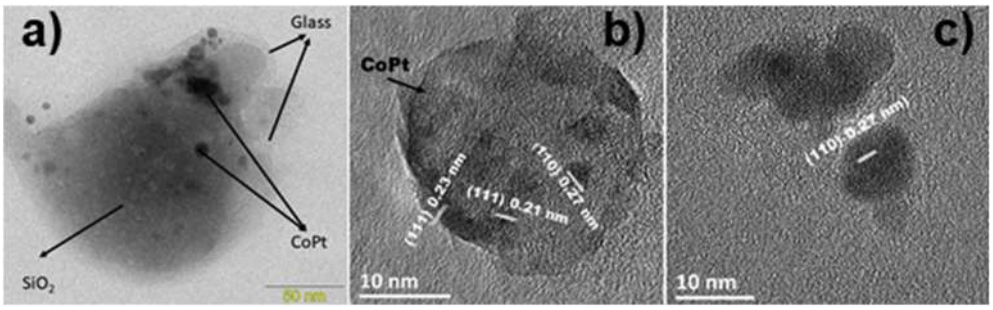


**Fig. 5.** a) TEM image of PG-2CoPtSi900 with scale of 500 nm. b-c) Magnification and identification of the crystalline planes of CoPt.

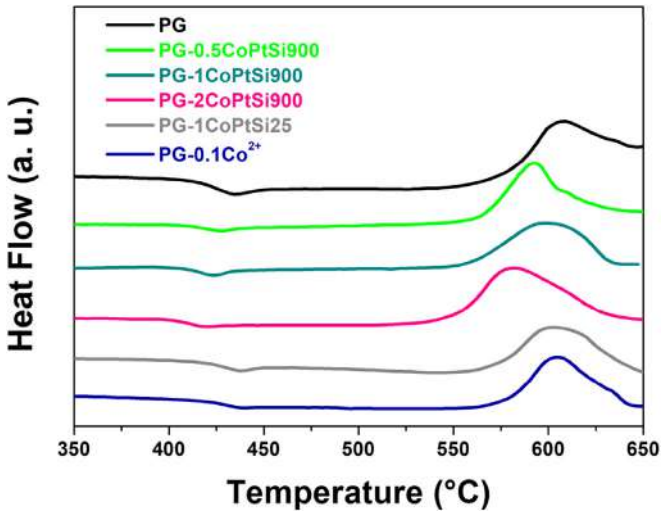


**Fig. 6.** DSC curves of glasses with and without nanoparticles.

**Table 1**
Characteristic temperatures of the PGs containing $Co^{2+}$, CoPtSi25 and CoPtSi900.

| Samples | $T_g$ (°C) | $T_x$ (°C) | $T_p$ (°C) | $T_x-T_g$ (°C) |
|---|---|---|---|---|
| PG | 414 | 570 | 609 | 154 |
| PG-0.5CoPtSi900 | 413 | 561 | 592 | 148 |
| PG-1CoPtSi900 | 410 | 556 | 600 | 146 |
| PG-2CoPtSi900 | 405 | 545 | 581 | 140 |
| PG-1CoPtSi25 | 418 | 573 | 605 | 155 |
| PG-0.1$Co^{2+}$ | 418 | 574 | 603 | 156 |

such differences are comprised in the experimental errors associated with the temperature's determination.

The sample PG-1CoPtSi25, in which the nanoparticles did not undergo heat treatment, presented values of $T_g$, $T_x$, and $T_p$, similar to the sample PG-0.1$Co^{2+}$. For samples containing CoPtSi900, $T_g$ and $T_p$ decrease with increasing percentage of nanoparticles. Lower values of $T_g$ occur due to the breaking of the polyphosphate chains, caused by the addition of nanoparticles.

The decrease of $T_g$ suggests that silica agglomerates remained mostly preserved due to heat treatment at 900 °C on the CoPtSi nanoparticles. The heat treatment induced the formation of cristobalite, which had an important role in consolidating the silica shell, promoting the protection of nanoparticles more effectively during the glass synthesis and avoiding its dissolution. In previous works [12,34], it was observed that the dissolution of the silica shell (prepared by another chemical route) promotes the formation of P—O—Si bonds, increasing $T_g$, which was not observed in the present study.

The stability parameter $T_x$-$T_g$ decreases from 154 °C (VF) to 140 °C (PG-2CoPtSi900). The small $SiO_2$—nanoparticles agglomerates may have induced the crystallization processes earlier during heating and, as a consequence, $T_x$ decreases as a function of the content of NP.

### 3.4. Raman spectroscopy analysis

The glasses were studied using Raman spectroscopy (Fig. 7). The spectra of the samples containing $Co^{2+}$ ions and CoPt nanoparticles showed the same profile as the PG sample, containing two main vibrational modes at 1172 and 692 $cm^{-1}$, assigned to the symmetrical stretches $\nu_s$(P—$O_{terminal}$) and $\nu_s$(P—$O_{bridged}$), respectively, and the O—P—O bending motions in the range of 400—300 $cm^{-1}$ [61].

The main bands for these samples did not widen or shift. Also, no signal of formation of P—O—Si bonds could be assigned from the Raman spectra, as done elsewhere [34].

### 3.5. UV—Vis spectroscopy analysis

Fig. 8 shows the absorbance spectra in the UV—Vis region, all samples were polished to 1 mm thickness.

The sample containing a low percentage of $Co^{2+}$ ions (0.1%) is blue. In fact, this ion gives intense colors to the phosphate matrix even in concentrations as low as 0.005% [62]. According to Navarro [62], phosphate glasses will show a purple color when the $Co^{2+}$ ions are six-fold coordinated in the structure, with a characteristic

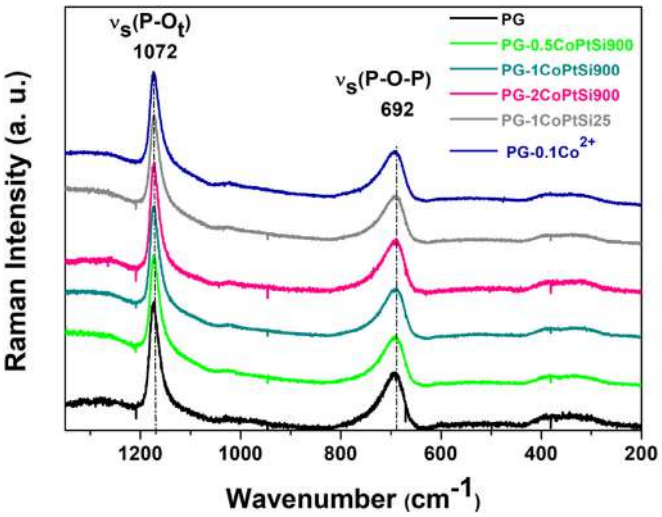


**Fig. 7.** Raman spectra obtained for the vitreous samples with and without nanoparticles.

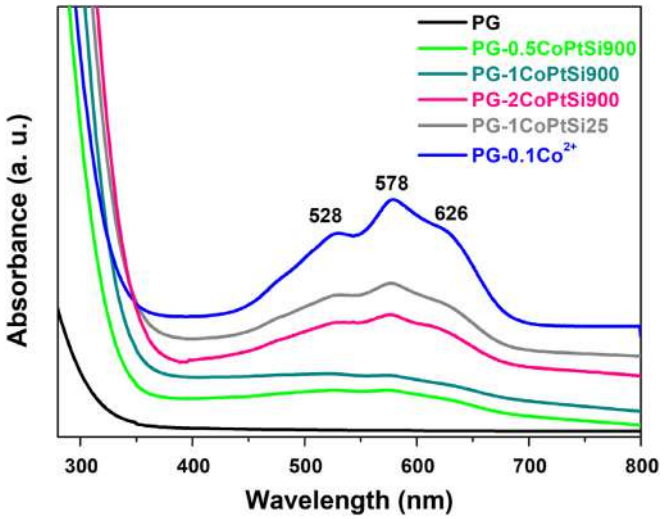


**Fig. 8.** Absorbance spectra in the UV–Vis region obtained for PGs containing $Co^{2+}$, CoPtSi25, and CoPtSi900. (The spectra have been moved vertically for better viewing.)

band at 510 nm. And they will show a blue color when the $Co^{2+}$ ions occupy tetrahedral sites characterized by a triple absorption band at 540, 590, 640 nm, which can be slightly displaced depending on the glass composition.

In two recent papers, the authors used CoO as precursor to prepare glasses in air atmosphere. The absorption spectra of glasses, in both works, show only the presence of $Co^{2+}$ ions, and the corresponding bands appear at 519, 586, and 639 nm in the first paper and at 520, 575, and ~625 nm in the second one, in complete agreement with our data [63,64].

Based on this information, we can infer that $Co^{2+}$ ions are coordinated tetrahedrically in the phosphate glass. The characteristic bands at 528, 578 and 626 nm, correspond to the transitions $^4A_2 \rightarrow {}^4T_2$, $^4A_2 \rightarrow {}^4T_1$, and $^4A_2 \rightarrow {}^4T_1(P)$, respectively; this unfolding is attributed to a Jahn-Teller distortion.

All investigated samples showed the characteristic band of $Co^{2+}$ ions, indicating that at least a small amount of NPs dissolved and $Co^{2+}$ ions were tetrahedrally coordinated in the matrix. Also, the sample PG-1CoPtSi25 had a more intense absorption than PG-1CoPtSi900, showing that heat treatment at 900 °C protected the nanoparticles more effectively during the melting process.

The presence of $Co^{2+}$ ions in phosphate glasses shifts the transmission window to higher wavelengths due to the $O^{2-}$ to metal charge transfer transitions [62].

### 3.6. Magnetic measurement of PG-2CoPtSi900

The PG and PG-CoPtSi900 samples were magnetically characterized as a function of the applied magnetic field at 300 K (Fig. 9a–b). The magnetization in emu/g was divided by the total mass of the glass sample, resulting in lower values due to the magnetic dilution caused by the phosphate matrix.

The PG sample showed a diamagnetic behavior, with a negative magnetic susceptibility, indicating that the phosphate glass contains no unpaired electrons and is not attracted to a magnetic field. The PG-CoPtSi900 sample showed a behavior close to ferromagnetic, with a low $H_c$ value of 178 Oe when compared to the CoPt900 sample that has a $H_c$ value of 2178 Oe.

The lower values of the magnetic properties presented by the PG-CoPtSi900 can be explained by their critical dependence on nanoparticles size distribution, interaction, and degree of aggregation. In the phosphate glass matrix, the nanoparticles are more separated, thus weakening dipolar interactions which become negligible [65].

In addition to the dilution effects, as observed by the TEM images, glass presented nanoparticles slightly smaller than the average size of the CoPtSi900. Also, in the UV–Vis graph, it was observed that part of the nanoparticles dissolved due to the presence of $Co^{2+}$ ions in tetrahedral coordination, corroborating this previous statement. This can cause spin-glass disorders on the surface of the nanoparticles, resulting in imperfections in the coordination number, thus influencing the magnetic properties obtained after incorporation into the glass. Anigrahawati et al. [11] also noticed this behavior after incorporating 70 nm $Fe_3O_4$ in a phosphate matrix.

Although the result was not the same as that of the nanoparticles, the sample showed a magnetic signal with a small hysteresis, showing that it is possible to prepare a ferromagnetic magnetic glass by incorporating previously synthesized nanoparticles.

The results obtained in this work can contribute to the development of glasse containing nanoparticles useful for application in magneto-optical devices. For this reason, static and dynamic

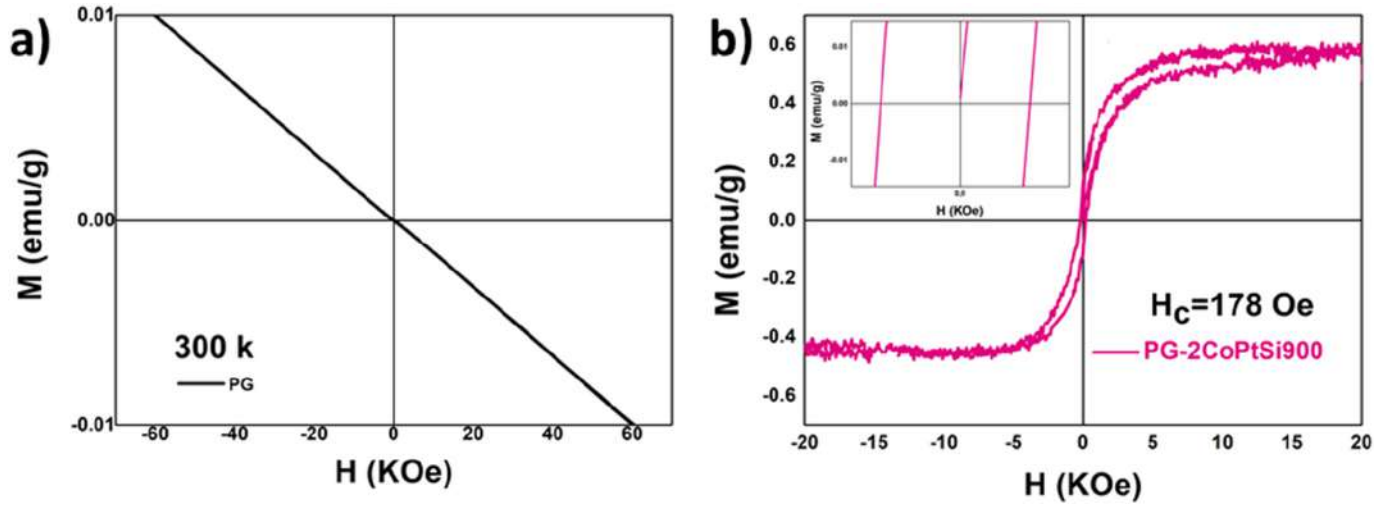


**Fig. 9.** M-H curve at 300 K of a) PG and b) PG-2CoPtSi900.

magneto-optical studies for these samples are also in progress.

## 4. Conclusions

This work shows that it is possible to obtain a phosphate glass containing bimetallic nanoparticles, by first synthesizing the CoPtSi900 nanoparticles and then melting the mixture between these and a precursor gel.

The magnetic measurements confirmed the presence of CoPt in the glass sample, which showed a behavior close to ferromagnetics, with a $H_c$ value of 178 Oe. TEM images also show the efficient incorporation of nanoparticles. UV–Vis region spectra showed that at least a small amount of NPs dissolved into the matrix, meaning that it is still necessary to improve the quality of the silica coating.

These results open the possibility of exploring new functionalities for such materials in the field of magneto-optical devices. These new hybrid glasses can play an interesting role in light manipulation by changing the magnetic field, which would allow applications such as magnetic sensors.

## CRediT authorship contribution statement

**Juliane Resges Orives:** Conceptualization, Investigation, Methodology, Writing - review & editing. **Wesley Renato Viali:** Conceptualization, Writing - review & editing. **Fabrício Benedito Destro:** Formal analysis, Writing - review & editing. **Sebastião W. da Silva:** Formal analysis. **Sidney J.L. Ribeiro:** Writing - review & editing. **Marcelo Nalin:** Conceptualization, Supervision.

## Declaration of competing interest

The authors declare that they have no known competing financial interests or personal relationships that could have appeared to influence the work reported in this paper.

## Acknowledgments

The authors are grateful to the Brazilian funding agencies Conselho Nacional de Desenvolvimento Científico e Tecnológi (CNPQ) and São Paulo Research Foundation FAPESP for the grants (2013/07793-6, 2018/07727-7. 2019/19609-1). This study was financed in part by Coordenação de Aperfeiçoamento de Pessoal de Nível Superior (CAPES)–Brazil - Finance Code 001 (Grant number 88882.332718/2019-01).

## Appendix A. Supplementary data

Supplementary data to this article can be found online at https://doi.org/10.1016/j.jallcom.2020.156576.

## References

[1] Y. Wei, H. Ebendorff-Heidepriem, J. Zhao, Recent advances in hybrid optical Materials: integrating nanoparticles within a glass matrix, Adv. Opt. Mater. 7 (2019), 1900702, https://doi.org/10.1002/adom.201900702.
[2] Q.B. Wang, N. Iancu, D.K. Seo, Preparation of large transparent silica monoliths with embedded photoluminescent CdSe@ZnS core/shell quantum dots, Chem. Mater. 17 (2005) 4762–4764, https://doi.org/10.1021/cm050962a.
[3] X. Liu, J. Zhou, S. Zhou, Y. Yue, J. Qiu, Transparent glass-ceramics functionalized by dispersed crystals, Prog. Mater. Sci. 97 (2018) 38–96, https://doi.org/10.1016/j.pmatsci.2018.02.006.
[4] M.R. Henderson, B.C. Gibson, H. Ebendorff-Heidepriem, K. Kuan, S. Afshar V, J.O. Orwa, I. Aharonovich, S. Tomljenovic-Hanic, A.D. Greentree, S. Prawer, T.M. Monro, Diamond in tellurite glass: a new medium for quantum information, Adv. Mater. 23 (2011) 2806–2810. https://doi:10.1002/adma.201100151.
[5] C.F. Wang, F.J. Fan, R.P. Sabatini, O. Voznyy, K. Bicanic, X.Y. Li, D.P. Sellan, M. Saravanapavanantham, N. Hossain, K. Chen, S. Hoogland, E.H. Sargent, Quantum dot color-converting solids operating efficiently in the kW/cm2 regime, Chem. Mater. 29 (2017) 5104–5112, https://doi.org/10.1021/acs.chemmater.7b00164.
[6] J. Zhong, D. Chen, Y. Peng, Y. Lu, X. Chen, X. Li, Z. Ji, A review on nanostructured glass ceramics for promising application in optical thermometry, J. Alloys Compd. 763 (2018) 34–48, https://doi.org/10.1016/j.jallcom.2018.05.348.
[7] I. Edelman, J. Kliava, Oxide glasses with magnetic nanoparticles: transparente magnets (Faraday rotation and electron magnetic resonance studies), Phys. Status Solidi B 246 (2009) 2216–2231, https://doi.org/10.1002/pssb.200945169.
[8] P. Ji, Y. Wang, M. Zhang, B. Li, G. Zhang, $P_2O_5$-$Fe_2O_3$-CaO-$SiO_2$ ferromagnetic glass ceramics for hyperthermia, Int. J. Appl. Ceram. Technol. 15 (2018) 1261–1267, https://doi.org/10.1111/ijac.12880.
[9] R. Berger, J. Kliava, J.C. Bissey, Magnetic resonance of superparamagnetic iron containing nanoparticles in annealed glass, J. Appl. Phys. 87 (2000) 7389–7396, https://doi.org/10.1063/1.372998.
[10] Q. Chen, L. Wan, Q. Chen, M. Zhang, Effect of magnetite nanoparticles doped glass with enhanced verdet constant for magnetic optical current transducer applications, Adv Mat Res 271–273 (2011) 13–18, https://doi.org/10.4028/www.scientific.net/AMR.271-273.13.
[11] P. Anigrahawati, M.R. Sahar, S.K. Ghoshal, Influence of $Fe_3O_4$ nanoparticles on structural, optical and magnetic properties of erbium doped zinc phosphate glass, Mater. Chem. Phys. 155 (2015) 155–161, https://doi.org/10.1016/j.matchemphys.2015.02.014.
[12] J.R. Orives, B.P. Pichon, D. Mertz, K. Sartori, S. Begin-Colin, W.R. Viali, M. Nalin, Phosphate glasses containing monodisperse $Fe_{3-\delta}O_4$@$SiO_2$ stellate nanoparticles obtained by melt-quenching process, Ceram. Int. 46 (2020) 12120–12127, https://doi.org/10.1016/j.ceramint.2020.01.257.
[13] Y. Ruan, D.A. Simpson, J. Jeske, H. Ebendorff-Heidepriem, D.W.M. Lau, H. Ji, B.C. Johnson, T. Ohshima, S. Afshar V, L. Hollenberg, A.D. Greentree, T.M. Monro, B.C. Gibson, Magnetically sensitive nanodiamond-doped tellurite glass fibers, Sci. Rep. 8 (2018) 1–6, https://doi.org/10.1038/s41598-018-19400-3.
[14] A. Stalmashonak, A. Abdolvand, G. Seifert, Metal-glass nanocomposite for optical storage of information, Appl. Phys. Lett. 99 (2011), 201904, https://doi.org/10.1063/1.3660740.
[15] J.C. Mauro, E.D. Zanotto, Two centuries of glass research: historical trends, current status, and grand challenges for the future, Int. J. Appl. Glass Sci. 5 (2014) 313–327, https://doi.org/10.1111/ijag.12087.
[16] D.L. Morse, J.W. Evenson, Welcome to the glass age, Int. J. Appl. Glass Sci. 7 (2016) 409–412, https://doi.org/10.1111/ijag.12242.
[17] J.H. Wray, J.T. Neu, Refractive index of several glasses as a function of wavelength and temperature, J. Opt. Soc. Am. 59 (1969) 774–776, https://doi.org/10.1364/JOSA.59.000774.
[18] L.G. Aio, A.M. Efimov, V.F. Kokorina, Refractive index of chalcogenide glasses over a wide range of compositions, J. Non-Cryst. Solids 27 (1978) 299–307, https://doi.org/10.1016/0022-3093(78)90015-7.
[19] C. Worsch, M. Büttner, P. Schhf, R. Harizanova, C. Rüssel, F. Schmidl, P. Seidel, Magnetic properties of multicore magnetite nanoparticles prepared by glass crystallisation, J. Mater. Sci. 48 (2013) 2299–2307, https://doi.org/10.1007/s10853-012-7009-7.
[20] J. Sheng, J. Zhang, L. Qiao, Long-term stability of X-ray induced color centers in silver-doped glass, J. Non-Cryst. Solids 352 (2006), https://doi.org/10.1016/j.jnoncrysol.2006.04.017, 2914-2616.
[21] J. Zhang, W. Dong, J. Sheng, J. Zheng, J. Li, L. Qiao, L. Jiang, Silver nanoclusters formation in ion-exchanged glasses by thermal annealing, UV-laser and X-ray irradiation, J. Cryst. Growth 310 (2008) 234–239, https://doi.org/10.1016/j.jcrysgro.2007.10.007.
[22] K. Sharma, S. Singh, C.L. Prajapat, S. Bhattacharya, Jagannath, M.R. Singh, S.M. Yusulf, G.P. Kothiyal, Preparation and study of magnetic properties of silico phosphate glass and glass-ceramics having iron and zinc oxide, J. Magn. Magn Mater. 321 (2009) 3821–3828, https://doi.org/10.1016/j.jmmm.2009.07.047.
[23] M. Gajc, H.B. Surma, A. Klos, K. Sadecka, K. Orlinski, A.E. Nikolaenko, K. Zdunek, D.A. Pawlak, Nanoparticle direct doping: novel method for manufacturing three-dimensional bulk plasmonic nanocomposites, Adv. Funct. Mater. 23 (2013) 3443–3451, https://doi.org/10.1002/adfm.201203116.
[24] Z.C. Li, L. Kong, S.Q. Huang, L. Li, Highly luminescent and ultrastable $CsPbBr_3$ perovskite quantum dots incorporated into a silica/alumina monolith, Angew. Chem. Int. Ed. 56 (2017) 8134–8138, https://doi.org/10.1002/anie.201703264.
[25] W. Baaziz, B.P. Pichon, S. Fleutot, Y. Liu, C. Lefevre, J.M. Greneche, M. Toumi, T. Mhiri, S. Begin-Colin, Magnetic iron oxide nanoparticles: reproducible tuning of the size and nanosized-dependent composition, defects, and spin canting, J. Phys. Chem. C 118 (2014) 3795–3810, https://doi.org/10.1021/jp411481p.
[26] K. Zhang, L.-L. Xu, J.-G. Jiang, N. Calin, K.-F. Lam, S.-J. Zhang, H.-H. Wu, G.-D. Wu, B. Albela, L. Bonneviot, P. Wu, Facile large-scale synthesis of monodisperse mesoporous silica nanospheres with tunable pore structure, J. Am. Chem. Soc. 135 (2013) 2427–2430, https://doi.org/10.1021/ja3116873.
[27] G. Sharma, A. Kumar, S. Sharma, M. Naushad, R.P. Dwivedi, Z.A. Alothman, G.T. Mola, Novel development of nanoparticles to bimetallic nanoparticles and their composites: a review, J. King Saud Univ. Sci. 31 (2019) 257–269, https://doi.org/10.1016/j.jksus.2017.06.012.
[28] J. Kliava, I. Edelman, O. Ivanova, R. Ivantsov, O. Bayukov, E. Petrakosvskaja,

V. Zaikovskly, I. Bruckental, Y. Yeshurun, S. Stepanov, Formation and evolution of magnetic nanoparticles in borate glass simultaneously doped with Fe and Mn oxides, J. Appl. Phys. 104 (2008), 103917, https://doi.org/10.1063/1.3021289.

[29] F. Bentivegna, M. Nyvlt, J. Ferré, J.P. Jamet, A. Brun, S. Visnovsky, R. Urban, Magnetically textured $\gamma$-$Fe_2O_3$ nanoparticles in a silica gel matrix: optical and magneto-optical properties, J. Appl. Phys. 85 (1999) 2270–2278, https://doi.org/10.1063/1.369537.

[30] S. Woltz, C. Russel, Self-organized nano crystallinity of magnetite precipitated from a $4.9Na_2O$ - 33.3CaO - $17.1Fe_2O_3$ - $44.7B_2O_3$ glass, J. Non-Cryst. Solids 337 (2004) 226–231, https://doi.org/10.1016/j.jnoncrysol.2004.04.015.

[31] W. Widanarto, M.R. Sahar, S.K. Goshal, R. Arifin, M.S. Rohani, Effendi, Thermal, structural and magnetic properties of zinc-tellurite glasses containing natural ferrite oxide, Mater. Lett. 108 (2013) 289–292, https://doi.org/10.1016/j.matlet.2013.06.109.

[32] W. Widanarto, M.R. Sahar, S.K. Goshal, R. Arifin, M.S. Rohani, K. Hamzah, Effect of natural Fe3O4 nanoparticles on structural and optical properties of $Er^{3+}$ doped tellurite glass, J. Magn. Magn Mater. 326 (2013) 123–128, https://doi.org/10.1016/j.jmmm.2012.08.042.

[33] H.K. Farag, M.A. Marzouk, Preparation and characterization of nanostructured nickel oxide and its influence on the optical properties of sodium zinc borate glasses, J. Mater. Sci. Mater. Electron. 28 (2017) 15480–15487, https://doi.org/10.1007/s10854-017-7435-z.

[34] J.R. Orives, W.R. Viali, S.H. Santagneli, C.R.M. Afonso, M.H. Carvalho, A.J.A. Oliveira, M. Nalin, Phosphate glasses via coacervation route containing $CdFe_2O_4$ nanoparticles: structural, optical and magnetic characterization, Dalton Trans. 47 (2018), https://doi.org/10.1039/C8DT00560E, 5771-5579.

[35] J.R. Orives, W.R. Viali, M. Magnani, M. Nalin, Incorporation of $CdFe_2O_4$-$SiO_2$ nanoparticles in $SbPO_4$-ZnO-PbO glasses by melt-quenching process, Eclét. Quím. 43 (2018) 32–43, https://doi.org/10.26850/1678-4618eqj.v43.2.2018.p32-43.

[36] C. Boeglin, E. Beaurepaire, V. Halté, V. López-Flores, C. Stamm, N. Pontius, H.A. Dürr, J.-Y. Bigot, Distinguishing the ultrafast dynamics of spin and orbital moments in solids, Nature 465 (2010) 458–461, https://doi.org/10.1038/nature09070.

[37] B. Amirsolaimani, P. Gangopadhyay, A.P. Persoons, S.A. Showghi, L.J. LaComb, R.A. Norwood, N. Peyghambarian, High sensitivity magnetometer using nanocomposite polymers with large magneto-optic response, Opt. Lett. 43 (2019) 4615–4618, https://doi.org/10.1364/OL.43.004615.

[38] Y. Bigot, M. Vomir, Ultrafast magnetization dynamics of nanostructures, Ann. Phys. 525 (2012) 2–30, https://doi.org/10.1002/andp.201200199.

[39] J.-Y. Bigot, H. Kesserwan, V. Halté, O. Ersen, M.S. Moldovan, T.H. Kim, J.-T. Jang, J. Cheon, Magnetic properties of annealed core–shell CoPt nanoparticles, Nano Lett. 12 (2012) 1189–1197, https://doi.org/10.1021/nl300306a.

[40] Y. Wang, X. Zhang, Y. Liu, Y. Jiang, Y. Zhang, J. Yang, Enhanced magnetic behaviors of CoPt nanoparticles by addition of $SiO_2$, J. Solid State Chem. 213 (2014) 204–209, https://doi.org/10.1016/j.jssc.2014.03.001.

[41] C. Petit, S. Rusponi, H. Brune, Magnetic properties of cobalt and cobalt–platinum nanocrystals investigated by magneto-optical Kerr effect, J. Appl. Phys. 95 (2004) 4251, https://doi.org/10.1063/1.1686906.

[42] L. Castaldi, K. Giannakopoulos, A. Travlos, D. Niarchos, S. Boukari, E. Beaurepaire, FePt and CoPt nanoparticles co-deposited on silicon dioxide-a comparative study, Nanotechnology 19 (2008), 085701, https://doi.org/10.1088/0957-4484/19/8/085701.

[43] F. Tournus, N. Blanc, A. Tamion, M. Hillenkamp, V. Dupuis, Synthesis and magnetic properties of size-selected CoPt nanoparticles, J. Magn. Magn Mater. 323 (2011) 1868–1872, https://doi.org/10.1016/j.jmmm.2011.02.024.

[44] Y. Yu, W. Yang, X. Sun, W. Zhu, X.-Z. Li, D.J. Sellmyer, S. Sun, Monodisperse MPt (M = Fe, Co, Ni, Cu, Zn) nanoparticles prepared from a facile oleylamine reduction of metal salts, Nano Lett. 14 (2014) 2778–2782, https://doi.org/10.1021/nl500776e.

[45] L. Uba, S. Uba, V.N. Antonov, A.N. Yaresko, R. Gontarz, Microscopic origin of the magneto-optical properties of CoPt alloys, Phys. Rev. B. 64 (2001), 125105, https://doi.org/10.1103/physrevb.64.125105.

[46] Š. Višňovský, E.J. Lišková, M. Nývlt, R. Krishnan, Origin of magneto-optic enhancement in CoPt alloys and Co/Pt multilayers, Appl. Phys. Lett. 100 (2012), 232409, https://doi.org/10.1063/1.4726121.

[47] C. Frommen, H. Rosner, D. Fensk, Wet-chemical synthesis and properties of CoPt and $CoPt_3$ alloy, J. Nanosci. Nanotechnol. 2 (2002) 509–515, https://doi.org/10.1166/153348802760394098.

[48] S. Karoui, H. Amara, B. Legrand, F. Ducastelle, Magnetism: the driving force of order in CoPt, a first-principles study, J. Phys. Condens. Matter 25 (2013), 056005, https://doi.org/10.1088/0953-8984/25/5/056005.

[49] M. Ohtake, S. Ouchi, F. Kirino, M. Futamoto, L10 ordered phase formation in FePt, FePd, CoPt, and CoPd alloy thin films epitaxially grown on MgO(001) single-crystal substrates, J. Appl. Phys. 111 (2012) 2012–2015, https://doi.org/10.1063/1.3672856.

[50] D.F. Franco, D. Manzani, H.S. Barud, S.G. Antonio, L.F.C. Oliveira, M.A.P. Silva, S.J.L. Ribeiro, M. Nalin, Structural investigation of nickel polyphosphate coacervate glass - ceramics, RSC Adv. 6 (2016) 91150–91156, https://doi.org/10.1039/C6RA20696D.

[51] J. Park, J. Joo, S.G. Kwon, Y. Jang, T. Hyeon, Synthesis of monodisperse spherical nanocrystals, Angew. Chem. Int. Ed. 46 (2007) 4630–4660, https://doi.org/10.1002/anie.200603148.

[52] Y. Kobayashi, M. Horie, M. Konno, B. Rodríguez-González, L.M. Liz-Marzán, Preparation and properties of silica-coated cobalt nanoparticles, J. Phys. Chem. B 107 (2003) 7420–7425, https://doi.org/10.1021/jp027759c.

[53] Y.J. Zhang, Y.T. Yang, Y. Liu, Y.X. Wang, L.L. Yang, M.B. Wei, H.G. Fan, H.J. Zhai, X.Y. Liu, Y.Q. Liu, N.N. Yang, Y.H. Wu, J.H. Yang, A novel approach to the synthesis of CoPt magnetic nanoparticles, J. Phys. D Appl. Phys. 44 (2011), 295003, https://doi.org/10.1088/0022-3727/44/29/295003.

[54] Y. Wang, X. Zhang, Y. Liu, Y. Jiang, Y. Zhang, J. Yang, Enhanced magnetic behaviors of CoPt nanoparticles by addition of SiO2, J. Solid State Chem. 213 (2014) 204–209, https://doi.org/10.1016/j.jssc.2014.03.001.

[55] C.N. Chinnasamy, B. Jeyadevan, K. Shinoda, K. Tohji, Polyol-process-derived CoPt nanoparticles: structural and magnetic properties, J. Appl. Phys. 93 (2003) 7583–7585, https://doi.org/10.1063/1.1558259.

[56] V.R. Stamenkovic, B.S. Mun, M. Arenz, K.J.J. Mayrhofer, C.A. Lucas, G. Wang, P.N. Ross, N.M. Markovic, Trends in electrocatalysis on extended and nanoscale Pt-bimetallic alloy surfaces, Nat. Mat. 6 (2007) 241–247, https://doi.org/10.1038/nmat1840.

[57] L. Chen, M.C.Y. Chan, F. Nan, C. Bock, G.A. Botton, P.H.J. Mercier, B.R. MacDougall, Compositional and morphological changes of ordered $Pt_xFe_y$/C oxygen electroreduction catalysts, ChemCatChem 5 (2013) 1449–1460, https://doi.org/10.1002/cctc.201200614.

[58] H. Chen, Y. Yu, H.L. Xin, K.A. Newton, M.E. Holtz, D. Wang, D.A. Muller, H.D. Abruña, F.J. DiSalvo, Coalescence in the thermal annealing of nanoparticles: an in-situ STEM study of the growth mechanisms of ordered Pt–Fe nanoparticles in a KCl matrix, Chem. Mater. 25 (2013) 1436–1442, https://doi.org/10.1021/cm303489z.

[59] G. Willot, F. Gomez, P. Vast, V. Andries, M. Martines, Y. Messaddeq, M. Poulain, Preparation of zinc sodium polyphosphates glasses from coacervates precursors. Characterisation of the obtained glasses, and their applications, Compt. Rendu. Chem. 5 (2002) 899–906, https://doi.org/10.1016/S1631-0748(02)01454-6.

[60] R. Ropp, Inorganic Polymeric Glasses, Studies in Inorganic Chemistry, Elsevier Science, Amsterdam, 1992.

[61] M.A.P. Silva, D.F. Franco, A.R. Brandão, H.S. Barud, F.A. Dias Filho, S.J.L. Ribeiro, Y. Messaddeq, L.F.C. De Oliveira, Spectroscopic studies on glassy Ni(II) and Co(II) polyphosphate coacervates, Mater. Chem. Phys. 124 (2010) 547–551, https://doi.org/10.1016/j.matchemphys.2010.07.008.

[62] J.M.F. Navarro, El Vidrio, third ed., CSIC Press, Madrid, 2003.

[63] M. Farouk, F. Ahmad, A. Samir, Ligant field and spectroscopic investigation of cobalt doped erbium-zinc borate glasses, Opt. Quantum Electron. 51 (292) (2019) 1–12, https://doi.org/10.1007/s11082-019-2009-3.

[64] A.M. Abdelghany, H.A. Elbatal, R.M. Ramadan, The effect of $Li_2O$ and LiF on structural properties of cobalt doped borate glasses", J. King Saud Univ. Sci. 29 (2017) 510–516, https://doi.org/10.1016/j.jksus.2016.09.003.

[65] G. Barrera, P. Tiberto, P. Allia, B. Bonelli, S. Esposito, A. Marocco, M. Pansini, Y. Leterrier, Magnetic properties of nanocomposites, Appl. Sci. 9 (2019) 212, https://doi.org/10.3390/app9020212.

Ceramics International xxx (xxxx) xxx–xxx

Contents lists available at ScienceDirect

Ceramics International

journal homepage: www.elsevier.com/locate/ceramint

# Phosphate glasses containing monodisperse $Fe_{3-\delta}O_4$@$SiO_2$ stellate nanoparticles obtained by melt-quenching process

Juliane Resges Orives[a,*], Benoit P. Pichon[b], Damien Mertz[b], Kevin Sartori[b], Sylvie Begin-Colin[b], Wesley Renato Viali[a], Sidney J. Lima Ribeiro[a], Marcelo Nalin[a,**]

[a] São Paulo State University - UNESP, Institute of Chemistry, P. O. Box 355, Araraquara, SP, 14800-060, Brazil
[b] Université de Strasbourg, CNRS, Institut de Physique et Chimie des Matériaux de Strasbourg, UMR 7504, F-67000, Strasbourg, France

ARTICLE INFO

*Keywords:*
Glass
Coacervate
Iron oxide nanoparticles
Magnetic materials

ABSTRACT

The challenge to obtain stable glasses containing monodisperse magnetic nanoparticles with controlled size and shape is an exciting and almost unexplored field of research. Such new materials can be used in magneto-photonics or ultra-sensitive magnetic sensors. In this work, for the first time, colorless and transparent bulk glasses containing monodisperse 20 nm $Fe_{3-\delta}O_4$ nanoparticles were prepared by a melt-quenching route. Magnetic nanoparticles were synthesized by thermal decomposition and covered with a stellate mesoporous silica shell in order to protect them against dissolution during the glass melting process. The incorporation of nanoparticles into glasses and the ideal parameters obtained for this system are discussed. The new nanocomposite materials were characterized in order to investigate the structure, thermal, and magnetic properties. Such an original approach is a very promising way to incorporate a wide panel of nanoparticles, including metallic, bimetallic and metal oxide nanoparticles, into a variety of glasses providing new properties to these materials.

## 1. Introduction

Glasses has found a vast field of applications in the last century. The limits for technological applications of these extraordinary materials seem to reach far in the future [1–3]. Due to the high flexibility of these compositions and their simple preparation, glasses are suitable materials to host nanoparticles for different purposes.

The study of glasses containing magnetic nanoparticles has attracted attention due to their potential for magneto-optical materials, ultra-sensitive magnetic sensors, biocompatible glasses for use in hyperthermia, optical fibers with magnetic properties, waveguides, among others [4–15]. In addition, the incorporation of nanoparticles into dielectric materials is of great interest from a fundamental point of view for studies with femtosecond lasers in order to understand the interaction of light with these new kinds of 3D materials, since most of the studies in this field have been conducted on 2D thin films [16–19].

The main method used to obtain glasses containing nanoparticles consists of melting all of the precursors together, followed by a controlled heat treatment or laser irradiation in order to grow the desired crystalline phase on a nanoscale [20–23]. Although this method is highly efficient for generating nanocomposites, the main drawbacks are the growth of spurious crystalline phases, a lack of control of the size of the nanoparticles, and a lack of homogeneity [5,10,21–23].

Two methods have been used recently in the incorporation of nanoparticles via melt-quenching. In the first, the natural or synthesized nanoparticles are added to the glass precursors before melting [12–15,24–26] while in the second the glass melting process is started and the nanoparticles are added below the melting temperature of the nanoparticles [27,28]. The most interesting advantage of this approach is the possibility of exploring the nanoparticle synthesis, which makes possible a high control of size and shape, and then incorporating any type of nanoparticle with any type of property into a glass.

Vitreous materials, for the production of magneto-optical devices, must be stable and contain nanoparticles with a narrow size distribution that are dispersed homogeneously in the bulk. However, the preparation of materials with these characteristics is still a great challenge, because even using methods where the nanoparticles are prepared with size control and then incorporated into the glasses, this can result in the dissolution of the nanoparticles due to the high melting temperatures used to obtain the glasses [14,24,29,30].

Phosphate glasses have high transparency in UV–Vis range, low melting points, and low glass transition temperatures (Tg) when

* Corresponding author.
** Corresponding author.
*E-mail addresses:* juliane.resges@unesp.br (J.R. Orives), marcelo.nalin@unesp.br (M. Nalin).

https://doi.org/10.1016/j.ceramint.2020.01.257
Received 21 November 2019; Received in revised form 12 January 2020; Accepted 28 January 2020
0272-8842/ © 2020 Elsevier Ltd and Techna Group S.r.l. All rights reserved.

compared to silicate glasses [31,32]. These characteristics make phosphate glasses suitable for preparing these kinds of materials. In addition, low temperature phosphate bulk glasses can be obtained by coacervation, which consists of adding an electrolyte in a solution of sodium polyphosphate $(NaPO_3)_n$, under constant stirring [33].

The main advantage of the coacervation process is that it allows one to incorporate ions or nanoparticles in the polyphosphate gel chains at room temperature and then to dry or melt this material to obtain glasses with a low melting temperature (about 950 °C–1150 °C) [33–36]. This may be an advantage in avoiding the dissolution of nanoparticles into the glass material. The use of fully polymerized structures like $(NaPO_3)_n$ allows the production of very stable phosphate glasses [37].

In this work we report, for the first time, the incorporation of monodispersed core@shell magnetic nanoparticles with controlled size into a phosphate glass. The nanoparticles were covered by a layer of silica to protect the magnetic core during the melting.

## 2. Experimental section

### 2.1. Preparation of $Fe_{3-\delta}O_4@SiO_2$ nanoparticles

$Fe_{3-\delta}O_4$ nanoparticles were synthesized by thermal decomposition. Initially, $Fe(stearate)_3$ (2.04 mmol), squalene (20 mL), and oleic acid (6.69 mmol) were added to a two necked round bottom flask and the mixture was stirred at 130 °C during 1 h. The reaction medium was then heated with a heating rate of 5 °C $min^{-1}$ up to 370 °C and kept at this temperature for 120 min under air. After cooling down to room temperature, the nanoparticles were washed 12 times with a mixture of chloroform/acetone (1/5) followed by centrifugation (14 000 rpm, 10 min). An aliquot of the resulting black solution was taken out for characterization of the iron oxide nanoparticles.

Subsequently, the silica coating was performed by adding cetyltrimethylammonium p-toluenesulfonate (CTATos) (0.48 g) in distilled water (50 mL). This solution was stirred at 80 °C for 60 min for complete dissolution of CTATos. Trizma® base (110 mg) were added and the mixture was stirred for 15 min [34]. Then, $Fe_{3-\delta}O_4$ nanoparticles dispersed in chloroform (4 mg Fe $mL^{-1}$) was added. Finally, TEOS (4 mL) were added and the mixture was maintained at 80 °C under stirring for 120 min. The nanoparticles were washed in order to extract the remaining surfactant from the silica shell pores by adding $NH_4NO_3$ in ethanol (20 mg $NH_4NO_3$ $mL^{-1}$) 3 times. The resulting $Fe_{3-\delta}O_4@SiO_2$ particles were treated at 350 °C for 2 h.

### 2.2. Preparation of glass precursor

The coacervate gel was prepared by slowly mixing an equal volume of 4.0 M of $Na(PO_3)n$ and 2.0 M of $CaCl_2{\cdot}2H_2O$ solutions under constant stirring [33]. While mixing, a colloidal solution was formed and a phase separation was observed, evidencing the formation of the coacervate. Four samples (one without nanoparticles and three containing 8% in mass of IO@SiNPs) were prepared using the resultant coacervate.

### 2.3. Preparation of polyphosphate glasses (PGs)

After homogenization of the coacervate containing IO@SiNPs, the mixtures were transferred to alumina crucibles and heat treated at 350 °C for 2 h to remove residual water from the coacervate. After that, the samples were melted at 1000 °C at three different times (15, 45, and 75 min) and cast into a preheated stainless-steel mold at 340 °C.

### 2.4. Characterization techniques

The TEM, HR-TEM, and electron diffraction images of the nanoparticles and glasses were performed with a JEOL 2100 LaB operating at 200 kV with a 0.2 nm point to point resolution. Glass samples were prepared by grinding a piece of glass and dispersing it in 1 mL of isopropyl alcohol using ultrasound. Afterwards, some drops of the suspension were applied to a copper grid coated with a carbon film. The nanoparticle sizes were calculated from TEM images using the Image J software. The granulometry measurements of the $Fe_{3-\delta}O_4$ nanoparticle suspensions in chloroform were performed using a Malvern Zetasizer Nano ZS instrument. FTIR spectroscopy was performed using a PerkinElmer 2000 spectrophotometer in the frequency range $800-400\ cm^{-1}$. X-ray powder diffraction of the nanoparticles were carried out with a Bruker D8 Advance diffractometer equipped with a monochromatic radiative copper source ($CuK_\alpha$). The measurements were performed in rotation at a 2θ angle ranging from 20 to 80° with a step pass of 0.03°. The ground glass diffractograms were obtained using a Rigaku Geiger-Flex diffractometer with Cu-$K_{\alpha1}$ (λ = 1.54056 Å) radiation. Samples were supported on a glass sample holder and measurements were recorded in the range of 2θ from 20 to 80° with a step pass of 0.02°. The Energy Dispersive X-ray Fluorescence analysis was performed on a Shimadzu-Ray Ny spectrometer. Magnetic measurements were recorded using a SQUID magnetometer (Quantum Design MPMS-XL 5). Magnetization curves as a function of a magnetic field were measured at 5 and 300 K with magnetic field between -70 and 70 kOe. SEM was performed on the glass sample using a JEOL 6700 microscope equipped with a field emission gun operating at an accelerating voltage of 3 kV. DSC measurements were carried out using a NETZSCH - DSC404 F3 Pegasus to study the glass samples. Small pieces (typically 10 mg) were heated in a platinum crucible from 25 to 750 °C at a heating rate of 10 °C $min^{-1}$ under $N_2$ atmosphere (70 mL $min^{-1}$). The estimated errors are ± 2 °C for both Tg and Tx. Raman scattering spectra were recorded using a HORIBA Jobin Yvon model LabRAM HR micro Raman apparatus equipped with a 632.8 nm laser delivering 17 mW at room temperature in a frequency range from 200 to 1300 $cm^{-1}$.

## 3. Results and discussion

### 3.1. $Fe_{3-\delta}O_4@SiO_2$ nanoparticles

Fig. 1(a) shows the steps of the synthesis used to obtain the $Fe_{3-\delta}O_4@SiO_2$ Nanoparticles. First, the $Fe_{3-\delta}O_4$ magnetic nanoparticles were synthesized by the thermal decomposition method [38,39]. Later, the $Fe_{3-\delta}O_4$ nanoparticles were coated with a large pore stellate $SiO_2$ shell [40]. This approach was used with the aim of protecting the $Fe_{3-\delta}O_4$ core from dissolution during the melting of the material and also due to the suitable chemical compatibility between the silica interface and the phosphate glass [24].

High resolution transmission electron microscopy (HR-TEM) images presented in Fig. 2(a) show that spherical, slightly faceted, and well crystallized nanoparticles were obtained. The nanoparticles present crystalline planes with values of 0.209 nm, 0.297 nm, and 0.253 nm corresponding to the (400), (220), and (311) planes of the magnetite (JCPDS card n° 19-0629 SEE SI), respectively.

The narrow size distribution (20.1 ± 0.6 nm) and the monomodal distribution of hydrodynamic diameter ($D_h$) (22.7 nm), measured from TEM micrographs and granulometry, respectively, show the high stability of the nanoparticle suspension in chloroform (Fig. 2(b)). The difference between these values is because $D_h$ includes the organic shell, corresponding to the oleic acid molecules and the solvation sphere [34]. The nanoparticles were also characterized by IR spectroscopy, electron diffraction scattering (EDS), and X-ray diffraction (XRD) and more details can be seen in Fig. S1, Supporting Information).

The organic coated iron oxide nanoparticles were dispersed in chloroform in order to transfer them into an aqueous phase containing the surfactant: cetyltrimethylammonium p-toluenesulfonate (CTAToS). This surfactant acts as a stabilizer and a phase transfer agent for the nanoparticles coated with oleic acid and allows for the dispersion of the nanoparticles in water; this methodology was reported earlier [41,42].

Fig. 2(c) presents the TEM images of the $Fe_{3-\delta}O_4@SiO_2$

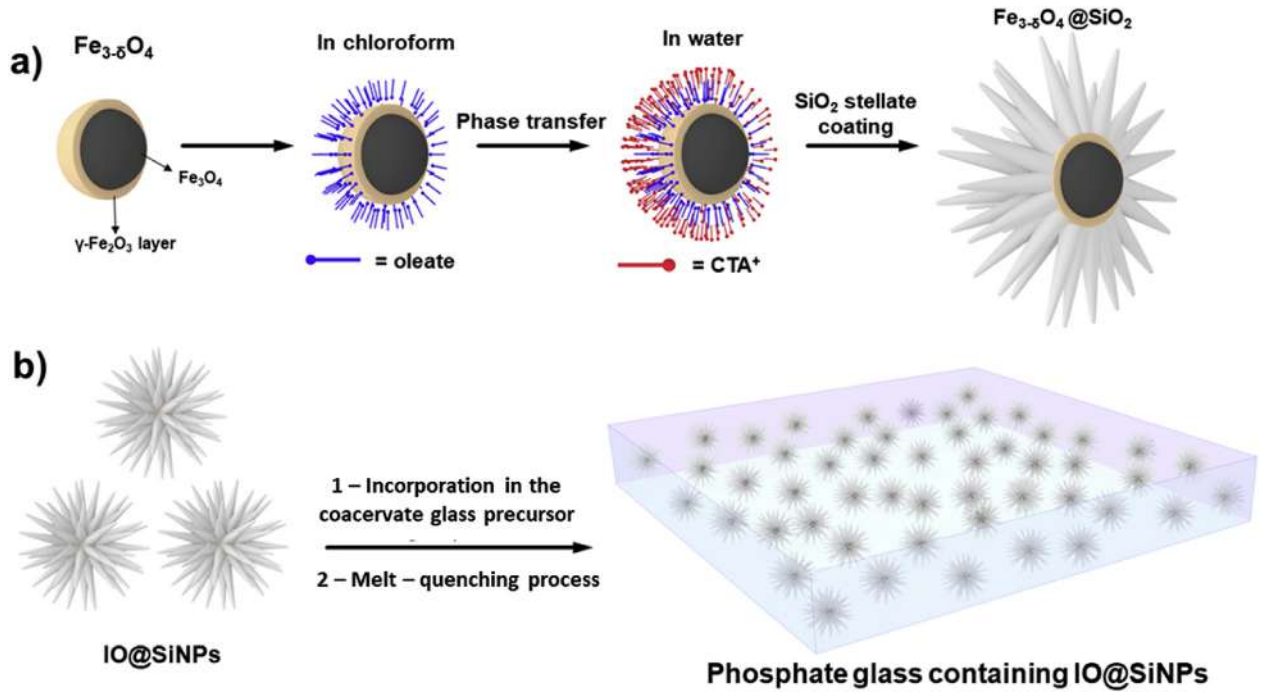


**Fig. 1.** Schematic illustration of **(a)** obtaining the $Fe_{3-\delta}O_4$@$SiO_2$ nanoparticles, **(b)** preparing the phosphate glasses containing monodisperse core@shell type nanoparticles.

nanoparticles obtained with stellate morphology. As observed in Fig. 2(d), the coating generates homogenously monodispersed nanoparticles with the size distribution centered at 99.4 ± 6.5 nm. The darker area in the center corresponds to the iron oxide nanoparticles with a size of approximately 20 nm, showing that it is preserved during the coating process. A thermal treatment at 350 °C for 2 h was carried out in order to eliminate the organic residues that were not extracted during washing. After this step, the nanoparticles were labelled as IO@

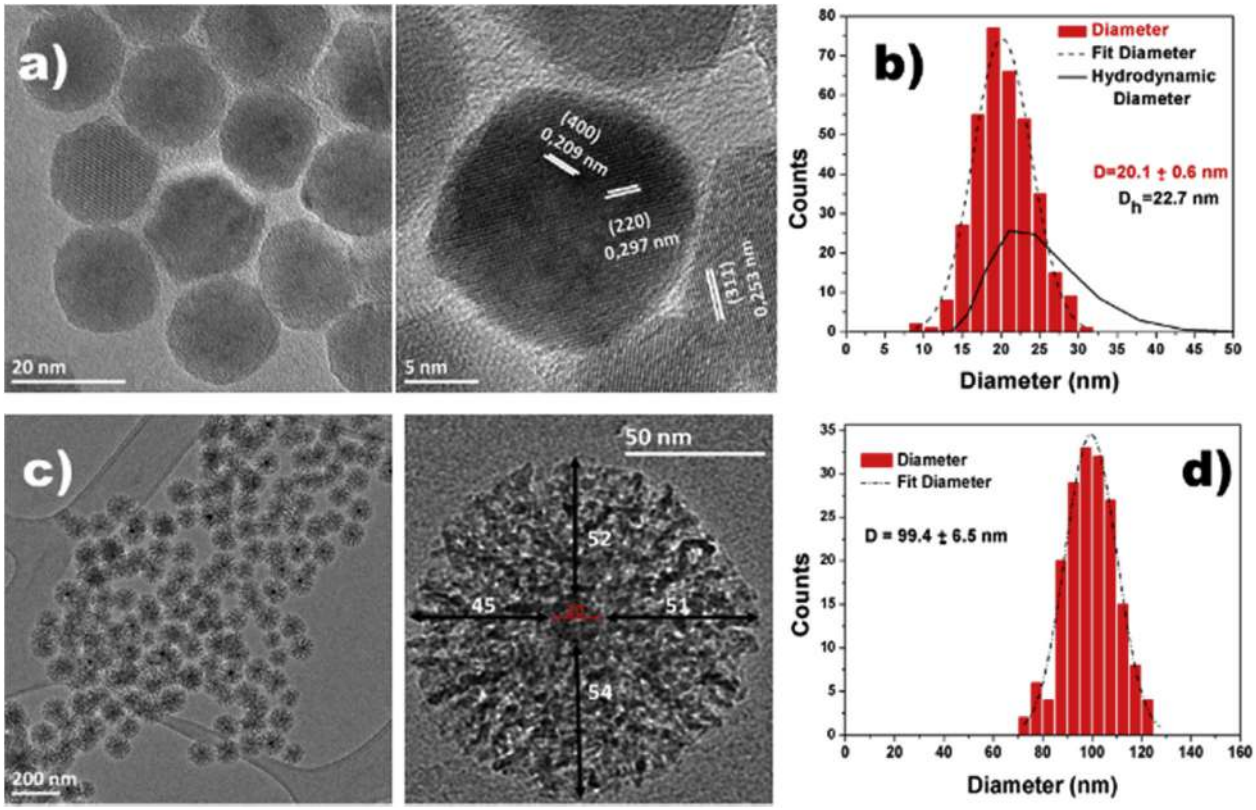


**Fig. 2. (a)** TEM micrograph of $Fe_{3-\delta}O_4$ nanoparticles (with scale of 20 and 5 nm). **(b)** Size distribution measured from a TEM micrograph and hydrodynamic diameter measured by granulometry from the nanoparticle suspension in chloroform. **(c)** TEM micrograph of $Fe_{3-\delta}O_4$@$SiO_2$ core–shell nanoparticles and **(d)** Size distribution of $Fe_{3-\delta}O_4$@$SiO_2$.

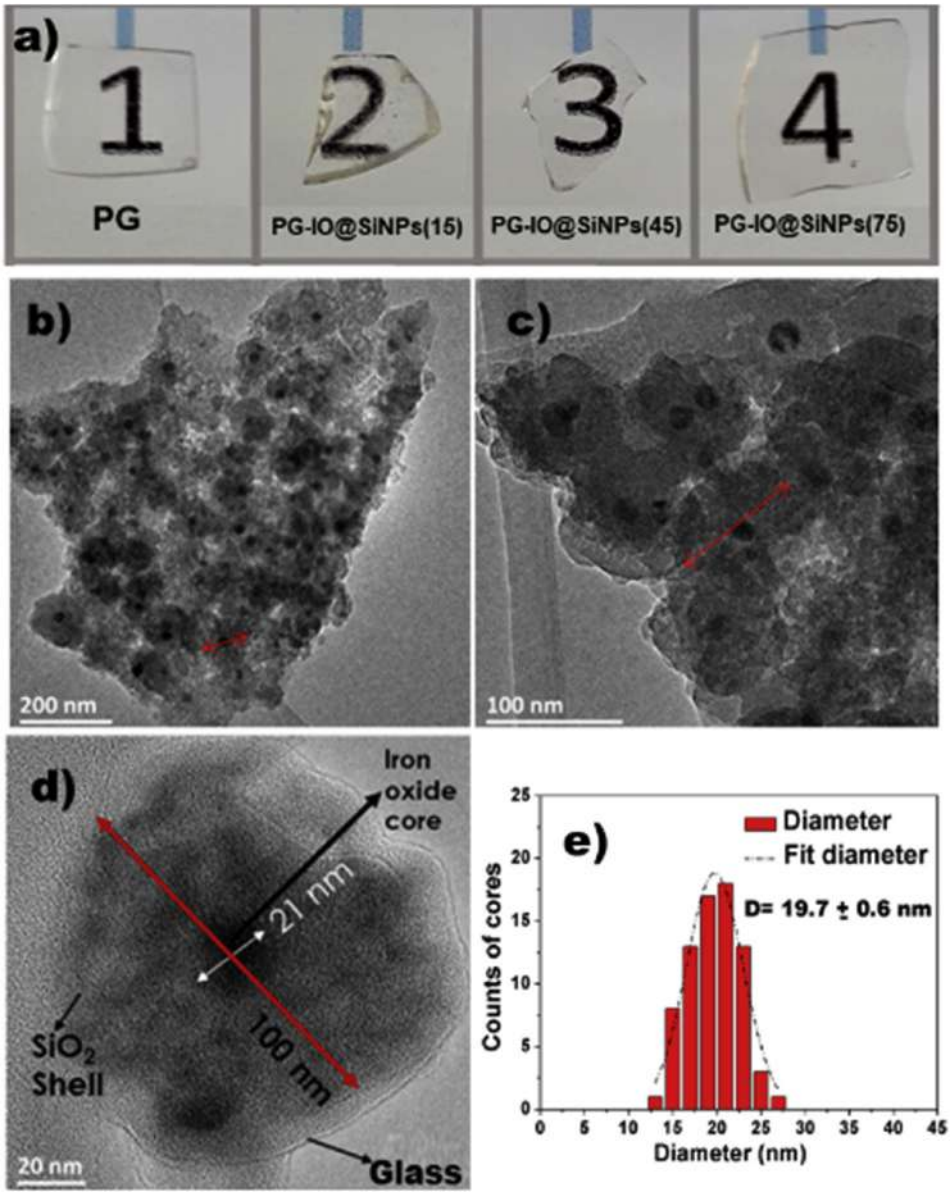


**Fig. 3.** (a) Pictures of PG and PGs-IO@SiNPs melted for 15, 45 and 75 min. **(b–d)** TEM micrographs of PG-IO@SiNPs(15) glass. **(e)** Histograms showing the size distribution of the iron oxide nanoparticles dispersed inside the glass.

SiNPs.

### 3.2. Phosphate glasses containing IO@SiNPs

For glass synthesis, the coacervate gel and IO@SiNPs (8% in mass) were mixed and melted at 1000 °C (Fig. 1(b)). Fig. 3(a) shows pictures of the phosphate glass without nanoparticles and of the three glasses containing 8% of IO@SiNPs that were melted during different times (15, 45, and 75 min); the samples were labelled as (PG-IO@SiNPs(15), PG-IO@SiNPs(45), and PG-IO@SiNPs(75), respectively). The samples showed no signs of hygroscopicity; they are transparent and totally colorless.

Sample PG-IO@SiNPs(15) presents very small bubbles which are attributed to the organic compounds and/or water that were not totally eliminated even after the extraction of surfactant and heat treatment of the nanoparticles. In the sample PG-IO@SiNPs(45), the amount of bubbles in the sample decreased significantly, and sample PG-IO@SiNPs(75) did not present bubbles. This shows that 75 min is long enough for the release of gases trapped within the glass precursor mixture.

Fig. 3(b-d) shows the TEM images of the PG-IO@SiNPs(15) sample, where it can be seen that the nanoparticles were efficiently dispersed in the phosphate glass without forming clusters. For this measurement, the sample was crushed and dispersed in isopropanol. A closer look allows one to identify a third contrast in the images, which is different from the iron oxide core and phosphate glass. As long as it corresponds to a phase with intermediate density, we assigned it to the silica shell used to protect the iron oxide nanoparticles. Furthermore, the size distribution of iron oxide nanoparticles (19.7 ± 0.6 nm) was preserved as shown by Fig. 3(e). This result is extremely interesting and proves that the size and shape of the $Fe_{3-\delta}O_4$ nanoparticles were preserved after their incorporation in the glass matrix. Therefore, the $SiO_2$ shell met the goal of protecting the core after melting for 15 min. The morphology of the PG-IO@SiNPs(15) sample was also investigated by scanning electron microscopy (SEM). Fig. 4(d) shows images magnified by 5000x and 20000x of the polished sample, it is possible to see spheres with size between 95 and 105 nm in the glass matrix. The images obtained by SEM are in agreement with the images obtained by TEM and corroborate with the fact that the nanoparticles coated with silica in a stellate

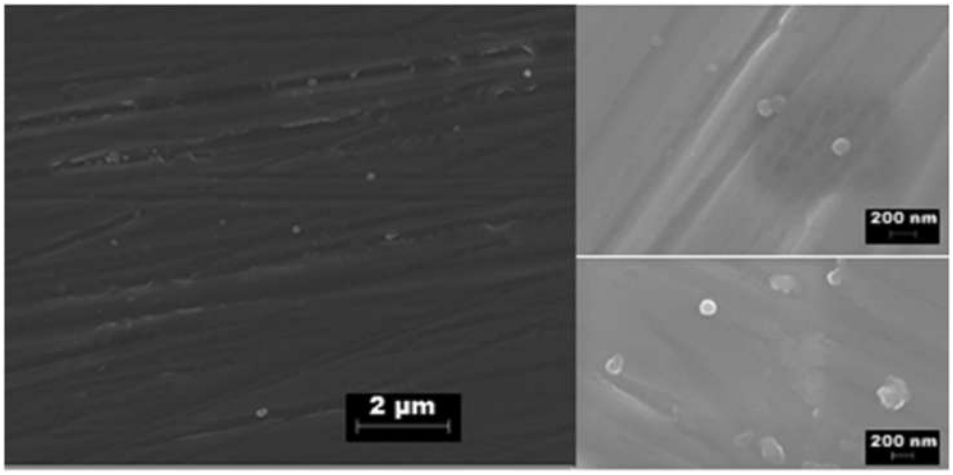


**Fig. 4.** SEM images of PG-IO@SiNPs(15) bulk sample with magnifications of 5 000x (image with 2 µm scale) and 20.000x (images with 200 nm scale).

morphology kept the spherical shape.

Samples obtained after melting for 45 and 75 min were also studied in order to determine whether the melting time could have any influence on the structure of the core-shell nanoparticles (Fig. S2). After 45 min, it is no longer possible to identify the silica shell, and the core size is no longer the same, as shown by the histogram plotted from the TEM images in which the average size was 9.4 ± 0.6 nm (Fig. S2(a)). For the sample PG-IO@SiNPs(75), the average size decreased to 4.3 ± 0.5 nm (Fig. S2(b)). This shows that the melting time is a decisive factor in preserving the core-shell structure of nanoparticles incorporated in the glass matrix.

The XRD patterns of nanocomposites presented only the diffraction halo characteristic of amorphous materials, showing that even introducing a considerable amount of nanocrystals (up to 8 wt %) into the glass matrix, which could easily cause instability and induce crystallization of the glass, there was no crystallization of the sample (see Fig. S3). Nanoparticle diffraction peaks were not observed due to the high dilution caused by dispersion in the phosphate matrix.

### 3.3. Raman of PG-IO@SiNPs

The glasses were studied by Raman spectroscopy (Fig. 5(a-b)). The addition of the nanoparticles resulted in a shift of the band at 1172 $cm^{-1}$ assigned to $\nu_s$(P-$O_{terminal}$) [43] to lower wavenumbers (1168, 1166, and 1165 $cm^{-1}$) and a shift of the band at 692 $cm^{-1}$ assigned to $\nu_s$(P–O–P) [43] to higher wavenumbers (694, 700, and 704 $cm^{-1}$) in the samples PG-IO@SiNPs(15), PG-IO@SiNPs(45), and PG-IO@SiNPs(75), respectively. The larger shifts for the samples melted for longer times indicate that the dissolved iron atoms were incorporated into the phosphate glass structure by means of P-$O_{terminal}$-Fe bonding, which causes a decrease in the electronic density of the P-$O_{terminal}$ bonds and an increase in the strength of the P–O–P bonds [43].

The insert of Fig. 5(a) shows a weak band at 1025 $cm^{-1}$ assigned to the Si–O–Si and P–O–Si linkage vibrations that contribute to this band [44]. The bands at 980 and 965 $cm^{-1}$ are assigned to stretches of non-bridging oxygens (Si-$O_{terminal}$) and the Si–O–Si–O–Si elongation, respectively [45].

A deconvolution was made in the region between 1350 and 1050 $cm^{-1}$ for the PGs containing nanoparticles (Fig. 5(b)). New bands were observed at 1135 (PG-IO@SiNPs(15)), 1038 VF PG-IO@SiNPs (45), and 1035 $cm^{-1}$ PG-IO@SiNPs(75) with areas of 28.6, 39.7, and 40, respectively. These bands are assigned to the stretches of the P–O–Si bonds [46]. These data show the increased formation of the novel P–O–Si bonds with increasing melting time. This is due to the dissolution of the silica layer and subsequent incorporation of the silicon atoms into the phosphate glass structure. The band at 1283 $cm^{-1}$ is attributed to P═O vibrations [45]. Since the composite (glass + IO@SiNP) remains transparent and homogeneous, it is believed that the formation of Si–O–P bonds can also contribute to the optical properties because they decrease the possibility of having a grain boundary and avoid drastic changes in the refractive index.

### 3.4. DSC of PG-IO@SiNPs

The characteristic temperatures of the glasses were studied by differential scanning calorimetry (DSC). Fig. 6 presents the heat flow curves as a function of the temperature for the prepared materials.

The glass transition temperatures (Tg) for samples PG-IO@SiNPs (15) and PG-IO@SiNPs(75) increased by 19 °C and 39 °C, respectively, when compared to pure PG (416 °C). The increase in the first case is attributed to the novel PO/$SiO_2$ interface at which P–O–Si bonds were formed. As the shells were dissolved in the sample PG-IO@SiNPs(75), a large amount of silicon and part of the iron was incorporated into the glass structure. This behavior has been observed when a phosphate glass is melted in a silica crucible and a percentage of silica is incorporated into the matrix[47]. This phenomenon increased the vitreous connectivity through bonds between two adjacent phosphate chains, so a higher temperature was required to bring the glass to the viscoelastic state [48,49].

The glass stability parameter (Tx-Tg) increased by about 70 °C for samples containing nanoparticles, from 154 °C in the PG to 227 °C in the PG-IO@SiNPs(15). This result shows that the silica layer significantly increased the stability of the phosphate glass against crystallization in addition to protecting the core during the melting step. This fact makes these glasses very interesting for applications in optical fibers or in devices that require thick bulk.

### 3.5. Magnetic characterization of IO@SiNPs and PG-IO@SiNPs(15)

The IO@SiNPs sample heated at 300 °C was magnetically characterized as a function of the applied magnetic field (Fig. 7(a-c)). The nanoparticles coated with silica present superparamagnetic behavior at 300 K and are ferromagnetic at 5 K. The value of saturation magnetization ($M_s$), measured in the applied field of 70 kOe, was 65 $emug^{-1}$. This demonstrates that the thermal treatment did not influences the magnetization significantly, because the value obtained is in accordance with that reported in the literature for 20 nm iron oxide nanoparticles [38]. It shows that the $SiO_2$ shell increases the thermal stability of the core structure preserving the oxidation of $Fe_3O_4$ to γ-$Fe_2O_3$ (maghemite) [50]. The sample presents a coercive field ($H_c$) of 136 Oe. Such value is lower when compared to $Fe_{3-\delta}O_4$ of 20 nm, reported in the literature, which presents $H_c$ of 325 Oe. This behavior can

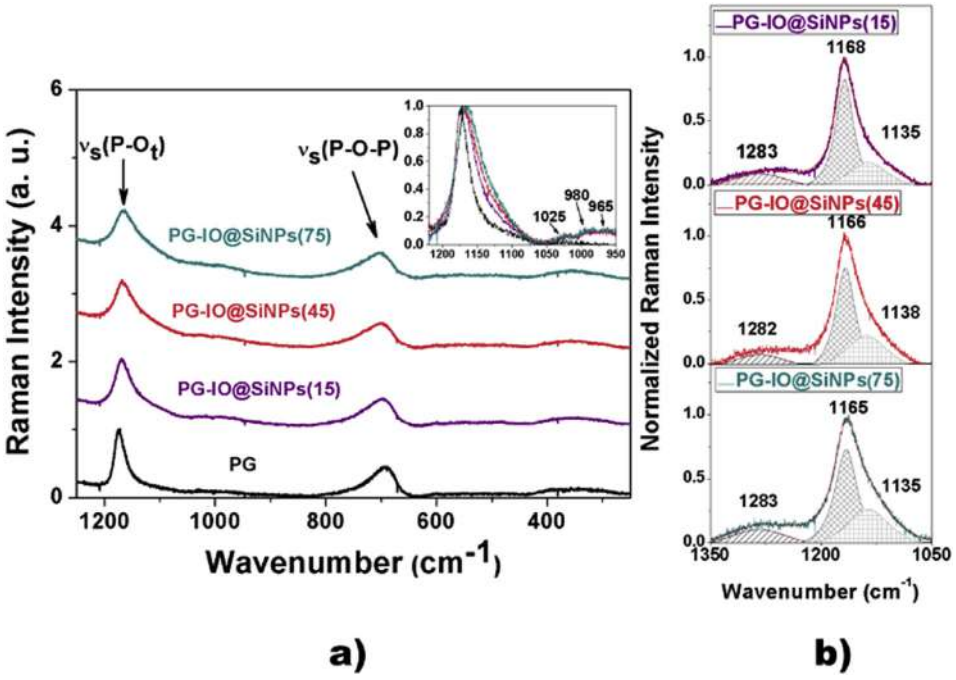


**Fig. 5.** Characterization of glasses with and without nanoparticles. **(a)** Raman spectra (the insert shows the zoom of the region between 1200 and 950 $cm^{-1}$), **(b)** Deconvolution of the region between 1350 and 1050 $cm^{-1}$ for samples melted at different times.

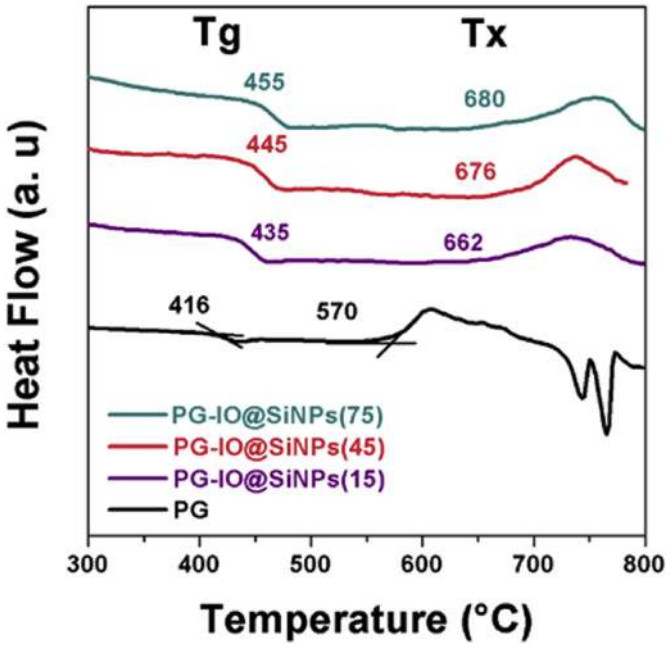


**Fig. 6.** DSC curves of glasses with and without nanoparticles.

be assigned to the total or partial phase change of magnetite to maghemite that may occur during the 2 h of heat treatment, because small degrees of non-stoichiometry can cause great changes in the $H_c$ [51].

The PG and PG-IO@SiNPs(15) samples were magnetically characterized at 300 K and 5 K (Fig. 7(d-e)). The magnetization of the sample was divided by the total mass of the glass, resulting in lower values due to the magnetic dilution caused by the phosphate matrix. The measurements at 300 K and 5 K showed a diamagnetic behavior for PG. For the sample PG-IO@SiNPs(15) a superparamagnetic signal with low magnetization was observed.

The magnetic properties obtained were different from the properties of the nanoparticles before their incorporation into the glass matrix. The results suggests that during the glass forming process the magnetite may be partially converted into maghemita. Moreover, the incorporation into a glass matrix significantly increases interparticle distances thus weakening dipolar interactions which become negligible [52,53].

The present results open a wide range of possibilities for exploring new functionalities for these hybrid glasses in the field of magneto-optics, photonics and magneto-photonics that can play a very interesting role in the development of magnetic sensors and materials useful for applications in magneto-optical devices. In addition, it is important to emphasize that this methodology can be used for other types of nanoparticles where size control is important such as in nanoparticle - rare earth energy transfer studies and nanoparticles with plasmonic properties, expanding thus, the range of studies in the area of glasses containing nanoparticles.

## 4. Conclusions

In summary, it has been proven that nanoparticles with controlled size and shape can be dispersed in glasses using the methodology of protection of the nanoparticles with a silica layer, as shown in the TEM and SEM images. The glasses, prepared for different times, showed that the melting time is a decisive factor in preserving the core-shell structure of nanoparticles within the glass. The structural and thermal investigations are in agreement and show that the incorporation of IO@SiNPs promotes the formation of new P–O–Si bonds conferring higher thermal stability to the phosphate glass, this feature is important for fabrication of optical devices. Our study provides useful information for further development of glasses containing nanoparticles for magneto-optical devices.

## Acknowledgements

The authors are grateful to the Brazilian funding agencies for the grants, CNPq (153762/2018-7), CAPES (88881.134870/2016-01) and São Paulo Research Foundation FAPESP (2013/07793-6, 2018/07727-7. 2019/19609-1).

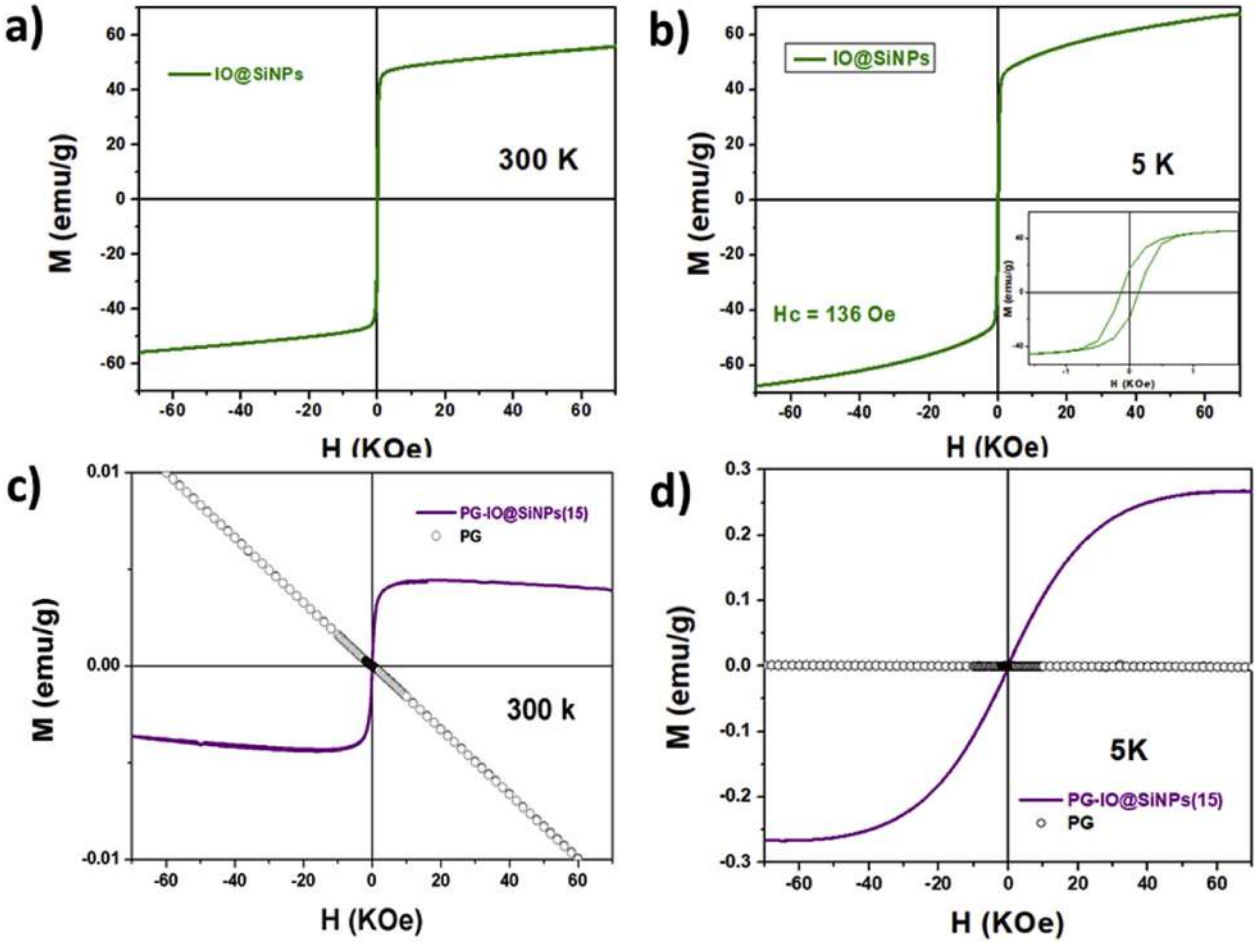


**Fig. 7.** Magnetic characteristics of IO@SiNPs and PG-IO@SiNPs(15) glass. Curves for nanoparticles. **(a)** M-H at 300 K, **(b)** M-H at 5 K. Curves for glass sample **(c)** M-H at 300 K and **(d)** M-H at 5 k.

## Appendix A. Supplementary data

Supplementary data to this article can be found online at https://doi.org/10.1016/j.ceramint.2020.01.257.

## References

[1] L. Wondraczek, J.C. Mauro, J. Eckert, U. Kühn, J. Horbach, J. Deubener, T. Rouxel, Towards ultrastrong glasses, Adv. Mater. 23 (2011) 4578–4586.
[2] J.C. Mauro, E.D. Zanotto, Two centuries of glass research: historical trends, current status, and grand challenges for the future, Int. J. Appl. Glass Sci. 5 (2014) 313–327.
[3] D.L. Morse, J.W. Evenson, Welcome to the glass age, Int. J. Appl. Glass Sci. 7 (2016) 409–412.
[4] Y. Wei, H. Ebendorff-Heidepriem, J. Zhao, Recent advances in hybrid optical Materials: integrating nanoparticles within a glass matrix, Adv. Opt. Mater. 7 (2019) 1900702.
[5] I. Edelman, J. Kliava, Oxide glasses with magnetic nanoparticles: transparent magnets (Faraday rotation and electron magnetic resonance studies), Phys. Status Solidi B 246 (2009) 2216–2231.
[6] J. Kliava, I. Edelman, O. Ivanova, R. Ivantsov, O. Bayukov, E. Petrakosvskaja, V. Zaikovskly, I. Bruckental, Y. Yeshurun, S. Stepanov, Formation and evolution of magnetic nanoparticles in borate glass simultaneously doped with Fe and Mn oxides, J. Appl. Phys. 104 (2008) 103917.
[7] P. Ji, Y. Wang, M. Zhang, B. Li, G. Zhang, $P_2O_5$-$Fe_2O_3$-CaO-$SiO_2$ ferromagnetic glass ceramics for hyperthermia, Int. J. Appl. Ceram. Technol. 15 (2018) 1261–1267.
[8] F. Bentivegna, M. Nyvlt, J. Ferré, J.P. Jamet, A. Brun, S. Visnovsky, R. Urban, Magnetically textured γ-Fe2O3 nanoparticles in a silica gel matrix: optical and magneto-optical properties, J. Appl. Phys. 85 (1999) 2270–2278.
[9] R. Berger, J. Kliava, J.C. Bissey, Magnetic resonance of superparamagnetic iron-containing nanoparticles in annealed glass, J. Appl. Phys. 87 (2000) 7389–7396.
[10] S. Woltz, C. Russel, Self-organized nano crystallinity of magnetite precipitated from a 4.9Na2O - 33.3CaO - 17.1Fe2O3 - 44.7B2O3 glass, J. Non-Cryst. Solids 337 (2004) 226–231.
[11] Q. Chen, L. Wan, Q. Chen, M. Zhang, Effect of magnetite nanoparticles doped glass with enhanced verdet constant for magnetic optical current transducer applications, Adv. Mater. Res. 271 (2011) 13–18.
[12] W. Widanarto, M.R. Sahar, S.K. Goshal, R. Arifin, M.S. Rohani, Effendi, Thermal, structural and magnetic properties of zinc-tellurite glasses containing natural ferrite oxide, Mater. Lett. 108 (2013) 289–292.
[13] W. Widanarto, M.R. Sahar, S.K. Goshal, R. Arifin, M.S. Rohani, K. Hamzah, Effect of natural Fe3O4 nanoparticles on structural and optical properties of Er3+ doped tellurite glass, J. Magn. Magn Mater. 326 (2013) 123–128.
[14] P. Anigrahawati, M.R. Sahar, S.K. Ghoshal, Influence of Fe3O4 nanoparticles on structural, optical and magnetic properties of erbium doped zinc phosphate glass, Mater. Chem. Phys. 155 (2015) 155–161.
[15] H.K. Farag, M.A. Marzouk, Preparation and characterization of nanostructured nickel oxide and its influence on the optical properties of sodium zinc borate glasses, J. Mater. Sci. Mater. Electron. 28 (2017) 15480–15487.
[16] C. Boeglin, E. Beaurepaire, V. Halté, V. López-Flores, C. Stamm, N. Pontius, H.A. Dürr, J.-Y. Bigot, Distinguishing the ultrafast dynamics of spin and orbital moments in solids, Nature 465 (2010) 458–461.
[17] B. Amirsolaimani, P. Gangopadhyay, A.P. Persoons, S.A. Showghi, L.J. LaComb, R.A. Norwood, N. Peyghambarian, High sensitivity magnetometer using nano-composite polymers with large magneto-optic response, Opt. Lett. 43 (2019) 4615–4618.
[18] J.-Y. Bigot, H. Kesserwan, V. Halté, O. Ersen, M.S. Moldovan, T.H. Kim, J.-T. Jang, J. Cheon, Magnetic properties of annealed core–shell CoPt nanoparticles, Nano Lett. 12 (2012) 1189–1197.
[19] J.-Y. Bigot, M. Vomir, Ultrafast magnetization dynamics of nanostructures, Ann. Phys. 525 (2012) 2–30.
[20] C. Worsch, M. Büttner, P. Schhf, R. Harizanova, C. Rüssel, F. Schmidl, P. Seidel, Magnetic properties of multicore magnetite nanoparticles prepared by glass crystallisation, J. Mater. Sci. 48 (2013) 2299–2307.
[21] J. Sheng, J. Zhang, L. Qiao, Long-term stability of X-ray induced color centers in silver-doped glass, J. Non-Cryst. Solids 352 (2006) 2914-2616.
[22] J. Zhang, W. Dong, J. Sheng, J. Zheng, J. Li, L. Qiao, L. Jiang, Silver nanoclusters formation in ion-exchanged glasses by thermal annealing, UV-laser and X-ray ir-radiation, J. Cryst. Growth 310 (2008) 234–239.
[23] K. Sharma, S. Singh, C.L. Prajapat, S. Bhattacharya, Jagannath, M.R. Singh, S.M. Yusulf, G.P. Kothiyal, Preparation and study of magnetic properties of silico phosphate glass and glass-ceramics having iron and zinc oxide, J. Magn. Magn Mater. 321 (2009) 3821–3828.

ARTICLE IN PRESS




[24] J.R. Orives, W.R. Viali, S.H. Santagneli, C.R.M. Afonso, M.H. Carvalho, A.J.A. Oliveira, M. Nalin, Phosphate glasses via coacervation route containing $CdFe_2O_4$ nanoparticles: structural, optical and magnetic characterization, Dalton Trans. 47 (2018) 5771-5579.

[25] Y. Zhou, D. Chen, W. Tian, Z. Ji, Monro, impact of $Eu^{3+}$ dopants on optical spectroscopy of $Ce^{3+}$:$Y_3Al_5O_{12}$-embedded transparent glass-ceramics, J. Am. Ceram. Soc. 98 (2015) 2445–2450.

[26] H. Nguyen, M. Tuomisto, J. Oksa, T. Salminen, M. Lastusaari, L. Petit, Upconversion in low rare-earth concentrated phosphate glasses using direct NaYF4:$Er^{3+}$,$Yb^{3+}$ particles doping, Scripta Mater. 139 (2017) 130–133.

[27] J. Zhao, X. Zheng, E.P. Schartner, P. Lonescu, R. Zhang, T.-L. Nguyen, D. Jin, H. Ebendorff-Heidepriem, Upconversion nanocrystal-doped glass: a new paradigm for photonic materials, Adv. Opt. Mater. 4 (2016) 1507–1517.

[28] M.R. Henderson, B.C. Gibson, H. Ebendorff-Heidepriem, K. Kuan, S. Afshar V, J.O. Orwa, I. Aharonovich, S. Tomljenovic-Hanic, A.D. Greentree, S. Prawer, T. M, Diamond in tellurite glass: a new medium for quantum information, Adv. Mater. 23 (2011) 2806–2810.

[29] N. Ojha, H. Nguyen, T. Laihinen, T. Salminen, M. Lastusaari, L. Petit, Decomposition of persistent luminescent microparticles in corrosive phosphate glass melt, Corrosion Sci. 135 (2018) 207–214.

[30] N. Ojha, T. Laihinen, T. Salminen, M. Lastusaari, L. Petit, Influence of the phosphate glass melt on the corrosion of functional particles occurring during the preparation of glass-ceramics, Ceram. Int. 44 (2018) 11807–11811.

[31] R.K. Brow, Review: the structure of simple phosphate glasses, J. Non-Cryst. Solids 263 (2000) 1–28.

[32] M. Karabulut, E. Melnik, R. Stefam, G.K. Marasinghe, C.S. Ray, C.R. Kurkjian, D.E. Day, Mechanical and structural properties of phosphate glasses, J. Non-Cryst. Solids 288 (2001) 8.

[33] D.F. Franco, D. Manzani, H.S. Barud, S.G. Antonio, L.F.C. Oliveira, M.A.P. Silva, S.J.L. Ribeiro, M. Nalin, Structural investigation of nickel polyphosphate coacervate glass - ceramics, RSC Adv. 6 (2016) 91150–91156.

[34] M.A. Silva, D.F. Franco, L.F.C. De Oliveira, New insight on the structural trends of polyphosphate coacervation processes, J. Phys. Chem. A 112 (2008) 5385–5389.

[35] P. Vast, F. Gomez, Optimization of the preparation of polyphosphate coacervates used as glass precursors, Phosphorus Res. Bull. 11 (2000) 61–68.

[36] G. Willot, F. Gomez, P. Vast, V. Andries, M. Martines, Y. Messaddeq, M. Poulain, Preparation of zinc sodium polyphosphates glasses from coacervates precursors. Characterisation of the obtained glasses, and their applications, Compt. Rendus Chem. 5 (2002) 899–906.

[37] R. Ropp, Inorganic Polymeric Glasses, Studies in Inorganic Chemistry, Elsevier Science, Amsterdam, 1992.

[38] W. Baaziz, B.P. Pichon, S. Fleutot, Y. Liu, C. Lefevre, J.M. Greneche, M. Toumi, T. Mhiri, S. Begin-Colin, Magnetic iron oxide nanoparticles: reproducible tuning of the size and nanosized-dependent composition, defects, and spin canting, J. Phys. Chem. C 118 (2014) 3795–3810.

[39] A. Demortière, P. Panissod, B.P. Pichon, G. Pourroy, D. Guillon, B. Donnio, S. Begin-Colin, Size-dependent properties of magnetic iron oxide nanocrystals, Nanoscale 3 (2011) 225–232.

[40] K. Zhang, L.-L. Xu, J.-G. Jiang, N. Calin, K.-F. Lam, S.-J. Zhang, H.-H. Wu, G.-D. Wu, B. Albela, L. Bonneviot, P. Wu, Facile large-scale synthesis of monodisperse mesoporous silica nanospheres with tunable pore structure, J. Am. Chem. Soc. 135 (2013) 2427–2430.

[41] K. Moller, J. Kobler, T. Bein, Colloidal suspensions of nanometer-sized mesoporous silica, Adv. Funct. Mater. 17 (2007) 605–612.

[42] L. Xiong, X. Du, B. Shi, J. Bi, F. Kleitz, S.Z. Qiao, Tunable stellate mesoporous silica nanoparticles for intracellular drug delivery, J. Mater. Chem. B 3 (2015) 1712–1721.

[43] M.A.P. Silva, D.F. Franco, A.R. Brandão, H. Barud, F.A.D. Filho, S.J.L. Ribeiro, Y. Messaddeq, L.F.C. De Oliveira, Spectroscopic studies on glassy Ni(II) and Co(II) polyphosphate coacervates, Mater. Chem. Phys. 124 (2010) 547–551.

[44] V.G. Plotnichenko, V.O. Sokolov, V.V. Koltashev, E.M. Dianov, On the structure of phosphosilicate glasses, J. Non-Cryst. Solids 306 (2002) 209–226.

[45] S. Agathopoulos, D.U. Tulyaganov, J.M.G. Ventura, S. Kannan, A. Saranti, M.A. Karakassides, J.M.F. Ferreira, Structural analysis and devitrification of glasses based on the CaO–MgO–SiO2 system with B2O3, Na2O, CaF2 and P2O5 additives, J. Non-Cryst. Solids 352 (2006) 322–328.

[46] N. Shibata, M. Horigudhi, T. Edahiro, Raman spectra of binary high-silica glasses and fibers containing GeO2, P2O5 and B2O3, J. Non-Cryst. Solids 45 (1981) 115.

[47] N. Sawangboon, A. Nizamutdinova, T. Uesbeck, R. Limbach, E. Meechoowas, K. Tapasa, D. Möncke, L. Wondraczek, E.I. Kamitsos, L.V. Wüllen, D.S. Brauer, Modification of silicophosphate glass composition, structure, and properties via crucible material and melting conditions, J. Appl. Glass. Sci. 11 (2020) 46–57.

[48] H. Said, R. Omrani, L.R. Arana, D.E. Bahri, S. Boussen, C. Bouzidi, H. Terraschke, A.H. Hamzaoui, A. M'nif, The effect of silica additive on the structural and luminescence properties of $Eu^{3+}$/$Tb^{3+}$ co-doped metaphosphate glasses, J. Mol. Struct. 1192 (2019) 42–48.

[49] P. Rajbhandar, L. Montagne, G. Tricot, Doping of low-Tg phosphate glass with $Al_2O_3$, $B_2O_3$ and $SiO_2$: Part I effect on glass property and stability, Mater. Chem. Phys. 183 (2016) 542–550.

[50] F. Chen, R. Shi, Y. Xue, L. Chen, Q.-H. Wan, Templated synthesis of monodisperse mesoporous maghemite/silica microspheres for magnetic separation of genomic DNA, J. Magn. Magn Mater. 322 (2010) 2439–2445.

[51] J.S. Salazar, L. Perez, O. Abril, L.T. Phuoc, D. Lhiawakrim, M. Vazquez, J.M. Greneche, S. Begin-Colin, G. Pourroy, Magnetic iron oxide nanoparticles in 10 – 40 nm range: composition in terms of magnetite/maghemite ratio and effect on the magnetic properties, Chem. Mater. 23 (2011) 1379–1386.

[52] S. Fleutot, G.L. Nealon, M. Pauly, B.P. Pichon, C. Leuvrey, M. Drillon, J.-L. Gallani, D. Guillon, B. Donnio, S. Begin-Colin, Spacing-dependent dipolar interactions in dendronized magnetic iron oxide nanoparticle 2D arrays and powders, Nanoscale 5 (2013) 1507–1516.

[53] D. Toulemon, B.P. Pichon, X. Cattoen, M.W.C. Man, S. Begin-Colin, 2D assembly of non-interacting magnetic iron oxide nanoparticles via “click” chemistry, Chem. Commun. 47 (2011) 11954–11956.

Journal of Non-Crystalline Solids 627 (2024) 122809

Contents lists available at ScienceDirect

Journal of Non-Crystalline Solids

journal homepage: www.elsevier.com/locate/jnoncrysol

# Nonlinear properties and structural rearrangements in thermally poled niobium germanate glasses

Lia Mara Marcondes [a,*], Juliane Resges Orives [a], Frederic Adamitez [d], Gael Yves Poirier [b], Thierry Cardinal [c], Marc Dussauze [d,*], Marcelo Nalin [a]

[a] Institute of Chemistry, São Paulo State University - UNESP, Araraquara, SP, Brazil
[b] Institute of Science and Technology, Federal University of Alfenas, Poços de Caldas-MG, Brazil
[c] Institut de Chimie de la Matière Condensée de Bordeaux, Université de Bordeaux, 87 Avenue du Dr Schweitzer, F-33608, Pessac, France
[d] Institut des Sciences Moléculaires, UMR 5255, Université de Bordeaux, 351 cours de la Libération, 33405 Talence Cedex, France

ARTICLE INFO

*Keywords:*
Glass
Thermal poling
Nonlinear optics

ABSTRACT

Second order nonlinear optical properties and structural rearrangements in $GeO_2$–$Na_2O$—$Nb_2O_5$ glasses were achieved by thermal poling. The effects of applied voltage as well as sodium and niobium contents on nonlinear optical (NLO)-active layer were investigated. Structural rearrangements in the anodic microlayer were investigated and occur due to sodium depletion promoting variation in bridging/non-bridging oxygen ratio and formation of a more polymerized network. Quantitative analysis of second harmonic generation signals confirm the electrooptical origin of the nonlinear optical response described by the electric-field-induced second harmonic model. $\chi^{(2)}$ susceptibility values range from 0.42 to 0.76 pm/V depending on the niobium content. Lastly, the charge compensation mechanism with increasing applied voltage was described in detail. A progressive decrease in $\chi^{(2)}$ for higher voltages was observed due to a greater poled thickness than expected by classical electrostatic models. In this case, the compensation mechanism occurs due to structural rearrangement, redox reactions, and motion of negative charges.

## 1. Introduction

Glassy materials as based materials for photonic devices have been increasingly highlighted due to the simple manufacture and the possibility of adjusting the composition, which consequently allows the adjustment of specific properties [1–3]. Glasses feature a high transmission window [4,5] and a wide variety of sizes and shapes such as cylindrical [6–8] and ribbon [9] fibers, bulk [10], powders [11] and thin films [12,13]. Furthermore, despite their isotropic nature, these materials may exhibit second order nonlinear optical susceptibility ($\chi^{(2)}$) by locally breaking the centrosymmetry using techniques such as thermal [14,15] and optical [16,17] poling. In this perspective, implemented nonlinear optical (NLO) properties and wide glass-based matrix transmission window have been promising for NLO photonic applications as wavelength conversion [18,19] and electro-optical devices [20].

Thermal poling process started in 1969 [21] and is a simple and low cost surface modification technique. By this technique, a non-crystalline material is heated, and a DC electric field is applied, resulting in modification of the anodic surface of the material [22]. The NLO responses after thermal poling was only reported more than twenty years later [23] and occurs due to a break of centrosymmetry associated with the space charge formation and a resulting static electric field [22]. In more detail, an effective second order optical susceptibility is induced by an electrooptical effect, coming from the interaction of a permanent implemented static electric field ($E_{stat}$) and the third order non-linear susceptibility $\chi^{(3)}$, according to the relationship $\chi^{(2)} = 3.\chi^{(3)}.E_{stat}$ [24–26].

NLO properties in thermally poled glasses have been studied in various glass systems covering pure silica [23], silicate [24,25], phosphate [27], germanate [28], sulfide [29], for example. Niobium germanate glasses are considered promising due to their transparency in a large spectral range including the mid-IR [30] and NLO properties of glasses with highly polarizable $NbO_6$ polyhedra [31]. These matrices have a mixed $GeO_4$–$NbO_6$ network and the high $Nb_2O_5$ content allows the formation of $NbO_6$ clusters [32] enhancing NLO properties [31,33]. Regarding the high efficiency of NLO devices, other dielectric crystalline

* Corresponding authors at: Instituto de Química, Universidade Estadual Paulista Júlio de Mendonça Filho – UNESP, Rua Prof. Franscisco Degni, 55 – Quitandinha - Araraquara, SP, Brazil - CEP 14800-060.
*E-mail addresses:* lia-marcondes@hotmail.com (L.M. Marcondes), marc.dussauze@u-bordeaux.fr (M. Dussauze).

https://doi.org/10.1016/j.jnoncrysol.2023.122809
Received 13 September 2023; Received in revised form 13 December 2023; Accepted 25 December 2023
Available online 13 January 2024
0022-3093/© 2024 Elsevier B.V. All rights reserved.

materials such as lithium niobate $LiNbO_3$ are commonly used for optical signal processing and nonlinear frequency conversion [34] but require complex fabrication and predetermined design of crystalline materials that prevents future applications such as fiber optics, for example. NLO properties induced by thermal poling in germanate glasses has not been much explored. Recently, $70GeO_2$–$20Ta_2O_5$–$10Na_2O$ glass composition has been reported with a $\chi^{(2)}$ susceptibility of 0.3 pm/V [35]. For niobium matrices, the $50GeO_2$–$25Nb_2O_5$–$25K_2O$ [36] and $52GeO_2$–$28Nb_2O_5$–$20K_2O$ [29] glasses were described with 0.003 and 0.6 pm/V values, respectively.

In this paper, besides studying the effect of sodium and niobium contents on the NLO response of $GeO_2$—$Nb_2O_5$—$Na_2O$ glasses with up to 25mol% of $Nb_2O_5$, the effect of the applied voltage during treatment was investigated. The polarization mechanisms were identified and discussed in detail, based on structural, Na-depletion thickness and SHG data. It has revealed a significant difference from classical models predictions which could be related to a strong influence of the negative charge motions mechanisms on the poling process efficiency. Finally, a successful test of microstructure design using an electrode structured by laser irradiation was demonstrated.

## 2. Experimental part

(100-x-y)$GeO_2$-x$Nb_2O_5$-y$Na_2O$ glasses with $x = 15$, 20 and 25 mol% and $y = 10$ and 15 mol% were synthesized using conventional melt-quenching and the glass compositions of the ternary system are described in Table 1. The samples were labeled as xNbyNa, with x and y according to the molar compositions. The glasses were prepared using high purity analytical grade chemicals. The raw materials were $GeO_2$ (Fox-Chemicals 99.999 %), $Nb_2O_5$ (Alfa Aesar 99.9985 %) and $Na_2CO_3$ (Alfa Aesar 99.95 %). A batch of 15 g of raw materials was homogenized in a mortar and melted in a pure Pt crucible at 1500 °C for 1 h. The melt was cast into a stainless-steel mold and then annealed at 500 °C for 6 h to release internal mechanical stress. The samples were cut and optically polished using alumina suspensions with particle sizes of 20, 9, and 3 μm. The pictures of all samples are shown in the Fig. 1 inset.

For thermal poling treatment, a piece of silicon wafer was used as cathode and a soda-lime silicate glass ($0.5 \times 0.5 \times 0.1$ $cm^3$) with deposited Pt film of 100 nm was used as anode (the anode was covered by a gold conductive thin film to ensure conductivity). The system was assembled using the cathode, a borosilicate coverslip to preserve the optical quality of the sample at the cathode side, the sample and finally the anode; the system was pressed with springs. Thermal poling was performed under a flow of $N_2$ atmosphere at 6 $L.min^{-1}$ at 265 °C using a heating rate of 15 °C/min. Once the temperature is stabilized, DC voltages (900, 1200 or 1500 V) were applied with a rate of 300 V/min for 30 min. After this time, the heating system was turned off, with the direct current (DC) field remaining until the temperature was close to room temperature. The optical absorption spectra were recorded using an Agilent Cary 5000 spectrophotometer in the wavelength region 200–2500 nm and Bruker Equinox 55 in the wavelength region 2500–25,000 nm. DSC analysis were obtained employing a DSC calorimeter STA 449 F3 Júpiter from Netzsch in the temperature range of 200 to 1000 °C, using Pt crucibles under a flow of $N_2$ atmosphere at 50 $cm^3.min^{-1}$ with a heating rate of 10 °$C.min^{-1}$. Linear refractive indices were measured using Brewster's angle method at 532, 639, 785 and 935 nm and the dispersion of the indices fitted by a Cauchy fit [37]. Density measurements were determined by Archimedes method using diethylphthalate at room temperature. Micro-Raman and micro-SHG correlative measurements were collected using a modified Jobin-Yvon Horiba-HR800 spectrometer equipment with a laser operating at 532 nm for Raman and a picosecond pulse laser at 1064 nm for SHG measurements [35]. Measurements were carried out on the surface and on the cross-section of the poled glasses. The objective 100x with a numerical aperture of 0.9 was used for Raman and SHG measurements. IR spectra were recorded by IR reflectance on a Fourier Vertex 70 V spectrometer with 200 scans and 2 $cm^{-1}$ of spectral resolution, the absorbance spectra were calculated by the Kramers-Krönig analysis [38]. The Secondary ion mass-spectrometry (SIMS) were performed on a PHI Adept 1010 dynamic SIMs system. This technique consists of bombarding a surface with beams of ions and the ionized material is analyzed by a mass spectrometer to determine its composition. In this way, the qualitative distribution of the elements was analyzed, and the etching rate was calculated considering the depth of the crater measured by optical profilometry. Finally, the second order nonlinear optical susceptibilities ($\chi^{(2)}$) were quantified using the Maker fringes technique in transmission mode using incident nanosecond laser at 1550 nm. θ-scan and ψ-scan measurements were made as a function of the incident angle with fixed harmonic polarization p (horizontally) or s (vertically); or as a function of the polarization of the incident beam with fixed incident angle and fixed polarization at the analyzer, respectively [35]. Quartz z-cut plate was used as reference for the calibration of the SHG setup and simulated data from general matrix formulation of linear and nonlinear optical responses [39].

## 3. Results

$GeO_2$-x$Nb_2O_5$-y$Na_2O$ ternary glass compositions were obtained by varying the sodium and niobium content. The niobium insertion limit is due to the low $Nb_2O_5$ solubility in the germanate liquid phase resulting in a liquid-liquid phase separation and spontaneous crystallization of the melt under cooling. The addition of 15 mol% of $Na_2O$ improves the $Nb_2O_5$ solubility in the germanate matrix up to 25 mol% of $Nb_2O_5$. This content of 25 mol% of $Nb_2O_5$ is higher than previously reported for alkali germanate glasses with 10mol% of potassium oxide [32]. Fig. 1 illustrates the wide transmission window from 0.4 to 5.2 μm with high transparency of around 80 % with two absorption bands at around 2.9 μm and 4.3 μm attributed to the vibrations of Ge-O-H bond [40].

Fig. 2 presents the refractive index and thermal data of all samples and Table 1 summarizes these data together with density values. An almost linear increase in density, refractive index and glass transition temperature occurs with higher niobium content as demonstrated in Fig. 3. Comparing the 15Nb10Na and 15Nb15Na samples also leads to an increase in the density and refractive index. Both compositions are below the level described for the effect known as germanate anomaly effect to occur [41]. Furthermore, for these samples, not only does the sodium concentration increase, but the Nb/Ge ratio variation also occurs as shown in Table 1 and the niobium content may be responsible for the observed changes. However, the sodium addition clearly influences the thermal stability parameter against crystallization ($\Delta T = Tx\text{-}Tg$, where Tg is a glass transition temperatures and Tx is onset of crystallization, Table 1) which increases from 85 °C to 134 °C. Glasses with high thermal stability are interesting for optical fibers manufacturing because they can prevent crystallization processes in the manufacturing process for

**Table 1**
Nominal molar composition, optical properties, density, and thermal stability against crystallization of sodium niobium germanate glasses.

| Sample | Molar composition | n (639 nm) | d ($g.cm^{-3}$) | Nb/Ge (at.%) | Na/(Nb+Ge) (at.%) | Tx-Tg ( °C) |
|---|---|---|---|---|---|---|
| 15Nb10Na | $75GeO_2$–$15Nb_2O_5$–$10Na_2O$ | 1.786 | 3.970 | 0.40 | 0.190 | 85 |
| 15Nb15Na | $70GeO_2$–$15Nb_2O_5$–$15Na_2O$ | 1.799 | 4.011 | 0.43 | 0.300 | 134 |
| 20Nb15Na | $65GeO_2$–$20Nb_2O_5$–$15Na_2O$ | 1.848 | 4.096 | 0.61 | 0.274 | 108 |
| 25Nb15Na | $60GeO_2$–$25Nb_2O_5$–$15Na_2O$ | 1.911 | 4.127 | 0.83 | 0.273 | 49 |

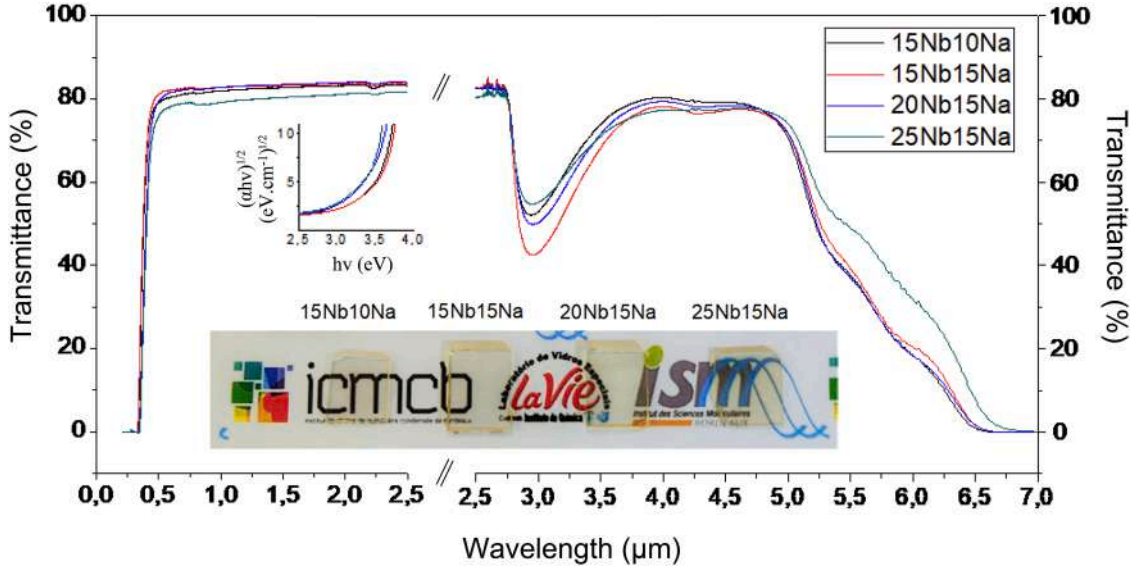


**Fig. 1.** Optical window of sodium niobium germanate glasses in the UV–Vis-MIR range and the pictures of all glass samples are shown in inset.

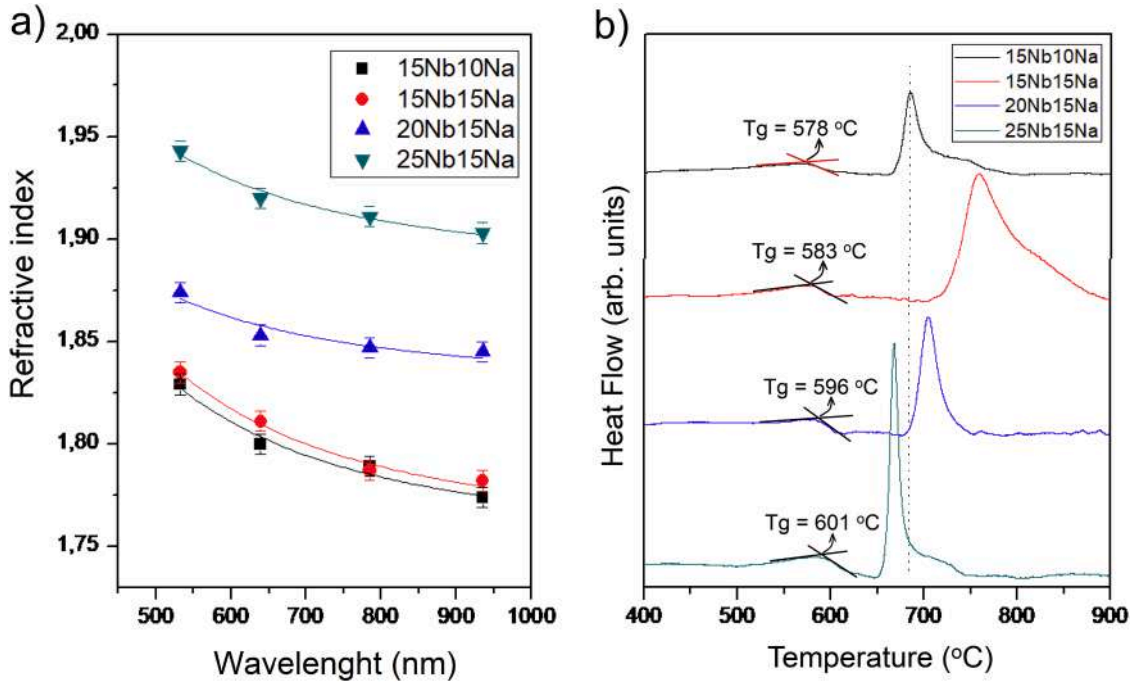


**Fig. 2.** (a) Refractive index dispersion of sodium niobium germanate glasses (the lines correspond to Cauchy fits) and (b) DSC curves.

fiber drawing.

All samples were subjected to thermal poling treatment at 265 °C and 1200 V and the 15Nb10Na sample at different DC voltages of 900, 1200 and 1500 V. Fig. 4(a) and (b) depict the thermal poling system assembly and the current curve as a function of thermal poling time, respectively. The current curve presented a typical profile of a successful thermal poling procedure [42]. Fig. 4(c) exhibits the SIMS profiles of 15Nb10Na sample after poling treatment at 900 V and describes the depth of the Na-depleted layer. As noted, the Na-depleted layer thickness is 2.42 ± 0.05 μm. The subanodic layer thicknesses of all samples are detailed in Table 2. The subanodic layer thickness almost doubles with increasing voltage from 900 to 1500 V and tends to increase with niobium content for the same voltage.

Fig. 5(a) and 5(b) present the infrared spectra of the samples before and after poling. In these spectra, two main absorption regions attributed to vibrations in germanate glasses are observed. An absorption region around 800–900 $cm^{-1}$ assigned to antisymmetric stretching of $GeO_4$ tetrahedra containing non-bridging and bridging oxygens and a second absorption region around 420–600 $cm^{-1}$ related to a symmetric stretching modes of Ge-O-Ge bridging bonds [43]. The bands in the region of 300 and 580–800 $cm^{-1}$ are assigned to the bending and stretching Nb-O(-Nb) bond [44], respectively. In general, some modifications with the niobium and sodium content are observed in Fig. 5(a). The increase in niobium content leads to a clear increase in the band at 610 $cm^{-1}$ assigned to the vibrational modes of the Nb-O-Nb bonds in $NbO_6$ units. Regarding the sodium content, a comparison between the 15Nb10Na and 15Nb15Na sample spectra shows that the sample with less sodium has a band around 800–900 $cm^{-1}$ wider in the 880 $cm^{-1}$

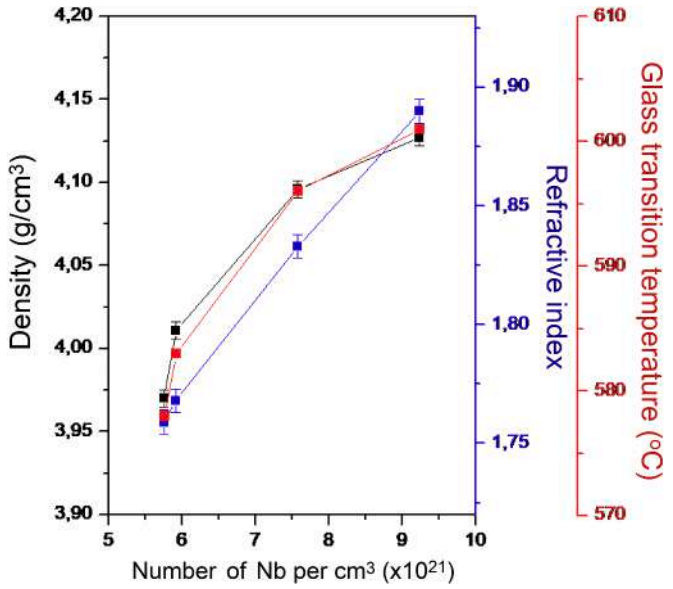


**Fig. 3.** Density, refractive index at 1550 nm and glass transition temperatures as a function of the niobium volume concentration.

region assigned to antisymmetric stretching of Ge-O bonds in $Q_4$ units without non-bridging oxygens (NBO), while the relative intensity of the band around 800 $cm^{-1}$ assigned to antisymmetric stretching of Ge-O bonds in $Q_3$ units, i.e. with one NBO bond and three bonding oxygen bridging two germanium ions, decreases. The same trend but to a greater magnitude is identified in the spectra of samples before and after thermal poling as shown in Fig. 5(b). A clear inversion between the bands at 805 and 880 $cm^{-1}$ is demonstrated.

Raman spectra of the mixed niobium-germanate network are shown in Fig. 6(a) and have among their main bands: (1) a band around 470 $cm^{-1}$ assigned to antisymmetric stretching of due to the Ge-O-Ge bond [45], (2) a band around 600 $cm^{-1}$ attributed to vibrational modes of non-distorted $NbO_6$ units [46], like perovskite crystals constituted by a 3D network of corner-sharing $NbO_6$ units, (3) a band at 770 $cm^{-1}$ associated with the vibrations of the distorted $NbO_6$ octahedra [47] and antisymmetric stretching of Nb-O(-Ge) bond [46] and finally, (4) a band at 880 $cm^{-1}$ assigned to the $NbO_6$ with NBO bonds [48,49]. Furthermore, around 860 $cm^{-1}$ a band referring to the asymmetric stretching of $GeO_4$ [50] also appears but is active mainly in the IR. Thus, the region at 600–800 $cm^{-1}$ is attributed to vibrational modes of $NbO_6$ octahedra without NBO bonds where the lower distortion degree appears at lower frequency. As described in the IR data for samples with different niobium contents, the niobium addition increases the band at 600 $cm^{-1}$

**Table 2**
Post-poling Na-depleted layer thickness and second order optical susceptibility $\chi^{(2)}_{zzz}$ value of sodium niobium germanate glasses determined by Maker fringes.

| Sample | Applied voltage (V) | Poled layer (μm) | $\chi^{(2)}$ (pm/V) |
|---|---|---|---|
| 15Nb10Na | 900 | 2.42 ± 0.05 | 0.42 ± 0.04 |
| 15Nb10Na | 1200 | 3.22 ± 0.05 | 0.39 ± 0.04 |
| 15Nb10Na | 1500 | 4.26 ± 0.05 | 0.33 ± 0.03 |
| 15Nb15Na | 1200 | 3.31 ± 0.05 | 0.42 ± 0.04 |
| 20Nb15Na | 1200 | 4.04 ± 0.05 | 0.60 ± 0.06 |
| 25Nb15Na | 1200 | 3.95 ± 0.05 | 0.76 ± 0.08 |

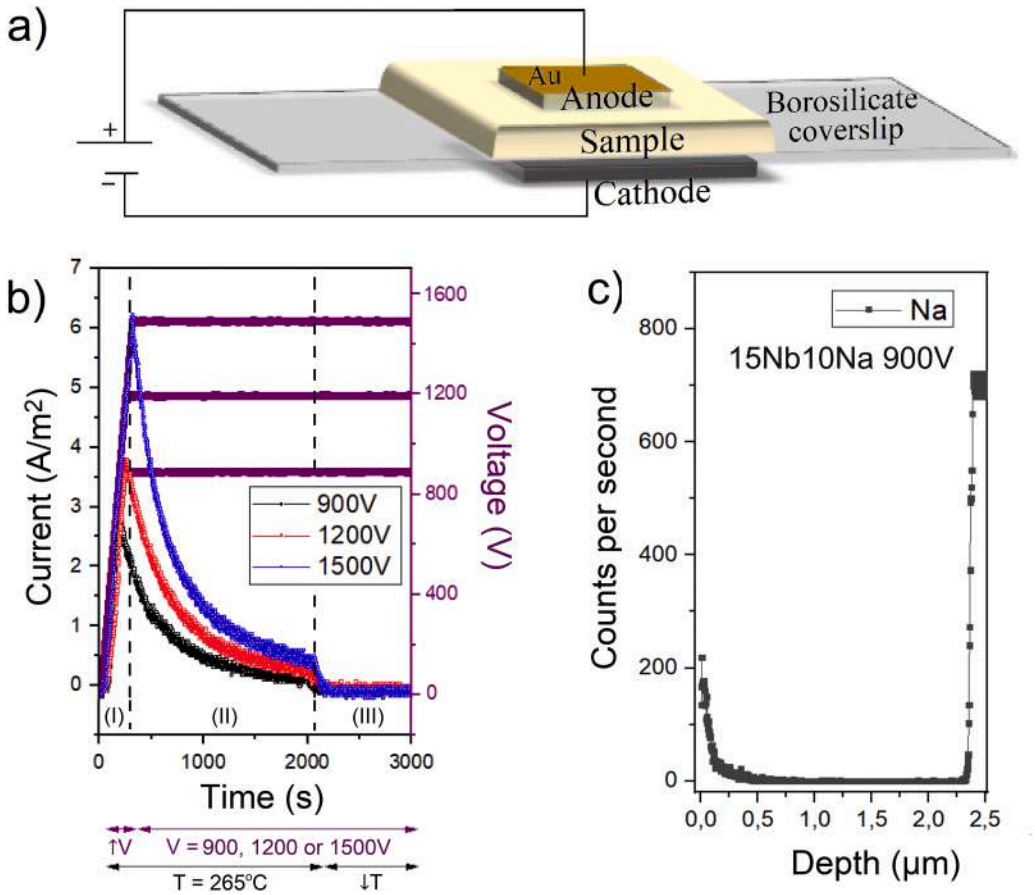


**Fig. 4.** (a) Thermal poling system assembly, (b) recorded voltage and current curves during thermal poling treatment and (c) SIMS depth profile after poling of sodium content in 15Nb10Na samples at 900 V.

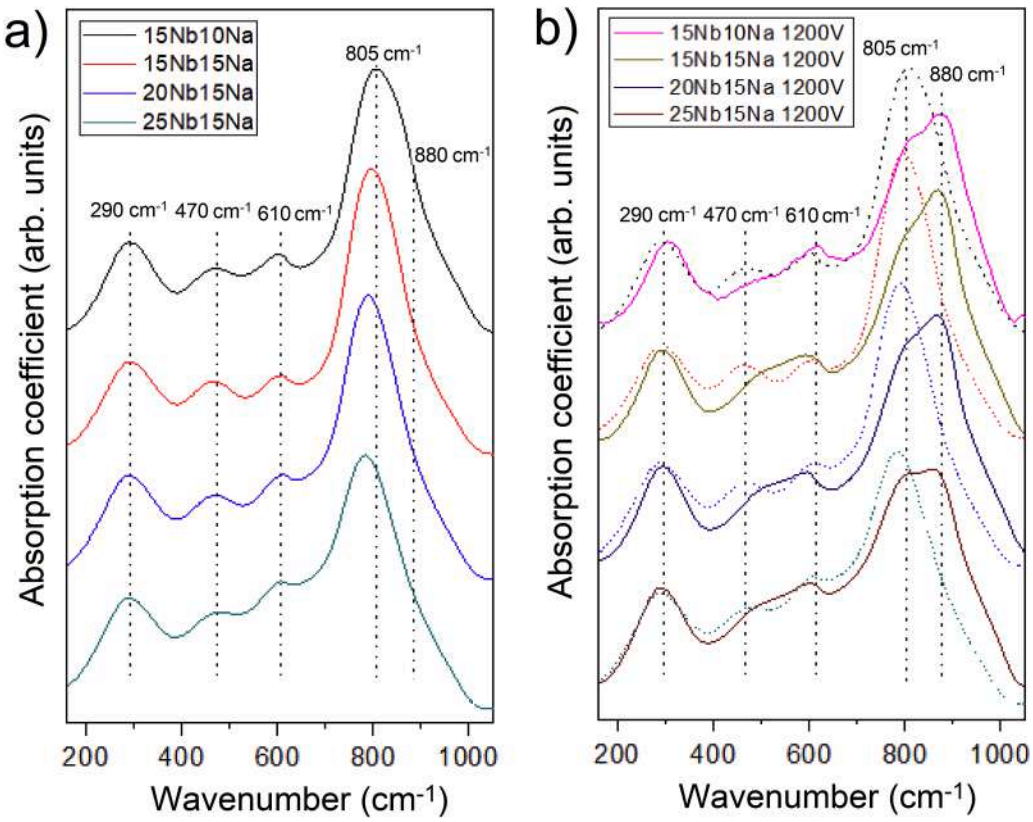


**Fig. 5.** Absorption coefficients obtained by the reflectance spectra Kramers-Krönig transformation of the samples (a) before and (b) after thermal poling of sodium niobium germanate glasses.

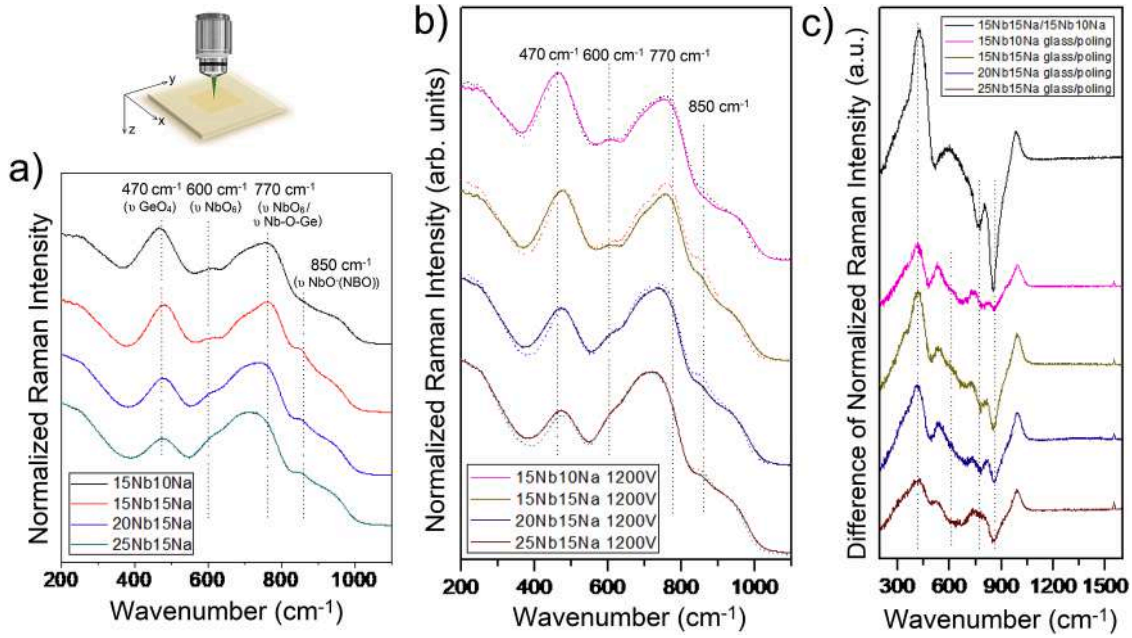


**Fig. 6.** Raman spectra top view of the samples (a) before and (b) after thermal poling; and (c) Raman spectra difference corresponding to the spectra of the highest sodium content glass (15Nb15Na) subtracted from the smallest content glass (15Nb10Na), and the others referring to the spectra of the glass without poling subtracted from the spectra of the poled zone.

due to the formation of interconnected $NbO_6$ units and, in the Raman spectra, there is an increase in the band around 600 $cm^{-1}$ and also a shift from 763 to 709 $cm^{-1}$ attributed to less and less deformed $NbO_6$ units. Finally, the spectra before and after thermal poling are shown in Fig. 6 (b). Fig. 6(c) presents the difference of normalized Raman intensity. Raman difference spectra between the 15Nb15Na and 15Nb10Na samples considering the decrease in sodium content (black line, Fig. 6c) was also inserted and has a similar profile with the Raman differences of the

samples before and after the poling treatment. In the Na-depleted subanodic microlayer spectra, a decrease occurs in the 770 and 850 $cm^{-1}$ bands and an increase in the band around 460 $cm^{-1}$ due to the shift from 471 to 459 $cm^{-1}$. Finally, a band at 1550 $cm^{-1}$ appears exclusively in the anodic microlayer and is assigned to the symmetric stretching of molecular oxygen trapped in the matrix [32]. Fig. 7 reports the Raman data recorded on the cross-section of the poled 20Nb15Na sample. Raman maps demonstrate that the structural rearrangements occur exclusively at 4 μm thickness, which corresponds to the Na-depleted microregion detected by SIMS and described in Table 2.

In addition to structural modification, thermal poling treatment breaks the glass centrosymmetry inducing a second order optical response such as second harmonic generation (SHG). Fig. 8(a) and 8(b) illustrate the subanodic layer characterized in its cross-section by μ-SHG polarized microscopy with linear incident polarization oriented either along the *Z* and *Y* axis, respectively, and fixed analyzed polarization along Z axis for the backscattered SHG signal. These configurations were noted as $I_{ZZ}$ and $I_{YZ}$, where the first and second letter refer to the configuration state of the incident light polarization and linear polarization of backscattered SHG signals, respectively. SHG intensity allows probing the second order susceptibility $\chi^{(2)}_{Z;ZZ}$ and $\chi^{(2)}_{Z;YY}$, respectively. As shown in Fig. 8(c), the $I_{ZZ}/I_{YZ}$ ratio is close to 9 (±10 %) and fits the ratio between the terms $\chi^{(2)}_{Z;ZZ} = 3.\chi^{(2)}_{Z;YY}$. Fig. 8(d) shows the SHG intensity versus the incident polarization state obtained by macro-SHG response using a Maker fringes setup. The scans were labeled as Ψ–p and Ψ–s scans for horizontal and vertical SHG detection polarization, respectively. The electric field induced second harmonic (EFISH) model based on $C_{\infty v}$ local symmetry along the z axis was used to simulate all the data [32]. The EFISH simulation describes all the data very well. A slight discrepancy was observed for the maximum value of the Ψ–p scan, nevertheless, one can consider that the SHG response is majority linked to an electrooptical origin. The $\chi^{(2)}$ values obtained from these analyzes are summarized in Table 2 and have an increase with niobium content from 0.42 to 0.76 pm/V and an unexpected decrease from 0.42 to 0.33 pm/V when the poling voltage increases from 900 to 1500 V. These values are not as high as for glasses containing higher levels of niobium, such as niobium borophosphate glasses with up to 48 mol% of $Nb_2O_5$ [51–54] or amorphous thin film in the $Nb_2O_5$–$Na_2O$ binary system [55]. However, the $\chi^{(2)}$ values of these samples are higher when compared to other germanate glasses. The sample with 25 mol% of $Nb_2O_5$ has a $\chi^{(2)}$ value twice as high as germanate glasses with 20 mol% of $Ta_2O_5$ [35] and also higher than another germanate glass with 28 mol% of $Nb_2O_5$ [29].

Finally, in order to demonstrate the promising potential of these samples for future microscale photonic applications, a poling treatment test on the 15Nb15Na sample using an ITO electrode microstructured by picosecond laser inscription was performed. Fig. 9(a) and (b) illustrate the microstructured surface by laser ablation on the electrode used as anode and a picture of the sample after poling treatment, respectively. The excellent resolution of the microlocalized SHG signal in the region in contact with the micromodified electrode can be observed in Fig. 8(c).

## 4. Discussion

As shown in Figs. 1 and 8, niobium germanate glasses have a spectral transmission up to 5200 nm and a SHG response induced by thermal poling. Although the NLO responses are less than in crystalline materials such as $LiNbO_3$ [56] or in niobium borophosphate glasses that allow a higher niobium content [54], niobium germanate glasses are highlighted for non-linear applications in the mid-IR region since they have

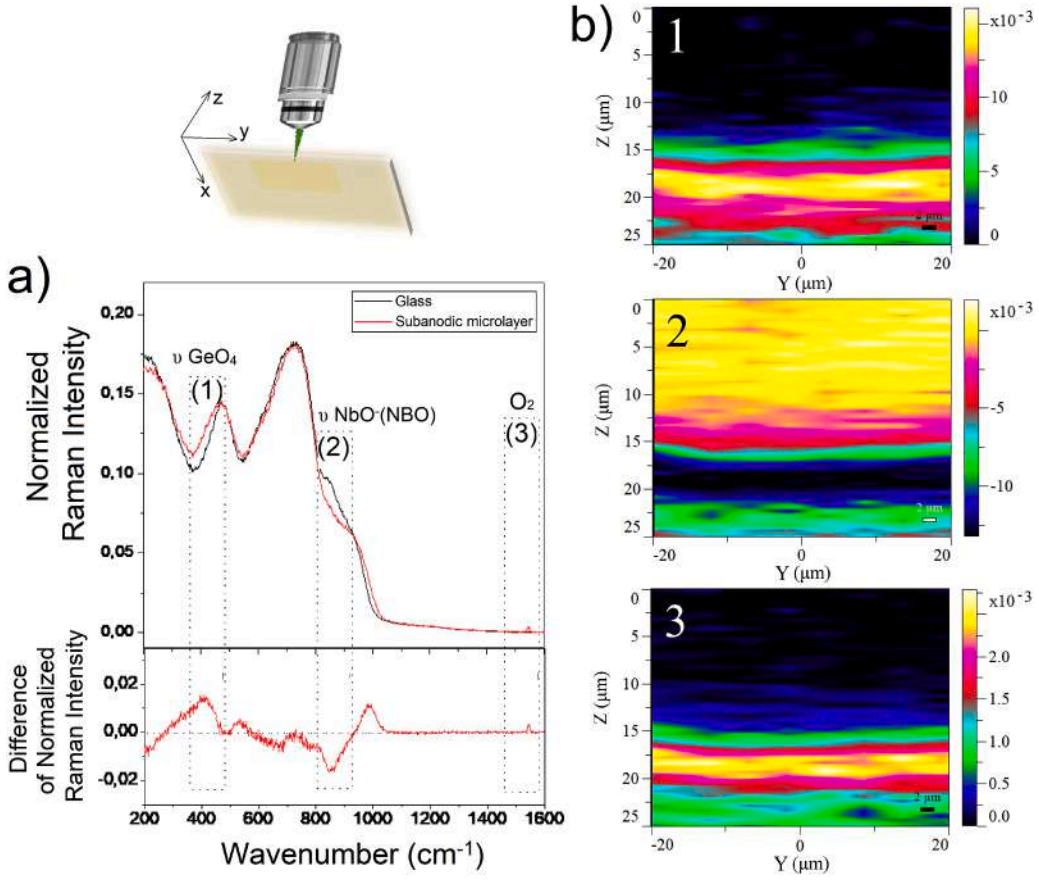


**Fig. 7.** (a) Raman spectra cross-section of 20Nb15Na sample in the anion sublayer where there was in contact with the electrode - in red - and the glass - in black, and (b) Raman intensity mapping of modes 1, 2 and 3 highlighted in a.

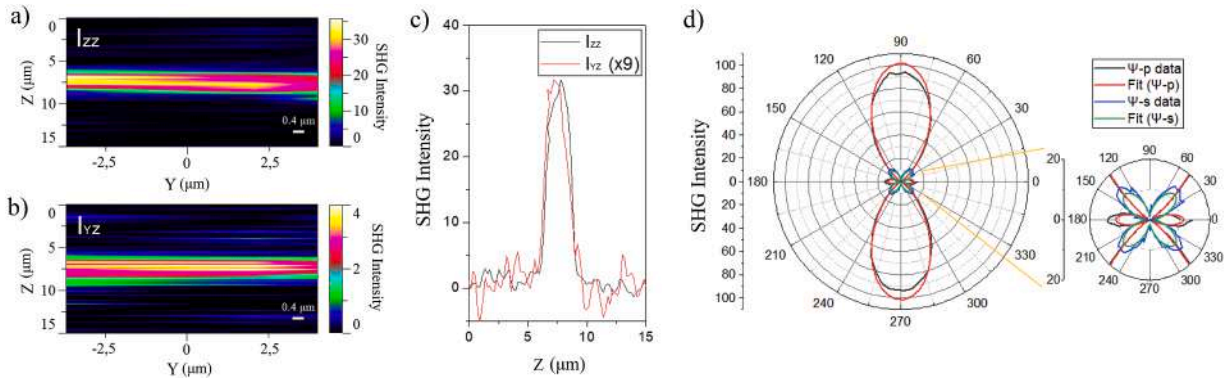


**Fig. 8.** (a) Micro-SHG maps, (b) comparison of SHG maps for different light polarization configurations and (c) macro-SHG measurements by Maker fringes and EFISH simulation.

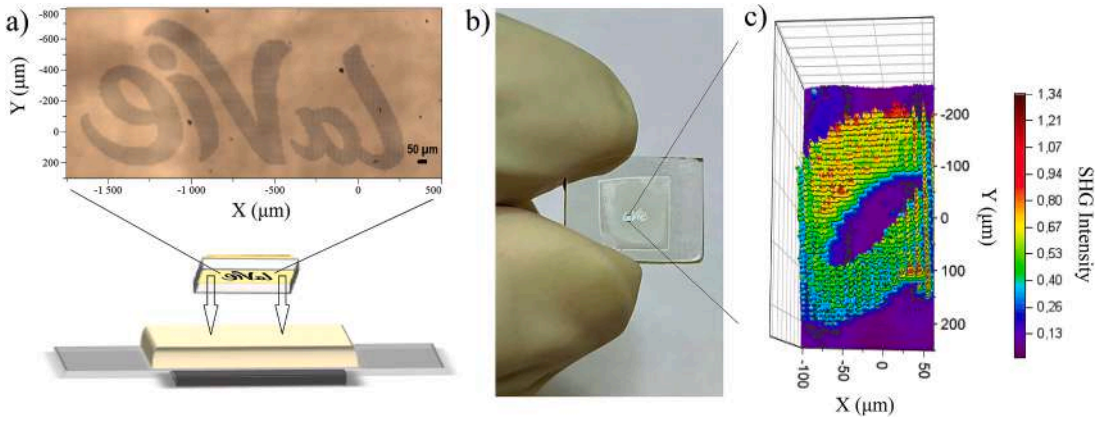


**Fig. 9.** (a) Optical micrographs of the surface of the structured ITO electrode, (b) picture of micromodified 15Nb15Na sample after poling treatment and (c) SHG Mapping realized on the modified surface with linearly polarized light perpendicular to the imprinted structure.

transparency in the mid-IR of the germanate matrix, are easy to synthesize and allow variation in the shape of the material as they are glass matrix. Alkaline niobium germanate glasses are described as a mixed $GeO_4$–$NbO_6$ network leading to the formation of $NbO_6$ clusters with increasing niobium content [57]. This $NbO_6$ polyhedra network was confirmed in the IR and Raman data of Figs. 5(a) and 6(a) due to the increase in the band around 600 $cm^{-1}$ assigned to the stretching of Nb-O-Nb bonds in $NbO_6$ units without NBO connections with niobium content. Furthermore, in the Raman spectra, an evident shift of the band from 763 to 709 $cm^{-1}$ was identified due to the formation of less-distorted $NbO_6$ polyhedra and decrease in the extension of the mixed $GeO_4$–$NbO_6$ network through Nb-O-(Ge) bonds. These structural modifications demonstrate a higher overall network connectivity with niobium content and are the main factors for the changes in certain properties, such as an increase in density [58], in the glass transition temperature [29], and in the NLO response [31] and finally a decrease in the parameters of thermal stability against crystallization [32].

After thermal poling, a sodium depletion on the surface of niobium germanate glasses formed a microlayer of 2.4 to 4.0 μm probed by time-of-flight secondary ion mass spectrometry (TOF-SIMs) and is the main cause of structural rearrangements in the subanodic layer. Structural modifications were investigated inside and outside of the Na-depletion microlayer and also between 15Nb15Na and 15Nb10Na samples with different sodium contents. As expected, both the decrease in sodium in the 15Nb15Na and 15Nb10Na bulk samples without thermal poling and the sodium depletion in the microlayer after poling treatment follow the same trend of structural rearrangement: a change in the ratio between bridging and non-bridging oxygens (NBO) bonds linked to variation in sodium contents. In the IR spectra of Fig. 5(b), the decrease in NBO bonds is evidenced by the reduction of the band at 800 $cm^{-1}$ and by the increase at 880 $cm^{-1}$ assigned to υ Ge-$O^-$ and υ Ge-O-Ge, respectively. A conversion from $Q^3$ $GeO_4$ units to $Q^4$ $GeO_4$ units occurs, and this effect is more pronounced in the post-poling Na-depletion microlayer than in samples with different sodium contents without treatment, since this subanodic region is empty of sodium. In the Raman spectra of Figure 69 (c), the decrease in NBO bonds is evidenced by the decrease in the band around 850 $cm^{-1}$, which in this case mainly refers to the vibration of terminal Nb-$O^-$ bonds. Furthermore, in the sodium-empty subanodic microlayer, a band decrease at 770 $cm^{-1}$ and band shift at 465 $cm^{-1}$ are identified and occur due to the formation of a glass network with less interconnections with Nb-O-Ge bonds and greater connections between $GeO_4$- and $NbO_6$-rich amorphous region: (1) the band at 770 $cm^{-1}$ is assigned to Nb-O-Ge bonds and deformed $NbO_6$ polyhedra and (2) the band shift around 470 $cm^{-1}$ occurs due to the increase in the average value of the intertetrahedral Ge-O-Ge bond angle [59]. One has to point out that the formation of this amorphous matrix with a high content of Ge-O-Ge and Nb-O-Nb linkages without NBO bonds is only achieved after thermal poling treatment, since traditional melt-quenching method results in a spontaneous crystallization due to low $Nb_2O_5$ solubility in the germanate liquid phase. This highly connected network and amorphous phase separation have also been reported for tantalum germanate glasses [35]. Finally, Fig. 7 shows that the band at 1550 $cm^{-1}$ is limited in the subanodic region and refers to the presence of trapped molecular oxygen after poling treatment with a blocking anode-electrode configuration [25]. This molecular oxygen results from the sodium ions departure and the rearrangement of the remaining glass network.

During thermal poling, a DC bias is applied across the heated sample and the current measured as a function of treatment time was plotted in

Fig. 4(b). This Figure shows that the current (I) increases until the voltage is held constant, (II) decreases when the voltage is held constant and (III) decreases again when the heater is turned off. After the last step, the DC bias is removed only when a sample is brought back to room temperature to prevent charge mobility in the glass network. In general, in stage I, the dissociation process of $Na^+$ ions starts. In stage II, a depletion layer in $Na^+$ ions is formed and the decrease in current occurs due to the gradual decrease in the dissociation process, forming the sodium free layer which exhibits a low ionic conductivity [60]. Finally, in stage III there is a sudden drop in current when the temperature is turned off [42]. This mobile cations depletion, confirmed by TOF-SIMs data and described structural changes, leads to a volumetric space charge, and allows the implementation of a static electrical field in the subanodic microlayer. Fig. 8 demonstrates the presence of SHG signal in the NLO-active layer and the thickness of the detected SHG signal region is consistent with the sodium depletion of around 4 μm obtained by TOF-SIMs analysis. Fig. 8(d) shows the fit of the SHG data considering the electric field induced second harmonic (EFISH) model and confirms the electrooptical origin of the NLO signal. Thus, in this case, both the third-order susceptibility ($\chi^{(3)}$) of an isotropic material and the magnitude of the permanent static electrical field are relevant to interpret the NLO response. Regarding the SHG data on different glass compositions for the same poling parameters, higher niobium contents promoted an increase in the poling induced $\chi^{(2)}$ susceptibility. This occurs due to the expected increase in $\chi^{(3)}$ susceptibility which can be attributed to the higher polarizability of $d^0$ transition ions such as niobium but also to the niobate structural arrangement forming a 3D network of octahedral $NbO_6$ units known to enhance the third order optical properties in various oxide glasses [61].

In the case of the increase of applied voltages for the same niobium content (15Nb10Na sample) an unexpected decrease in the $\chi^{(2)}$ values was identified and will be discussed in detail below. Thermal poling causes a depletion of positive charges and consequently an excess of negative charges in the subanodic microlayer, In the case of blocking anode configuration, i.e. prohibiting the possibility of positive charge injection in the poled glass, the compensation mechanisms are dictated by the motion of negative charge carriers from the glass network. These polarizations mechanisms are known to induce structural rearrangements and formation of neutral isolated species trapped in the glass matrix upon oxidation reactions [27]. In this study, FTIR and Raman data confirm the structural changes and Raman mapping of Fig. 7(b) demonstrates the $O_2$ formation exclusively in the subanodic microlayer. Two main mechanisms have been proposed in the literature to explain $O_2$ generation after thermal poling in blocking anode configuration. [24]. The first process is described by the electronic conductivity in the region depleted of positive ions and is caused by the self-healing dielectric breakdown that allows electrons hopping between oxygen sites without the need for motion of oxygen ions [25,26]. In this case, a series of intermediate reactions occur involving the recombination of all adjacent pairs of NBO bonds, peroxide radicals and finally leading to the formation of molecular oxygen and resulting in an increase in the degree of the glass matrix polymerization [25,29]. The second process is related to anionic conduction [25]. In this case, the polymerization of the structure occurs due to oxidation reactions within the space charge layer that led to sodium release: $2[Ge\text{-}O^-\ldots Na^+] \rightarrow Ge\text{-}O\text{-}Ge + O^{2-} + 2Na^+$, and formation of $O_2$ from oxygen anions: $O^{2-} \rightarrow \frac{1}{2}O_2 + 2e^-$ [29]. In the case of our glass samples, both charge recombination mechanisms can be expected, and no additional observation allowed concluding on one predominant process. Nevertheless, as shown in Table 2, an unexpected decrease in $\chi^{(2)}$ was identified for the 15Nb10Na sample with increasing applied voltages. According to a classical model describing the formation of a polarized layer in glassy materials, if the applied voltage increase, the strength of the induced static electric field in the space charge layer is expected to increase and the thickness of the poled layer should vary according to the square root of the applied voltage [27]. This trend is clearly not observed in this study, as shown in Table 2. The sodium depleted layer thickness increases almost linearly with the applied field and the induced EFISH $\chi^{(2)}$ susceptibility decreases. In this case, this unusual tendency may be related to an increase of the negative charge carriers mobility with the applied voltage. In a previous work, it was necessary to consider an exponential growth of the negative charge carrier mobility with the magnitude of the local electric field to model charge motions during a poling process of an ionic glassy matrix. This model considers constant activation energy and thus mobilities of the charge carriers. In this perspective, a variation in the negative charge motion activation energy may be the cause of the model divergence. If the mobility of negative charge carriers (oxygen anions or electrons) varies with the applied voltage, a strong increase in applied voltage may have led to a significant decrease in the activation energy of negative charge motion facilitating sodium compensation and allowing for greater sodium migration. This phenomenon is consistent with that described for insulating materials under a high electric field, where activation energy and electrical conduction are dependent on the applied field [61] and the effect of high voltage described by the Poole-Frenkel effect [62]. In this way, a Na-depleted thickness greater than expected can then be explained together with a decrease of the EFISH $\chi^{(2)}$ susceptibility, since a greater space charge layer thickness results in a decrease in the induced static electric field strength and consequently in the second order optical response.

## 5. Conclusion

Structural and optical properties were investigated in sodium niobium germanate glasses before and after thermal poling. The increase in niobium content in glass germanate led to the formation of $NbO_6$ polyhedra with a coordination number greater than $GeO_4$ units, increasing connectivity in the mixed covalent niobium-germanate chains, and consequently an increase in glass transition temperature and density of the material. Furthermore, the niobium content improves the NLO response in the subanodic layer after poling treatment, since increasing the amount of highly polarizable $NbO_6$ units improves the $\chi^{(3)}$ susceptibility, which is directly related to the $\chi^{(2)}$ susceptibility, according to the EFISH model. Finally, regarding the increase in voltage in the thermal poling, an unexpected linear increase in the thickness of the NLO-active space charge layer and a decrease in $\chi^{(2)}$ susceptibility was observed. A different response from the classical space charge formation model occurs due to the decrease in the activation energy of negative charge motion in the material under high tensions. In this sense, the decrease in this activation energy facilitates sodium compensation and allows greater migration of sodium ions, which consequently reduces the magnitude of the induced electric field by thermal poling.

## CRediT authorship contribution statement

**Lia Mara Marcondes:** Formal analysis, Investigation, Writing – original draft, Writing – review & editing. **Juliane Resges Orives:** Investigation, Validation, Writing – review & editing. **Frederic Adamitez:** Investigation, Writing – review & editing. **Gael Yves Poirier:** Conceptualization, Validation, Writing – review & editing. **Thierry Cardinal:** Validation, Writing – review & editing. **Marc Dussauze:** Conceptualization, Investigation, Formal analysis, Writing – review & editing, Supervision. **Marcelo Nalin:** Conceptualization, Investigation, Resources, Writing – review & editing, Supervision.

## Declaration of competing interest

The authors declare that they have no known competing financial interests or personal relationships that could have appeared to influence the work reported in this paper.

## Data availability

Data will be made available on request.

## Acknowledgments

The authors acknowledge the financial supports from São Paulo Research Foundation Agency, FAPESP (grants nº 2013/07793-6, 2019/19609-1, 2020/01786-1, 2021/11494-0). The Raman and SHG experiments were conducted using the SIV platform at the University of Bordeaux founded by the FEDER and the Region Aquitaine. This project has also received funding from the European Union's Horizon 2020 research program under the Marie SkłodowskaCurie grant agreement no. 823941 (FUNGLASS), New Aquitaine region (Grant 2016–1R10107) and Idex Bordeaux (Research Program GPR Light).

## References

[1] W. Blanc, Y.G. Choi, X. Zhang, M. Nalin, K.A. Richardson, G.C. Righini, M. Ferrari, A. Jha, J. Massera, S. Jiang, J. Ballato, L. Petit, The past, present and future of photonic glasses: a review in homage to the united nations international year of glass 2022, Prog. Mater. Sci. 134 (2023) 101084, https://doi.org/10.1016/j.pmatsci.2023.101084.

[2] V.S. Shiryaev, M.F. Churbanov, Recent advances in preparation of high-purity chalcogenide glasses for mid-IR photonics, J. Non-Cryst. Solids 475 (2017) 1–9, https://doi.org/10.1016/j.jnoncrysol.2017.09.021.

[3] V. Ghergia, New materials for optoelectronic devices, Ceram. Int. 19 (1993) 181–190, https://doi.org/10.1016/0272-8842(93)90039-T.

[4] W.H. Kim, V.Q. Nguyen, L.B. Shaw, L.E. Busse, C. Florea, D.J. Gibson, R.R. Gattass, S.S. Bayya, F.H. Kung, G.D. Chin, R.E. Miklos, I.D. Aggarwal, J.S. Sanghera, Recent progress in chalcogenide fiber technology at NRL, J. Non-Cryst. Solids 431 (2016) 8–15, https://doi.org/10.1016/j.jnoncrysol.2015.03.028.

[5] V.G. Ta'eed, N.J. Baker, L. Fu, K. Finsterbusch, M.R.E. Lamont, D.J. Moss, H. C. Nguyen, B.J. Eggleton, D.Y. Choi, S. Madden, B. Luther-Davies, Ultrafast all-optical chalcogenide glass photonic circuits, Opt. Express 15 (15) (2007) 9205–9221, https://doi.org/10.1364/OE.15.009205.

[6] M. Tang, Y. Ma, S. Wen, G. Du, J. Chen, X. Li, S. Lv, S. Zhou, Gallosilicate glass and fiber for radiation detection, J. Am. Ceram. 106 (6) (2023) 3438–3445, https://doi.org/10.1111/jace.19058.

[7] Z. Qiu, S. Dai, C. Liu, W. Wu, Z. Xu, Y. Wang, Y. Fu, Novel Ge-As-Se chalcogenide glass for potential high Brillouin gain coefficient of fiber, Ceram. Int. 49 (10) (2023) 16433–16439, https://doi.org/10.1016/j.ceramint.2023.02.004.

[8] S. Kang, Z. Huang, W. Lin, D. Yang, J. Zhao, X. Qiao, X. Xiao, S. Xu, J. Qiu, J. Du, G. Dong, Enhanced single-mode fiber laser emission by nano-crystallization of oxyfluoride glass-ceramic cores, J. Mater. Chem. C 7 (2019) 5155–5162, https://doi.org/10.1039/C9TC01170F.

[9] S. Danto, F. Désévédavy, Y. Petit, J.-C. Desmoulin, A.A. Khalil, Marc Dussauze C. Strutynski, F. Smektala, T. Cardinal, L. Canioni, Photowritable silver-containing phosphate glass ribbon fibers, Adv. Opt. Mater. 4 (1) (2016) 162–168, https://doi.org/10.1002/adom.201500459.

[10] X. Wang, Y. Tian, Y. Zhang, D. Tang, B. Li, J. Zhang, S. Xu, Effect of $Al(PO_3)_3$, NaF, and $SrF_2$ on structure and properties of fluorophosphate glass, J. Non-Cryst. Solids 602 (2023) 122089, https://doi.org/10.1016/j.jnoncrysol.2022.122089.

[11] M. Ghanad, N. Akrami, P. Keil, H. Bradtmüller, M.R. Hansen, J.V. Khaki, S. M. Beidokhti, Single-step solution combustion synthesis of porous 1393-B3 glass powders and structural characterization via solid-state NMR spectroscopy, Ceram. Int. 49 (9) (2023) 14689–14701, https://doi.org/10.1016/j.ceramint.2023.01.061.

[12] S. Das, P. Priyadarshini, D. Alagarasan, S. Vardhrajperumal, R. Ganesan, R. Naik, Role of tellurium addition on the linear and non-linear optical, structural, morphological properties of $Ag_{60}$-x$Se_{40}Te_x$ thin films for nonlinear applications, J. Am. Ceram. 105 (5) (2022) 3469–3484, https://doi.org/10.1111/jace.18361.

[13] A.M. Abd-Elnaiem, A.Z. Mahmoud, S. Moustafa, Structural and optical properties of thermally evaporated and annealed $Ge_{20}Se_{76}Sn_4$ thin films, Opt. Mater. 111 (2021) 110607, https://doi.org/10.1016/j.optmat.2020.110607.

[14] Z. Rajaofara, P. Leproux, M. Dussauze, A. Tonello, V. Rodriguez, L. Karam, H. Kano, J.-R. Duclére, V. Couderc, Mapping the second and third order nonlinear susceptibilities in a thermally poled microimprinted niobium borophosphate glass, Opt. Mater. Express 11 (10) (2021) 3411–3420, https://doi.org/10.1364/OME.433809.

[15] H.-Y. Chen, Y.-S. Lin, Influence of multi-energy boron difluoride implantation on the second-harmonic generation of thermally poled fused silica, Opt. Mater. 109 (2020) 110451, https://doi.org/10.1016/j.optmat.2020.110451.

[16] X. He, B. Poumellec, Q. Liu, F. Brisset, M. Lancry, One-step photoinscription of asymmetrically oriented fresnoite-type crystals in glass by ultrafast laser, Opt. Lett. 39 (18) (2014) 5423–5426, https://doi.org/10.1364/OL.39.005423.

[17] E.O. Smetanina, B. Chimier, Y. Petit, A. Royon, T. Cardinal, L. Canioni, G. Duchateau, Laser writing of nonlinear optical properties in silver-doped phosphate glass, Opt. Lett. 42 (9) (2017) 688–1691, https://doi.org/10.1364/OL.42.001688.

[18] Y. Li, L. Wang, M. Liao, L. Zhang, W. Bi, T. Xue, Y. Liu, R. Zhang, Y. Ohishi, Suspended-core fluoride fiber for broadband supercontinuum generation, Opt. Mat. 96 (2019) 109281, https://doi.org/10.1016/j.optmat.2019.109281.

[19] I. Alamgir, F. St-Hilaire, M. Rochette, All-fiber nonlinear optical wavelength conversion system from the C-band to the mid-infrared, Opt. Lett. 45 (4) (2020) 857–860, https://doi.org/10.1364/OL.386272.

[20] S. Ohara, H. Masai, Y. Takahashi, T. Fujiwara, Y. Kondo, N. Sugimoto, Space-selectively crystallized fiber with second-order optical nonlinearity for variable optical attenuation, Opt. Lett. 34 (7) (2009) 1027–1029, https://doi.org/10.1364/OL.34.001027.

[21] G. Wallis, D.I. Pomerantz, Field assisted glass-metal sealing, J. Appl. Phys. 40 (1969) 946, https://doi.org/10.1063/1.1657121.

[22] F. de Lucia, P.J.A. Sazio, Thermal poling of optical fibers: a numerical history, Micromachines 11 (2) (2020) 139, https://doi.org/10.3390/mi11020139.

[23] R.A. Myers, N. Mukherjee, S.R.J. Brueck, Large second-order nonlinearity in poled fused silica, Opt. Lett. 16 (1991) 1732–1734, https://doi.org/10.1364/OL.16.001732.

[24] M. Dussauze, T. Cremoux, F. Adamietz, V. Rodriguez, E. Fargin, G. Yang, T. Cardinal, Thermal poling of optical glasses: mechanisms and second-order optical properties, Int. J. Appl. Glass Sci. 3 (4) (2012) 309–320, https://doi.org/10.1111/ijag.12001.

[25] M. Dussauze, V. Rodriguez, A. Lipovskii, M. Petrov, C. Smith, K. Richardson, T. Cardinal, E. Fargin, E.I. Kamitsos, How does thermal poling affect the structure of soda-lime glass, J. Phys. Chem. C 114 (29) (2010) 12754–12759, https://doi.org/10.1021/jp1033905.

[26] U.K. Krieger, W.A. Lanford, Field assisted transport of $Na^+$ ions, $Ca^{2+}$ ions and electrons in commercial soda-lime glass I: experimental, J. Non-Cryst. Solids 102 (1988) 50–61, https://doi.org/10.1016/0022-3093(88)90112-3.

[27] M. Dussauze, E.I. Kamitsos, E. Fargin, V. Rodriguez, Structural rearrangements and second-order optical response in the space charge layer of thermally poled sodium-niobium borophosphate glasses, J. Phys. Chem. C 111 (39) (2007) 14560–14566, https://doi.org/10.1021/jp074335f.

[28] G. Guimbretière, M. Dussauze, V. Rodriguez, E.I. Kamitsos, Correlation between second-order optical response and structure in thermally poled sodium niobium-germanate glass, Appl. Phys. Lett. 97 (2010) 171103, https://doi.org/10.1063/1.3506501.

[29] H. Zeghlache, M. Guignard, A. Kudlinski, Y. Quiquempois, G. Martinelli, V. Nazabal, F. Smektala, Stabilization of the second-order susceptibility induced in a sulfide chalcogenide glass by thermal poling, J. Appl. Phys. 101 (2007) 084905, https://doi.org/10.1063/1.2719008.

[30] W.D. Dumbaugh, Infrared transmitting germanate glasses, SPIE Emerg. Optic. Mater. 297 (1982) 80–85, https://doi.org/10.1117/12.932488.

[31] D. Manzani, T. Gualberto, J.M.P. Almeida, M. Montesso, C.R. Mendonça, V.A. G. Rivera, L. de Boni, M. Nalin, S.J.L. Ribeiro, Highly nonlinear $Pb_2P_2O_7$-$Nb_2O_5$ glasses for optical fiber production, J. Non-Cryst. Solids 443 (2016) 82–90, https://doi.org/10.1016/j.jnoncrysol.2016.04.01.

[32] L.M. Marcondes, S. Maestri, B. Souza, R.R. Gonçalvez, F.C. Cassanjes, G.Y. Poirier, High niobium oxide content in germanate glasses: thermal, structural, and optical properties, J. Am. Ceram. Soc. 101 (2018) 220–230, https://doi.org/10.1111/jace.15215.

[33] D. Munoz-Martin, A.R. de La Cruz, J.M. Fernandez-Navarro, C. Domingo, J. Solis, J. Gonzalo, Structural origin of the nonlinear optical properties of lead niobium germanate film glasses, J. Appl. Phys. 110 (2011) 023522, https://doi.org/10.1063/1.3608172.

[34] M.R. Karim, N. Al Kayed, M.R. Hossain, B.M.A. Rahman, Study of low-peak-power highly coherent broadband supercontinuum generation through a dispersion-engineered Si-rich silicon nitride waveguide, Appl. Opt. 59 (20) (2020) 5948–5956, https://doi.org/10.1364/AO.395705.

[35] G. Poirier, M. Dussauze, V. Rodriguez, F. Adamietz, L. Karam, T. Cardinal, E. Fargin, Second harmonic generation in sodium tantalum germanate glasses by thermal poling, J. Phys. Chem. C 123 (43) (2019) 26528–26535, https://doi.org/10.1021/acs.jpcc.9b0822.

[36] Y. Benino, Y. Takahashi, T. Fujiwara, T. Komatsu, Second order optical non-linearity of transparent glass-ceramic materials induced by alternating field, J. Non-Cryst. Solids 345–346 (2004) 422–427, https://doi.org/10.1016/j.jnoncrysol.2004.08.056.

[37] J.E. Shelby, Introduction to Slass Science and Technology, 2nd ed., Royal Society of Chemistry, Cambridge, 2005.

[38] E.I. Kamitsos, A.P. Patsis, M.A. Karakassides, G.D. Chryssikos, Infrared reflectance spectra of lithium borate glasses, J. Non-Cryst. Solids 126 (1–2) (1990) 52–67, https://doi.org/10.1016/0022-3093(90)91023-K.

[39] V. Rodriguez, C. Sourisseau, General Maker-fringe ellipsometric analyzes in multilayer nonlinear and linear anisotropic optical media, J. Opt. Soc. Am. B 19 (2002) 2650, https://doi.org/10.1364/JOSAB.19.002650.

[40] H. Hosono, Y. Abe, Temperature dependence of infrared absorption spectra of hydroxyl groups in soda germanate glasses, J. Am. Ceram. Soc. 72 (1) (1989) 44–48, https://doi.org/10.1111/j.1151-2916.1989.tb05951.x.

[41] Y.D. Yiannopoulos, C.P.E Varsamis, E.I. Kamitsos, Density of alkali germanate glasses related to structure, J. Non-Cryst. Solids 293–295 (2001) 244–249, https://doi.org/10.1016/S0022-3093(01)00677-9.

[42] G. Yang, J. Cao, Y. Qi, X. He, C. Peng, Y. Lu, F. Tang, K. Tang, B. Liu, H. Chen, G. Chen, Y. Gao, D. Chen, Imprinting gradient refractive index micro-structure in $GeS_2$–$Ga_2S_3$–KCl glass for broadband diffraction grating, Opt. Mat. 101 (2020) 109766, https://doi.org/10.1016/j.optmat.2020.109766.

[43] G.S. Henderson, R.T. Amos, The structure of alkali germanophosphate glasses by Raman spectroscopy, J. Non-Cryst. Solids 328 (1–3) (2003) 1–19, https://doi.org/10.1016/S0022-3093(03)00478-2.
[44] R.R. Pereira, F.T. Aquino, A. Ferrier, P. Goldner, R.R. Gonçalves, Nanostructured rare earth doped $Nb_2O_5$: structural, optical properties and their correlation with photonic applications, J. Lumin. 170 (2016) 707–717, https://doi.org/10.1016/j.jlumin.2015.08.068.
[45] G. Monteiro, L.F. Santos, R.M. Almeida, F. D'Acapito, Local structure around $Er^{3+}$ in $GeO_2$–$TeO_2$–$Nb_2O_5$–$K_2O$ glasses and glass-ceramics, J. Non-Cryst. Solids 377 (2013) 129–136, https://doi.org/10.1016/j.jnoncrysol.2012.12.019.
[46] M.R. Cicconi, D.K. Dobesh, B. Schroeder, T. Otsuka, T. Hayakawa, D. de Ligny, Alkali-niobate aluminosilicate glasses: structure and properties, Opt. Mater. X 18 (2023) 100228, https://doi.org/10.1016/j.omx.2023.100228.
[47] I. Enomoto, Y. Benino, T. Fujiwara, T. Komatsu, Synthesis of nanocrystals in KNb(Ge,Si)$O_5$ glasses and chemical etching of nanocrystallized glass fibers, J. Solid State Chem. 179 (6) (2006) 1821–1829, https://doi.org/10.1016/j.jssc.2006.03.028.
[48] Y. Takahashi, H. Masai, M. Osada, T. Fujiwara, Precursive stage of nanocrystallization in niobium oxide-containing glass, Appl. Phys. Lett. 95 (2009) 071909, https://doi.org/10.1063/1.3211989.
[49] P. Pernice, A. Paleari, M. Ferraris, M. Fokine, E. Fanelli, R. Lorenzi, G. Spinolo, A. Aronne, Electric field induced structural modification and second order optical nonlinearity in potassium niobium silicate glass, J. Non-Cryst. Solids 355 (52–54) (2009) 2578–2582, https://doi.org/10.1016/j.jnoncrysol.2009.09.005.
[50] M. Micoulaut, L. Cormier, G.S. Henderson, The structure of amorphous, crystalline and liquid $GeO_2$, J. Phys. Condens. Matter 18 (45) (2006) 753–784, https://doi.org/10.1088/0953-8984/18/45/R01.
[51] M. Dussauze, E. Fargin, M. Lahaye, V. Rodriguez, F. Adamietz, Large second-harmonic generation of thermally poled sodium borophosphate glasses, Opt. Express 13 (11) (2005) 4064–4069, https://doi.org/10.1364/OPEX.13.004064.
[52] A. Malakho, M. Dussauze, E. Fargin, O. Bidault, V. Rodriguez, F. Adamietz, B. Poumellec, Effect of sodium to barium substitution on the space charge implementation in thermally poled glasses for nonlinear optical applications, J. Solid State Chem. 182 (5) (2009) 1156–1163, https://doi.org/10.1016/j.jssc.2009.02.016.
[53] G. Yang, M. Dussauze, V. Rodriguez, F. Adamietz, N. Marquestaut, K.L.N. Deepak, D. Grojo, O. Uteza, P. Delaporte, T. Cardinal, E. Fargin, Large scale micro-structured optical second harmonic generation response imprinted on glass surface by thermal poling, J. Appl. Phys. 118 (2015) 043105, https://doi.org/10.1063/1.4926866.
[54] L. Karam, F. Adamietz, V. Rodriguez, F. Bondu, A. Lepicard, T. Cardinal, E. Fargin, K. Richardson, M. Dussauze, The effect of the sodium content on the structure and the optical properties of thermally poled sodium and niobium borophosphate glasses, J. Appl. Phys. 128 (2020) 043106, https://doi.org/10.1063/5.0013383.
[55] L. Karam, F. Adamietz, D. Michau, C. Gonçalves, M. Kang, R. Sharma, G. S. Murugan, T. Cardinal, E. Fargin, V. Rodriguez, K.A. Richardson, M. Dussauze, Electrically micro-polarized amorphous sodo-niobate film competing with crystalline lithium niobate second-order optical response, Adv. Opt. Mater. 8 (13) (2020) 2000202, https://doi.org/10.1002/adom.202000202.
[56] Y. Qi, Y. Li, Integrated lithium niobate photonics, Nanophotonics 9 (6) (2020) 1287–1320, https://doi.org/10.1515/nanoph-2020-0013.
[57] L.M. Marcondes, H. Bradtmüller, S.N.C. dos Santos, L.K. Nolasco, C.R. Mendonça, S.H. Santagneli, G.Y. Poirier, M. Nalin, Structural and luminescence characterization of europium-doped niobium germanate glasses and glass-ceramics: novel insights from $^{93}Nb$ solid-state NMR spectroscopy, Ceram. Int. 48 (14) (2022) 20801–20808, https://doi.org/10.1016/j.ceramint.2022.04.062.
[58] P. Mošner, T. Hostinský, L. Koudelka, Thermal, structural and crystallization study of $Na_2O$–$P_2O_5$–$Nb_2O_5$ glasses, J. Solid State Chem. 316 (2022) 123545, https://doi.org/10.1016/j.jssc.2022.123545.
[59] E.I. Kamitsos, Y.D. Yiannopoulos, M.A. Karakassides, G.D. Chryssikos, H. Jain, Raman and infrared structural investigation of $xRb_2O{\cdot}(1-x)GeO_2$ glasses, J. Phys. Chem. 100 (28) (1996) 11755–11765, https://doi.org/10.1021/jp960434+.
[60] M. Dussauze, O. Bidault, E. Fargin, M. Maglione, V. Rodriguez, Dielectric relaxation induced by a space charge in poled glasses for nonlinear optics, J. Appl. Phys. 100 (2006) 034905, https://doi.org/10.1063/1.2218998.
[61] M. Dussauze, T. Cardinal, Nonlinear optical properties of glass, in: J.D. Musgraves, J. Hu, L. Calvez (Eds.), Springer Handbook of Glass, Springer International Publishing, 2019, pp. 157–189, https://doi.org/10.1007/978-3-319-93728-1. Springer Handbooks.
[62] P. Dash, M. Yuan, J. Gao, E. Furman, M.T. Lanagan, High electric field conduction in low-alkali boroaluminosilicate glass, J. Appl. Phys. 123 (2018) 054102, https://doi.org/10.1063/1.5004672.

Ceramics International xxx (xxxx) xxx

Contents lists available at ScienceDirect

Ceramics International

journal homepage: www.elsevier.com/locate/ceramint

# Quaternary bioactive glass-derived powders presenting submicrometric particles and antimicrobial activity

Sara Novak [a], Juliane Resges Orives [b], Marcelo Nalin [b], Irem Unalan [c], Aldo R. Boccaccini [c], Emerson R. de Camargo [a,*]

[a] Department of Chemistry, Federal University of São Carlos (UFSCar), Rod. Washington Luis km 235, CP 676, São Carlos, São Paulo, 13565-905, Brazil
[b] São Paulo State University (UNESP), Institute of Chemistry, Rua Prof. Francisco Degni 55, Araraquara, SP, 14800-060, Brazil
[c] Institute of Biomaterials, Department of Materials Science and Engineering, Friedrich-Alexander-Universität Erlangen-Nürnberg, Cauerstrasse 6, 91058, Erlangen, Germany

ARTICLE INFO

*Keywords:*
Bioactive glass-ceramic particles
Antimicrobial glass
Ion release
Mineralization

ABSTRACT

The biomedical engineering advances in the last years have been rising demand for multifunctional biomaterials. Bioactive glass (BG) submicron particles are potential candidates for the formulation of composites with improved dispersion and homogeneity between the constituents. This work presents the preparation of $SiO_2$–$Na_2O$–CaO–$P_2O_5$ glass-derived powders composed of particles with homogenous shapes and sizes between 300 and 500 nm. Two types of synthesis were employed for the preparation of the BG powders, the melt-quenching method, and a citric acid-assisted sol-gel route at a low citric acid concentration (0.005 mol $L^{-1}$). The morphology of the particles was achieved by a low-energy process using a ball mill. These powders were characterized for their structure and surface area and evaluated for *in vitro* mineralization and antibacterial behavior. X-ray diffraction (XRD) analysis revealed different crystalline silicate phases in the sol-gel-derived powder and confirmed the amorphous structure of the melt-quenching-derived one. The surface of the particles was covered by hydroxycarbonate-apatite (HCA) after five days in simulated body fluid (SBF). The antibacterial activity against *Staphylococcus aureus* was higher for the sol-gel-derived powder, showing inhibition >99% of the bacteria growth in 24 h for all concentrations studied. These BG-based powders present a set of characteristics useful for the formulation of multifunctional composites for orthopedic applications.

## 1. Introduction

Several bioactive glasses and glass-ceramics have been developed for living tissue regeneration since the 45S5 bioactive glass (BG) was first reported almost 50 years ago [1]. The quaternary composition of 45S5 BG (*wt* %) (45$SiO_2$, 24.5$Na_2O$, 24.5CaO, 6$P_2O_5$) became popular in tissue engineering due to its bioactivity and capacity to regenerate hard and soft tissues [1,2]. The 45S5 BG composition was designed to provide $P_2O_5$ and large amounts of CaO in a sodium-silicate glass matrix [1]. The purpose of the network modifier $Na_2O$ was only to decrease the melting temperature of the precursor mixture, enabling the fabrication of implants with complex shape by the melting route [1,3].

It is well established that the bioactivity provided by bioactive glasses and glass-ceramics for bone regeneration derives from the hydroxyapatite (HA) phase formed onto their surfaces when exposed to physiological conditions [1]. Besides that, the release of $Ca^{2+}$, $PO_4^{3-}$, and orthosilicate acid ($Si(OH)_4$) into the body during the dissolution process is responsible for stimulating the growth and differentiation of osteoblasts cells through the activation of different intracellular pathways [1,4,5]. Although $Na^+$ cations releasing is not essential for bone bioactivity, $Na_2O$ acts as an effective network modifier compound, enhancing the dissolution and providing a higher reactivity to the bioglass, which can be desirable (or not) depending on the application [3,6].

Although the importance of 45S5 BG, other bioactive glasses with alternative compositions also have been investigated for tissue regeneration, such as phosphate and borate-based glasses [7,8]. Regarding their fabrication, bioactive glasses can be obtained by the conventional melt-quenching method, which is widely used to fabricate implants of complex shapes, or by the sol-gel route, a method attractive to prepare powder glasses presenting high specific areas by controlling the porosity or morphology of the particles [9]. In this regard, two sol-gel approaches can be employed according to the purpose, namely the acid-assisted and

* Corresponding author.
*E-mail address:* camargo@ufscar.br (E.R. de Camargo).

https://doi.org/10.1016/j.ceramint.2022.06.266
Received 13 April 2022; Received in revised form 6 June 2022; Accepted 26 June 2022
Available online 27 June 2022
0272-8842/© 2022 Published by Elsevier Ltd.

the Stöber-derived syntheses. The Stöber method is a well-known procedure for the fabrication of spherical silica nanoparticles, but controlling the morphology is challenging for bioactive systems since the addition of calcium makes the particles irregular [10,11]. Furthermore, hydroxyapatite can precipitate via this method for compositions presenting phosphorus [11]. On the other hand, the acid-assisted approach is suitable for fabricating porous materials by forming an interconnected 3D silica network. In this method, a porous structure forms when the precursor gel is dried [12]. However, entering biological ions such as calcium into the glass structure requires thermal treatment at relatively high temperatures (≥600 °C), which causes loss of the porosity and reduction of the surface area [10,11,13]. Previous studies have investigated modifications in the sol-gel approaches to overcome these drawbacks, such as employing polymer templates to help control the morphology of the particles or changing the precursors to decrease the stabilization temperature [14,15].

Despite the efforts over the years, obtaining $SiO_2$–$Na_2O$–CaO–$P_2O_5$ bioactive glass powders with submicron particle size remains a challenge. Decreasing the size of the particles can be helpful for the formulation of polymer-based composites, considering that an improved dispersion of the particles is required for obtaining materials with reproducible properties. Furthermore, particles with morphological and textural properties on the nanoscale can improve the final characteristics of the composite materials, such as mechanical performance and biological functionality. Indeed, organic-inorganic composites have gained considerable attention in the last years due to their attractive properties for tissue engineering applications and the possibility of employing them in combination with advanced processing techniques such as 3D printing and electrospinning [16,17].

In this work, we proposed the preparation of $SiO_2$–$Na_2O$–CaO–$P_2O_5$ glass and glass-ceramic submicrometric powders employing instrumentation of easy access to laboratories and industry. Our main aim was to explore differences in the physicochemical properties between sol-gel-derived and melt-quenching-derived glasses submitted to the same milling process. The bioactivity of the prepared powders for bone mineralization was preliminarily accessed by scanning electron microscopy (SEM) and infrared spectroscopy (FTIR) analyses upon immersion in simulated body fluid (SBF). The inhibition of *S. aureus* upon exposure to the ionic products released from the BG powders was determined to access their antibacterial activities. We discussed in this study the properties and future perspectives of the prepared submicrometric bioactive glass-derived powders.

## 2. Materials and methods

**Synthesis:** A *precursor solution* with the composition (*wt* %) 11.4$SiO_2$: 6.2$Na_2O$: 6CaO: 1.4$P_2O_5$: 75$H_2O$ was prepared for the citric acid-assisted sol-gel synthesis. 10.96 g of tetraethyl orthosilicate (TEOS 98%, Sigma-Aldrich) was added dropwise to 20.97 g of a citric acid solution (0.005 mol $L^{-1}$) in ultra-pure water under stirring and temperature at 25 °C to obtain 45 g of the precursor. Then, 1.08 g of triethyl phosphate (TEP ≥99.8%, Sigma-Aldrich), sodium nitrate ($NaNO_3$ ACS grade, Synth), and calcium nitrate tetrahydrate ($Ca(CO_3)_2$. 4$H_2O$ 99%, Sigma-Aldrich) were added. Next, the system was kept static for four days for the precursor gelation and aging, respectively. After that, the resulting gel was dried at 60 and 200 °C for 24 h, respectively. The as-synthesized sample (dry-gel) was then thermally treated at 700 °C for 20 h in a high-temperature oven heated at 5 °C $min^{-1}$. The system was cooled naturally at the end of the process. The elemental composition of the resulting powder was verified by X-ray fluorescence spectroscopy (XRF) evidencing a final composition (*wt* %) (39.3$SiO_2$, 37.3$Na_2O$, 21.4CaO, 2$P_2O_5$).

The following chemicals were employed in the melt-quenching synthesis: silica ($SiO_2$ 99.9%, amorphous powder, Alfa Aesar), calcium carbonate ($CaCO_3$ ≥99.0%, powder, Sigma-Aldrich), sodium carbonate ($Na_2CO_3$ ≥99.5%, powder, Sigma-Aldrich), ammonium phosphate monobasic ($NH_4H_2PO4$ ≥98%, powder, Sigma-Aldrich). The chemicals were mixed according to the 45S5 BG composition (composition given above) mixing 6.28 g of $SiO_2$, 6.02 g of $Na_2CO_3$, 6.28 g of $CaCO_3$, and 3.20 g of $NH_4H_2PO_4$, followed by a decarbonation step at 300, 400, 500 °C for 1 h and 900 °C at 2 h to obtain 15 g of the glass. The resulting powder was then melted at 1400 °C in a Pt crucible. The quenching was fast enough to maintain an amorphous phase as checked by X-ray diffraction (XRD) analysis. The final chemical composition by XRF analysis revealed a composition close to the 45S5 BG, with (*wt* %) (40.2$SiO_2$, 34.7$Na_2O$, 18CaO, 7.1$P_2O_5$).

**Milling:** After their synthesis, the powders were milled in a ball mill with yttrium stabilized zirconia (Y-TZP) recipient and 2 mm zirconia balls. The milling process was performed in isopropanol (100% USP grade, Synth) at 30 rpm for 48 h. After that, the resulting suspensions were centrifuged, and the milled powders were dried at 60 °C. In the sequence, they were disaggregated in a mortar. The granulometric (≤300 μm) was selected through a sieve (Tylor mesh 48) and the powders were then characterized by different techniques (see below). The milled powders were named "nBG" and "nBGC" for melt-quenching-derived and sol-gel-derived samples, respectively.

**Characterization:** XRD analysis of the powders was carried out using a Rigaku DMax 2500 PC diffractometer operating at 40 kV and 150 mA, with Cu-Kα radiation, in the 2$\theta$ range of 10–70° and with steps of 2°/min. The elemental composition was analyzed by XRF using a MiniPaI4 PANalytical spectrometer. The results for atomic % are reported in Supplementary Information (Table S1) and were employed to calculate the chemical composition in the quaternary system $SiO_2$–$Na_2O$–CaO–$P_2O_5$.

For infrared spectroscopy, the spectra were taken at 48 scans with a resolution of 4 $cm^{-1}$ from 4000 to 400 $cm^{-1}$ by a Fourier transform infrared spectrometer (FTIR) (Vertex 70, Bruker) with attenuated total reflectance accessory (ATR, diamond crystal).

Evaluation of the thermal events in the as-synthesized sol-gel sample was performed by differential thermal analyses (TGA-DTA) using a Netzsch STA-409 Cell. The sample was placed inside aluminum oxide crucibles in an oxidizing atmosphere with a 50 mL $min^{-1}$ flux and heated from room temperature to 1300 °C at a rate of 5 °C $min^{-1}$.

The morphological characteristic of the powders was analyzed by micrographs acquired using a scanning electron microscope (SEM) (Philips XL 30 FEG) for the samples previously sputter-coated with gold. The particle size distribution was obtained using ImageJ software [18].

The specific area ($m^2$ $g^{-1}$) of the powders was assessed by $N_2$ physisorption. The adsorption isotherms were obtained at 77 K using a Micrometrics ASAP 2020 device. The samples had been maintained for 24 h under vacuum at 150 °C to remove physisorbed gases before the analyses. The surface areas were obtained by the BET equation [19,20].

For zeta potential measurements, the powders were added to a phosphate-buffered saline (PBS) solution resulting in a concentration of 100 mg $mL^{-1}$. The particle suspensions were then diluted 100 times in ultrapure water, and three measurements were carried out at 37 °C for each sample using a Zetasizer Malvern NanoZS Zen3600 instrument.

***In vitro* mineralization:** The investigation of the mineralization activity was made according to the Kokubo protocol [21]. For that, specimens of the powders with 50 mg were immersed in 40 mL of simulated body fluid (SBF) for 1 and 5 days. Images of the samples were obtained by a Zeiss Supra 35 scanning electron microscope for the samples previously sputter-coated with gold to verify the hydroxyapatite (HA) formation on the surface. Further investigation of the sample surfaces was made by FTIR spectroscopy. The pH values of the solutions in SBF experiments were determined in time intervals of 24 h. The SBF solution was replaced each 48 h.

The calcium, sodium, and phosphorous concentrations in ppm (*w/v*) released by the samples in SBF solution were determined for the powders exposed to SBF. For that, 0.075 mg of the powders were added to Falcon tubes containing 15 mL of SBF solution which were maintained at 37 °C for five days. After that, the samples were centrifugated and the

supernatants were collected for determination of the present elements using inductively coupled plasma optical emission spectrometer (ICP OES) (iCAP 6000 spectrometer, Thermo Fisher, Madison, WI, USA) applying axial and radial viewing, and using argon (99.996%, White Martins-Praxair, Sertãozinho, SP, Brazil).

**Antibacterial activity:** The antibacterial property of the glass-derived powders was evaluated using the extracts obtained from the incubation of culture medium with different concentrations of the powders. For that, sterile LB medium (Luria/Miller medium, Carl Roth, Germany) was incubated with the samples in the concentration range of 12.5–100 mg $mL^{-1}$ for 24 h at 37 °C, centrifugated, and the supernatant collected. At the same time, *S. aureus* bacteria (gram-positive) suspension was inoculated in a sterile LB medium overnight. The optical density was then adjusted to 0.015, aliquots of the bacteria suspension were added to the collected extracts, and pure LB medium was also measured as a control group. After the incubation for 24 h at 37 °C, these extracts were carefully homogenized, and 100 μL aliquots were added to 96 well-plates ($n = 4$). The optical density measurement was performed by a microreader (PHOmo, anthos Mikrosysteme GmbH, Germany) at 600 nm. The statistical analysis of data was carried out by ANOVA and Tukey's test using Origin software. Statistical significances were determined for $p < 0.05$ and $p < 0.01$. The results presented were calculated by the average and standard deviation from two independent tests.

## 3. Results and discussion

### 3.1. Physicochemical characteristics of the powders

The microstructure of the glass-derived powders was investigated by XRD (Fig. 1). It is possible to verify that the sol-gel-derived powder (nBGC) exhibits several diffraction signals that are not present in the melt-quenching-derived material (nBG). The crystalline phases identified in nBGC correspond to sodium-calcium silicates, namely $Na_2Ca_2Si_2O_7$ (JCPDS 10-0016), $Na_2Ca_2Si_3O_9$ (JCPDS 79-1087), $Na_2CaSi_3O_8$ (JCPDS 12-0671), and a sodium-calcium phosphate phase ($NaCaPO_4$) (JCPDS 76-1456). These phases have been found in glass-ceramics obtained by the controlled crystallization of quaternary systems $SiO_2$–CaO–$Na_2O$–$P_2O_5$ [22]. In this work, the crystalline phases formed due to the thermal treatment employed to obtain the sol-gel-derived sample. The following paragraphs discuss the crystallization temperature and residue elimination found by thermal treatment of the as-synthesized sol-gel-derived powder.

The diffractograms of the nBG and nBGC samples correlate well with the IR spectra (Fig. 2). The nBGC powder exhibits well-defined signals in the region 620-575 $cm^{-1}$ associated with the deformation modes of P–O in crystalline phosphates, reinforcing the presence of $NaCaPO_4$ crystalline phase. In the nBG sample, a single peak is observed in this region related to amorphous phosphate [23–25]. Another relevant observation is in the region 550-400 $cm^{-1}$, in which the split of the peak in the nBGC sample indicates the presence of crystalline silicates at 520 $cm^{-1}$, and around 460 $cm^{-1}$ associated with Si–O bending modes in the polymeric silica from the residual glassy phase [26,27]. Other Si–O signals, in the range 1000-880 $cm^{-1}$ are assigned to the symmetric stretching, the non-bridging oxygen bonds (NBO) bending vibration, and the NBO asymmetric stretching of Si–O bonds, respectively [27]. The asymmetric stretching of C–O bonds in $CO_2^{3-}$ at ~1460 $cm^{-1}$ is associated with the surface carbonatation of the samples. This reaction occurs spontaneously when the sample is exposed to the atmosphere [28,29].

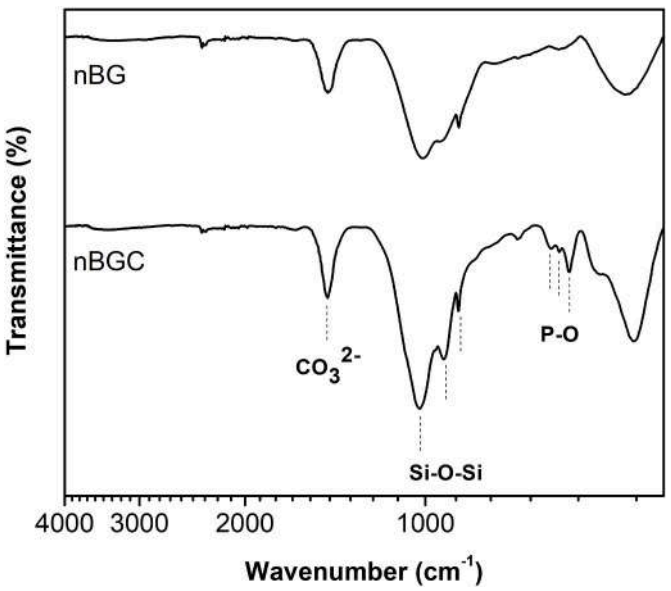


**Fig. 2.** IR spectra of the prepared powders by different synthesis routes: melt-quenching-derived (nBG) and sol-gel-derived (nBGC).

In the sol-gel approach, the as-synthesized sample consists of a dried gel which was thermally treated to stabilize the 3D silica network. The investigation of the thermal processes involved in the as-synthesized nBGC was carried out by TGA-DTA (Fig. 3). According to DTA, the

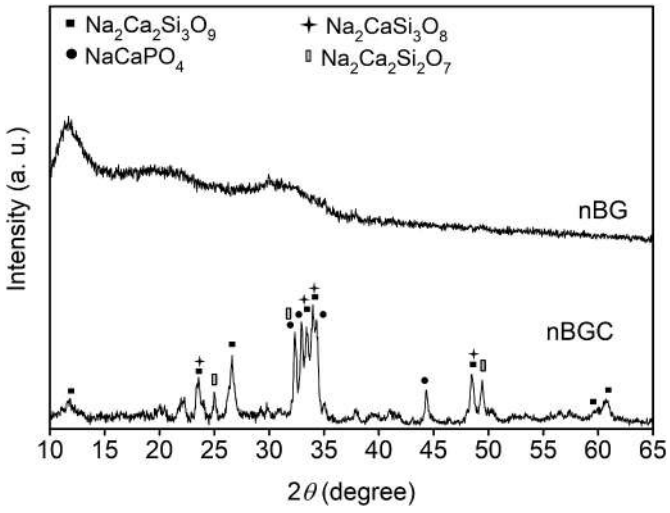


**Fig. 1.** Diffractograms of the prepared powders by different synthesis routes: melt-quenching-derived (nBG) and sol-gel-derived (nBGC).

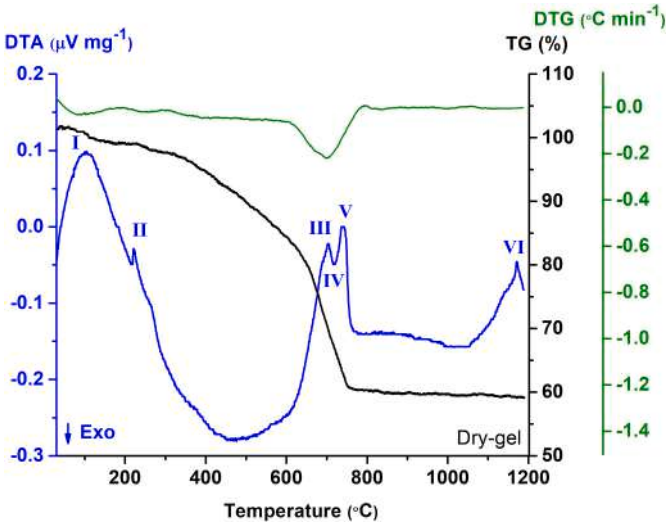


**Fig. 3.** Differential thermal analysis (TGA-DTA) of the as-synthesized sol-gel-derived sample.

crystallization in the nBGC sample occurs by an exothermic event (IV) with a maximum at 719 °C. This result conforms with the study of Massera et al. [30], in which the authors verified the crystallization for 45S5 sol-gel-derived BG from 600 °C to 715 °C. On the other hand, the diffractogram of the as-synthesized nBGC (Fig. S1.1 – Supplementary Information) reveals a sodium nitrate phase. This residual phase was identified in DTA as eliminated by endothermal events in the 600–780 °C range with $Na^+$ incorporation in the glass structure [13]. Besides that, it is possible to observe the contribution of two individual endothermal events in the range 600–780 °C with a total weight loss of 25%. Because citric acid was employed in the sol-gel synthesis, it is possible that citrate is present in the as-synthesized sample. Therefore, these two individual events can be associated with the removals of both nitrate and citrate residues. Furthermore, the mass invariant event (II) close to 220 °C was associated with the melting of calcium citrate [31]. On the other hand, events I and VI are related to ethanol and adsorbed water removal from the pores of the silica network, while the melting of the crystallized phases occurs during event IV, respectively [12,30]. The temperatures corresponding to the different events in the DTA curve are given in Table 1. A second differential thermal analysis for the reproduced sol-gel sample is shown in Supplementary Information (Fig. S1.2). Considering the present DTA results and other studies [13,27], we set 700 °C and 20 h to ensure the elimination of the residues in the as-synthesized sol-gel-derived dried gel. Also, while our DTA results suggested the presence of citrate, this phase was not identified in the X-ray diffractograms.

The chemical composition of the prepared powders evidences a similar but not identical formula to 45S5-Bioglass® (Table 2). The main difference verified is the sodium content with approximately 40 and 50% higher $Na_2O$ content for nBG and nBGC compositions, respectively, regarding 45S5 Bioglass. The main implication of the high sodium content is an increased reactivity which can make the glass-derived powders prepared in this work exhibit a higher dissolution rate than 45S5 Bioglass [8].

The nBG and nBGC powders reveal negative zeta potentials, namely $-3.1 \pm 1.6$ and $-4.93 \pm 0.60$ mV at pH ~7.00, respectively, indicating the negatively charged surface of the investigated powders at pH close to the values of the physiological environment [32]. A negative zeta potential has been shown to lead to a significant improvement of the attachment and proliferation of bone cells on bioactive glasses [33,34]. Therefore, the BG powders developed in this work can be promising materials for bone tissue engineering as their favorable surface characteristics should facilitate osteoblastic attachment.

The surface area of the powders was measured by $N_2$ adsorption to investigate possible effects of the synthesis history on this property. The sol-gel-derived nBGC exhibited approximately 30% higher specific area, 11 $m^2\ g^{-1}$, than the melt-quenching nBG sample, 7.8 $m^2\ g^{-1}$. This result indicates that the sol-gel-derived nBGC powder maintained a superior surface area in comparison to the melt-quenching-derived powder even after crystallization, which is a process accompanied by a significant loss of the porous structure [12,35]. According to SEM analysis (Fig. 4), the surface area of the samples is associated with powders composed of submicrometric particles with size distribution centered at 392 and 321 nm for nBG and nBGC, respectively, showing that the powders present particles with similar size. In both samples, the submicrometric particles are distributed in secondary aggregates. Nevertheless, melt-quenching-derived glass powders are known to result in particles exhibiting low specific area, typically in the range of 0.15–3.0 $m^2\ g^{-1}$. On the contrary, the sol-gel-derived ones can reach surface areas ~100 $m^2\ g^{-1}$ for more simple compositions such as $SiO_2$–CaO by controlling the surface charge and growth of the particles via chemical synthesis, which is particularly challenging for quaternary systems due to the difficulties in stabilizing the surface charges avoiding the coalescence of the particles during both synthesis and thermal treatment [10–12,15,36–38].

**Table 1**
The main thermal events identified in differential thermal analysis (TGA-DTA) of the as-synthesized sol-gel-derived sample.

| Event | $T_{max}$ (°C)[a] ± SD | Type of the process |
|---|---|---|
| I | 102 ± 3 | Endothermic |
| II | 222 ± 1 | Endothermic |
| III | 706 ± 0 | Endothermic |
| IV | 720 ± 1 | Exothermic |
| V | 739 ± 1 | Endothermic |
| VI | 1175 ± 5 | Endothermic |

[a] Corresponds to the temperature at the maximum point of the thermal event. The standard deviation (SD) for $n = 2$. Another analysis was performed for the reproduced synthesis and is available in Supplementary Information (Fig. S1. 2).

**Table 2**
Chemical composition by XRF analysis of the prepared powders: melt-quenching-derived (nBG) and sol-gel-derived (nBGC).

| | Chemical composition (*wt* %) | | | |
|---|---|---|---|---|
| | $SiO_2$ | $Na_2O$ | CaO | $P_2O_5$ |
| **nBG** | 40.2 | 34.7 | 18 | 7.1 |
| **nBGC** | 39.3 | 37.3 | 21.4 | 2 |
| **45S5*** | 45 | 24.5 | 24.5 | 6 |

(*) Established 45S5-Bioglass® composition.

Another observation that can be made from the SEM images is regarding the morphology of the particles. It is possible to identify that the nBGC sample shows a thinner length distribution associated with particles with rod-like morphology, while the nBG sample is composed of rounded particles (Fig. 4(a and b)). Nawaz et al., studied the crystallization process in a sol-gel-derived 45S5 BG [22]. These authors showed that the rod-like morphology is characteristic of sodium-calcium-silicate phases, such as $Na_2Ca_2Si_3O_9$, known as Combeite. Combeite is one of the crystalline phases identified in our XRD diffractogram for the nBGC powder. This crystalline phase has revealed osseointegration characteristics in *in vivo* studies [39]. From this set of results, it is possible to state that the glass-derived powders obtained in this work show potential to be applied in the biomedical field, particularly in the engineering of hard tissues, considering their favorable physicochemical characteristics. The powders were then evaluated regarding their *in vitro* mineralization capability and antibacterial effects.

### 3.2. Biological properties of the powders

*In vivo* bone-bonding ability of a material can be predicted by immersion tests in SBF solution by assessing the HA formation on the material's surface [21]. The apatite-forming ability of a material is strongly influenced by the materials' composition [21]. Standard bioactive glasses, for example, form an apatite-like phase within 5 days when soaking in SBF [21]. Therefore, the powders synthesized in this study were investigated regarding the presence of HA within five days of immersion in SBF. SEM micrographs obtained for the soaked specimens are shown in Fig. 5.

It is possible to observe in the micrographs that the surfaces of both nBG and nBGC samples are completely covered by a HA phase, evidencing that these powders are bioactive and should be capable of inducing mineralization in contact with body fluids (Fig. 5). The melt-quenching glass-derived sample exhibited micrometric HA crystals (micrographs A-C). Differently, the sol-gel-derived sample showed nanometric HA crystals (micrographs D-F). This result indicates the excellent ability of the powders to form HA in SBF in a short time. On the other hand, the difference observed in the HA crystal morphology suggests that the degree of mineralization in nBG was higher than in nBGC.

The IR spectra of the samples exposed to SBF revealed similar profiles for nBG and nBGC powders on the first day of immersion (Fig. 6). In these spectra, the shift of the Si–O vibrations around 1000-880 $cm^{-1}$

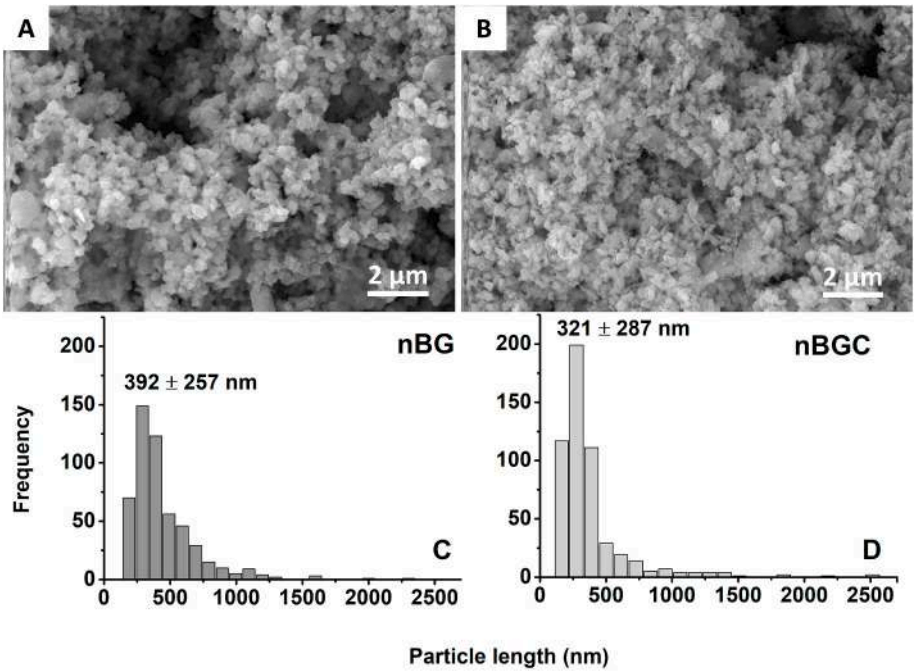


**Fig. 4.** SEM micrographs of the prepared powders by different synthesis routes: melt-quenching-derived (nBG, micrograph A), and sol-gel-derived (nBGC, micrograph B). Particle size distribution ($n = 524$): nBG (C) and nBGC (D).

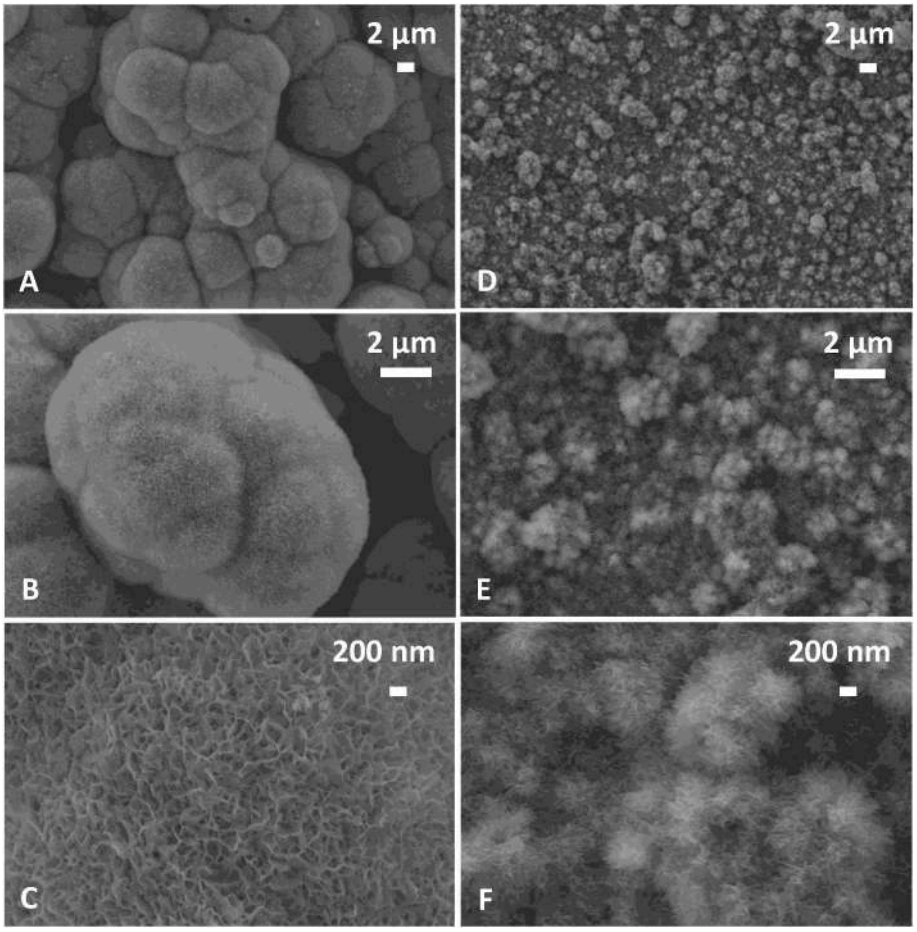


**Fig. 5.** SEM micrographs of the prepared powders by different synthesis routes immersed 5 days in SBF: melt-quenching-derived (nBG, micrographs A, B, and C), and sol-gel-derived (nBGC, micrographs D, E, and F).

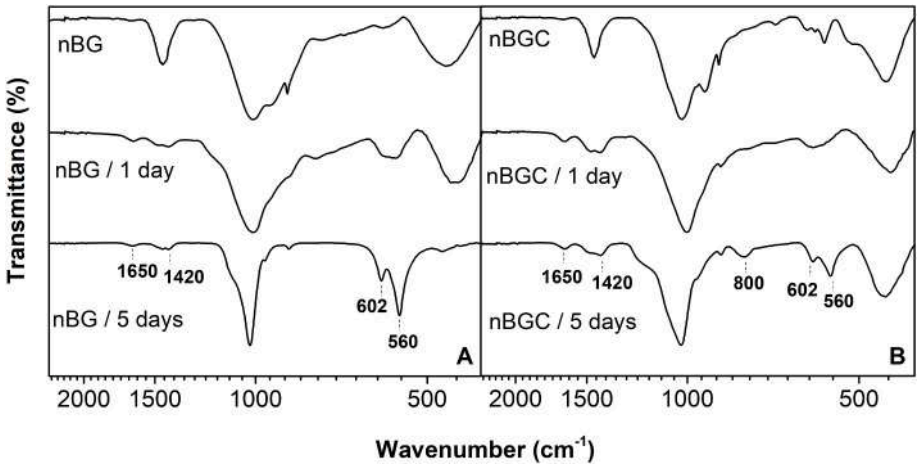


**Fig. 6.** IR spectra of the prepared powders by different synthesis routes and immersed for 1 and 5 days in SBF: melt-quenching-derived (nBG), and sol-gel-derived (nBGC).

indicates the beginning of the dissolution process. Unlike what was verified on the first day, it is possible to see remarkable changes after five days of immersion. The presence of vibrations at 1024 $cm^{-1}$, 602-506 $cm^{-1}$, and 1650, 1480-1420, and 800 $cm^{-1}$, assigned to the asymmetric stretching of P–O, crystalline phosphate, and new carbonate signals, respectively, evidence the formation of hydroxycarbonate-apatite (HCA) on the samples on the fifth day of immersion, complementing the SEM observations (Fig. 5). Furthermore, the disappearance of the peak associated with the Si–O bending mode at 460 $cm^{-1}$ in nBG reinforces the idea of a higher degree of HCA formation on their surfaces in comparison to nBGC. This difference can be attributed to the distinct structural characteristics showed by these materials. As expected, because glasses are in a thermodynamically unstable state, bioactive glasses present higher reactivity and faster HA formation than their corresponding glass-ceramics [40,41].

Bioactive glasses exposure to physiological conditions can lead to an initial increase in the pH of the medium. As discussed in the literature, the glass first releases cations such as $Na^+$ and $Ca^{2+}$ into the physiological solution and then captures protons to form a silica-gel layer on its surface [1,42]. However, a dramatic increase of pH (pH > 8.5) can reduce the attachment and stability of proteins related to bone regeneration, such as collagen [43,44]. Therefore, pH changes induced by the samples in SBF solution were measured. Fig. 7 shows that both samples demonstrated a major pH increase in the first 24 h (nBG = 7.82 ± 0.02, nBGC 7.94 ± 0.04). After 48 h, the systems reached saturation. At 72 h a pH decrease occurred due to the replace of the SBF solution. Next, pH increase was observed again but in a less extent, verified at 96 h (nBG = 7.73 ± 0.02, nBGC = 7.85 ± 0.02). This result suggests a rapid release of cations with $H^+$ consumption in the first hours, followed by an overall pH decrease over time. Bellucci et al., found that pH changes induced by 45S5 BG dissolution in SBF stabilizes after three weeks [44]. On the other hand, the higher increase for nBGC indicates a faster initial dissolution than for nBG. This feature can be related to the higher specific area exhibited by the sol-gel-derived glass-ceramic, which may enhance the contact of the material with the solution supplementing the diffusion of ions and the capture of $H^+$ species.

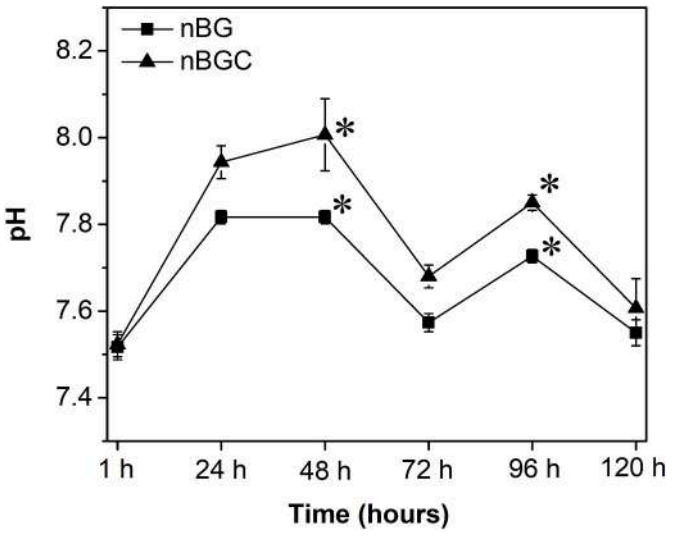


**Fig. 7.** pH values of the prepared powders by different synthesis routes and immersed in SBF: melt-quenching-derived (nBG), and sol-gel-derived (nBGC). * Indicates SBF solution replacement.

The concentrations of sodium, calcium, and phosphorous in SBF solution after five days of exposure to SBF were determined by ICP-OES, and the results are presented in Fig. 8. The samples released similar concentrations of $Na^+$ cations (~17%) in SBF (Table 3). However, the $Ca^{2+}$ concentration was significantly different between the samples decreasing by 40% for nBG and increasing by 46% for nBGC (Table 3). The phosphorus concentration was similar in both samples, decreasing 95%. The calcium and phosphorous reduction observed in SBF are related to the HCA formation on the surface of the powders. On the other hand, the higher calcium concentration (68%) in the solution exposed to the nBGC sample suggests that this powder released more calcium cations than consumed. This observation can be related to at least two mechanisms. First, the nBGC powder presents approximately 12.5% (*w/w*) more calcium atoms in its composition than nBG, therefore it can release a higher amount of this element in the SBF solution (Table 2). The second aspect relates to the amount of HCA formed on the powders' surfaces, in which the lower concentration of calcium in SBF exposed to nBG evidences a higher degree of HCA formed onto the surface of this sample. This last observation correlates well with the tendency verified by SEM for nBG, showing the surface covered by micrometric HCA crystals as discussed in the previous paragraphs (Fig. 5).

### 3.3. Antibacterial activity

The ability of a biomedical implant to prevent infections increases its implantation success [45]. Bioactive glasses and glass-ceramics can present antibacterial activity by releasing their respective ionic products in a controlled manner under physiological conditions. This release causes changes in pH and osmolarity of the microenvironment, leading to bacterial cell permeability, followed by the unbalancing of the

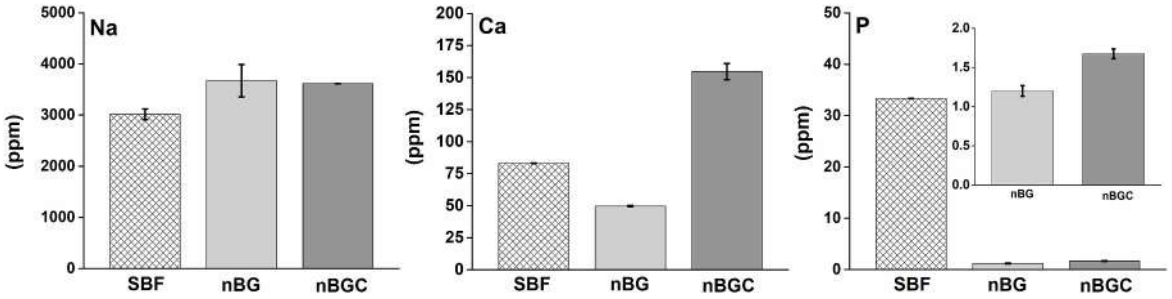


**Fig. 8.** Different concentration of sodium (Na), calcium (Ca), and phosphorous (P) were determined by ICP OES in SBF solution exposed to nBG and nBGC powders for five days.

**Table 3**
Sodium, calcium, and phosphorus concentrations in ppm (mg $L^{-1}$) were investigated for the SBF solution exposed to nBG and nBGC powders for five days at 37 °C, and determined by ICP OES analysis.

| Element | SBF | nBG | nBGCs |
|---|---|---|---|
| | (ppm)* | (ppm)* | (ppm)* |
| Na | 3016 ± 103 | 3671 ± 312 | 3616 ± 1.8 |
| Ca | 83.1 ± 0.12 | 49.7 ± 0.42 | 154.8 ± 6.3 |
| P | 33.3 ± 0.02 | 1.20 ± 0.067 | 1.67 ± 0.062 |

(*) Standard deviation for $n = 2$.

intracellular alkaline ions. The death of the pathogen occurs with the bacterium cell membrane depolarization in a subsequent step [27]. Besides that, researchers have doped bioactive glasses with various metal ions (e. g. Ag, Cu, Zn) to improve the antibacterial activity [46].

Here, we investigated the bactericidal effect of the powders developed against *S. aureus*. This gram-positive bacterium is the major opportunistic human pathogen found in hospital environments and can cause invasive infections when it grows in internal tissues such as bone [47–50]. The *S. aureus* growth was evaluated for the extracts obtained by culture medium in contact with different powder concentrations for 24 h, and the results are shown in Fig. 9.

The extracts for both glass-derived powders resulted in significantly lower optical densities than the control, indicating that the powders present a bactericidal effect against *S. aureus* (Fig. 9). All concentrations of both samples killed bacteria, with an optical density close to zero, except for 12.5 mg $mL^{-1}$ of nBG powder, which demonstrated an inhibitory action controlling the growth in 60%. The measured pH values from the extracts' aliquot for the samples at 12.5 mg $mL^{-1}$ before incubation with bacteria were: 6.70 ± 0.01 (Control), 9.30 ± 0.07 (nBG), and 9.72 ± 0.05 (nBGC). The higher pH found for the extracts exposed to the nBGC sample provides a possible explanation for the superior bactericidal performance of these particles compared to nBG at the same concentration (12.5 mg $mL^{-1}$). Still, more detailed studies are necessary to elucidate the release profile of the different powders over time. Another observation is that the pH values in the LB medium were higher than those verified in SBF. This variation can be explained by using particulate powders instead of compacted powders in addition to the different types of media (Fig. 7).

Our results for antibacterial activity contrasts with a study of Mubina et al. [27]. That study exploited the antibacterial properties of a quaternary sol-gel-derived glass-ceramic at 10 and 50 mg $mL^{-1}$ concentrations. The authors observed only an inhibitory effect against *S. aureus*, but not the bacteria death. However, there is no mention of the pH values for the extracts in those antibacterial tests. On the other hand, this difference verified can be related to the specific physicochemical characteristics of each glass-ceramic, such as morphology and particle size. In another study, the authors identified a pH of around nine as effective for growth inhibition of various aerobic bacteria species [51]. Additionally, the authors verified the contribution of the alkali ionic concentration released by the glasses to the antibacterial effect [51]. However, the bactericidal effect was achieved only for concentrations of 50 and 100 mg $mL^{-1}$. On the contrary, nBG and nBGC powders in this study showed antibacterial behavior for concentrations from 12.5 mg $mL^{-1}$, which also was superior to the bactericidal effect for particulate 45S5-Bioglass® against *S aureus* as demonstrated by Hu et al. [52]. In this last case, an inhibition >98% with pH > 9 was verified only for concentrations from 50 mg $mL^{-1}$, suggesting that nBG and nBGC powders present higher reactivity than the commercial 45S5 bioactive glass as previously discussed in Section 3.1. Therefore, the prepared glass-derived powders present bioactivity for tissue mineralization and potential as raw materials for the fabrication of antimicrobial composites. Future investigations based on the findings of this work will focus on studying the long-term dissolution kinetics of these glass-derived powders and the viability assessment of osteoblast cells in contact

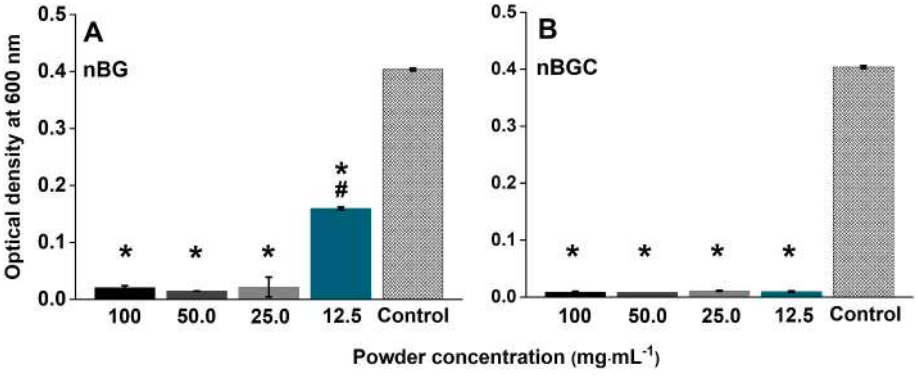


**Fig. 9.** The optical density of gram-positive bacteria *Staphylococcus aureus* cultured for 24 h with the extract's medium previously incubated with sterile LB medium for 24 h in a series of powder concentrations (12.5–100 mg $mL^{-1}$): melt-quenching-derived (A), and sol-gel-derived (B). * Indicates statistical significance ($p < 0.05$) with the control, and # indicates statistical significance ($p < 0.01$) between the samples.

with the dissolution products of the glass-derived powders.

## 4. Conclusions

$SiO_2$–$Na_2O$–CaO–$P_2O_5$ glass-derived powders presenting antibacterial behavior and bioactivity for bone mineralization were successfully prepared using the melt-quenching and sol-gel approaches. These synthesis routes promoted different structural, morphological, and textural characteristics in the materials, leading to distinct biological properties. The melt-quenching-derived powder showed an *in vitro* pH close to the physiological conditions, and micrometric HCA crystals formed on the surface after immersion in SBF. The sol-gel-derived powder exhibited an elevated biocidal effect against *S. aureus* attributed to the increase in the physiological pH value. This increase was induced by the dissolution of the remaining glassy phase in the glass-ceramic structure and supplemented by the relatively high specific area demonstrated by the powder. From the outcomes of this work, it is possible to conclude that the bioactive BG powders developed show potential as inorganic bioactive biomaterials for preventing infection and regenerating hard tissues.

## Author contributions

Emerson R. de Camargo and Sara Novak conceptualized the study. Sara Novak performed the biological tests, characterization, and sol-gel synthesis. Juliane R. Orives and Marcelo Nalin prepared the melt-quenching glass. Irem Unalan designed and supervised the antibacterial tests. Emerson R. de Camargo and Aldo R. Boccaccini contributed with resources and supervision. Sara Novak wrote the original draft of the manuscript, and all authors commented on previous versions and approved the final manuscript.

## Declaration of competing interest

The authors declare that they have no known competing financial interests or personal relationships that could have appeared to influence the work reported in this paper.

## Acknowledgements

The authors acknowledge the funding agencies: This study was financed in part by Coordenação de Aperfeiçoamento de Pessoal de Nível Superior (CAPES, Finance Code 001), Conselho de Desenvolvimento Científico e Tecnológico (CNPq, grant #309711/2019-3), São Paulo State Research Foundation (FAPESP, grants #2013/07296-2, #2013/07793-6 and #2019/19609-1), and Deutscher Akademischer Austauschdienst (DAAD) (Co-financed Short-Term Research Grant 57552395).

Dr. Ricardo Luis Tranquilin for the SEM images.

## Appendix A. Supplementary data

Supplementary data to this article can be found online at https://doi.org/10.1016/j.ceramint.2022.06.266.

## References

[1] L.L. Hench, The story of Bioglass, J. Mater. Sci. Mater. Med. 17 (2006) 967–978, https://doi.org/10.1007/s10856-006-0432-z.
[2] J.R. Jones, Reprint of: review of bioactive glass: from Hench to hybrids, Acta Biomater. 23 (2015), https://doi.org/10.1016/j.actbio.2015.07.019. S53–S82.
[3] K.E. Wallace, R.G. Hill, J.T. Pembroke, C.J. Brown, P.v. Hatton, Influence of sodium oxide content on bioactive glass properties, J. Mater. Sci. Mater. Med. 10 (1999) 697–701, https://doi.org/10.1023/A:1008910718446.
[4] L. Souza, J.H. Lopes, D. Encarnação, I.O. Mazali, R.A. Martin, J.A. Camilli, C. A. Bertran, Comprehensive in vitro and in vivo studies of novel melt-derived Nb-substituted 45S5 bioglass reveal its enhanced bioactive properties for bone healing, Sci. Rep. 8 (2018), 12808, https://doi.org/10.1038/s41598-018-31114-0.
[5] N.J. Lakhkar, I.-H. Lee, H.-W. Kim, V. Salih, I.B. Wall, J.C. Knowles, Bone formation controlled by biologically relevant inorganic ions: role and controlled delivery from phosphate-based glasses, Adv. Drug Deliv. Rev. 65 (2013) 405–420, https://doi.org/10.1016/j.addr.2012.05.015.
[6] X. Chen, X. Chen, D.S. Brauer, R.M. Wilson, R.v. Law, R.G. Hill, N. Karpukhina, Sodium is not essential for high bioactivity of glasses, Int. J. Appl. Glass Sci. 8 (2017) 428–437, https://doi.org/10.1111/ijag.12323.
[7] W.S. Abushanab, E.B. Moustafa, R.A. Youness, Evaluation of the dynamic behavior, elastic properties, and in vitro bioactivity of some borophosphosilicate glasses for orthopedic applications, J. Non-Cryst. Solids 586 (2022), 121539, https://doi.org/10.1016/j.jnoncrysol.2022.121539.
[8] H.R. Fernandes, A. Gaddam, A. Rebelo, D. Brazete, G.E. Stan, J.M.F. Ferreira, Bioactive glasses and glass-ceramics for healthcare applications in bone regeneration and tissue engineering, Materials 11 (2018) 2530, https://doi.org/10.3390/ma11122530.
[9] K. Zheng, A.R. Boccaccini, Sol-gel processing of bioactive glass nanoparticles: a review, Adv. Colloid Interface Sci. 249 (2017) 363–373, https://doi.org/10.1016/j.cis.2017.03.008.
[10] O. Tsigkou, S. Labbaf, M.M. Stevens, A.E. Porter, J.R. Jones, Monodispersed bioactive glass submicron particles and their effect on bone marrow and adipose tissue-derived stem cells, Adv. Healthc. Mater. 3 (2014) 115–125, https://doi.org/10.1002/adhm.201300126.
[11] G.M. Luz, J.F. Mano, Preparation and characterization of bioactive glass nanoparticles prepared by sol–gel for biomedical applications, Nanotechnology 22 (2011), 494014, https://doi.org/10.1088/0957-4484/22/49/494014.
[12] L.L. Hench, J.K. West, The sol-gel process, Chem. Rev. 90 (1990) 33–72, https://doi.org/10.1021/cr00099a003.
[13] H. Pirayesh, J.A. Nychka, Sol-gel synthesis of bioactive glass-ceramic 45S5 and its in vitro dissolution and mineralization behavior, J. Am. Ceram. Soc. 96 (2013) 1643–1650, https://doi.org/10.1111/jace.12190.
[14] E. Rezabeigi, P.M. Wood-Adams, R.A.L. Drew, Synthesis of 45S5 Bioglass® via a straightforward organic, nitrate-free sol–gel process, Mater. Sci. Eng. C 40 (2014) 248–252, https://doi.org/10.1016/j.msec.2014.03.042.
[15] S. Labbaf, O. Tsigkou, K.H. Müller, M.M. Stevens, A.E. Porter, J.R. Jones, Spherical bioactive glass particles and their interaction with human mesenchymal stem cells in vitro, Biomaterials 32 (2011) 1010–1018, https://doi.org/10.1016/j.biomaterials.2010.08.082.
[16] M. Erol-Taygun, I. Unalan, M.I.B. Idris, J.F. Mano, A.R. Boccaccini, Bioactive glass-polymer nanocomposites for bone tissue regeneration applications: a review, Adv. Eng. Mater. 21 (2019), 1900287, https://doi.org/10.1002/adem.201900287.
[17] K. Kolan, Y. Liu, J. Baldridge, C. Murphy, J. Semon, D. Day, M. Leu, Solvent based 3D printing of biopolymer/bioactive glass composite and hydrogel for tissue engineering applications, Procedia CIRP 65 (2017) 38–43, https://doi.org/10.1016/j.procir.2017.04.022.
[18] C.A. Schneider, W.S. Rasband, K.W. Eliceiri, NIH Image to ImageJ: 25 years of image analysis, Nat. Methods 9 (2012) 671–675, https://doi.org/10.1038/nmeth.2089.
[19] S. Brunauer, P.H. Emmett, E. Teller, Adsorption of gases in multimolecular layers, J. Am. Chem. Soc. 60 (1938) 309–319, https://doi.org/10.1021/ja01269a023.
[20] S.J. Gregg, K.S.W. Sing, Adsorption, Surface Area and Porosity, second ed., Academic Press, London, 1982.
[21] T. Kokubo, H. Takadama, How useful is SBF in predicting in vivo bone bioactivity? Biomaterials 27 (2006) 2907–2915, https://doi.org/10.1016/j.biomaterials.2006.01.017.
[22] Q. Nawaz, A. de Pablos-Martín, J. Martins de Souza e Silva, K. Hurle, A.T. C. Jaimes, D.S. Brauer, A.R. Boccaccini, New insights into the crystallization process of sol-gel–derived 45S5 bioactive glass, J. Am. Ceram. Soc. 103 (2020) 4234–4247, https://doi.org/10.1111/jace.17124.
[23] Q.Z. Chen, Y. Li, L.Y. Jin, J.M.W. Quinn, P.A. Komesaroff, A new sol-gel process for producing Na2O-containing bioactive glass ceramics, Acta Biomater. 6 (2010) 4143–4153, https://doi.org/10.1016/j.actbio.2010.04.022.
[24] L. Lefebvre, J. Chevalier, L. Gremillard, R. Zenati, G. Thollet, D. Bernache-Assolant, A. Govin, Structural transformations of bioactive glass 45S5 with thermal treatments, Acta Mater. 55 (2007) 3305–3313, https://doi.org/10.1016/j.actamat.2007.01.029.
[25] A.R. Boccaccini, Q. Chen, L. Lefebvre, L. Gremillard, J. Chevalier, Sintering, crystallisation and biodegradation behaviour of Bioglass®-derived glass-ceramics, Faraday Discuss 136 (2007) 27–44, https://doi.org/10.1039/b616539g.
[26] A. Lucas-Girot, F.Z. Mezahi, M. Mami, H. Oudadesse, A. Harabi, M. le Floch, Sol-gel synthesis of a new composition of bioactive glass in the quaternary system SiO2-CaO-Na2O-P2O5: comparison with melting method, J. Non-Cryst. Solids 357 (2011) 3322–3327, https://doi.org/10.1016/j.jnoncrysol.2011.06.002.
[27] M.S.K. Mubina, S. Shailajha, R. Sankaranarayanan, L. Saranya, In vitro bioactivity, mechanical behavior and antibacterial properties of mesoporous SiO2-CaO-Na2O-P2O5 nano bioactive glass ceramics, J. Mech. Behav. Biomed. Mater. 100 (2019), https://doi.org/10.1016/j.jmbbm.2019.103379.
[28] A. Perardi, M. Cerruti, C. Morterra, Carbonate formation on sol-gel bioactive glass 58S and on Bioglass® 45S5, Stud. Surf. Sci. Catal. 155 (2005) 461–469, https://doi.org/10.1016/S0167-2991(05)80173-9.
[29] M. Cerruti, C. Morterra, Carbonate formation on bioactive glasses, Langmuir 20 (2004) 6382–6388, https://doi.org/10.1021/la049723c.
[30] J. Massera, S. Fagerlund, L. Hupa, M. Hupa, Crystallization mechanism of the bioactive glasses, 45S5 and S53P4, J. Am. Ceram. Soc. 95 (2012) 607–613, https://doi.org/10.1111/j.1551-2916.2011.05012.x.
[31] S.A.A. Mansour, Thermal decomposition of calcium citrate tetrahydrate, Thermochim. Acta 233 (1994) 243–256, https://doi.org/10.1016/0040-6031(94)85118-2.

[32] J.C. Berkmann, A.X.H. Martin, A. Ellinghaus, C. Schlundt, H. Schell, E. Lippens, G. N. Duda, S. Tsitsilonis, K. Schmidt-Bleek, Early pH changes in musculoskeletal tissues upon injury—aerobic catabolic pathway activity linked to inter-individual differences in local pH, Int. J. Mol. Sci. 21 (2020), https://doi.org/10.3390/ijms21072513.

[33] N.C. Teng, S. Nakamura, Y. Takagi, Y. Yamashita, M. Ohgaki, K. Yamashita, A new approach to enhancement of bone formation by electrically polarized hydroxyapatite, J. Dent. Res. 80 (2001), https://doi.org/10.1177/00220345010800101201, 1925–1929.

[34] A. Doostmohammadi, A. Monshi, R. Salehi, M.H. Fathi, Z. Golniya, A.U. Daniels, Bioactive glass nanoparticles with negative zeta potential, Ceram. Int. 37 (2011) 2311–2316, https://doi.org/10.1016/j.ceramint.2011.03.026.

[35] R. Bento, A. Gaddam, J.M.F. Ferreira, Sol–gel synthesis and characterization of a quaternary bioglass for bone regeneration and tissue engineering, Materials 14 (2021), https://doi.org/10.3390/ma14164515.

[36] T.H. Dang, T.H. Bui, E.v. Guseva, A.T. Ta, A.T. Nguyen, T.T.H. Hoang, X.V. Bui, Characterization of bioactive glass synthesized by sol-gel process in hot water, Crystals 10 (2020) 1–10, https://doi.org/10.3390/cryst10060529.

[37] P. Sepulveda, J.R. Jones, L.L. Hench, Characterization of Melt-Derived 45S5 and Sol-Gel-Derived 58S Bioactive Glasses, 2001, https://doi.org/10.1002/jbm.0000.

[38] S. Agathopoulos, D.U. Tulyaganov, J.M.G. Ventura, S. Kannan, M.A. Karakassides, J.M.F. Ferreira, Formation of hydroxyapatite onto glasses of the CaO-MgO-SiO2 system with B2O3, Na2O, CaF2 and P2O5 additives, Biomaterials 27 (2006) 1832–1840, https://doi.org/10.1016/j.biomaterials.2005.10.033.

[39] M. Plewinski, K. Schickle, M. Lindner, A. Kirsten, M. Weber, H. Fischer, The effect of crystallization of bioactive bioglass 45S5 on apatite formation and degradation, Dent. Mater. 29 (2013) 1256–1264, https://doi.org/10.1016/j.dental.2013.09.016.

[40] O.P. Filho, G.P. la Torre, L.L. Hench, Effect of crystallization on apatite-layer formation of bioactive glass 45S5, J. Biomed. Mater. Res. 30 (1996) 509–514. https://doi.org/10.1002/(SICI)1097-4636(199604)30:4<509::AID-JBM9>3.0.CO;2-T.

[41] E.D. Zanotto, J.C. Mauro, The glassy state of matter: its definition and ultimate fate, J. Non-Cryst. Solids 471 (2017) 490–495, https://doi.org/10.1016/j.jnoncrysol.2017.05.019.

[42] O. Peitl, E. Dutra Zanotto, L.L. Hench, Highly bioactive P2O5–Na2O–CaO–SiO2 glass-ceramics, J. Non-Cryst. Solids 292 (2001) 115–126, https://doi.org/10.1016/S0022-3093(01)00822-5.

[43] Q.Z. Chen, I. Ahmed, J.C. Knowles, S.N. Nazhat, A.R. Boccaccini, K. Rezwan, Collagen release kinetics of surface functionalized 45S5 Bioglass®-based porous scaffolds, J. Biomed. Mater. Res. 86A (2008) 987–995, https://doi.org/10.1002/jbm.a.31718.

[44] D. Bellucci, V. Cannillo, A. Sola, F. Chiellini, M. Gazzarri, C. Migone, Macroporous Bioglass®-derived scaffolds for bone tissue regeneration, Ceram. Int. 37 (2011) 1575–1585, https://doi.org/10.1016/j.ceramint.2011.01.023.

[45] E. Zhang, X. Zhao, J. Hu, R. Wang, S. Fu, G. Qin, Antibacterial metals and alloys for potential biomedical implants, Bioact. Mater. 6 (2021) 2569–2612, https://doi.org/10.1016/j.bioactmat.2021.01.030.

[46] A. Hoppe, N.S. Güldal, A.R. Boccaccini, A review of the biological response to ionic dissolution products from bioactive glasses and glass-ceramics, Biomaterials 32 (2011) 2757–2774, https://doi.org/10.1016/j.biomaterials.2011.01.004.

[47] G. Mancuso, A. Midiri, E. Gerace, C. Biondo, Bacterial antibiotic resistance: the most critical pathogens, Pathogens 10 (2021) 1310, https://doi.org/10.3390/pathogens10101310.

[48] F. Li, D. Zhai, Z. Wu, Y. Zhao, D. Qiao, X. Zhao, Impairment of the cell wall ligase, LytR-CpsA-psr protein (LcpC), in methicillin resistant Staphylococcus aureus reduces its resistance to antibiotics and infection in a mouse model of sepsis, Front. Microbiol. 11 (2020), https://doi.org/10.3389/fmicb.2020.00557.

[49] J.M. Monteiro, G. Covas, D. Rausch, S.R. Filipe, T. Schneider, H.G. Sahl, M. G. Pinho, The pentaglycine bridges of Staphylococcus aureus peptidoglycan are essential for cell integrity, Sci. Rep. 9 (2019), https://doi.org/10.1038/s41598-019-41461-1.

[50] Q. Wen, F. Gu, Z. Sui, Z. Su, T. Yu, The process of osteoblastic infection by Staphylococcus aureus, Int. J. Med. Sci. 17 (2020) 1327–1332, https://doi.org/10.7150/ijms.45960.

[51] D. Zhang, O. Leppäranta, E. Munukka, H. Ylänen, M.K. Viljanen, E. Eerola, M. Hupa, L. Hupa, Antibacterial effects and dissolution behavior of six bioactive glasses, J. Biomed. Mater. Res., Part A 93 (2010) 475–483, https://doi.org/10.1002/jbm.a.32564.

[52] S. Hu, J. Chang, M. Liu, C. Ning, Study on antibacterial effect of 45S5 Bioglass, J. Mater. Sci. Mater. Med. 20 (2009) 281–286, https://doi.org/10.1007/s10856-008-3564-5.

# Managing the growth of micrometer-sized TGG single crystals from heavy metal oxide glass melts-The supersaturated solution methodology

Juliane Resges Orives, Thiago A. Lodi, Lia Mara Silva Marcondes, Camila Batista Pinto, Victória Mamelli, Antonio Eduardo Souza, Fabricio B. Destro, Juliani Caland, Javier Alcides Ellena, Thierry Cardinal, Marc Dussauze, Jorlandio Felix, Marcelo Nalin

(*) Corresponding author.

(**) Corresponding author

E-mail: juliane.resges@unesp.br (J. R. Orives), marcelo.nalin@unesp.br (M. Nalin).

**Key words**: terbium gallium garnet, melt-quenching, heavy metal glasses, glass ceramics

## 1. Introduction

The development of new materials with special photonic properties is essential to address the main current challenges in applications such as scintillators, mid-infrared greenhouse gas sensors, luminescent thermometry, light emitting diodes, magneto-optical and magneto-luminescent devices, among others. [1-8]

Special ceramics, such as those based on garnets, have attracted attention in many recent applications. Among the garnets, those based on aluminum and gallium are applied in many of the applications mentioned above. $RE_3Ga_5O_{12}$ and $RE_3Al_5O_{12}$(RE = rare earth) garnet crystals in glass matrices has recently been highlighted due to its important fundamental and technological properties. Among the garnet-type crystals, the terbium gallium garnet ($Tb_3Ga_5O_{12}$ or TGG) is the single crystal most used commercially as a Faraday rotator device due to its high verdet constant. [7-9]

In addition to its magnetic and magneto-optical properties, TGG has excellent optical quality, it is mechanically hard, chemically stable, and has interesting luminescent properties since the $Tb^{3+}$ ion exhibits green emission near 544 nm due to the $^5D_4 \rightarrow {}^7F_5$ transition. [9-15]

TGG can be obtained in different formats, such as single crystals, nanoparticles, polycrystalline ceramics and bulk.[12,16-20] Several synthesis methods have been reported, for example, solid-state reaction, micro-pulling-down, floating-zone, metal-organic decomposition, co-precipitation of nanoparticles, and the most popular Czochralski method.[21-28]

Despite the various synthesis methods, the production on a large scale faces some difficulties such as low quality of the crystal, significant long time for crystal growth and high cost to manufacture.[26] In this way, due to the great possibility of TGG applications, the need to find new methodologies of obtaining these single crystals remains in focus.

The synthesis of new glass compositions, as well as the advances in understanding of the chemistry of their formation, allows us to obtain

compositions where the formation of crystals in the glass phase can be controlled. The glass materials have a structure similar to its original super-cooled liquid, and one of its most interesting properties is the possibility of dispersing other chemical elements in its composition, such as, for example, metal ions or rare-earths, and from them it is possible to grow nanocrystals and mocrocrystals in the glass matrix.[29-32]

In addition to being able to explore the properties of glass ceramics, there is also the possibility of removing crystals from the glass matrix, which has not yet been explored in the literature. This approach could generate a wide range of applications.

Heavy metal oxide glasses can be a good alternative for obtaining single crystals of TGG, as they are materials that are easy to obtain on a large scale, they have important properties such as good infrared transparency from the visible up to medium infrared region, low phonon energy, high refractive index, good chemical stability, among others.[32-33]

The growth of TGG single phase within a glassy matrix is a complicated task. The main challenge is to obtain a glass with good optical properties, with crystals having active terbium ions within the crystalline phase distributed in a homogeneous way in the matrix. Furthermore, in multicomponent compositions, other phases in addition to TGG can also be obtained.

Promising results of obtaining $Er^{3+}/Tm^{3+}$- doped cubic $Yb_3Ga_5O_{12}$ single-crystals dispersed in a germano-gallate glass system were presented by Nalin et al, showing that it may be possible to obtain the TGG crystal once the two crystals belong to the same garnet family.[32]

The obtaining of crystals in glasses can occur by heat treating the sample above glass transition temperature or from the melt of glass precursors at high temperatures followed by controlled cooling to induce nucleation and consequently crystal growth.[28-31] Crystallization from the melt is a complex process that requires the formation of supersaturated solutions, since a new phase can occur only when a system is in a non-equilibrium condition, followed by the aggregation of dissolved ions to relieve the supersaturation allowing the system to move toward equilibrium.[34-35]

Both composition and cooling rate conditions have an important role in determining the structural phase and size of the resulting crystals. Furthermore,

uniform nucleation and growth are important to have crystals distributed throughout the glass volume.[34-35]

In this context, the objective of this work was to synthesize micrometric TGG single crystals embedding in heavy metal oxide glass in an easy, controlled and reproducible way. Furthermore, a method for extracting the crystals from the glass matrix is demonstrated. A systematic study of the structural, morphological, optical, luminescent and magnetic properties of glass ceramics and single crystals is also presented.

## 2. Experimental

### 2.1. Glass ceramics preparation and crystal isolation

Multicomponent heavy metal oxide bulk glasses with molar composition 40PbO-25$Bi_2O_3$-20$GeO_2$-15$Ga_2O_3$ and 98.5(40PbO-25$Bi_2O_3$-20$GeO_2$-15$Ga_2O_3$)-1,5$Tb_4O_7$ were studied. The following analytical grade raw materials were used: $GeO_2$ (99.999%), $Ga_2O_3$ (99.99%) and $Bi_2O_3$ (99.975%) from Alfa Aesar, PbO (99.0% - Fluka), $Tb_4O_7$ from REEtec (99,96%).

To control the quantity and the size of crystals obtained, two methodologies were used; The first consisting of pouring the melt into the mold by melt-quenching process at different times and the second carried out by controlled cooling of the melt inside the furnace.

In the first case, the precursors were melted at 1250 °C for 2 h for full homogenization. Then, samples containing terbium were stirred at 0, 2, 3 and 4 seconds before being poured into a steel mold preheated at 350 ºC and labeled respectively as (PGBG-Tb-0), (PGBG-Tb-2), (PGBG-Tb-3) (PGBG-Tb-4) (Figure S1). The sample without terbium was labeled as PGBG. The glasses were polished with sandpapers for improving their optical quality.

In the second case, the precursors were melted at 1250 °C for 2 h for full homogenization and then the furnace was programmed to cool down at a rate of 10 °C/ min until reaching 900° C, then the sample was removed from the furnace at this temperature.

To extract the crystals from the glass matrix, the glass ceramic was immersed into concentrated nitric acid during 24 h. Finally, after dissolving the

glass material, the crystals were washed with distilled water for several times and dried in an oven at 100 ºC.

### 2.2. Characterization techniques

Optical images were collected using an optical microscope Leica DM2500M model. The UV-Vis absorption spectra (in the spectral range from 450 to 2500 nm) were recorded using a Varian Cary 5000 UV-Vis-Near infrared (NIR) spectrophotometer, on the polished samples of 1.5 mm thickness. Micro-luminescence data was acquired using a Labram (Horiba) spectrometer with a laser source at 488 $cm^{-1}$, a 150 grooves·$cm^{-1}$ grating and 50× (N.A.= 0.54) objective. Then, micro-Raman was acquired from a spectrometer HR800 (Horiba/Jobin Yvon) with a 100× (N.A.= 0.9) objective with an CW laser operating at 532 nm. The X-ray powder diffraction of (PGBG-Tb-4) was carried out with a Bruker D8 Advance diffractometer operating with a Ni filtered CuKα radiation source at 2θ angle ranging from 10 to 80 º with a step pass of 0.02 º and a step time of 2 s. Scanning electron microscopy images, Energy-dispersive X-ray spectroscopy (EDS) and elemental mapping were obtained on a microscopy JEOL-SJSMT-IT500HR. The crystals were carbon-coated to about 5 nm thickness using a Sample Sputter Coater SCD 050™ (Bal-Tec, Wallruf, Germany). X-ray data collection for the single crystal was performed on a XtaLAB Synergy-S Dualflex diffractometer, equipped with a HyPix-6000HE detector and microfocus sealed tube X-ray source. Data was collected at 100 K using Mo *Kα* radiation (λ = 0.71073 Å). Data collection, reduction and absorption correction were conducted with the CrysAlisPro software.[36] The structure was solved with SHELXT 2018/2 program[37] using the Intrinsic Phasing method and refined on $F^2$ with SHELXL 2019/2[38] through the full-matrix least-squares method, using *Olex2*[39] as graphical interface. The program VESTA[40] was used for preparation of graphics as well as for calculations concerning the coordination centers. Further experimental details are found in Table 1.

**Table 1.** X-ray experimental details for the single crystal.

| | |
|---|---|
| ***Crystal data*** | |
| Chemical formula | $Tb_3Ga_5O_{12}$ |
| $M_r$ | 1017.36 |

| | |
|---|---|
| Crystal system, space group | Cubic, $Ia\bar{3}d$ |
| Temperature (K) | 100 |
| $a$ (Å) | 12.3539 (3) |
| $V$ (Å$^3$) | 1885.44 (14) |
| $Z$ | 8 |
| Radiation type | Mo $K\alpha$ |
| $\mu$ (mm$^{-1}$) | 36.32 |
| Crystal size (mm) | 0.14 × 0.11 × 0.11 |
| ***Data collection*** | |
| Diffractometer | XtaLAB Synergy, Dualflex, HyPix |
| Absorption correction | Gaussian<br>Numerical absorption correction based on gaussian integration over a multifaceted crystal model. Empirical absorption correction using spherical harmonics, implemented in SCALE3 ABSPACK scaling algorithm. |
| $T_{min}$, $T_{max}$ | 0.062, 0.126 |
| No. of measured, independent and observed [$I > 2\sigma(I)$] reflections | 1740, 211, 196 |
| $R_{int}$ | 0.039 |
| $(\sin \theta/\lambda)_{max}$ (Å$^{-1}$) | 0.675 |
| ***Refinement*** | |
| $R[F^2 > 2\sigma(F^2)]$, $wR(F^2)$, $S$ | 0.022, 0.060, 1.30 |
| No. of reflections | 211 |
| No. of parameters | 18 |
| $\Delta\rho_{max}$, $\Delta\rho_{min}$ (e Å$^{-3}$) | 1.14, −0.85 |

Magnetization measurements have been carried out using a VSM-SQUID from Quantum Design PPMS3 with a DC field ranging from 70 to 70 kOe at 5 and 300 K. Temperature-dependent magnetic susceptibilities were studied under a magnetic field of 100 Oe and temperature ranging from 5 to 300 K. The diamagnetic correction was done from the undoped glass.

## 2. Results and discussion

The 98.5(40PbO-25$Bi_2O_3$-20$GeO_2$-15$Ga_2O_3$)-1,5$Tb_4O_7$ composition was chosen based on a previous study by Nalin, M et al, which has demonstrated

possibility of obtaining $Yb_3Ga_5O_{12}$ single crystals doped with $Er^{3+}/Tm^{3+}$ in a germano-gallate glass system containing 3 mol % of rare-earth.[32] For this work the concentration of 1.5 mol % of terbium oxide was sufficient to present the supersaturated condition for the formation of crystals from the glass melt.

Figure 1a) shows the photograph of the samples obtained and it is observed that with increasing stiring time before pouring the melted glass into the steel mold there is an increment in the opacity of the glass. In Figure 1b-e) it is possible to verify from the optical microscopy images that crystal formation occurred in all PGBG-Tb samples.

These crystals, with size between 10 and 20 µm, are composed of smaller crystals forming a polycrystal. The shape of this polycrystalline material is governed by the symmetry of the single crystals that compose it. In this manner, the shape of the polycrystals in Figure 1b-e is related to the cubic crystal system, as observed through X-ray diffraction techniques (see below). It is possible to observe the increase in the number of crystals in the sample as the stiring time increases which explains the higher opacity and shows that small variations in this parameter play an important role. For the PGBG-Tb-4 sample, it is possible to observe, in addition to the polycrystals, the formation of some cubic crystals with more defined faces, suggesting the formation of single crystals due to the longer time for organization of the structure.

The X-ray diffractogram of sample PGBG-Tb-4 shows a diffuse-halo of diffraction at 28° (Figure S2)), characteristic of amorphous glasses, which indicated that the amorphous state remains in the sample despite the large amount of crystals observed microscopically. Furthermore, it presents the diffraction peaks at 28.9°, 32.3°, 35.5°, 53.3° and 59.7° which were indexed to the crystalline phase of $Tb_3Ga_5O_{12}$ that crystallizes in the cubic space group Ia-3d (ICSD-20831). The peaks were assigned to the planes 004, 420, 422, 046 and 080, respectively. These results confirm that the glass ceramic obtained is a complex material composed of the glass phase and the TGG crystals.

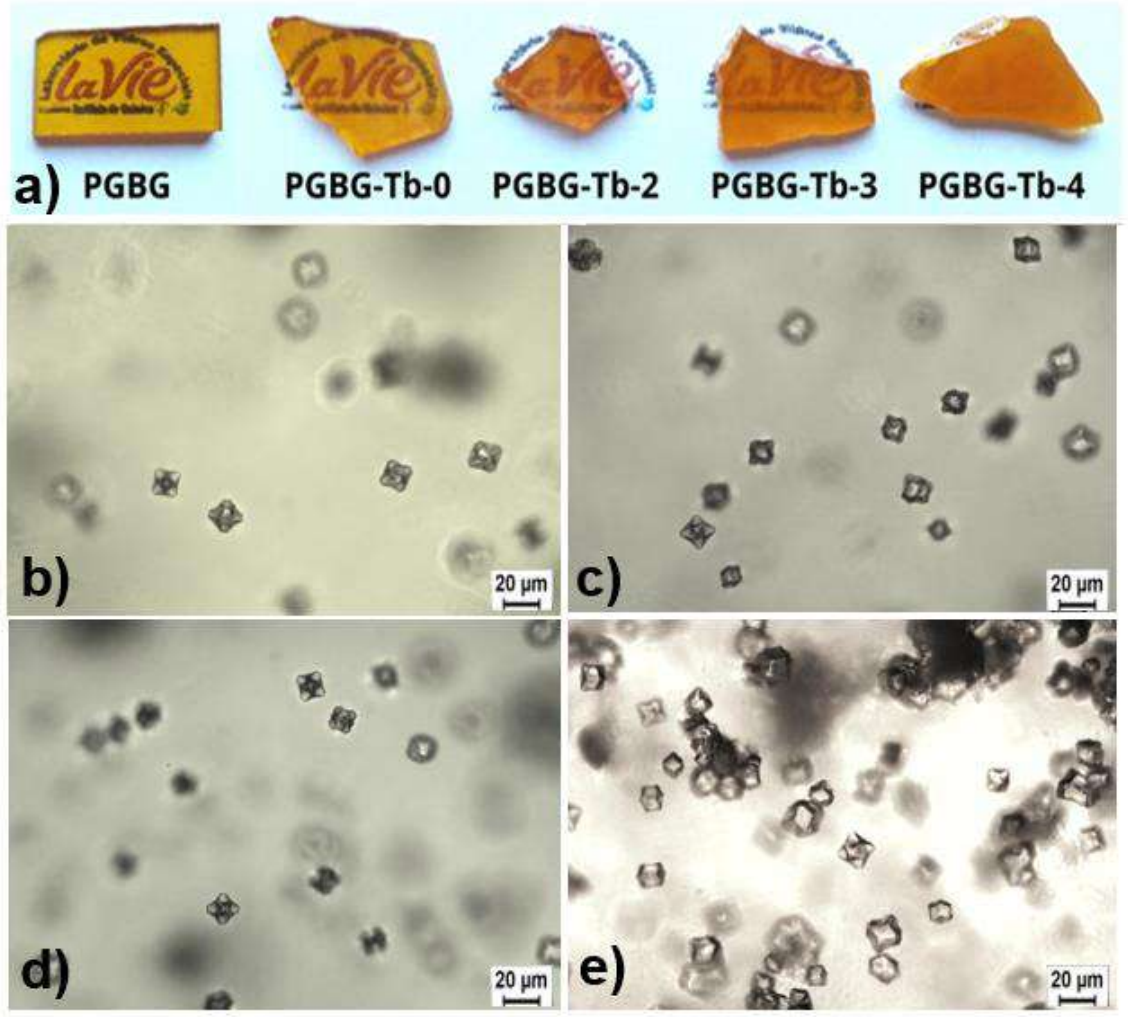


**Figure 1 – a)** Photograph of PGBG pristine glass and PGBG-Tb samples. Optical microscopy images of **b**) PGBG-Tb-0 **c)** PGBG-Tb-2 **d)** PGBG-Tb-3 and **e)** PGBG-Tb-4.

The optical absorption spectra of samples in UV-Vis-NIR wavelength range are shown in Figure 2 a). Several absorption bands would appear before 500 nm assigned to the transitions of $Tb^{3+}$ ions, however, the f-f absorption bands are covered by the UV cut-off edge that limits the transmission window.

The in-homogeneously broadened bands originating from f-f transitions of $Tb^{3+}$ ions are observed in the NIR range. In this region, bands around 1780, 1890, 1950 and 2215 nm appear due to transitions within ground state multiplets $^7F_6 \rightarrow {}^7F_0$, $^7F_1$, $^7F_2$ and $^7F_3$ levels of $Tb^{3+}$ ions, respectively.[41] However, it could be noticed that with the increase pouring time, the absorption bands become progressively more defined. Absorption band profile is modified due to a change of the magnitude and symmetry of the coordination sphere of the $Tb^{3+}$ ions energy

levels. In this perspective, one can suggest the $Tb^{3+}$ ions are likely to occupy crystalline environments due to the lower number of symmetry sites and lower degeneracy of $Tb^{3+}$ energy levels.

The structural changes were evaluated carrying out a micro-Raman mapping experiment, consisting in collecting a series of spectra at different points in a region containing a crystal inside of the glass (Figure 2b), an area of 30 x 30 $\mu m^2$ was mapped with 1 µm step along X and Y axes. The map was generated for the band at 356 $cm^{-1}$ (Figure 2 d)) and shows the difference in composition between the glassy and crystalline part of the sample. The spectra were collected from the map for the polycrystalline $Tb_3Ga_5O_{12}$ (TGG-PC) and for the PGBG-Tb-0 vitreous phase (Figure 2c). The spectrum for the commercial pattern single crystal TGG was also obtained.

For the measurement performed in the vitreous phase the spectra obtained presented broad bands characteristic of a glassy material corresponding to the range of 300~800 $cm^{-1}$.[32] In the region around 380 $cm^{-1}$ there are vibrations of Ga-O-Bi/Ge-O-Bi (or Ga-O-Pb/ Ge-O-Bi), due to the similarities between polyhedra $GaO_4$ and $GeO_4$, it is difficult to separate these vibrations. The Raman band at 520 $cm^{-1}$ have been assigned to the vibrations from $GaO_4$ and $GeO_4$ structures. The band at 765 $cm^{-1}$ are assigned to a $Ga\text{-}O^-$ e $Ge\text{-}O^-$ bonds involving non-bridging oxygen.[42-43] A detailed discussion has been described by Nalin, M et al.[32]

Gallium Garnets like $Tb_3Ga_5O_{12}$, $Eu_3Ga_5O_{12}$, $Gd_3Ga_5O_{12}$, $Y_3Ga_5O_{12}$, for example, are isostructural and they have a similar Raman spectrum.[42-44] The Raman bands for the TGG-PC inside the glass showed a profile very similar to the commercial TGG crystal and the spectra reported in the literature for $RE_3Ga_5O_{12}$ structures.[44-47]

The spectrum of garnets has modes that can be attributed to tetrahedral ($GaO_4$), octahedral ($GaO_6$) and dodecahedral ($REO_8$) units. However, the vibrations of the different polyhedra in the structure are strongly coupled to each other and therefore distinguish each Raman band to a single polyhedron is difficult, for this reason not all bands were assigned.[46-47]

The vibrational mode at 356 $cm^{-1}$ can be assigned to the rotational mode of $GaO_6$ and a small contribution of a rotational mode of the $GaO_4$, while the mode at 526 $cm^{-1}$ is related to the bending mode of $GaO_4$ and $GaO_6$. The band at 745

$cm^{-1}$ corresponds to the symmetric stretching mode of the $GaO_4$ and $GaO_4$. The following modes at 168, 177, and 238 $cm^{-1}$ are mainly related to translational movements of the $GaO_4$ tetrahedra, whereas the band at 383 $cm^{-1}$ may be related with the rotational mode of $GaO_4$ tetrahedra and $GaO_6$ octahedra.[44-47]

Finally, Tb atoms contribute in the low-frequency region between 100 and 270 $cm^{-1}$, and the translational movements of $TbO_8$ dodecahedra can be observed at 110 $cm^{-1}$.[47]

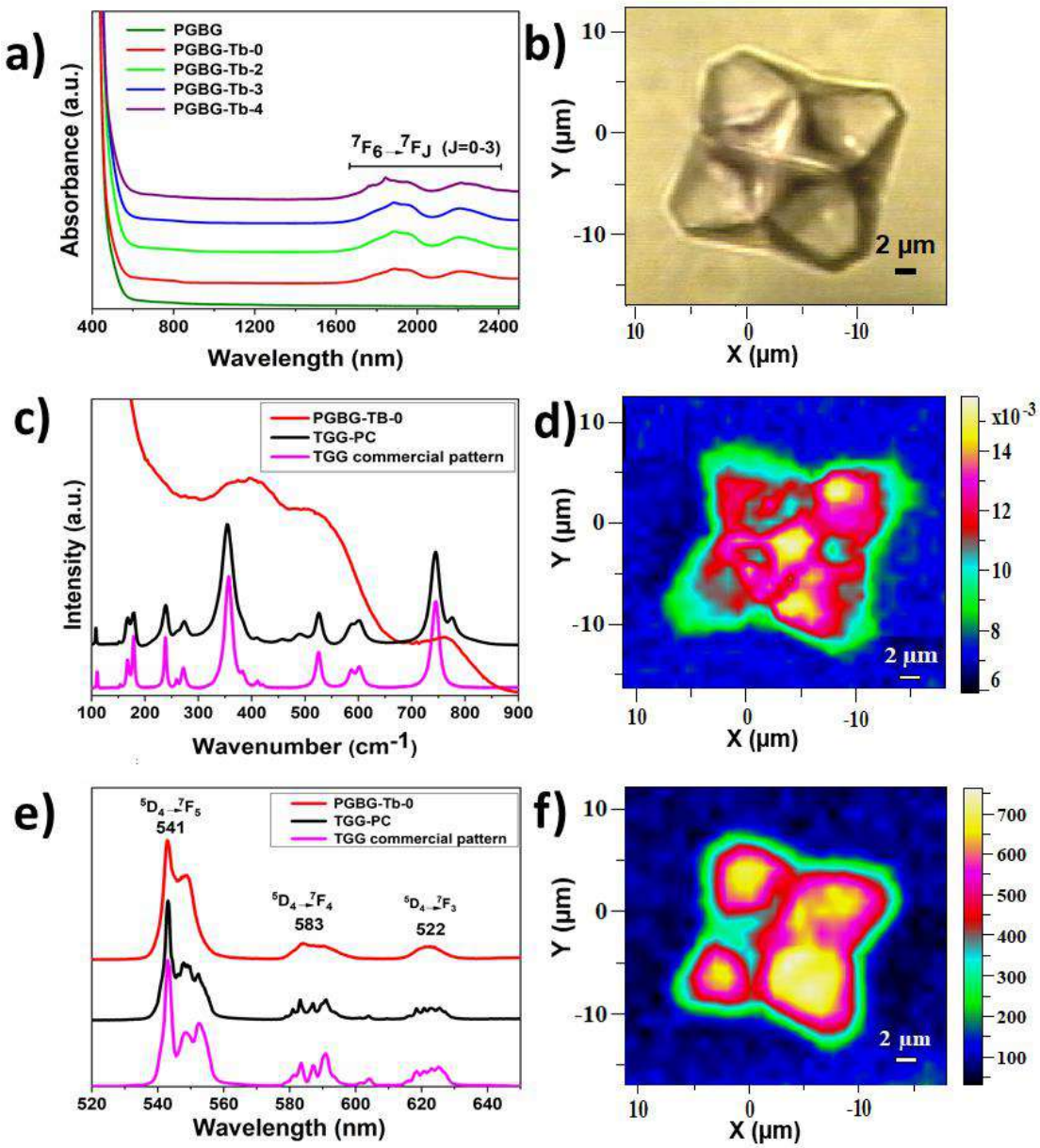


**Figure 2 – a)** Absorbance spectra in the UV-Vis region obtained for PGBG and PGBG-TB samples (The spectra have been moved vertically for better viewing). **b)** Optical microscopy image of a representative crystal of the sample PGBG-Tb-

0. **c)** Normalized Raman spectra acquired for PGBG-Tb-0 vitreous phase, TGG-PC and TGG commercial pattern. d) micro-Raman map for band at 356 $cm^{-1}$. e) emission spectra acquired for PGBG-Tb-0 vitreous phase, TGG-PC and TGG commercial pattern. f) Luminescence map for emission bands between 530 and 560 nm.

To evaluate the luminescent properties of terbium ions in a glassy and crystalline environment, a micro-luminescence mapping was performed in a 30 x 30 $\mu m^2$ area using for excitation a 488 nm wavelength. The map was generated for emission bands between 530 and 560 nm (Figure 2f)).

Two luminescence spectra (Figure 2e)) were extracted from the map one for PGBG-Tb-0 vitreous phase and other for TGG-PC region. The emission spectra were normalized at 547 nm, which is originated from the $^5D_4 \rightarrow {}^7F_5$ transitions. In addition to this green emission, yellow and red emission bands were observed at 587 and 624 nm assigned to $^5D_4 \rightarrow {}^7F_j$ (J= 4 and 3) transitions of $Tb^{3+}$ ions.[9-10]

The spectrum collected in the PGBG-Tb-0 vitreous phase shows the presence of $Tb^{3+}$ ions in the remaining glass matrix since an inhomogeneous broadening emission is still observed and occurs due to the large number of different symmetry sites, characteristic of rare-earth emission in glasses materials. While the luminescent spectrum for TGG-PC shows a definition of $Tb^{3+}$ ions energy levels such behavior can be assigned to formation of Stark levels where $Tb^{3+}$ ions are in crystalline environments with lower number of symmetry sites and, consequently, lower degeneracy of $Tb^{3+}$ energy levels. The spectra data from the commercial TGG crystal were performed for comparison and corroborate the presence of terbium in TGG crystals precipitated in the glass matrix.

The distribution of chemical elements in the PGBG-Tb-0 and TGG crystal area was studied by EDS and SEM elemental mapping in a polished sample with an exposed crystal on the surface (Figure 3a-c)).

The signals obtained from EDS in the PGBG-Tb-0 glass area (1) in Figure 3a) were attributed to Ga at 0.95 (edge L1) and 1.098 keV (edge La1), to Ge at 1.19 keV (edge La1), to Bi at 2.42 keV (edge Ma12) and to Pb at 1.84 keV (edge Mx). The shoulder at 1.24 is attributed to energy of Tb (Ec(M5)). The EDS results

for TGG-PC area (2) shows that the chemical composition of crystals is Tb with signals at 1.24 (Ec(M5)), 6.27 (edge La1), 6.97 (edge Lβ1) and 7.36 (edge Lβ2) and Ga with energies attributed at 0.95 (edge L1) and 1.098 keV (edge La1) (Figure 3b)).

The elemental mapping shows the distribution of chemical elements contained in both crystal and glass phases (Figure 3c)). The mapping of crystal region is composed of Ga and Tb and rules out the presence of Bi and Pb ions into the crystal. Ge and Ga elements have close atomic numbers, thereby exhibiting similar transitions, making difficult to separate both signals, but EDS data makes it clear that the crystal is composed by Ga instead of Ge.

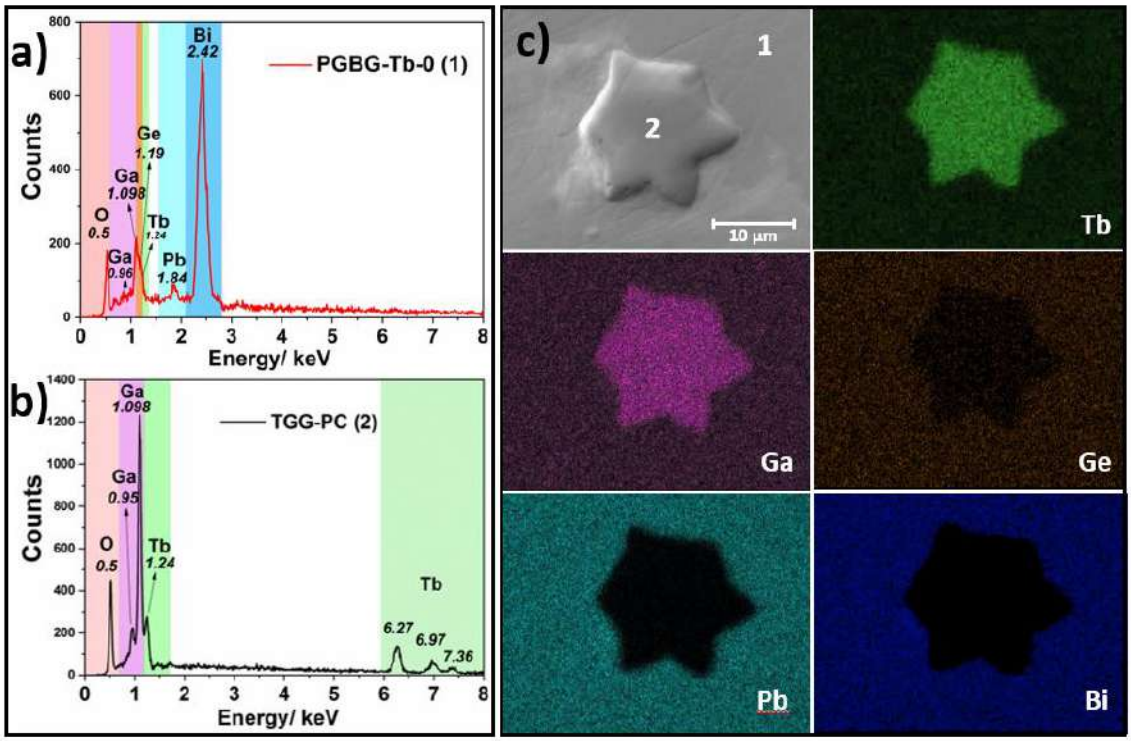


Figure 3- a) SEM-EDS spectrum of PGBG-Tb-O glass (1) and TGG crystal (2) area. b) SEM image c) elemental mapping results of PGBG-Tb-0 of each element.

These results show that it is possible to use a heavy metal glass as reactor to obtain TGG-PC dispersed throughout the glass matrix. It is important to highlight that the crystals were formed in the bulk during pouring, without the need for any further thermal treatment. Furthermore, the data indicate that with an increase in the time for crystal formation, it would be possible to obtain

monocrystals and possibly larger crystals. For this reason, based on this set of data, a new strategy for the growth of these crystals has been implemented.

In this new approach, the PGBG-Tb vitreous precursors were melted at 1250 °C and then cooled inside the furnace at 10°C/min until they reached 900°C, in a total of 35 min, then the crucible was removed from the furnace. Using this methodology, it was possible to obtain crystals between 50 µm and 100 µm wiyh a perfect cubic shape (See Figure 4a). This glass ceramic was immersed into concentrated nitric acid for 24 h and in this way the vitreous part was dissolved and the crystals could be recovered in large quantities and characterized.

Figure 4b) shows a scanning electron microscopy image of one of the crystals obtained and extracted from the glass showing in detail the topography of the TGG-SC, it is possible to observe that the acid does not attacks the surface of the crystalline structure. This new methodology for obtention of TGG-SC opens up a range of new applications in which these micro single crystals can be exploited, such as microleds.

The structural determination of the crystal was carried out using Single-crystal X-ray diffraction which confirms that the synthesized minerals are composed of terbium gallium garnets single crystals (TGG-SC). The mineral crystallizes in the cubic system, with $a$ = 12.3539 Å and space group $Ia\bar{3}d$, as expected for TGG.[46]

The obtained crystal structure is depicted in Figure 4c), in which it is possible to see the $Tb^{3+}$ cations coordinated to eight oxygen atoms, and two independent units of $Ga^{3+}$ cations, one of which is hexacoordinated in an octahedral geometry, while the other is tetracoordinated, in a tetrahedral geometry, with $\tau'_4$ = 0.98. The calculated distortion index (D) for Tb is 0.02017, while it is zero for the Ga atoms, highlighting the regularity of the coordination sphere. The quadratic elongation (<λ>) for the Ga atoms are of 1.0077 for the Ga hexacoordinated (Ga1) and 1.0148 for the tetracoordinated (Ga2).

The $Tb^{3+}$ cations are 3.783 Å from each other, while the separation between different $Ga^{3+}$ atoms (Ga1–Ga2) is of 3.453 Å and between two tetracoordinated Ga atoms (Ga2–Ga2) is 3.783 Å. Meanwhile, the distances Tb1–Ga1 and Tb1–Ga2 are 3.453 Å and 3.088 Å, respectively, and Ga1–Ga1 is

5.349 Å. A complete list on geometric parameters can be found in the Supplementary Material (Table S1).

In Figure 4d is possible to see the green emission arising from the TGG cubic crystals after excitation with a blue LED light (488 nm). As already explained, such emission comes from the $^{5}D_{4}\leftarrow{}^{7}F_{6}$ transition of $Tb^{3+}$ present into crystalline sites of the structure, as confirmed by the appearance of the Starks emissions observed in Figure 4e. Even if the molar content of $Tb^{3+}$ in the crystals would lead to quenching the emission, the luminescence of the crystals are intense enough under illumination of a weak LED of 488 nm source. Thus, the use of such crystals as green micro-LED´s is also promising.

The micro-Luminescence and micro-Raman mapping were obtained from the square surface of one crystal and it is possible to observe the homogeneity of the luminescence and Raman spectra over the entire surface (Figure 4 f-g)).

Furthermore, the luminescence spectrum of the single crystal, Figure 4f), exhibits a higher definition of $Tb^{3+}$ ion energy levels compared to the polycrystal (Figure 2e). The Raman spectrum profile obtained for the TGG-SC, Figure 4g), also presents bands with higher definition than the TGG-PC shown in figure 2c), in addition, the TGG-SC spectrum is very similar to that of the commercial TGG obtained byCzochralski.

This data set presented in Figure 4 shows the accuracy of the supersaturated solution methodology for obtaining TGG sigle crystals from the glass melt.

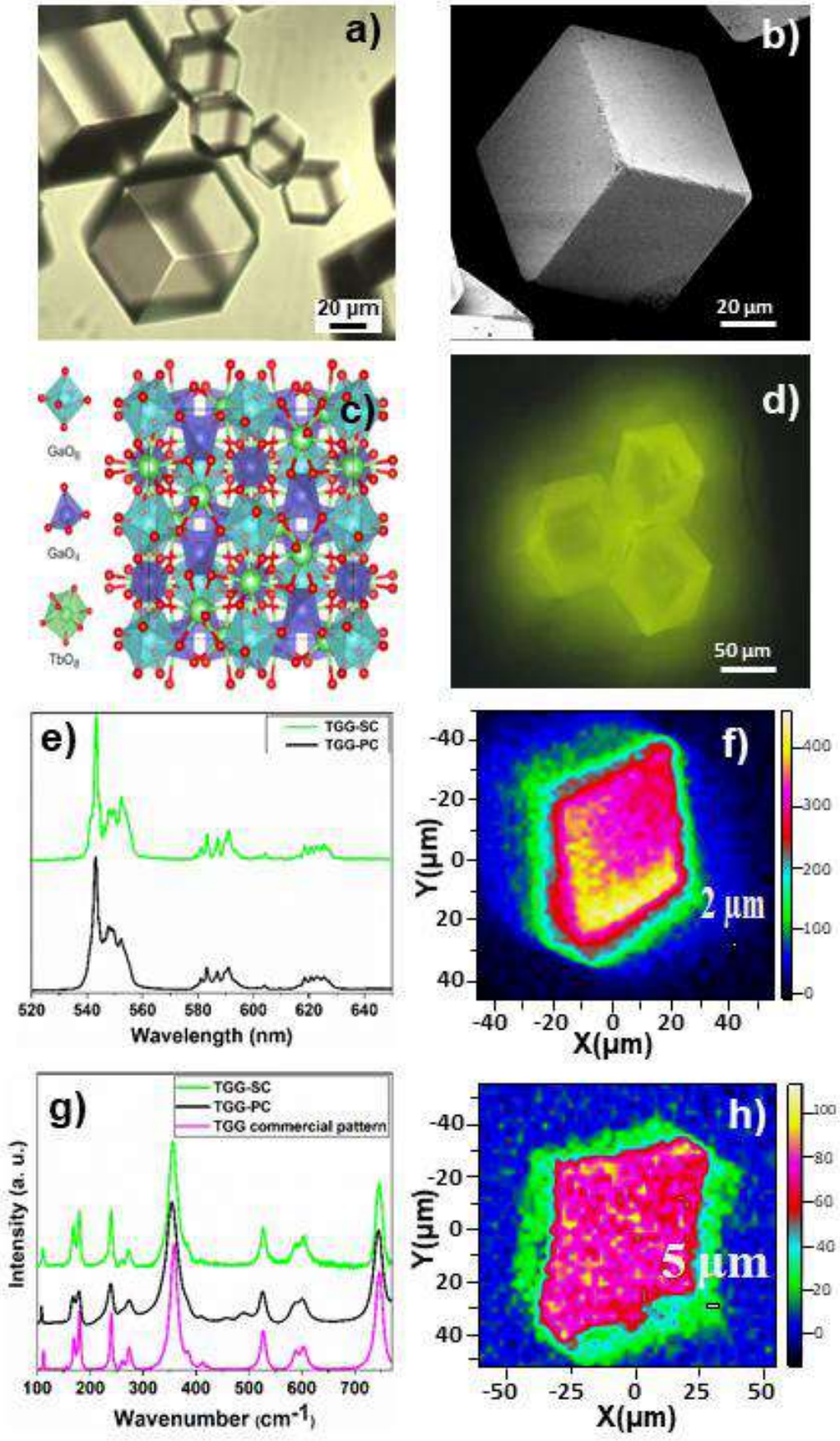


**Figure 4- a)** Optical microscopy image of TGG single crystas inside glass. b)

Scanning electron microscopy image of TGG-SC. c) Crystal packing for TGG-SC obtained using the Vesta software, highlighting the $TbO_8$, $GaO_6$ and $GaO_4$ units. d) Photograph of crystals under ultraviolet lamp. e) emission spectra acquired for TGG-SC, TGG-PC and TGG commercial pattern. f) Luminescence map for emission bands between 530 and 560 nm. g**)** Normalized Raman spectra acquired for TGG-SC, TGG-PC and TGG commercial pattern. h) TGG-SC micro-Raman map for band at 356 $cm^{-1}$.

## Magnetic properties

The magnetic properties of PGBG-Tb glasses were investigated by measurements of magnetic susceptibility in the temperature range of 2–300. The ZFC and FC magnetic susceptibility, χ, of the glasses as a function pouring time and temperature measured in a field of 100 Oe is shown in figure 9(a) and (b). The inverse of magnetic susceptibility vs. temperature curves of samples can be fit to the Curie-Weiss law $\chi_M = C/T - \theta + \chi_0$, where C is the Curie constant, θ is the Weiss temperature and $\chi_0$ represents the temperature-independent term. When the experimental data for $1/\chi_M$ vs T between 2 and 300 K were fitted according to the Curie−Weiss law, we obtained the negative θ values (see Table 2), which indicates the presence of weak antiferromagnetic interactions between the $Tb^{3+}$ ions. As can be seen from Table 2, Weiss temperature module increases with the increase of the pouring time, which suggest that the antiferromagnetic interaction between terbium ions becomes higher, which could be a strong indication of the formation of TGG crystals, corroborating the previous results. Indeed, the PGBG-Tb-0 sample has a smaller amount of TGG crystals when compared to the PGBG-Tb-4 sample, consequently the PGBG-Tb-0 sample has a higher amount of terbium ions in its glass matrix and, as expected, the antiferromagnetic interaction of these ions will be smaller. Finally, it is important to emphasize that the magnitudes of the values of θ from Curie-Weiss law fits of $\chi_m^{-1}$ vs. T data are sufficiently near zero, suggesting paramagnetism. Table-2 Weiss temperature ($\theta_n$) obtained by fitting the data with the Curie–Weiss law from 2–300 K.

| Method | PGBG-Tb-0<br>$\theta_0$ (K) | PGBG-Tb-2<br>$\theta_2$ (K) | PGBG-Tb-3<br>$\theta_3$ (K) | PGBG-Tb-4<br>$\theta_4$ (K) |
|---|---|---|---|---|
| ZFC | -0.445 ±0.007 | -0.506 ±0.009 | -0.544 ±0.009 | -0.65 ±0.01 |
| FC | -0.444 ±0.007 | -0.507 ±0.009 | -0.541 ±0.009 | -0.64 ±0.01 |

Our results did not show significant difference between ZFC and FC measurements, which indicate that, the PGBG-Tb samples are not superparamagnetic materials, and also confirm that magnetic nanoclusters are not formed. In fact, all our results show the formation of bulk TGG structures.

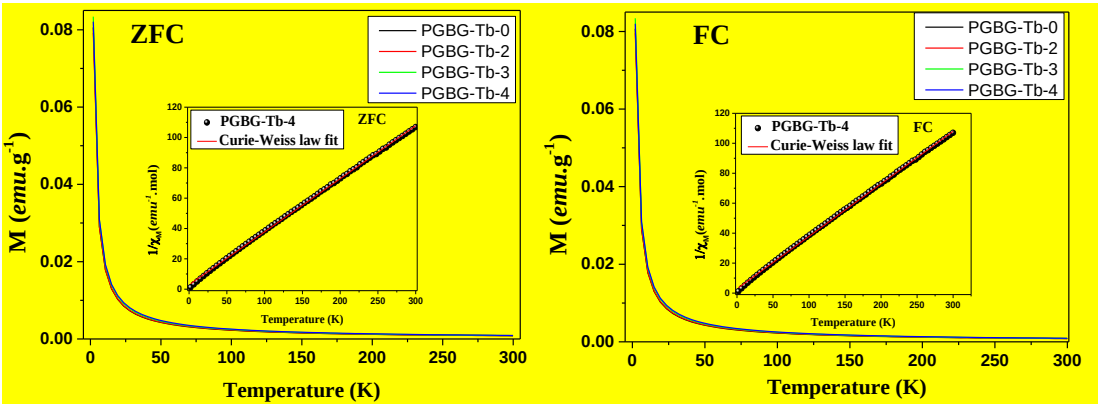


**Figure 9**- Temperature dependence (ZFC and FC) of the M×T at 100 Oe. The inset shows the temperature dependence of the inverse of the molar magnetic susceptibility, $\chi_M$, of TGBT-Tb-4 sample and solid red line shows fit to the Curie-Weiss law.

Figure 10 (a) and (b) magnetization of the sample as a function of the applied dc field at 5  and 300 K, respectively. The magnetization became almost saturated under magnetic fields higher than 60 kOe. No hysteresis loop was observed down to 2 K for all the four PGBG-Tb samples. Instead, the isothermal magnetization curves show typical paramagnetic characteristics.

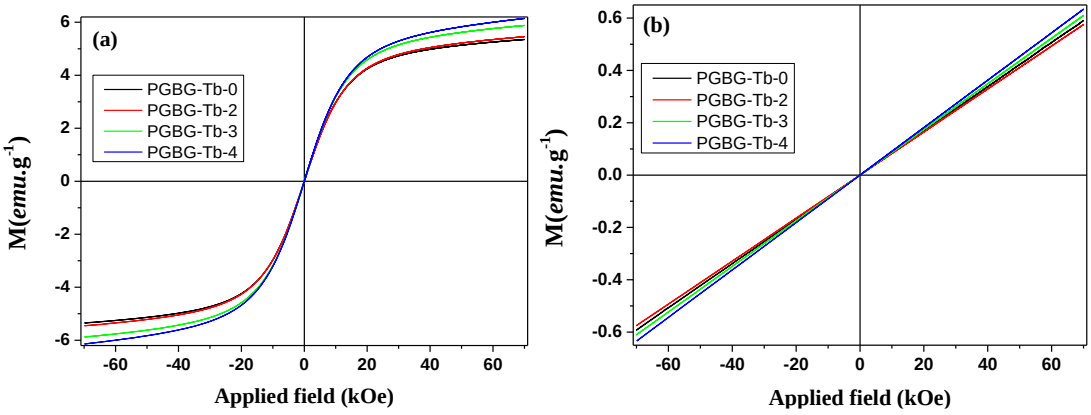


Fig. 10 Magnetization as a function of applied magnetic field performed at (a) 5 K and(b) 300 K .

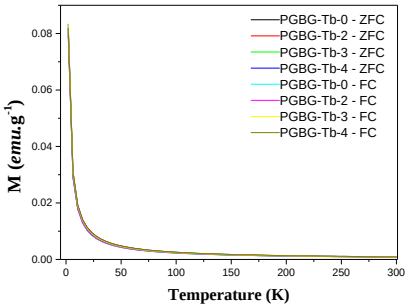


**Figure Sx**- Temperature dependence (ZFC and FC) of the M×T at 100 Oe.

## Resultados do mono cristal

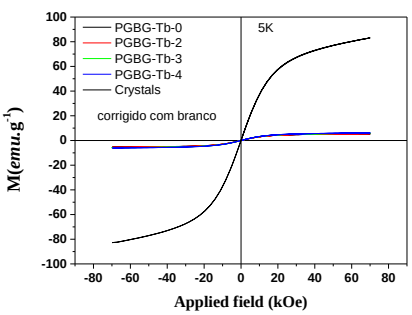


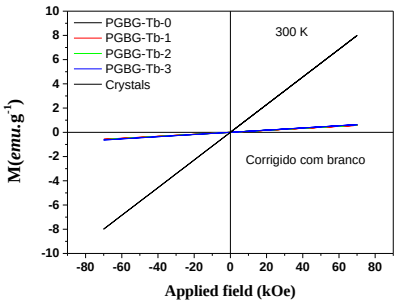


## CONCLUSION

## Acknowledgments

The authors are grateful to the Brazilian funding agencies CNPQ and São Paulo Research Foundation FAPESP for the grants (2013/07793-6, 2019/19609-1, 2020/01786-1). ( por favor, colocar seus projetos para agradecimento)

**References ( vou arrumar após escolha da revista)**

1- Light-yield improvement trends in mixed scintillation crystals, Oleg Sidletskiy*,1, Alexander Gektin1, and Andrei Belsky, Phys. Status Solidi A, 1–4 (2014) / DOI 10.1002/pssa.201431137

2- D. Popa F. Udrea “Towards Integrated Mid-Infrared Gas Sensors”, Sensors, 19(9) (2019) 2076.

3-Carlos D. S. Brites, Riccardo Marin, Markus Suta, Albano N. Carneiro Neto, Erving Ximendes, Daniel Jaque, Luís D. Carlos, Spotlight on Luminescence Thermometry: Basics, Challenges, and Cutting-Edge Applications, adv material, **Volume35, Issue36**September 7, 2023, 2302749

4-Lohe, P.P., Nandanwar, D.V., Belsare, P.D. *et al.* $Tb^{3+}$ activated garnets for some novel applications. *J Opt* (2023). https://doi.org/10.1007/s12596-023-01495-1

5- The comparison of the thermometric performance of optical ceramics, microcrystals and nanocrystals of $Cr^{3+}$- doped $Gd_3Ga_5O_{12}$ garnets
Journal of Alloys and Compounds Volume 963, 10 November 2023, 171284

6- Journal of Advanced Ceramics 2019, 8(3): 389–398
YAGG:Ce transparent ceramics with high luminous efficiency for solid-state lighting application Hui HUAa,b,†, Shaowei FENGa,b,†, Zhongyu OUYANGc , Hezhu SHAOb , Haiming QINb,*, Hui DINGb , Qiping DUa,b , Zhijun ZHANGa,*, Jun JIANGb,*, Haochuan JIANG

7- Photoluminescence and unique magnetoluminescence of transparent **(Tb1-xYx)3Al5O12 ceramicsZhifeng Xing, Mengmeng Lun, Wanying Wu, Hanzhao Song, Aihua Yao, Xunsheng Zhou,** Ceramics International Volume 46, Issue 7, May 2020, Pages 8971-8978

8- Myerson, Allan S.; Erdemir, Deniz; Lee, Alfred Y. (2019). Handbook of Industrial Crystallization || Crystal Nucleation. , 10.1017/9781139026949(Chapter 3), 76–114. doi:10.1017/9781139026949.003

9-Franco, D.F., Ledemi, Y., Correr, W. et al. Magneto-optical borogermanate glasses and fibers containing $Tb^{3+}$. Sci Rep 11, 9906 (2021). https://doi.org/10.1038/s41598-021-89375-1 D. F. Franco, Y. Ledemi, W. Correr, S. Morency, C. R. Afonso, Y. Messaddeq, S. H. Messaddeq, and M. Nalin, Sci. Rep. 11 (1), 9906 (2021).

10- Fundamental studies of magneto-optical borogermanate glasses and derived optical fibers containing $Tb^3$ .D. F. Franco, R. G. Fernandes, J. F. Felix, V. R. Mastelaro, H. Eckert, C. R. Afonso, J. Mater. Res. Technol.11, 312 (2021).

11- Mo, X. Z. et al. Luminescence properties of magneto-optical glasses containing Tb3+ ions. J. Alloys Compd. 658 (2016) 967-972

12-Kenji Sawada et al 2017 ECS J. Solid State Sci. Technol. 6 R97, An Orange-Light Emitting Garnet Phosphor: Tb3Ga5O12:Eu3+

13-R. Yasuhara, H. Nozawa, T. Yanagitani, S. Motokoshi, J. Kawanaka, Temperature dependence of thermo-optic effects of single-crystal and ceramic TGG, Opt. Express 21 (2013) 31443e31452.

14- Leonardo Vieira Albino, Marc Dussauze, Olivier Toulemonde, Mathieu Duttine, Véronique Jubera, Douglas Faza Franco, Thierry Cardinal, Marcelo Nalin, Paramagnetic borotungstate glasses with high terbium concentration for magneto-optical applications, Journal of Non-Crystalline Solids, Volume 627, 2024, 122811,

15-Douglas F. Franco, Fábio J. Caixeta, Leonardo V. Albino, Thiago A. Lodi, Juliane R. Orives, Eduardo O. Ghezzi, Marcelo Nalin, Terbium-doped transparent glass-ceramics containing TbPO4 crystals: A promising material for photonic applications, Optical Materials: X, Volume 20, 2023,100272

16- R. Yasuhara, H. Nozawa, T. Yanagitani, S. Motokoshi, J. Kawanaka, Temperature dependence of thermo-optic effects of single-crystal and ceramic TGG, Opt. Express 21 (2013) 31443e31452.

17- R. Yasuhara, S. Tokita, J. Kawanaka, T. Kawashima, H. Kan, H. Yagi, H. Nozawa, T. Yanagitani, Y. Fujimoto, H. Yoshida, M. Nakatsuka, Cryogenic temperature characteristics of Verdet constant on terbium gallium garnet ceramics, Opt. Express 15 (2007) 11255e11261

18-V. I. Chani, A. Yoshikawa, H. Machida, T. Satoh, and T. Fukuda, J. Cryst. Growth, 210, 663 (2000).

19- Weizhao Jin, Liangyu Gai, Jie Chen, Hai Lin, Chun Li, Liangbi Su, Anhua Wu, Fanming Zeng Fabrication and magneto-optical properties of TGG transparent ceramics

20-Wenjing Zhang, Feiyun Guo, Jianzhong Chen, Growth and characterization of Tb3Ga5xAlxO12 single crystal, Journal of Crystal Growth 306 (2007) 195–199

21-Y. Feng, H. Lin, C. Chen, X. Yi, Y. Tang, S. Zhang, T. Yu, W. Chen, and S. Zhou, Chin. Opt. Lett., 13, 031602 (2015).

22 -K. Sawada and S. Adachi, J. Lumin., 165, 138 (2015)

23- Z. Chen, L. Yang, X. Wang, J. Wang, and Y. Hang, Opt. Mater., 46, 12 (2015).

24-. N. I. Tsidaeva, V. V. Abaeva, E. V. Enaldieva, S. A. Khaimanov, A. G. Ramonova, T. G. Butkhuzi, and A. M. Turiev, IEEE Trans. Magn., 50, 1001704 (2014).),

25- Y. P. Udalov, R. M. Rakhmankulov, T. Y. Chemekova, and O. L. Belousova, Glass Phys. Chem., 29, 200 (2003).

26. N. Zhuang, C. Song, L. Guo, R. Wang, X. Hu, B. Zhao, S. Lin, and J. Chen, J. Cryst. Growth, 381, 27 (2013).

27- Z. Chen, L. Yang, X. Wang, and Y. Hang, Opt. Mater., 62, 475 (2016)),

28- J.R. Carruthers, M. Kokta, R.L. Barns, M. Grasso, Nonstoichiometry and crystalgrowth of gadolinium gallium garnet, J. Cryst. Growth 19 (1973) 204e208

[29-] M. Yamane e Y. Asahara, “Glasses for photonics”, Cambridge University Press, Cambridge, UK (2000).

30 Edgar D. Zanottoa, John C. Maurob, The glassy state of matter: Its definition and ultimate fate , Journal of Non-Crystalline Solids Volume 471, 1 September 2017, Pages 490-495

31-MARCONDES, LIA MARA; EVANGELISTA, RENATO OLIVEIRA ; GONÇALVES, ROGÉRIA ROCHA ; DE CAMARGO, ANDREA S.S. ; MANZANI, DANILO ; NALIN, MARCELO ; CASSANJES, FABIA CASTRO ; POIRIER, GAEL YVES . Er3+-doped niobium alkali germanate glasses and glass-ceramics: NIR and visible luminescence properties. JOURNAL OF NON-CRYSTALLINE SOLIDS JCR, v. 521, p. 119492, 2019.

32- A.E. Souza, S.G. Antonio, S.J.L. Ribeiro et al. Journal of Alloys and Compounds 864 (2021) 158804.

33- Varshineya, A. K.; Fundamental of Inorganic Glasses, Academic Press Inc.: San Diego, 1994

34- Myerson, Allan S.; Erdemir, Deniz; Lee, Alfred Y. (2019). Handbook of Industrial Crystallization || Crystal Nucleation. 10.1017/9781139026949(Chapter 3), 76–114. doi:10.1017/9781139026949.003

35- R.T. Southin, G.A. Chadwick, Crystallization from the melt, Science Progress. 1969, 57, 353-370.

36- Rigaku Oxford Diffraction (2023). CrysAlisPRO 1.171.42.84a, Rigaku Oxford Diffraction, Yarnton, England.
37- Sheldrick, G. M. (2015a). *Acta Cryst.* A**71**, 3-8.
38-Sheldrick, G. M. (2015b). *Acta Cryst.* C**71**, 3-8

39- Dolomanov, O. V.; Bourhis, L. J.; Gildea, R. J.; Howard, J. A. K.; Puschmann, H. (2009). *J. Appl. Cryst*. **42**, 339-341.
40-Momma, K.; Izumi, F. (2011). *J. Appl. Cryst.*, **44**, 1272-1276.
41- Atul D. Sontakke, Kaushik Biswas, K. Annapurna Concentration-dependent luminescence of Tb3+ ions in high calcium aluminosilicate glasses. Journal of Luminescence **Volume 129, Issue 11, November 2009, Pages 1347-1355**

42- M. Montesso, D. Manzani, J.P. Donoso, C.J. Magon, M. Nalin, Synthesis and structural characterization of a new SbPO4-GeO2 glass system, J. Non-Cryst. Solids 500 (2018) 133–140, https://doi.org/10.1016/j.jnoncrysol.2018.07.005

43- T. Guèrineau, C. Strutynski, T. Skoak, S. Morency, A. Hanafi, F. Calvazala, Y. Ledemi, S. Danto, T. Cardinal, Y. Messaddeq, E. Fargin, Extended germanogallate fiber drawing domain: from germanates to gallates optical fibers, Opt. Mater. Express 9 (2019) 2437–2445, https://doi.org/10.1364/OME.9.002437

44-(Europium gallium garnet (Eu3Ga5O12) and Eu3GaO6: Synthesis and material properties Kenji Sawada, Toshihiro Nakamura, and Sadao Adachi)

45-(**High-pressure spectroscopic studies of europium gallium and gadolinium aluminum garnets R.C. Middletona , D.V.S. Muthua,b,∗ , M.B. Kruger (Solid State Communications 148 (2008) 310–313)**

**46-(**Lattice Dynamics Study of Nanocrystalline Yttrium Gallium Garnet at High Pressure V. Monteseguro,† P. Rodríguez-Hernandez,´ †,‡ R. Vilaplana,§ F. J. Manjon,´ ∥ V. Venkatramu,⊥ D. Errandonea,# V. Lavín,†,¶ and A. Muñ oz*,†), *J. Phys. Chem. C* 2014, 118, 24, 13177–13185

47- V. Monteseguro,a P. Rodrı ´guez-Herna´ndez,ab H. M. Ortiz,cde V. Venkatramu,f F. J. Manjo´n,c C. K. Jayasankar,g V. Lavı ´nah and A. Mun˜oz*Structural, elastic and vibrational properties of nanocrystalline lutetium gallium garnet under high pressure, ***Phys.Chem.Chem.Phys.,*** 2015, 17, 9454

## Supplementary Material

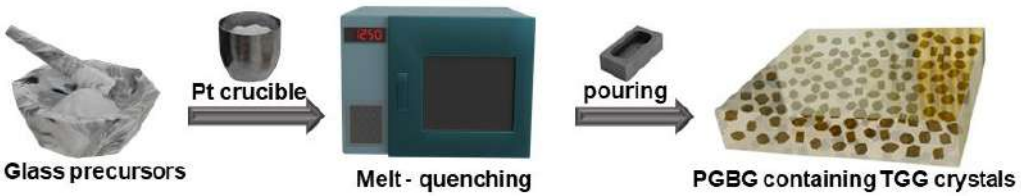

**Figure S1-** Schematic illustration of obtention of PGBG-Tb glasses containing TGG crystals.

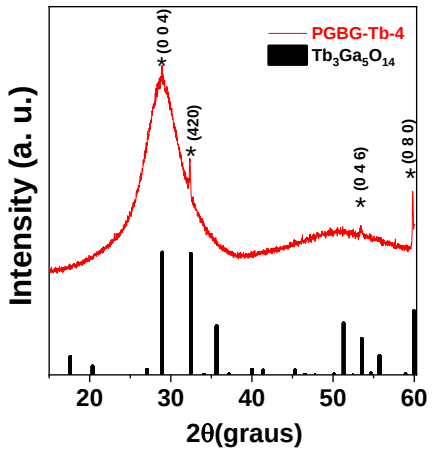


**Figure S2-** a) XRD of PGBG-Tb-4 glass ceramic compared to TGG commercial pattern (ICSD- 20831).

**Table S1.** Geometric parameters for TGG (Å, °)

| | | | |
|---|---|---|---|
| Tb1—O1$^{i}$ | 2.460 (3) | Ga1—O1$^{viii}$ | 1.996 (3) |
| Tb1—O1 | 2.363 (3) | Ga1—O1$^{ix}$ | 1.996 (3) |
| Tb1—O1$^{ii}$ | 2.363 (3) | Ga1—O1$^{x}$ | 1.996 (3) |
| Tb1—O1$^{iii}$ | 2.460 (3) | Ga1—O1$^{vi}$ | 1.996 (3) |
| Tb1—O1$^{iv}$ | 2.363 (3) | Ga1—O1$^{xi}$ | 1.996 (3) |
| Tb1—O1$^{v}$ | 2.460 (3) | Ga2—O1$^{iv}$ | 1.849 (3) |
| Tb1—O1$^{vi}$ | 2.460 (3) | Ga2—O1$^{xii}$ | 1.849 (3) |
| Tb1—O1$^{vii}$ | 2.363 (3) | Ga2—O1 | 1.849 (3) |
| Ga1—O1 | 1.996 (3) | Ga2—O1$^{xiii}$ | 1.849 (3) |
| | | | |
| O1—Tb1—O1$^{iii}$ | 125.04 (7) | O1$^{vii}$—Tb1—O1$^{vi}$ | 96.08 (10) |
| O1$^{iii}$—Tb1—O1$^{vi}$ | 165.89 (15) | O1$^{ii}$—Tb1—O1$^{vi}$ | 72.37 (12) |
| O1$^{vii}$—Tb1—O1$^{i}$ | 125.04 (7) | O1$^{vii}$—Tb1—O1$^{ii}$ | 73.39 (16) |
| O1$^{vii}$—Tb1—O1$^{iii}$ | 72.37 (12) | O1—Ga1—O1$^{xi}$ | 95.15 (14) |

| | | | |
|---|---|---|---|
| O1—Tb1—O1$^{iv}$ | 73.39 (16) | O1$^{x}$—Ga1—O1$^{viii}$ | 84.85 (14) |
| O1$^{ii}$—Tb1—O1$^{iii}$ | 96.08 (10) | O1—Ga1—O1$^{x}$ | 95.15 (14) |
| O1$^{iv}$—Tb1—O1$^{vi}$ | 125.04 (7) | O1$^{x}$—Ga1—O1$^{xi}$ | 84.85 (14) |
| O1$^{iv}$—Tb1—O1$^{iii}$ | 67.84 (16) | O1$^{xi}$—Ga1—O1$^{viii}$ | 84.85 (14) |
| O1—Tb1—O1$^{vii}$ | 160.35 (16) | O1$^{vi}$—Ga1—O1$^{xi}$ | 95.15 (14) |
| O1$^{i}$—Tb1—O1$^{iii}$ | 74.65 (15) | O1—Ga1—O1$^{viii}$ | 180.0 |
| O1$^{ii}$—Tb1—O1$^{iv}$ | 160.35 (16) | O1—Ga1—O1$^{ix}$ | 84.85 (14) |
| O1—Tb1—O1$^{v}$ | 96.08 (10) | O1$^{vi}$—Ga1—O1$^{viii}$ | 95.15 (14) |
| O1$^{iv}$—Tb1—O1$^{i}$ | 96.08 (10) | O1$^{x}$—Ga1—O1$^{ix}$ | 95.15 (14) |
| O1$^{vii}$—Tb1—O1$^{v}$ | 67.84 (16) | O1$^{ix}$—Ga1—O1$^{viii}$ | 95.15 (14) |
| O1$^{i}$—Tb1—O1$^{vi}$ | 107.15 (16) | O1$^{vi}$—Ga1—O1$^{ix}$ | 84.85 (14) |
| O1$^{ii}$—Tb1—O1$^{v}$ | 125.04 (7) | O1$^{x}$—Ga1—O1$^{vi}$ | 180.00 (18) |
| O1$^{v}$—Tb1—O1$^{vi}$ | 74.65 (15) | O1$^{xi}$—Ga1—O1$^{ix}$ | 180.0 |
| O1$^{iv}$—Tb1—O1$^{v}$ | 72.37 (12) | O1—Ga1—O1$^{vi}$ | 84.85 (14) |
| O1—Tb1—O1$^{ii}$ | 110.12 (16) | O1$^{iv}$—Ga2—O1$^{xii}$ | 114.63 (11) |
| O1$^{i}$—Tb1—O1$^{v}$ | 165.89 (15) | O1$^{xiii}$—Ga2—O1 | 114.63 (11) |
| O1$^{vii}$—Tb1—O1$^{iv}$ | 110.12 (16) | O1$^{xii}$—Ga2—O1 | 114.63 (11) |
| O1$^{iii}$—Tb1—O1$^{v}$ | 107.15 (16) | O1$^{iv}$—Ga2—O1 | 99.6 (2) |
| O1—Tb1—O1$^{i}$ | 72.37 (12) | O1$^{iv}$—Ga2—O1$^{xiii}$ | 114.63 (11) |
| O1—Tb1—O1$^{vi}$ | 67.84 (16) | O1$^{xiii}$—Ga2—O1$^{xii}$ | 99.6 (2) |
| O1$^{ii}$—Tb1—O1$^{i}$ | 67.84 (16) | | |

Symmetry code(s): (i) −*x*+1/4, −*z*+5/4, −*y*+5/4; (ii) *z*−1/4, −*y*+7/4, *x*+1/4; (iii) *y*−1/2, *z*+1/2, *x*+1/2; (iv) −*x*+1/2, *y*, −*z*+1; (v) *x*+1/4, −*z*+5/4, *y*−1/4; (vi) −*y*+1, *z*+1/2, −*x*+1/2; (vii) −*z*+3/4, −*y*+7/4, −*x*+3/4; (viii) −*x*+1/2, −*y*+3/2, −*z*+1/2; (ix) −*z*+1/2, −*x*+1, *y*−1/2; (x) *y*−1/2, −*z*+1, *x*; (xi) *z*, *x*+1/2, −*y*+1; (xii) −*z*+3/4, −*y*+5/4, *x*+1/4; (xiii) *z*−1/4, −*y*+5/4, −*x*+3/4.

# 1º Workshop de Materiais Fotônicos do IQAr

# CERTIFICADO

Certificamos que **Juliane Resges Orives** participou como **organizadora** do **1º Workshop de Materiais Fotônicos do IQAr**, realizado no período de 31 de Julho a 02 de Agosto de 2023, no Instituto de Química da UNESP em Araraquara – SP.

Araraquara – SP, 02 de Agosto de 2023

_____

Prof. Dr. Marcelo Nalin

(Organizador)